FATIGUE BEHAVIOR OF WELDED CONNECTIONS ENHANCED WITH UIT AND BOLTING

By

Brian Vilhauer
Caroline Bennett
Adolfo Matamoros
Stan Rolfe

A Report on Research Sponsored by

THE KANSAS DEPARTMENT OF TRANSPORTATION
K-TRAN PROJECT No. KU-07-1

Structural Engineering and Engineering Materials
SM Report No. 91
March 2008

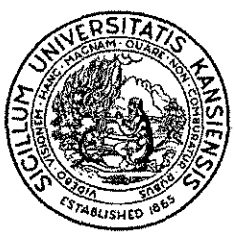

THE UNIVERSITY OF KANSAS CENTER FOR RESEARCH, INC.
2385 Irving Hill Road – Campus West, Lawrence, Kansas 66045

FATIGUE BEHAVIOR OF WELDED CONNECTIONS ENHANCED WITH UIT AND BOLTING

By

Brian Vilhauer
Caroline Bennett
Adolfo Matamoros
Stan Rolfe

A Report on Research Sponsored by

THE KANSAS DEPARTMENT OF TRANSPORTATION
K-TRAN Project No. KU-07-1

Structural Engineering and Engineering Materials
SM Report No. 91

THE UNIVERSITY OF KANSAS CENTER FOR RESEARCH, INC.
LAWRENCE, KANSAS

March 2008

ABSTRACT

A common problem in bridges employing welded steel girders is development of fatigue cracks at the ends of girder coverplates. Fatigue cracks tend to form at the toes of the transverse welds connecting a coverplate to a girder flange since this detail has a region of very high stress concentration. Because many aging bridges employ these fatigue-prone, AASHTO fatigue Category E or E' details, a means to effectively enhance the fatigue lives of these details is being sought. A research project funded by the Kansas Department of Transportation was undertaken at the University of Kansas to investigate the fatigue life enhancement afforded by two retrofit methods. One retrofit method was similar to a method described in the AASTHO Bridge Design Specification (AASHTO 2004) and involved pretensioned bolts being added to the ends of coverplates near the transverse welds. Unlike the AASHTO bolting procedure, the modified bolting procedure studied during this project utilized coverplates having transverse fillet welds that were left in the as-fabricated state. The other retrofit method was the use of a proprietary needle peening procedure called Ultrasonic Impact Treatment (UIT). Results of the research project showed that UIT was highly effective at enhancing the fatigue lives of coverplate end details while the bolting procedure was ineffective. Weld treatment with UIT resulted in an improvement in fatigue life over control specimens by a factor of 25. This translated in an improvement from an AASTHO fatigue Category E detail rating to and AASHTO fatigue Category A detail rating. The modified coverplate bolting procedure tested during this project had either no effect on fatigue life or, in some cases, had a detrimental effect on fatigue life. The coverplate bolting procedure included in the AASHTO specification allows a coverplate end detail to achieve a fatigue Category B resistance when bolted rather than transversely welded.

Therefore, the modified bolting procedure tested during this project was much less effective at enhancing fatigue life than either the AASHTO bolting procedure or UIT.

ACKNOWLEDGEMENTS

The researchers are grateful to the Kansas Department of Transportation for funding this research.

The researchers would like to thank the businesses that donated materials, labor, and other resources to the project. All specimens were fabricated and donated to the project by Builders Steel Company of Kansas City, Missouri. UIT treatment was performed free-of-charge by Applied Ultrasonics in Birmingham, Alabama.

TABLE OF CONTENTS

LIST OF FIGURES

LIST OF TABLES

CHAPTER 1 INTRODUCTION

1.1 PROBLEM STATEMENT

The Kansas Department of Transportation (KDOT), like most other state transportation departments, maintains a large inventory of bridges built in the mid-1900's that are supported by welded steel girders and bracing. Unfortunately, these bridges were designed at a time when little was known about the causes of fatigue crack initiation and propagation in welded structural steel. As a result, numerous details having fatigue-prone combinations of geometry and design stress were included in the design of many of these structures. A number of bridges in the KDOT inventory that incorporate these fatigue-prone details have developed fatigue cracks. Considering the escalating cost of bridge replacement, coupled with the large number of aging bridges having fatigue-prone details in their inventory, KDOT is seeking a means to efficiently extend the usable lives of bridges incorporating fatigue-prone details as an alternative to replacement.

Existing retrofit methods used to mitigate cracking at fatigue-prone details in steel structures include, among others, hammer peening, shot peening, tungsten inert gas (TIG) remelting, and weld toe grinding. These conventional methods, although somewhat effective at extending fatigue life, have several disadvantages. Some disadvantages shared by the conventional methods are that skilled, specialized laborers are required to effectively perform the retrofits, large amounts of time are required to complete the retrofits, and the extensions in fatigue life resulting from the retrofits are not great enough to warrant performing the retrofits. Most importantly, a structure being retrofitted using conventional methods typically must be taken out of service for the duration of the retrofit. Additionally, the hammer peening technique poses health hazards to the equipment operators from excessive noise and vibration. Obviously, there is a need to find a safe, efficient alternative to conventional methods for extending the fatigue life of bridge details.

One simple technique that is hypothesized to extend the life of fatigue-prone details is a modification of a bolting procedure included in the American Association of State Highway and Transportation Officials (AASHTO) Load and Resistance Factor Design (LRFD) Bridge Design Specification (AASHTO 2004). The AASHTO Specification describes a procedure by which pretensioned bolts are used to attach the last 30 to 46 mm (12 to 18 in.) of a coverplate to a girder flange in lieu of fillet welds. This is done to eliminate the need for transverse fillet welds at the coverplate ends, which are highly prone to fatigue failure. Transverse fillet weld details at coverplate ends are classified as AASHTO fatigue Category E details or Category E' details (depending on coverplate thickness), which are the most fatigue-prone details defined by AASHTO. Using pretensioned bolts for the last 30 to 46 mm (12 to 18 in.) of the coverplate in lieu of transverse and longitudinal fillet welds improves the end details of a coverplate to AASHTO fatigue Category B details, which are the second-least fatigue-prone detail defined by AASHTO. A detailed discussion of the AASHTO fatigue categories is included in section 3.2.2. A summary of the research that led to the addition of this procedure to the AASHTO Specification can be found in section 2.5. This procedure, although highly effective at extending fatigue life for conventional coverplate details, is best suited for new construction. Use of this procedure as a retrofit technique requires both longitudinal and transverse welds near the ends of a coverplate to be ground out prior to the addition of pretensioned bolts, making it a very labor intensive procedure.

The hypothesized method of extending fatigue life is similar the AASHTO method except that it is designed specifically to be used as a retrofit for existing bridges having fatigue-prone coverplate details. Similar to the AASHTO procedure, the hypothesized retrofit method includes the addition of pretensioned bolts to the ends of an existing coverplate that is fillet welded to a bridge girder. Unlike the AASHTO procedure, the transverse fillet welds at the ends of the coverplate will

remain in their original state. This procedure is hypothesized to transfer the tensile forces in the girder flange to the coverplate through the slip-critical bolted connections rather than through the transverse fillet welds. Additionally, it is hypothesized that the compressive stresses introduced into the flange and coverplate by the pretension in the bolts will be large enough to reduce the residual tensile stresses in the transverse welds to some degree.

Similar bolting procedures have already been used, both alone and in combination with other retrofit methods, to extend the lives of fatigue-prone details for bridges in the KDOT inventory. Because these retrofits were performed recently, their effectiveness at enhancing the fatigue lives of these details has not yet been determined. Although a finite element analysis performed at the University of Kansas as part of a previous research project indicated that the addition of pretensioned bolts to fatigue-prone details decreased stress concentration and significantly enhanced fatigue performance, the modified bolting procedure must be experimentally shown effective at extending fatigue life for its use as a retrofit technique to be continued. This retrofit technique, although simple, was hoped to be as effective at increasing the fatigue life of existing coverplate details as the existing AASHTO procedure is at increasing the fatigue life of new coverplate details.

A second new and promising retrofit technique for extending the lives of fatigue-prone weld details is the use of Ultrasonic Impact Treatment (UIT). UIT is a proprietary needle peening procedure developed in the 1970's by Dr. Efim Statnikov for use by the Soviet navy. The technology was only recently introduced in the United States in the late 1990's. Thus, a limited amount of research investigating the use of UIT as it applies to fatigue-prone bridge details has been performed in the United States The developers of UIT claim that the fatigue life of a weld detail treated with UIT is enhanced by (1) introducing compressive stress at the treated surface through physical deformation, (2) relaxing residual tensile stress in the weld

through ultrasonic stress wave propagation, (3) reducing stress concentration at the detail by improving the geometry of the weld toe, and (4) reducing micro-discontinuities in the material at the treated surface. A thorough discussion of the theory underlying UIT as well as a comprehensive review of previous research that has been performed with regards to UIT can be found in Chapter 2. Previous research performed in Europe as well as preliminary research performed in the United States indicates that the lives of fatigue-prone weld details can be significantly enhanced through treatment with UIT.

1.2 OBJECTIVE

Although the effectiveness of UIT has been demonstrated by a limited amount of previous research, no investigations to determine the effectiveness of the proposed modified coverplate bolting technique have been performed. In addition, little research has been performed to investigate the effectiveness of UIT when it is used in combination with other fatigue life improvement methods.

To allow KDOT and other state transportation departments to safely and confidently employ UIT and the proposed modified coverplate bolting technique alone and in combination, the methods must first be shown to be effective at enhancing fatigue life. To that end, a research project funded by KDOT was performed at the University of Kansas. The objective of the research project was to determine the effectiveness of UIT and the proposed modified coverplate bolting technique, both individually and in combination, at improving the fatigue performance of weld details similar to those found on the bridges in the KDOT inventory. The objective was achieved by performing fatigue tests on a series of steel specimens employing combinations of the two retrofit techniques. Chapters 3 and 4 discuss the test methods and results of the fatigue testing, respectively. A secondary objective of this research project was to compare the results of the experimental testing to the results of a series of finite element models. The results of the finite

element models are discussed in Chapter 5. Conclusions and recommendations are provided in Chapter 6.

CHAPTER 2 BACKGROUND

2.1 THEORY OF UIT

Ultrasonic Impact Treatment (UIT) was developed in the late 1960's and 1970's by a team of researchers headed by Dr. Efim Statnikov at the Northern Scientific and Technology Company (NSTC) in Severodvinsk, Russia. The UIT process was developed as a means to improve the state of stress and geometric characteristics of a metal weldment to extend its fatigue life. The following sections describe the various mechanisms through which UIT improves the fatigue characteristics of a weldment as well as the equipment and procedure used for treatment.

2.1.1 Ultrasound and Metal Plasticity

One of the primary mechanisms through which UIT improves the fatigue characteristics of a weldment is the relaxation of residual welding stresses through introduction of ultrasonic stress waves at the surface of the weld. The phenomenon of altering material properties using ultrasonic stress waves was discovered by multiple groups of researchers in the late 1950's. One of the earliest studies regarding ultrasound and metal plasticity was performed by Bertwin Langenecker at the U.S. Naval Ordinance Test Station in California (Langenecker 1966). In this study, tensile specimens made of various metals were stressed while an ultrasonic transducer horn intermittently applied various intensities of ultrasound to the specimens throughout the duration of each tension test. It was found that during application of ultrasound above a specific intensity, the metals would continue to deform during the tension test but the stress in each specimen would fall to nearly zero. This phenomenon of plastic deformation under zero stress during application of ultrasonic stress waves was termed "acoustic softening." It was determined that the principle of acoustic softening is very similar to that of heating metal. Similar to heating, acoustic energy from an ultrasonic source is absorbed at dislocations in the

metal lattice, causing a reduction in shear stress in the metal. However, much less energy is required for effective acoustic softening than heating because application of heat is distributed homogeneously to all atoms of the lattice rather than just the dislocations in the lattice that control deformation of the material. When this research was published, the author suggested the benefits of using ultrasound in metal forming and drawing wires, not realizing its potential as a post-weld treatment.

Soon after the effects of ultrasound on metal plasticity were discovered, Dr. Statnikov and the research team at NSTC began experimenting with application of ultrasonic stress waves to weldments to eliminate residual tensile stresses that exist as a result of weld cooling. The research team found it difficult to consistently apply ultrasound to a weldment because high-quality acoustic contact between the ultrasonic oscillating system and the item being treated could not be achieved (Statnikov et al. 2005). Their solution to this problem was the development of the UIT method, which combined the concepts of ultrasound and needle peening. During UIT treatment, freely moving needle indenters are excited by pulses from an ultrasonic oscillation system. The needle indenters, when excited, travel axially along guide holes and impact a weld surface. As the weld surface deforms plastically under the impact from an individual needle, ultrasonic stress waves efficiently transfer into the weld (Statnikov 2004). Research programs utilizing metallographic and X-ray diffraction analysis (Statnikov 1997) have shown that propagation of ultrasonic stress waves imparted by UIT causes a 50% reduction in residual weld stress to a depth of 12 mm (0.47 in.) below the weld surface.

2.1.2 Other Mechanisms of UIT

Along with ultrasonic stress wave propagation, other mechanisms of the UIT process contribute to enhancing fatigue properties of weldments (Statnikov 2005). As described in the previous section, the UIT process involves plastic deformation of the weld metal at the immediate location of treatment. Depending on the diameter of the

needle indenters and model of UIT equipment used, the zone of plastic deformation ranges from 4.00-7.00 mm (0.157-0.276 in.) wide and 0.100-0.600 mm (0.004-0.024 in.) deep, referred to as "undercut." As a result of this plastic deformation, a compressive stress on the order of the yield strength of the weld metal is induced adjacent to the deformed surface. Because fatigue cracks form primarily at regions of high tensile stress, the introduction of this large compressive stress greatly retards or eliminates formation of fatigue cracks at the immediate location of treatment. Since UIT is generally performed at regions having the greatest tensile stress concentrations, usually the weld toes and weld discontinuities, the regions most prone to fatigue crack growth benefit the most from induced compressive stresses.

When UIT treatment is performed at the toe of a fillet weld, the geometry of the zone of plastic deformation also reduces the concentration of stress at the weld toe. This is due to the fact that the treated surface has a larger radial shape than does an untreated weld toe. A typical profile of a fillet weld treated with UIT is shown in Figure 2.1.

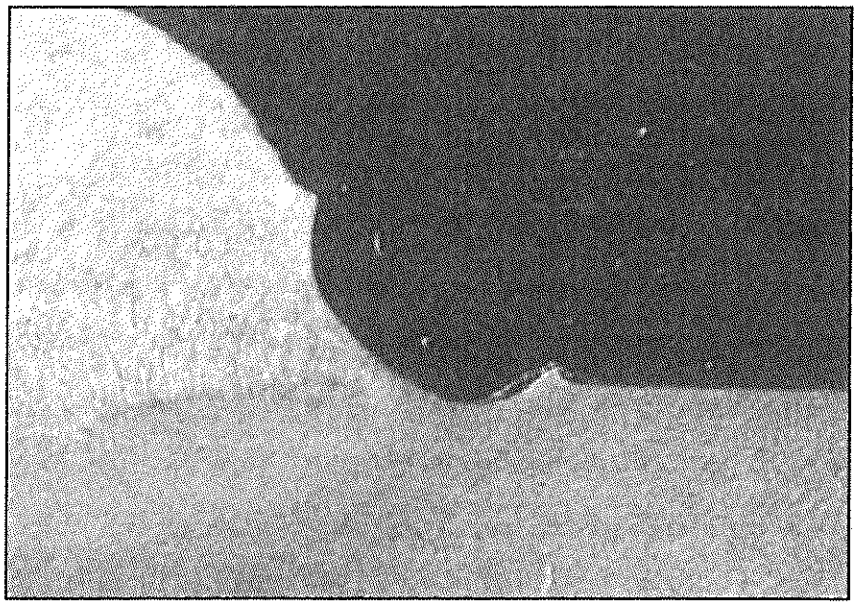

Figure 2.1. Profile of a weld toe treated with UIT (Galtier et al. 2003).

Other benefits of UIT include a reduction of micro-discontinuities at the treated surface and an improvement in corrosion-fatigue resistance at the treated surface. It is well-known that a reduction in size of micro-discontinuities at the surface of a metal object subjected to cyclic loading increases the number of cycles to fatigue crack initiation.

2.1.3 UIT Equipment and Procedure

The equipment used to perform UIT consists of a handheld application tool connected to an ultrasonic generator. The application tool contains an ultrasonic magnetostrictive transducer made from permendure, which is an iron-cobalt alloy containing vanadium, and the needle indenters. Permendure transducers having operating frequencies of 27, 36, 44, and 55 kHz have been developed for use with UIT equipment. A recent study (Statnikov el at. 2004) comparing the effectiveness of UIT treatment using the different transducers determined that all of the transducers provided similar surface compressive stresses. However, transducers with higher frequencies provided a greater treatment capacity in a unit of time as well as smoother treated surfaces. In addition, the application tools with higher frequency transducers are smaller, lighter, and easier to operate than the older, lower frequency transducers. Figure 2.2 shows the 27 kHz UIT ultrasonic generator and handheld application tool. Figure 2.3 shows the different handheld UIT application tools and Table 2.1 lists their size and weight. The needle indenters used to treat the weld surface are manufactured in a variety of configurations and are replaceable. Most needles measure 2.00-5.00 mm (0.079-0.197 in.) in diameter. Figure 2.4 shows a common needle configuration and the treated surface produced by the configuration.

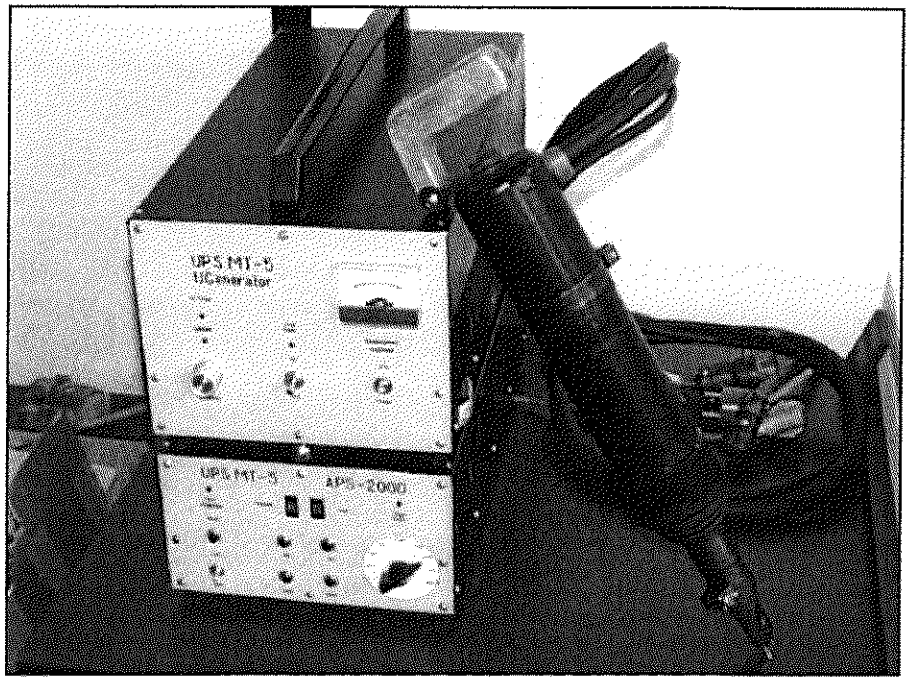

Figure 2.2. 27 kHz UIT generator and application tool (Lihavainen et al. 2003).

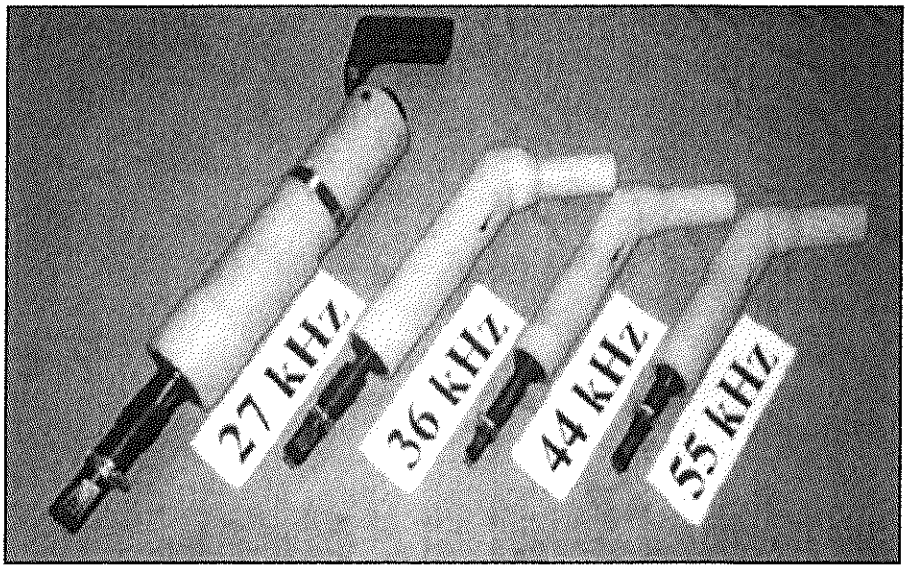

Figure 2.3. Range of UIT handheld application tools (Statnikov 2004).

Table 2.1. UIT handheld tool characteristics (Statnikov 2005).

UIT Tool Characteristics		Frequencies, kHz			
		27	36	44	55
Maximum Power, W		1500	1200	900	600
Maximum Amplitude, mm (in.)	Without Load	0.0600 (0.0024)	0.0500 (0.0020)	0.0450 (0.0018)	0.0400 (0.0016)
	Under Load	0.0320 (0.0013)	0.0280 (0.0011)	0.0250 (0.0010)	0.0200 (0.0008)
Weight, kg (lb.)		2.70 (5.95)	1.10 (2.43)	0.63 (1.4)	0.50 (1.1)

Figure 2.4. UIT needle configuration and the treated surface (Lihavainen et al. 2003).

The procedure for applying UIT to a weld surface has been documented in a publication authored by Dr. Statnikov (Statnikov 1999). The UIT procedure consists of an operator holding the handheld application tool at an angle of approximately 45° with respect to the base metal and gradually moving the needle indenters along the weld toe. Multiple passes are usually made to ensure complete coverage. Adequacy

of treatment is easily monitored by visual examination of the treated surface and feedback from the ultrasonic generator. One of the biggest benefits of UIT over conventional peening processes is the ease with which the system is operated. Treatment with UIT requires the operator to apply no pressure to the application tool, has small vibrations, is ergonomically friendly to operate, and requires little operator training or degree of skill. The rate at which UIT can be performed varies depending on the frequency of the transducer but generally ranges from 5.0-25 mm/sec (0.20-0.98 in/sec). Treatment parameters and considerations specific to various weld configurations can be found in Dr. Statnikov's publication (Statnikov 1999).

2.2 PREVIOUS UIT RESEARCH

Although UIT was invented more than thirty years ago, limited research has been performed in the United States and abroad to quantify its effectiveness as a means of fatigue life enhancement. Abroad, the majority of published research has been performed at the E.O. Paton Electric Welding Institute in Kiev, Ukraine. Recent research has also been performed in France, Japan, Norway, and Sweden. In the United States, research regarding the effectiveness of UIT has been performed at Lehigh University in Bethlehem, Pennsylvania and at the University of Texas at Austin.

2.2.1 Early Research

After receiving a USSR Inventor's Certificate for the UIT equipment in 1972 (Statnikov et al. 1972), Dr. Statnikov and his associates, in collaboration with many prominent research institutes in the USSR, began testing the effectiveness of the UIT process. Much of the early research was performed for the Soviet naval program and shipbuilding industry, and was not widely published or was published in the Russian language only. Initial research performed in the 1970's focused on evaluating improvement in corrosion-fatigue strength and stress corrosion resistance for high-strength steels with high manganese content when treated with UIT (Statnikov et al.

2005). This research was carried out by Dr. Statnikov at Sevmash in collaboration with the Acoustic Institute of the Academy of Sciences of the USSR in Moscow. It was also during the 1970's that the first third-party tests of the technological effectiveness of UIT were conducted at the E.O. Paton Electric Welding Institute in Kiev, Ukraine by professors V.I. Trufyakov and P.P. Mikheev (Statnikov et al. 2005).

In the 1980's, a wide range of applications for the UIT process were beginning to be realized (Statnikov et al. 2005). The UIT process continued to find additional usefulness in the Soviet shipbuilding industry when UIT was demonstrated to improve fatigue resistance of welded joints in hull structures. At the same time, the first investigations into the applicability of UIT to fatigue-prone welded bridge details were conducted at the E.O Paton Electric Welding Institute with the help of Dr. Statnikov. The results of these programs were not published internationally.

2.2.2 International Research

After more than two decades of research and development of UIT, the first internationally published results were presented by the International Institute of Welding (IIW) in the mid-1990's. Much of early internationally published work is the result of research carried out by Dr. Statnikov at NSTC in collaboration with many leading welding institutes in Europe and Russia. The various research programs investigated the effectiveness of UIT for different weld geometries and material types and compared UIT to other fatigue enhancement procedures.

2.2.2.1 Butt Welded and Fillet Welded Joints

One of the first projects to be published by the IIW was a collaborative effort among the NSTC, the E.O. Paton Institute, and the Welding Institute of France (Janosch et al. 1996). This project was an effort to quantify the improvement in fatigue strength of butt weld details and fillet weld details treated with UIT for small specimens fabricated from various metals. The three metals used in the study were a high strength E460 steel having a yield strength of 543 MPa (78.7 ksi), a high

strength E690 steel having a yield strength of 763 MPa (111 ksi), and a 6061 T6 aluminum alloy having a yield strength of 240 MPa (34.8 ksi). The butt welded specimens had overall dimensions of 10×95×400 mm (0.40×3.7×15.8 in.) with a reduced width at the weld and were welded using robotic MIG welding. The fillet welded specimens measured 10×140×60 mm (0.40×5.51×2.4 in.) and were welded using arc welding with covered electrodes. The weld toes were treated with UIT for half of the specimens and the rest were left in the as-welded condition for comparison. Fatigue testing was conducted under constant amplitude tensile loading and 4-point bending for the butt weld and fillet weld specimens, respectively. Testing was carried out at varying stress ranges, a constant stress ratio of 0.1, and a frequency of 30 Hz until complete failure or run-out defined as 6×10^6 cycles.

Bastenaire's method was used to statistically determine 10%, 50%, and 90% equiprobability curves on the S-N diagram for each of the combinations of weld type and metal. To evaluate the effectiveness of UIT, the endurance limit (stress range) achieved for the 50% equiprobability curve at 2×10^6 cycles for each of the treated specimen types was compared to that of the corresponding as-welded specimen type. For the E460 fillet welded specimen, the endurance limit of the treated specimen was 73% larger than that of the as-welded specimen. The treated E690 fillet welded specimen had an endurance limit roughly three times as large as the as-welded specimen (192% increase). The treated E690 butt welded specimen had an endurance limit that was 74% larger than that of the as-welded specimen. Finally, the treated 6061 T6 butt welded specimens had an endurance limit that was 21% larger than that of the as-welded specimens.

Although these results were positive, there was a great deal of variability in the results. Possible explanations given for the variability included varying weld quality between the two welding methods, different modes of loading, and an

apparent proportionality between yield strength and obtainable gain in fatigue limit. It was obvious that more research had to be done to resolve these issues.

2.2.2.2 Welded Tubular Connections

Because of the complex geometry and high stress concentrations associated with welded tubular connections, the results of previous research for planar specimens (Janosch et al. 1996) could not be used for the design of such connections utilizing UIT. To quantify the improvement in fatigue strength of welded tubular connections treated with UIT, a research program was conducted at the E.O. Paton Welding Institute in conjunction with the NSTC (Mikheev et al. 1992; Mikheev et al. 1996).

For this program, T-shaped welded connections were fabricated from round tubes made of low-alloy steel with a minimum yield strength of 296 MPa (42.9 ksi). The specimens consisted of a "brace" member having a diameter ranging from 159.0-219.0 mm (6.260-8.622 in.) welded to the side of a "chord" member having a diameter ranging from 216.0-245.0 mm (8.504-9.646 in.). The thicknesses of the tubes were also varied from 4.4-8.4 mm (0.17-0.33 in.). The weld toes of half of the specimens were treated with UIT while the remaining specimens were left in the as-welded condition for comparison. A fully-reversed cyclic load was applied to the end of the brace to cause an alternating moment in the connection between the two members. Fatigue testing consisted of constant amplitude, stress-controlled cycling at various stress ranges, a constant stress ratio of -1.0, and a frequency of 10 Hz.

All of the specimens tested failed from cracking initiating in the connection weld and propagating into the chord element. Tube size did not have a significant effect on fatigue life. Results showed that the amount of improvement in fatigue life afforded by UIT varied proportionally with decreasing stress range, suggesting that a slope other than -3 may be a better fit for the curve for UIT treated details on the S-N diagram. On the S-N diagram, the curve for the treated specimens intersected the

curve for the as-welded specimens at roughly 10,000 cycles. At or below this number of cycles, UIT showed no improvement over the as-welded specimens. At lower stress ranges near the endurance limit, the improvement afforded by UIT was dependent on the definition of failure. When failure was defined as the formation of a macrocrack with a surface length of 15.0-20.0 mm (0.591-0.787 in.), the fatigue limit of treated specimens was twice that of as-welded specimens. When failure was defined as total fracture corresponding to a crack length equal to 75% of the perimeter of the welded joint, the fatigue limit of treated specimens was increased by 40-50% that of as-welded specimens. Regardless of how failure was defined, UIT treatment was shown to have a significant effect on improving the fatigue strength of a welded tubular connection. Tests on a limited number of larger welded tubular specimens supported the data on improvement found from the smaller specimens.

2.2.2.3 Lap Joints and Longitudinal Stiffeners

An investigation performed by the Norwegian University of Science and Technology, the NSTC, and Swedish Steel AB (SSAB) evaluated the effectiveness of UIT at improving the fatigue lives of steel and aluminum specimens with lap joint welds and longitudinal stiffener welds (Haagensen et al. 1998). The materials used in this program were Weldox 700 steel with a specified yield strength of 700 MPa (102 ksi) and AA5083 (or AlMg4.5Mn) aluminum with a minimum yield strength of 250 MPa (36.3 ksi). For the set of steel specimens, longitudinal stiffeners measuring 150 mm (5.91 in.) long by 6.0 mm (0.24 in.) thick were fillet welded to both sides of 6.0 mm (0.24 in.) thick steel plates. No lap joint specimens were fabricated from steel. Each of the steel specimens was then either treated with UIT, TIG dressed, or TIG dressed and then treated with UIT. For the set of aluminum specimens, lap joint specimens with full-thickness end welds on both sides of the lap joint were fabricated from 8.0 mm (0.31 in.) thick plates in addition to specimens with longitudinal stiffeners similar in dimension to those made of steel. Each of the aluminum

specimens was either left in the as-welded condition or treated with UIT. All specimens were then tested under constant amplitude tensile fatigue loading at varying stress ranges, a constant stress ratio of 0.1, and a frequency ranging from 3-10 Hz.

By testing the specimens at various stress ranges, a failure curve or envelope could be drawn on an S-N diagram for each of the combinations of material type and treatment. Results of the testing showed that for the steel specimens, the failure curves on the S-N diagram for the UIT-treated specimens and the TIG dressed plus UIT-treated specimens were virtually identical. This suggested that little or no additional gain in fatigue life could be achieved by TIG dressing prior to UIT treatment when compared to UIT treatment alone. On the S-N diagram, the failure curve for the UIT-treated steel specimens intersected 2×10^6 cycles at a stress range of 190 MPa (27.6 ksi), which was approximately 120% larger than the stress range of 86 MPa (13 ksi) achieved by the failure curve for the as-welded steel specimens at the same number of cycles.

Aluminum specimens with longitudinal stiffeners showed slightly lower gains in fatigue strength. On the S-N diagram, the failure curve for the aluminum specimens treated with UIT intersected 2×10^6 cycles at a stress range of 68 MPa (9.9 ksi), which was 94% larger than the stress range of 35 MPa (5.1 ksi) achieved by the failure curve for the as-welded aluminum specimens at the same number of cycles. These results demonstrated that the improvement in fatigue life from UIT was less for aluminum than for steel. This phenomenon has been observed in other studies (Janosch et al. 1996) and is due mainly to the lower compressive residual stress left by UIT in aluminum because of its lower yield strength. The lap joint specimens achieved gains in fatigue strength that were similar to the results for aluminum specimens with longitudinal stiffeners. On the S-N diagram, the failure curve for the lap joint specimens treated with UIT intersected 2×10^6 cycles at a stress range of 35

MPa (5.1 ksi), which was 77% larger than the stress range of 20 MPa (2.9 ksi) achieved by the failure curve for the as-welded lap joint specimens at the same number of cycles. The results of this project showed a gain in fatigue strength from UIT ranging from 77-120%.

2.2.2.4 Comparison of Fatigue Life Improvement Methods

By the late 1990's, many different fatigue life improvement methods had been developed and all were touted as highly effective techniques. To compare the effectiveness of some of the most common techniques, a research program was undertaken at the E.O. Paton Welding Institute in cooperation with Applied Ultrasonics of Birmingham, Alabama and SSAB (Statnikov et al. 2000). The specimens used in this study were fabricated from Weldox 420 steel with a minimum yield strength of 420 MPa (60.9 ksi). All specimens had identical dimensions of 750×60×20 mm (29.5×2.4×0.79 in.) with a reduced width in the middle of the plate where a transverse stiffener was fillet welded to one face of the plate. Each of the specimens was then given one of the following weld treatments: as-welded (no treatment), UIT, hammer peening, shot peening, TIG dressing, and TIG dressing followed by UIT. The specimens were then tested to failure under 4-point bending at various constant amplitude stress ranges, a stress ratio of 0.1, and a frequency of 7 Hz.

Results of the testing showed that UIT outperformed all other improvement methods in the high-cycle regime. By testing the specimens at various stress ranges, a failure curve could be drawn on an S-N diagram for each of the different improvement methods. On the S-N diagram, the failure curve for the specimens treated with UIT intersected 2×10^6 cycles at a stress range of 328 MPa (47.6 ksi), which was 65% larger than the stress range of 198 MPa (28.7 ksi) achieved by the failure curve for the as-welded specimens at the same number of cycles. When compared to the specimens treated with UIT alone, specimens treated with UIT after

being TIG dressed showed a lower improvement of 51% over the as-welded specimens at 2×10^6 cycles. This reduction in improvement is similar to that found in other research (Haagensen et al. 1998). The improvement for all other methods ranged from 41-44% at 2×10^6 cycles when compared to the as-welded specimens. At shorter fatigue lives (higher stress ranges), the improvement in fatigue life from UIT was comparable to those of the other improvement methods. Also, the linear regression for specimens treated with UIT had a slope of roughly -17.5, which is much flatter than the value of -3 used on the AASHTO S-N diagram (AASHTO 2004).

2.2.2.5 UIT as a Weld Repair Technique

Recent investigations have aimed to evaluate the effectiveness of UIT as a weld repair technique to extend the fatigue lives of aging structures. One such study, performed at the University of Stuttgart in Germany, evaluated the effectiveness of UIT at extending the fatigue lives of welded joints that had already been subjected to 75-90% of their average as-welded fatigue lives prior to treatment (Günther et al. 2005). The purpose of this was to simulate the behavior of a UIT retrofit after a certain amount of fatigue damage had been sustained.

The specimens were fabricated from grade S460M steel having a yield strength of 460 MPa (66.7 ksi). For the purpose of replicating a fillet weld detail connecting a transverse stiffener to a girder flange, each small-scale specimen consisted of a plate with a T-joint fillet welded to the front and back of the plate. In addition to testing specimens that were UIT retrofitted after being cycled to 75-90% of their fatigue lives, both as-welded specimens and specimens treated with UIT immediately after fabrication were tested to establish a comparison. Each of the UIT-treated specimens was visually examined under 10× magnification and inspected using magnetic particle inspection prior to UIT treatment to ensure that no cracks existed. No cracks larger than 1.0-1.5 mm (0.04-0.06 in.) were detected. Fatigue

testing was performed under constant amplitude tensile loading at various stress ranges and a stress ratio of 0.1.

The results of this testing showed that specimens treated with UIT immediately after fabrication had a failure curve on an S-N diagram that intersected 2×10^6 cycles at approximately double the stress range achieved by the failure curve for the as-welded specimens at the same number of cycles. In comparing the UIT-retrofitted specimens to the as-welded specimens, it was found that the fatigue lives of the retrofitted details were extended by a minimum factor of 2.5 times the age at which they were treated, which was approximately equal to the as-welded life. This means that retrofitted details treated with UIT were, at a minimum, restored to their original fatigue resistance. However, none of the UIT-retrofitted specimens achieved lives equal to the specimens that were treated immediately after fabrication. This may indicate that during the initial cycling of retrofitted specimens, some damage occurred in that was not entirely removed during UIT treatment.

A similar research program was undertaken at Lehigh University investigating specimens of AL-6XN superaustenitic stainless steel with a minimum yield stress of 310 MPa (45.0 ksi) (Cheng et al. 2004). This program studied the effectiveness of various weld repair methods such as gas tungsten arc (GTA) remelting, grinding plus welding, air hammer peening, and UIT. Through testing, the range of flaw sizes that could effectively be repaired by each method was established. This study found that for very shallow cracks less than 1.6 mm (0.063 in.) in depth, UIT extended the fatigue lives of the details but was less effective than air hammer peening. The researchers also suggested using UIT only when detectable flaws cannot be found in the weld. This data demonstrated the limited applicability of UIT as a retrofit technique. To safely extend the fatigue life of a structure using UIT, all of the welds must be free of detectable cracks prior to treatment, meaning that considerable effort must be expended to inspect these welds.

2.2.3 FHWA Research

Ultrasonic Impact Treatment was first introduced in the United States on June 6, 1996 when a demonstration of the procedure was held at the Federal Highway Administration's (FHWA) Turner-Fairbank Highway Research Center in McLean, Virginia. Fenix Technology International demonstrated the UIT process on a large welded plate girder fabricated from 345 MPa (50.0 ksi) structural steel conforming to ASTM A-572 standards with transverse stiffeners fillet welded to both sides of the girder web. All weld toes attaching the transverse stiffeners to the girder were treated with UIT. According to AASHTO (2004) design specifications, the stiffener welds were Category C' details. Preliminary testing of the UIT process was performed on cruciform samples that were cut from the web of the girder where the stiffeners were attached (Wright 1996). Each of the specimens was tested under fatigue loading at a stress range of 130 MPa (18.8 ksi), a stress ratio of 0.5, and a frequency of 20 Hz until complete failure of the specimen occurred.

The test results showed that, on average, the fatigue lives of the treated weldments were approximately eight times greater than those of the untreated weldments. Using statistical analyses, it was found that weldments treated with UIT achieved an AASHTO Category B detail and the untreated weldments remained a Category C' detail. Although the results of this study showed that UIT was effective under the given conditions, more research was suggested to examine effects of variable stress range, stress ratio, untreated detail type, weldment type, and specimen size.

2.2.4 Lehigh University Research

Following promising results of preliminary testing, the FHWA and the Pennsylvania Department of Transportation funded an extensive research program at Lehigh University to further evaluate the effectiveness of UIT. Since all previous research abroad focused on small-scale specimens, and since the FHWA's interest in

UIT was primarily focused on large bridge girders, Lehigh University began a three-phase research project on full-scale welded plate girders and rolled beams. The goal of the research was to determine the fatigue strength of UIT-treated fillet welds at stiffener and coverplate details commonly used in existing and new bridge girders. The three phases of the full-scale testing were carried out at Lehigh University's ATLSS Engineering Research Center. Additional research was also conducted on smaller specimens to measure the residual compressive stresses induced by UIT.

2.2.4.1 Phase I

The first phase of research was a pilot study performed on three large plate girders (Takamori and Fisher 2000). Each of the three identical welded plate girders was fabricated from HPS-485W (70W) structural steel and was approximately 1000 mm (36.00 in.) deep and 6700 mm (264.0 in.) long. Full-depth transverse stiffeners were welded to the web and flanges of each girder at four locations and 25.4 mm (1.00 in.) thick coverplates were welded to the bottom flange at both ends of each girder. The stiffeners and coverplates were fabricated from A588 Grade 345 (50) structural steel.

According to AASHTO (2004) specifications, the stiffeners and coverplates were Category C' and E' details, respectively. To compare the performance of UIT-treated details to untreated details, eight of the 12 stiffeners were treated with UIT at the toes of the fillet welds connecting the stiffeners to the bottom flange. Three of the six coverplates were treated with UIT at the toes of the transverse fillet welds at the coverplate ends. Constant amplitude fatigue testing was performed under four-point bending at a constant stress ratio of approximately 0.1. To determine fatigue performance at different stress ranges, the local stress range at all details was varied from 55-131 MPa (8.0-19.0 ksi).

Results of the testing showed that, similar the FHWA results, all treated stiffener details exceed Category B requirements while untreated stiffener details fell

near the Category C curve. Only one of the treated stiffener details developed a fatigue crack. An even larger improvement was seen in the coverplate details; all three treated details exceeded Category C requirements, none of which developed cracks. The untreated coverplate details remained Category E' details. These results proved that UIT treatment was effective at improving the fatigue life of welded details. However, more research was needed to examine the effects of dead load, additional stress ranges, and existing cracks.

2.2.4.2 Phase II

Since all of the girders tested in Phase I failed due to longitudinal web-flange weld defects, this Phase II utilized 18 W27×129 wide flange beams rolled from structural steel conforming to ASTM A588-97B Grade 50W specifications with a minimum yield stress of 366-435 MPa (53.1-63.1 ksi) (Roy el at. 2003). Full-depth transverse stiffeners and coverplates fabricated from 407 MPa (59.0 ksi) structural steel conforming to ASTM A709-97B Grade 50W specifications were welded to each of the girders similar to the first phase of research. The untreated stiffener and coverplate details were classified as AASHTO fatigue Categories C' and E', respectively.

Unlike Phase I, both the minimum stress and maximum stress were varied to investigate the effects of stress ratio and stress range on the fatigue performance of UIT treated details. The local stress range at all details varied from 52-200 MPa (7.5-29.0 ksi) and the stress ratio varied from less than 0.10 to 0.55. In addition, the sizes of the transverse fillet welds at the ends of the coverplates were varied to determine if this would have an effect on fatigue performance of treated coverplates. The fatigue-prone weld toes of all stiffener and coverplate details were treated with UIT on all specimens. Constant amplitude fatigue testing was performed under four-point bending.

Under fatigue loading, all of the 18 specimens failed at critical coverplate details; none of the stiffener details developed fatigue cracks. Results indicated that larger treated coverplate end welds showed greater increases in fatigue life than did smaller treated coverplate end welds. For instance, all treated coverplate end welds having sizes greater than or equal to half the thickness of the coverplate exceeded Category D resistance at high stress ranges, while all treated coverplates having no end welds only exceeded Category E resistance at high stress ranges.

It was found that enhancement in fatigue strength due to application of UIT was greater for low stress ranges than for high stress ranges. At low stress ratios (less than 0.1), coverplates with full-thickness end welds achieved Category D resistance at high stress ranges and Category B resistance at low stress ranges. This indicates that fatigue behavior of treated details may not fit the fixed slope of -3 on the S-N diagram used by AASHTO. In addition, an increase in stress ratio appears to have a negative impact on the effectiveness of UIT. At higher stress ratios (approximately 0.5), coverplates with full-thickness end welds achieved Category D resistance at high stress ranges and Category C resistance at low stress ranges. Thus, increasing the stress ratio decreased the fatigue limit from Category B to Category C resistance.

Completion of this phase of the testing led to the conclusion that under optimum loading and treatment conditions, UIT treatment has the capability to greatly raise the fatigue limit of a Category E' detail. For analysis and design, the authors of this paper suggested increasing the fatigue strength of a treated E' detail to Category D in the finite life region and Category B in the infinite life region when the stress ratio is less than or equal to 0.1. For stress ratios between 0.1 and 0.5, increasing the fatigue strength of a treated E' detail to Category E in the finite life region and Category C in the infinite life region was suggested. The reduced improvement suggested for higher stress ratios demonstrates the need to perform the UIT treatment after the service dead loads have been applied to the member.

2.2.4.3 Phase III

Since no pertinent data was collected for stiffener details in the first two phases of the project, a follow-up phase was undertaken for that purpose. The third phase of research was performed by Dr. Sougata Roy and Dr. John W. Fisher (Roy and Fisher 2004). In this phase, eight built-up plate girders were fabricated from HPS-690W, having a minimum yield strength of 725-760 MPa (105-110 ksi). The depth of the each of girders was either 750 mm (29.5 in.) or 850 mm (33.5 in.) and all girders were approximately 5500 mm (216.5 in.) long.

To isolate the critical stiffener details, no coverplates were welded to any of the specimens. At four locations along each of the specimens, full-depth transverse stiffeners were fillet welded to the web and flanges of the girder. The stiffeners were AASHTO Category C' details. Weld toes considered critical for fatigue were treated with UIT on all specimens. To investigate the effects of both stress range and stress ratio, the minimum local stress was varied from 63-166 MPa (9.2-24.1 ksi) and the local stress range was varied from 97-138 MPa (14 to 20.0 ksi), resulting in a range of stress ratios from 0.32-0.60. Constant amplitude fatigue testing was performed under four-point bending.

Results showed that at low stress ratios ($R \leq 0.5$), none of the critical stiffener details developed fatigue cracks. These tests were ended when either the longitudinal web-flange weld root developed fatigue cracks or run-out was achieved at 7.5×10^6 cycles. At high stress ratios ($R > 0.5$), the critical stiffener details failed after exceeding the Category B resistance curve. Considering the positive results of this phase of testing, the authors recommended improving the fatigue limit of Category C' details treated with UIT to a Category B resistance if the stress ratio is maintained below 0.5. Due to lack of data, no improvement in fatigue life was recommended in the finite-life region for a Category C' detail treated with UIT.

2.2.4.4 Residual Stress Measurement

Similar to previous work done abroad, researchers at Lehigh University measured changes in residual stress induced by UIT to gain an understanding of how UIT treatment affects crack growth as related to the principles of fracture mechanics. This research was considered necessary due to the fact that previous researchers measured residual stresses using outdated or ambiguous procedures and the results were inconsistent. Residual stresses were measured in both base metal and at weld toes that were treated with UIT.

One study coordinated by Xiaohua Cheng and Dr. John W. Fisher compared the residual stress at a weld toe treated with UIT to the residual stress at a weld toe without treatment (Cheng et al. 2003). The specimen tested was a cruciform shape cut from the web-flange fillet weld of a previously fatigue-tested plate girder fabricated from AL-6XN superaustenitic stainless steel with a minimum yield stress of 310 MPa (45.0 ksi). The weld on one side of the web was treated with UIT and the weld on the other side was left in the as-welded condition. For both the as-welded and treated weld toes, residual stresses perpendicular to the weld beads were measured at Lambda Research in Cincinnati, Ohio using the X-ray diffraction method. Since the X-ray diffraction method can only measure stress very near the surface (less than 10^{-3} inch in depth), surface material was removed electrolytically in eight steps so that subsurface stress measurements could be taken to a maximum depth of 2.8 mm (0.11 in.).

Results showed that for the as-welded side, perpendicular residual stresses were in tension ranging from 338 MPa (49.0 ksi) near the surface to 166 Mpa (24.1 ksi) at a depth of 2.8 mm (0.11 in.). This supported previous research showing that tensile residual stresses at as-welded weld toes were on the order of the yield strength of the material. For the treated weld toe, residual stresses were compressive from the surface to a depth of 1.0 mm (0.039 in.) and tensile thereafter. The maximum

compressive stress occurred very near the surface and was 869 MPa (126 ksi). This value was greater than the 750 MPa (110 ksi) ultimate strength of AL-6XN steel, indicating that the steel had been considerably work-hardened by UIT. The quite shallow depth of the compressive zone induced by treatment was also noted. This suggests that UIT improves fatigue performance primarily by greatly extending fatigue initiation life and should be used with extreme caution in retrofitting where cracks deeper than 1.0 mm (0.039 in.) may exist.

A similar research program to determine residual stresses induced by UIT on un-welded base metal was also performed at Lehigh University (Fisher et al. 2003). In this program, three plates of thickness varying from 13 mm (0.50 in.) to 25.4 mm (1.00 in.) were cut from A572 Grade 50 steel. On two of the plates, the centerline of the plate normal to the direction of rolling was treated with UIT; four passes were performed on one plate and 10 passes were performed on the other. For the third plate, the entire surface was treated with shot peening for comparison. Residual stresses parallel and perpendicular to the rolling direction of each plate as a function of the depth below the plate surface were found using either X-ray diffraction in combination with electrolytic surface removal or neutron diffraction. Neutron diffraction has an advantage over X-ray diffraction because it can measure residual stresses to 50 mm (2.0 in.) below the surface, thus enabling subsurface triaxial stress distributions to be mapped using a non-destructive procedure. Neutron diffraction testing was performed at the Center for Neutron Research of the National Institute of Standards and Technology in Maryland.

Results showed that the depth of the UIT induced compression layer was 1.65 mm (0.0650 in.) for the four-pass specimen and 1.60 mm (0.0630 in.) for the 10-pass specimen. This demonstrated that UIT treatment has a point of diminishing returns at which no further stress relaxation or cold working can be achieved with further treatment. Maximum compressive stresses perpendicular to the UIT treatment line

occurred very near the treated surface and were 302 MPa (43.8 ksi) and 460 MPa (66.7 ksi) for the four-pass and 10-pass specimen, respectively. Maximum stresses parallel to the treatment line were slightly greater than those perpendicular to the treatment line for both specimens, but were of little importance in extending fatigue life. The specimen that was treated with shot peening had maximum residual compressive stresses comparable to UIT treatment, but the depth of the compression layer was only roughly half that of UIT. The results of this work for UIT-treated specimens were in close agreement with results from previous research done at Lehigh University.

The results of these studies show that, in general, UIT treatment induces a layer of residual compressive stress that extends to a depth ranging from 1.0-1.5 mm (0.039-0.059 in.) below the surface. The maximum residual compressive stress perpendicular to the direction of treatment is found just below the treated surface and has a value approximately equal to the yield strength of the steel.

2.2.5 University of Texas-Austin Research

Recent investigations involving the use of UIT to extend the fatigue lives of traffic signal structures have been performed at the University of Texas at Austin. Cantilever traffic mast-arm structures are subjected to intense fatigue loading due to flutter from natural and traffic-induced wind forces. Thus, many aging traffic mast-arm connections have recently failed due to fatigue cracking. Two separate research programs were sponsored by the Texas Department of Transportation and are discussed in the following sections.

2.2.5.1 Socket and Stiffened Signal Mast Connections

One broad study performed at the University of Texas at Austin explored using multiple methods to attempt to solve the mast arm fatigue problem (Koenigs et al. 2003). One phase of this project explored the use of UIT at a welded socket connection between the mast arm and support as well as the use of UIT at the ends of

gusset-type stiffener plates installed at the same connection. For specimens employing only the socket connection, UIT was performed in two passes using 3.0 mm (0.12 in.) needle indenters for the first pass and 5.0 mm (0.20 in.) needle indenters for the second pass. For specimens with four gusset-type stiffeners welded at equidistant locations around the perimeter of the mast-arm connection, UIT was performed at both ends of each of the stiffeners and continued along both sides of the stiffeners for a distance of 51 mm (2.0 in.) from each end. Treatment of these details was performed in two passes as described previously. To determine the effects of stress ratio, specimens with socket details and specimens with stiffener details were UIT-treated with and without a simulated traffic signal dead load. Specimens employing socket type connections that were treated under dead loading were only treated on the half circumference subjected to tensile stress while specimens employing socket connections that were treated under no load were treated along the full circumference. All specimens were tested in fatigue loading simulating flutter at various levels of resultant connection stress and loading frequency.

Similar to the results of the testing programs performed at Lehigh University, the results of this testing showed that the effectiveness of UIT at extending fatigue life is highly dependent on the load/stress ratio. All of the specimens that were treated with UIT under no dead load showed no improvement in fatigue life over the control specimens. These specimens were treated at zero stress, subjected to a maximum stress of 193 MPa (28.0 ksi), and subjected to a stress range of 79.3 MPa (11.5 ksi). These stresses were the stresses at the connection detail as a result of the applied load. The stress ratio, with respect to the state of stress at UIT treatment, resulting from these loading conditions was 0.59. This large stress ratio has been shown to significantly reduce the performance of UIT, as demonstrated by the Lehigh test program (Roy et al. 2003). All specimens treated at no dead load developed fatigue cracks at the weld toes that were treated with UIT.

The specimens that were treated with UIT during the application of dead load, however, showed a vast improvement in fatigue life. These specimens were treated at 114 MPa (16.5 ksi), subjected to a maximum stress of 197 MPa (28.5 ksi), and subjected to a stress range of 82.7 MPa (12.0 ksi). The stress ratio, with respect to the state of stress during UIT treatment, resulting from these loading conditions was 0.0, meaning that the minimum stress was equal to the stress at treatment. Low stress ratios were shown by the Lehigh research to accommodate the greatest improvement in fatigue life possible for UIT (Roy et al. 2003). Many of these specimens treated with UIT under simulated dead load, both socket and stiffener type, achieved run-out defined at 4.5 million cycles, improving the AASTHO categorization from Category E' when untreated to a category B' when treated. Generally, when these specimens did fail, they developed cracks at locations away from the weld toes that were treated with UIT. Results of this research clearly demonstrate the significant improvement in fatigue life that is achieved when UIT is performed under optimal loading conditions and the futility of UIT when it is not performed under optimal loading conditions. Care must be taken to ensure that dead load is applied to structure during treatment to minimize the service stress ratio.

One interesting result of this test was the effect that post-UIT galvanization had on the effectiveness of UIT. Specimens that were treated with UIT prior to being galvanized, regardless of whether or not dead load was applied during UIT treatment, showed no improvement in fatigue life over control specimens. It was determined that heat applied to the welds during galvanization removed the beneficial compressive stresses induced by UIT. Therefore, UIT must be performed after galvanization or application of heat.

2.2.5.2 Field-Treated Signal Mast Connections

A second research program undertaken by the University of Texas to determine the effectiveness of UIT at preventing fatigue failure in traffic signal mast

arm connections was performed on traffic structures that had been in service for a period of time (Palmatier and Frank 2005). In this investigation, two mast arms having similar geometries were removed from an intersection in Denton, Texas. One of the mast arms had been treated with UIT five months prior to being removed and the other mast arm was untreated. The former mast arm was treated with UIT at both toes of the fillet weld attaching the mast arm to the end plate. UIT treatment was performed at only the top hemisphere of the mast arm-to-base-plate connection using 3.0 mm (0.12 in.) needle indenters. The untreated specimen was cycled in fatigue at a connection stress range of 82.7 MPa (12.0 ksi) and the treated specimen was cycled at a stress range of 75.2 MPa (10.9 ksi). The minimum stress applied to each specimen was chosen to closely simulate the dead load applied to the mast arm during service loading conditions, thus providing a stress ratio, with respect to the state of stress during UIT treatment, of nearly zero.

Results of this testing showed that although the treated mast arm connection outperformed the untreated mast arm connection, neither connection exceeded the AASHTO Category E' limit. The treated connection failed shortly before reaching the Category E' limit. Results of this test show a marked difference from the results of laboratory testing done previously at the University of Texas. However, the end plate thickness of the field-treated specimen of 25.4 mm (1.00 in.) was much less than the end plate thickness 38.1 mm (1.50 in.) used for the specimens treated with UIT in the laboratory testing. The authors of this research program point out that end plate thickness plays a major role in the fatigue performance of a socketed end plate. The mast arm treated in the field produced a fatigue life comparable to untreated specimens with a thicker 31.8 mm (1.25 in.) end plate, indicating that some improvement was attained through the field application of UIT. In addition, previous damage incurred by the treated field specimen during its service life both prior to and

after UIT treatment was not considered when categorizing the life of the specimen. Had this been considered, the AASHTO Category E' limit would have been achieved.

2.3 UIT CASE STUDIES

In addition to laboratory research, the effectiveness of UIT is being studied on various bridge retrofits in North America. To date, UIT has been used as a cost-effective alternative to conventional retrofits of fatigue-cracked bridges in numerous states including Pennsylvania, Georgia, Virginia, Kansas, Oklahoma, and Texas as well as in Canada (Verma et al. 2004).

2.3.1 Lake Allatoona, Georgia

One example of a retrofit demonstrating the effectiveness of UIT was that of the twin bridge over Lake Allatoona, Georgia (Statnikov et al. 2005). In 1997, after 20 years of service, the structure underwent a retrofit to repair numerous cracks at various fatigue-prone details. Although all of the cracked locations were repaired using conventional methods, 12 of the fatigue-critical weld details that had not yet cracked were treated with UIT by the NSTC in collaboration with the E.O. Paton Welding institute to demonstrate the effectiveness of UIT. Twelve fatigue-critical weld details that had not yet cracked were left in the as-welded condition for comparison. After monitoring the bridge for a short period of time, the effectiveness of UIT was apparent. All 12 details left in the as-welded condition developed cracks within the first six months, whereas none of the details treated with UIT have developed cracks as of 2003.

2.3.2 Virginia Interstate I-66

A case study that displayed the cost-effectiveness of UIT was the repair of four bridges along Interstate 66 in Virginia (Fisher et al. 2001). All of these bridges were experiencing fatigue cracking in the fillet welds attaching the diaphragm connecting plate to the top of the girder web where no positive attachment to the top

girder flange was established. The coverplate end welds and the welds connecting the diaphragm connecting plate to the bottom of the web were also fatigue-critical details.

To positively attach the connecting plate to the top flange, fillet welds treated with UIT were used in lieu of conventional bolted angles. The coverplate ends and bottoms of the diaphragm connecting plates were also treated with UIT in lieu of bolting. The decision to use UIT was made because of the dramatic savings in labor cost, time, and the ability to leave the bridges open to traffic during repairs. However, as is the case with most of the bridges treated with UIT in the U.S., the Interstate 66 project was performed recently and cannot yet provide data on the long-term effectiveness of UIT. It may be many years until the effectiveness of UIT on actual structures can be quantified.

2.4 THEORY OF COVERPLATE BOLTING

As mentioned in Chapter 1, it was hypothesized that the addition of pretensioned bolts to the ends of a girder coverplate would enhance the fatigue lives of the transverse welds at the ends of the coverplate. It was believed that pretensioned bolts would transfer forces developed in the girder flange to the coverplate by means of friction between the flange and coverplate, similar to the behavior of a slip critical connection. Under these circumstances, the amount of force to be transferred from the girder flange to the coverplate by the transverse welds would be small. The small force and corresponding low tensile stress in the welds would lead to extended fatigue life at these details. It is also believed that pretensioning a bolt near the end of a coverplate would generate a resultant compressive stress at the toe of the transverse weld because of the close vicinity of the bolt to the weld. This resulting compressive stress would lower the residual stress in the weld and contribute to extended fatigue life.

2.5 PREVIOUS COVERPLATE BOLTING RESEARCH

The AASHTO LRFD Bridge Design Specification (AASHTO 2004) contains a procedure whereby the fatigue life of a girder coverplate can be significantly improved by bolting the ends of the coverplate to the girder flange rather than fillet welding the ends of the coverplate to the girder flange. The addition of this procedure to the AASHTO specification was the result of research performed at the University of Maryland in the early 1980's (Wattar et al. 1985).

This research program consisted of fatigue testing ASTM A588 steel W14×30 beams with 13×146 mm (0.50×5.75 in.) coverplates attached to the bottom of the lower flanges. The coverplates varied in length but were each connected to a girder flange with 914 mm (36.0 in.) longitudinal fillet welds along both edges of the center portion of the coverplate. In lieu of longitudinal and transverse fillet welds, each end portion of a coverplate was then bolted to the flange using six, four, or two ASTM A325 22.2 mm (0.875 in.) diameter bolts pretensioned to slip-critical specifications. These three different bolt patterns were used to test whether the full allowable stress of the coverplate had to be developed by the slip-critical bolts to effectively extend fatigue life. The details employing six, four, or two bolts were capable of developing 114%, 76%, or 38% of the allowable stress in the coverplate, respectively. The end portions of the coverplates extended lengths of 230, 150, or 76 mm (9.0, 6.0, or 3.0 in.) past the termination of the longitudinal welds, corresponding to the coverplates having six, four, or two bolts at each end, respectively. In addition to varying the number of bolts used to connect the coverplate ends, the stress range at which the specimens were fatigue tested was also varied. The stress ranges used were 124, 159 and 214 MPa (18.0, 23.0, and 31.0 ksi) and the maximum stress for all specimens was maintained at 224 MPa (32.5 ksi). All specimens were tested in four-point-bending on a 4570 mm (180 in.) span with equal loads applied 610 mm (24 in.) apart. The sinusoidal loading rate was not indicated.

Results of this testing program showed that the fatigue lives of the bolted details were significantly improved over those of conventional transversely welded details. Of the nearly 50 details tested, the fatigue lives of all but one of the details fell above the AASHTO Category C limit, the vast majority fell above the Category B limit, and a few fell above the Category A limit. As testing progressed, it was discovered that details that had fatigue lives below the Category B limit had gotten lubrication between the flange and coverplate during bolt installation and were not behaving as slip-critical connections. Therefore, it was concluded that all coverplate details that had genuine slip-critical connections, regardless of stress range or bolt configuration, performed at or above the AASHTO Category B limitations. Since the fatigue lives of the different bolt configurations had no statistical difference, it was also concluded that the allowable stress of the coverplate did not have to be developed by the slip-critical bolted connection to extend fatigue life. However, some of the details employing only two bolts did not transfer enough force into the coverplate to prevent cracking at the termination of the weld toe. These cracks did not significantly reduce the improvement in fatigue life.

Upon the recommendation of this research, AASHTO adopted a procedure whereby the ends of coverplates attached to girder flanges are considered Category B details if slip-critical bolts are used to connect the ends of the coverplate to the girder flange rather than transverse fillet welds. Using this AASHTO procedure, the number of bolts to be installed at each detail is that required to develop the coverplate's portion of the maximum design moment at the theoretical cutoff point of the coverplate rather than the full allowable stress of the coverplate.

CHAPTER 3 EXPERIMENTAL SET-UP

3.1 FATIGUE SPECIMENS

To investigate the effects of performing UIT and adding coverplate bolts on enhancing the fatigue performance of welded steel, an experimental fatigue testing program was established. The testing program was funded by the Kansas Department of Transportation (KDOT) and all testing was performed at the University of Kansas material testing laboratory.

3.1.1 Specimen Design

As demonstrated by the research programs discussed in the previous chapter, significant improvements in fatigue life can be obtained through the use of UIT. Considering these results, it was determined that the specimens to be tested in the current program needed to incorporate severe fatigue details for multiple reasons. Primarily, by incorporating severe fatigue details into the specimens, the greatest possible amount of fatigue life enhancement caused by either UIT or coverplate bolting could be measured. For example, if a moderate AASHTO Category C detail were to surpass Category A detail requirements when treated, it could only be stated that the treatment caused an improvement of two categories. However, if a much poorer Category E' detail was to surpass Category A detail requirements when treated, it could be stated that the treatment caused an improvement of seven categories. A second important reason for incorporating severe fatigue details into the specimens was to ensure timely completion of the fatigue tests for the improved specimens. Additionally, one of the motivations for KDOT to fund this testing program was the persistent problem of bridges in their inventory developing fatigue cracks in the fillet welds at the ends of girder coverplates, which are severe AASHTO Category E or E' details. Although the objective of this testing program was to provide a comparison between the improvement methods rather than to recreate or simulate girder coverplate cracking, it was imperative that the program yielded results

that were applicable to the immediate problems facing KDOT. To that end, Category E' details having geometry similar to that of a girder coverplate were incorporated into the specimen design.

Since many existing bridges suffering fatigue cracking were built prior to the invention of modern high-strength steels, the specimens used for the testing program were fabricated from A36 steel. The geometry and dimensions of the specimens were chosen after carefully considering the size and capacity of the testing machine used, the dimensional restrictions governing fatigue categorization established by the AASHTO LRFD bridge design specification (AASHTO 2004), and the total weight of a specimen.

The final specimen geometry consisted of a simulated girder coverplate (henceforth referred to as the "coverplate") fillet-welded to a simulated girder flange (henceforth referred to as the "flange"). This configuration was chosen for its symmetry, its simplicity, and because the geometry provided the desired Category E' details as well as replicated the actual geometry of bridge coverplates. In conforming to AASHTO fatigue Category E' specifications, the thickness of the coverplates used for the specimens had to be at least 20 mm (0.80 in.). To simplify fabrication, 25.4 mm (1.00 in.) thick steel bars were used for the flanges as well as the coverplates. After considering the testing machine's size and capacity, bars having dimensions PL 25.4×114×1270 (PL 1.00×4.50×50.0) were chosen for the flanges. Bars with dimensions PL 25.4×76.2×660 (PL 1.00×3.00×26.0) were chosen for the coverplates. The coverplate width was chosen to be as wide as possible while still allowing ample flange surface on each side to accommodate the selected fillet weld size. The coverplate length was chosen as a balance between shear lag effects and St. Venant's Principle considerations. The coverplates had to be long enough to allow full transfer of forces into the coverplate but short enough to maintain sufficient distance between the weld toes and the local stresses induced in the flange by the crosshead grips.

Upon recommendation from KDOT, 7.94 mm (0.313 in.) fillet welds were used to connect the coverplates to the flanges on all sides of the coverplates. This weld size and configuration are commonly used for bridge coverplates as it is the largest size fillet weld that can be laid in a singe pass. Four completed specimens are shown in Figure 3.1. Specimen dimensions and specifications are shown in Figure 3.2.

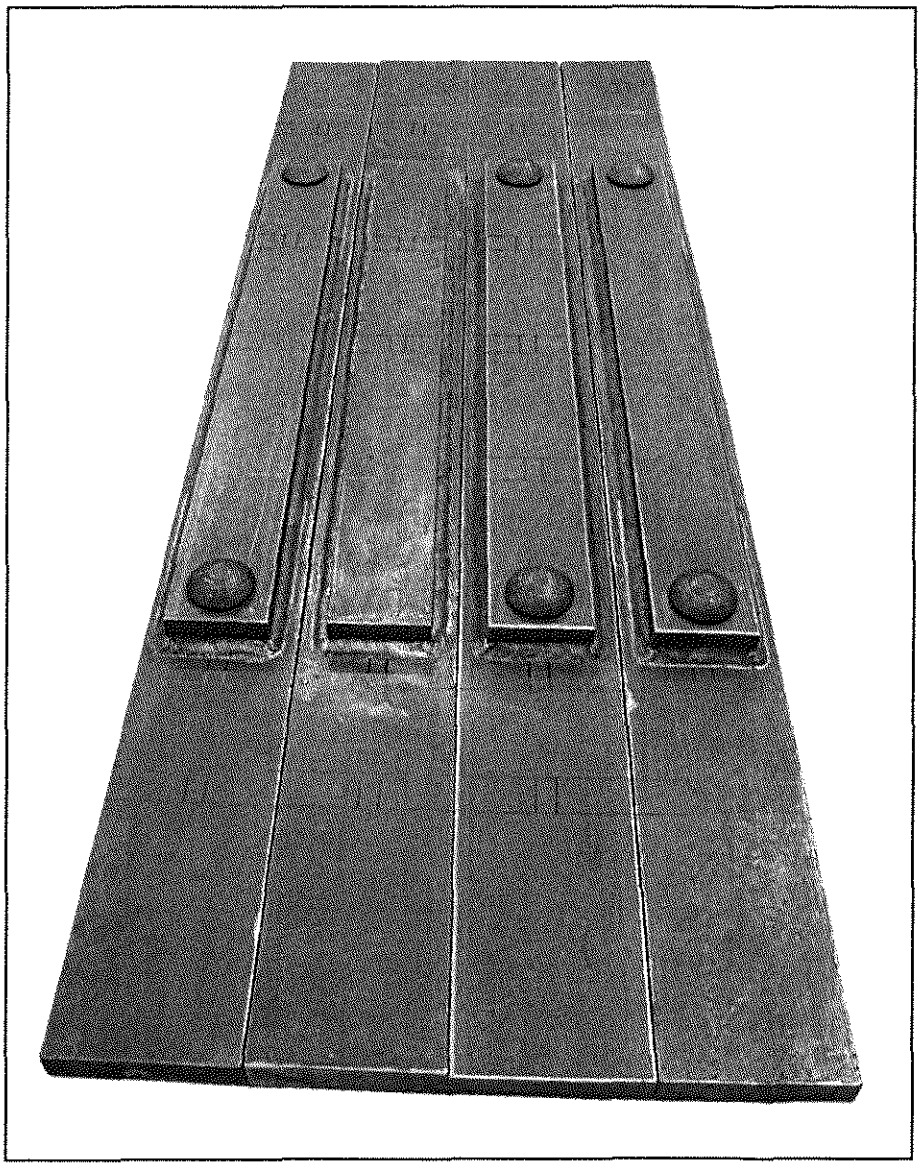

Figure 3.1. Fatigue Specimens.

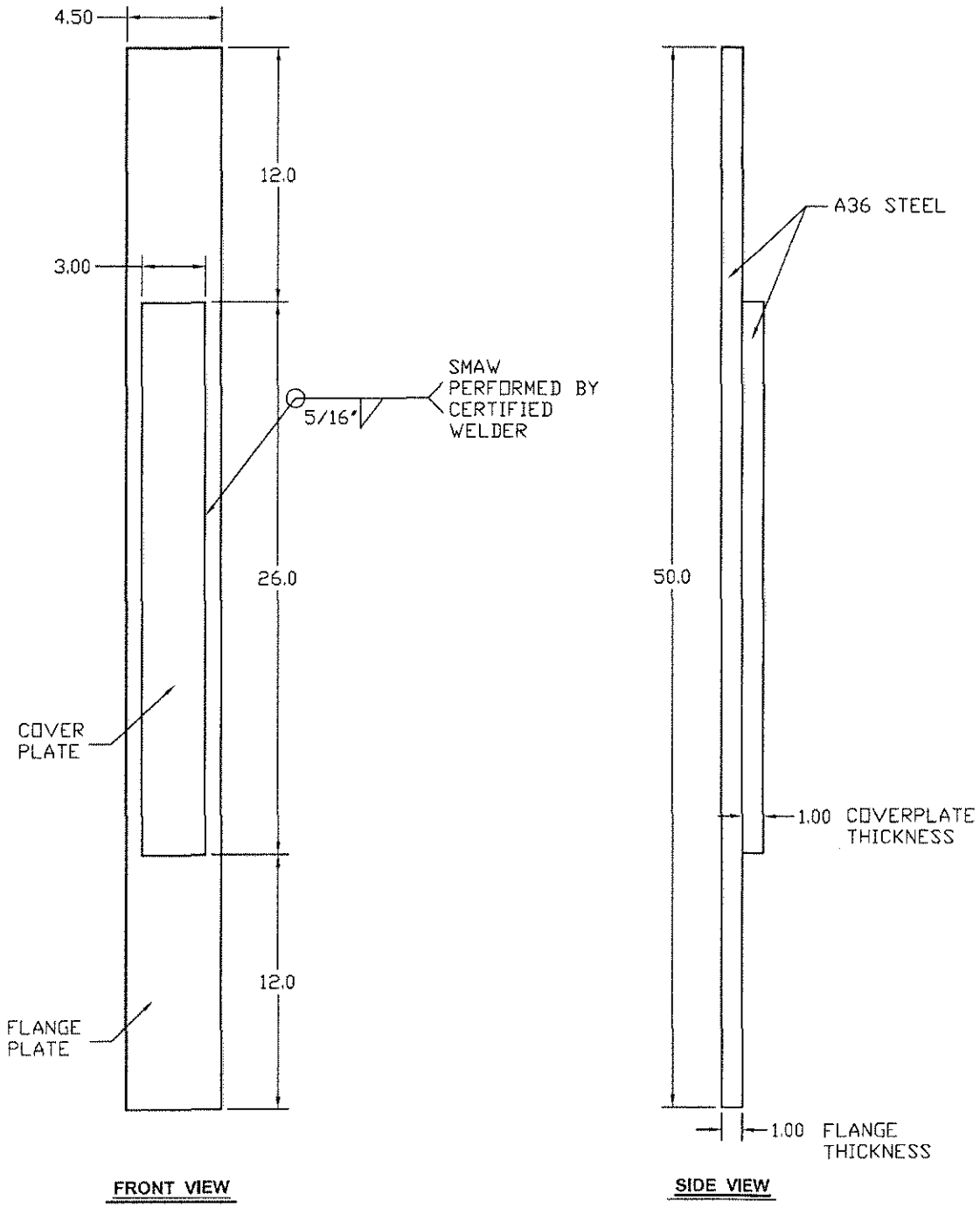

Figure 3.2. Fatigue Specimen Dimensions.

3.1.2 Specimen Fabrication

All specimens were fabricated by Builders Steel Company located in Kansas City, Missouri. The 7.94 mm (0.313 in.) submerged metal arc fillet welds were welded using E-70 electrodes by a certified welder employed by Builders Steel. A visual inspection of the welds upon receipt of the specimens indicated that all welds appeared to be adequately sized, consistently performed, free of injurious flaws, and of good overall quality. To examine potential fatigue life enhancement resulting from coverplate bolting, pretensioned bolts were installed at both ends of the coverplate for a number of the specimens. Coverplate bolts were also installed by Builders Steel Company. On both ends of a coverplate being retrofitted, one 25.4 mm (1.00 in.) diameter ASTM A325 carriage bolt was tightened to a minimum bolt pretension of 227 kN (51.0 kips) using a calibrated pneumatic wrench. Two-hundred twenty-seven kN (51.0 kips) is the standard minimum bolt pretension specified for this size and grade of bolt by the American Institute of Steel Construction (AISC) Specification for Structural Steel Buildings (AISC 2005). Per the AISC specification, the nominal diameter of the hole drilled for each bolt was 27.00 mm (1.063 in.). The bolts were each provided with a standard flat washer installed on the nut-side of the connection. Since the purpose of adding a bolt to the end of a coverplate was to physically transfer forces from the flange to the coverplate as well as possibly induce compressive stress in the weld, it was ideal to place the bolts as close as possible to the ends of the coverplates. Therefore, the holes for the bolts were placed at a distance of 31.75 mm (1.25 in.) measured from the edge of the coverplate to the center of the hole. An installed coverplate bolt can be seen in Figure 3.3. Typical Bolt placement dimensions are shown in Figure 3.4.

Ultrasonic Impact Treatment was performed by Applied Ultrasonics in Birmingham, Alabama. UIT is currently a proprietary procedure and is only performed in the United States by Applied Ultrasonics. Specimens being treated

were shipped to and from Birmingham for treatment. For each specimen receiving UIT, the weld toes adjacent to the flange were treated at both ends of the coverplate. At either end of a given coverplate, treatment was performed across the entire length of the transverse fillet weld and continued along the longitudinal fillet welds on both sides of the coverplate for a distance of 6". The interior portions of the longitudinal fillet welds did not receive UIT because they were classified as AASHTO fatigue Category B details and were not prone to fatigue failure. At the ends of each treated coverplate, additional UIT treatment was performed at all obvious stress concentrations such as weld terminations. Typical UIT treatment is shown for one end of a coverplate in Figure 3.3. The locations on the specimens where UIT was performed are shown in Figure 3.4.

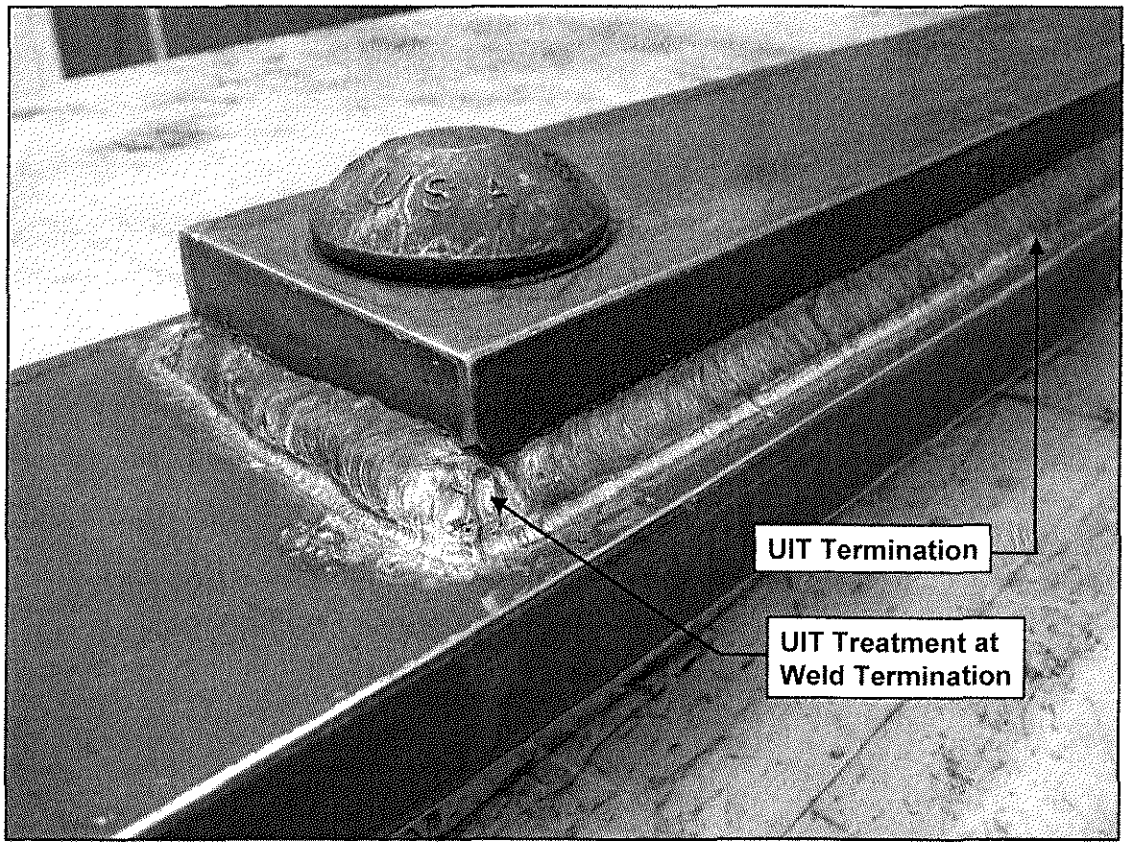

Figure 3.3. Coverplate end region of a specimen treated with UIT and bolted.

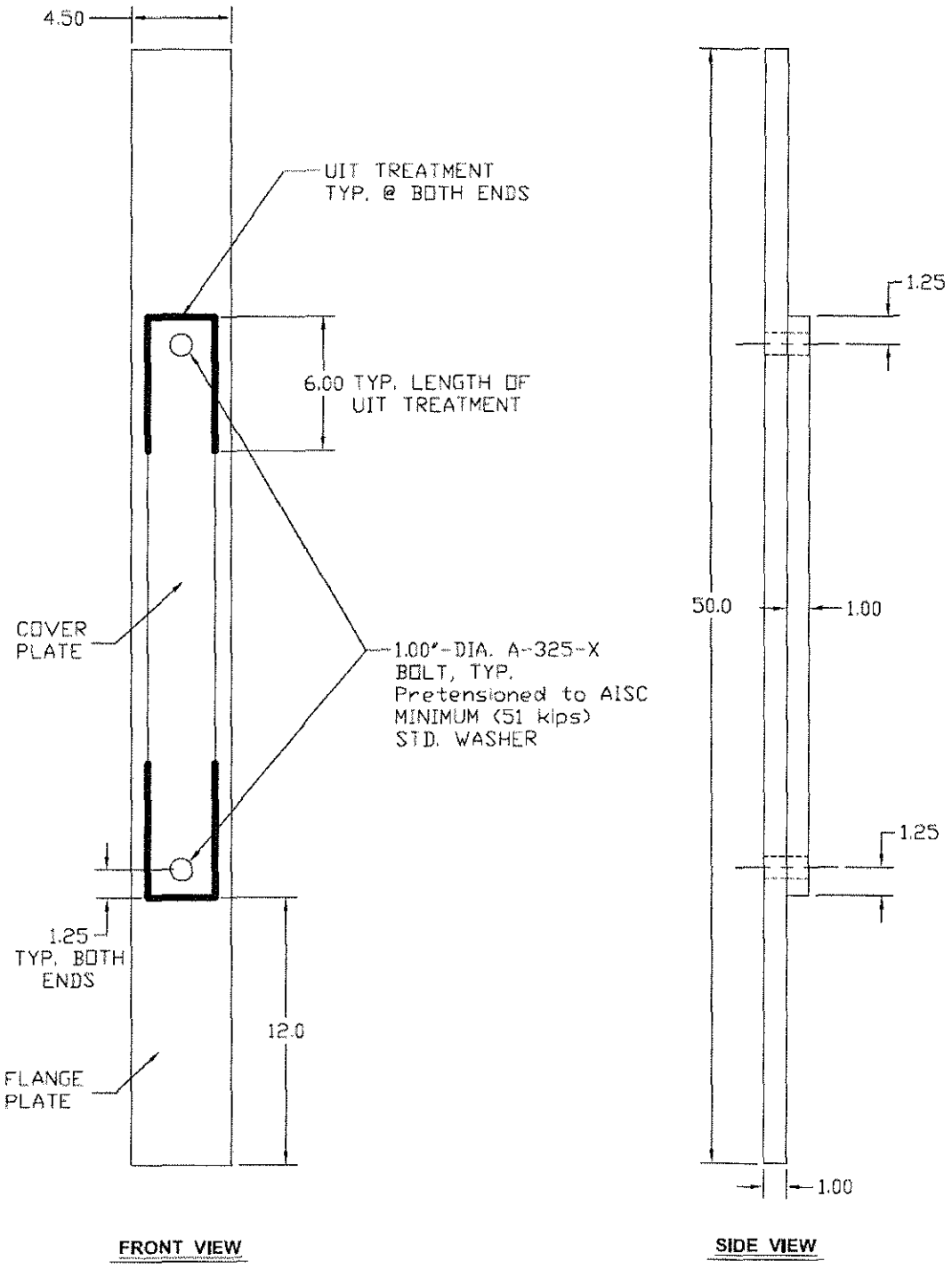

Figure 3.4. Dimensions of bolt placement and UIT treatment.

3.2 FATIGUE TEST METHODS

3.2.1 Test Groups

To compare the effects of performing UIT and coverplate bolting on specimen fatigue life, four different types of specimens were fabricated and tested in fatigue until failure or run-out. Originally, three specimens of each type were fabricated, resulting in total of 12 specimens to be tested. The first group of specimens, referred to as the CONTOL group, was left untreated and unbolted from the original fabricated state. A second group of specimens, referred to as the BOLT group, had pretensioned bolts installed at both ends of the coverplates as described previously in this chapter. The specimens in the third group, referred to as the UIT specimens, were treated with UIT at the weld toes as described previously. The final group of specimens, referred to as the UIT/BOLT group, had pretensioned bolts installed at the ends of the coverplates as well as UIT performed at the weld toes. The specimens in the latter group will also be referred to as "combination specimens" in the following chapters. This pool of specimens, although limited in number, provided sufficient data to quantify fatigue behavior achieved by performing UIT and coverplate bolting individually. Additionally, results from the UIT/BOLT specimen group were compared with the individual results from the UIT group and the BOLT group to determine any additive effects of performing both improvement procedures on a specimen.

3.2.2 Stress Ranges

The AASHTO LRFD Bridge Design Specification (AASHTO 2004) is the governing document used in the design of most public roadway bridges in the United States. Section 6.6 of the AASHTO specification outlines the procedure used to design bridge members against fatigue failure. The design procedure is a process of selecting a fatigue category for a member or connection and determining the number of load cycles that the member or connection will be subjected to during its design

life. Assigning a fatigue category is a way of quantifying the susceptibility of a member or connection to fatigue failure. AASHTO differentiates between eight fatigue categories based primarily on geometry. Once a member or connection has been assigned a fatigue category and the design cycle count has been determined, a nominal design stress range for that member or connection can be calculated using Equation 6.6.1.2.5-2 of the AASHTO specification. This equation, in U.S. Customary units as presented in the AASHTO specification, is as follows:

$$(\Delta F)_n = (A/N)^{1/3} \geq (\Delta F)_{TH} \qquad \text{(Eqn 3.1)}$$

where:

$(\Delta F)_n$ = Nominal fatigue resistance, ksi

A = Constant taken from Table 3.1

N = Number of expected load cycles in design life

$(\Delta F)_{TH}$ = Constant-amplitude fatigue threshold taken from Table 3.1

Table 3.1. Detail Category Constant, A, and constant-amplitude fatigue threshold.

Detail Category	Constant, A, $\times 10^8$ (ksi^3)	Threshold, MPa (ksi)
A	250.0	165 (24.0)
B	120.0	110 (16.0)
B'	61.0	82.7 (12.0)
C	44.0	68.9 (10.0)
C'	44.0	82.7 (12.0)
D	22.0	48 (7.0)
E	11.0	31 (4.5)
E'	3.9	18 (2.6)

To convert the nominal fatigue resistance of a detail from U.S. Customary units to SI units, $(\Delta F)_n$ calculated by Eqn. 3.1 is multiplied by 6.895. If the stress range in the member or connection when subjected to the design loads specified by AASHTO is less than $(\Delta F)_n$ calculated by Eqn. 3.1, the member or connection will not fail in fatigue for the design life of the bridge.

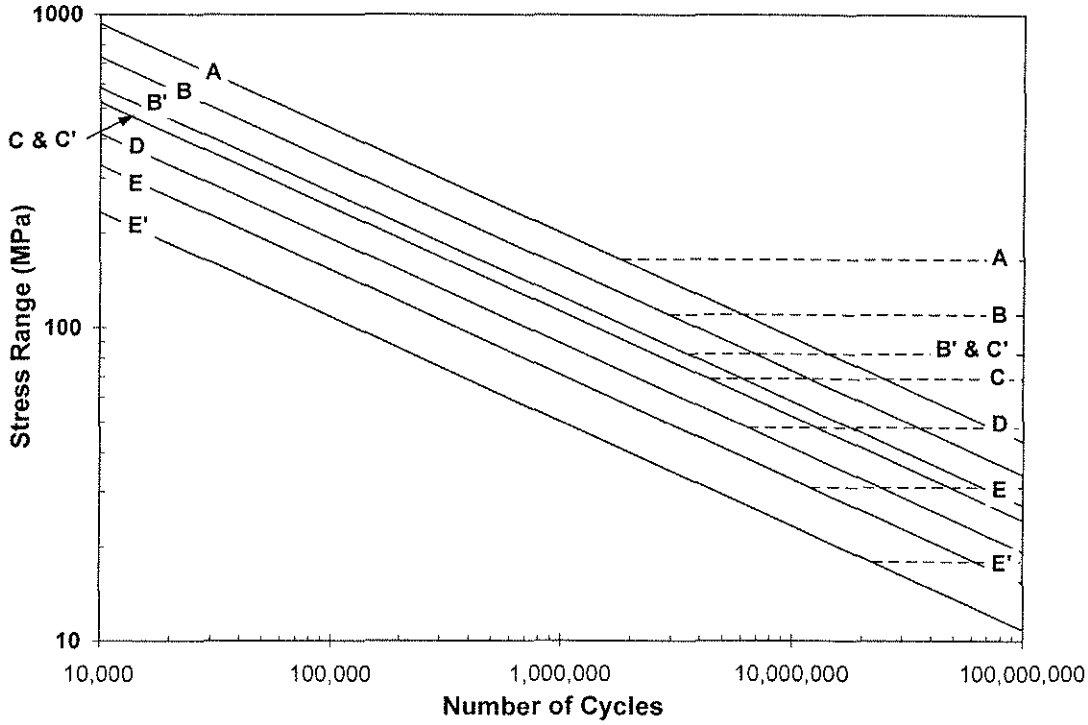

Figure 3.5. S-N diagram showing fatigue curves determined by Eqn. 3.1 (SI).

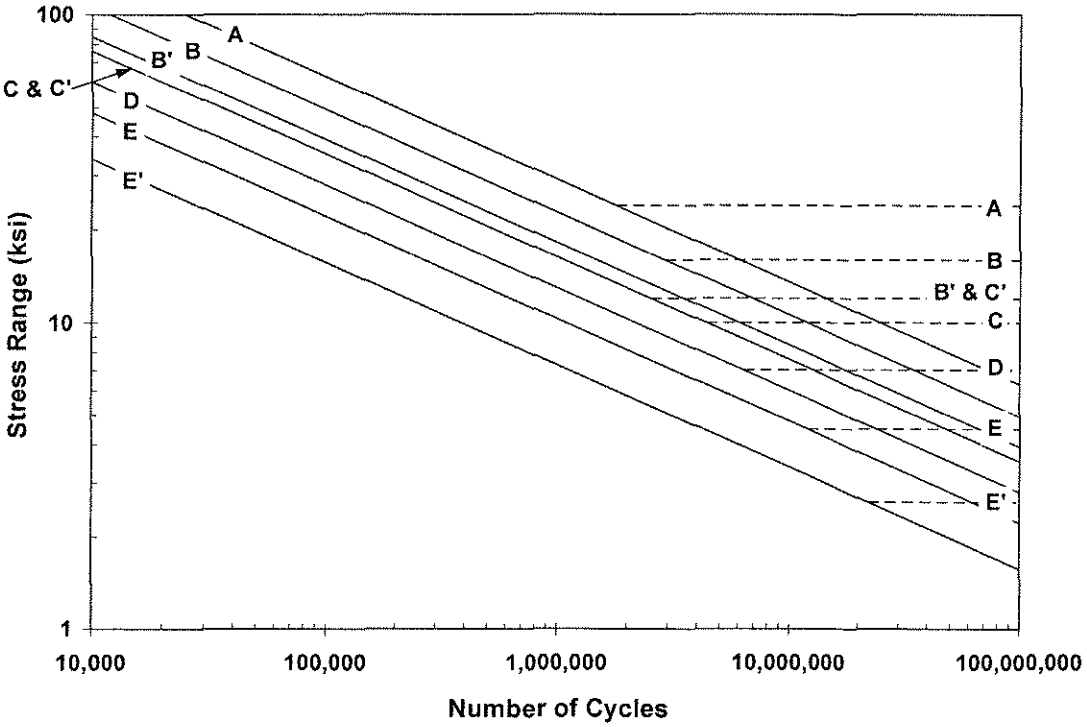

Figure 3.6. S-N diagram showing fatigue curves determined by Eqn. 3.1 (US Custom.).

By substituting the value of A for a given AASHTO fatigue category (see Table 3.1) into Eqn. 3.1 and solving $(\Delta F)_n$ for various values of design life N, a fatigue life curve for that detail category can be plotted on an S-N diagram. S-N diagrams presented in Figures 3.5 and 3.6 show fatigue life curves determined by Eqn. 3.1 for all eight AASHTO fatigue categories in SI and U.S. Customary units, respectively. These S-N diagrams provide a means to graphically determine the design fatigue strength of a detail. In addition, they may also be used to graphically compare fatigue test results using the AASHTO fatigue equation. Each horizontal dashed line in Figures 3.5 and 3.6 represents the constant-amplitude fatigue threshold for a given AASHTO fatigue category. If the stress range applied to a given detail is less than the fatigue threshold for the category in which that detail is classified, the detail will have infinite design fatigue life.

Since KDOT and essentially all other state departments of transportation use the AASHTO code to design bridges against fatigue failure, the most logical method to compare the results of this testing program was to relate all data to the AASHTO fatigue life equation (Eqn. 3.1) and the corresponding S-N diagrams. To do this, each specimen was tested in fatigue at a constant stress range until the specimen failed or achieved run-out. This approach is essentially the reverse process of designing a member or connection against fatigue failure. Once a test specimen failed or reached run-out, a data point for that specimen was then drawn on the AASHTO fatigue chart. After testing all of the specimens, the data points drawn for all of the specimens were then compared to each other as well as to the lines on the chart corresponding to the design fatigue life curves for the different AASHTO categories. This is the predominant method used to compare the results of fatigue testing performed in the United States.

Because the current testing program was limited in the number of specimens to be tested as well as the amount of time to complete testing, it was initially decided

that all 12 specimens would be tested at a single stress range. For each of the four specimen types described previously, testing the three specimens at one stress range would allow an average fatigue life and a variation in fatigue life for that specimen type to be determined. This was important because fatigue tests, in general, have a relatively large amount of variation in the results. After estimating the increase in fatigue life that might be caused by the improvement methods through significant literature review, a nominal tensile stress range at the transverse weld toe of 59 MPa (8.5 ksi) was chosen for the fatigue tests. Determination of the corresponding load applied to a specimen is discussed in more detail in section 3.2.5.2. At this stress range, the untreated control specimens, which incorporated E' details, were expected to fail after approximately 635,000 cycles as calculated by Eqn. 3.1. This stress range was chosen as a balance between a stress range that was low enough to allow the control specimens to cycle longer than a few hundred thousand cycles before failure and high enough to cause the improved specimens to fail in a timely manner.

However, after the first control specimen cycled for six times its estimated fatigue life with no development of fatigue cracks (detection of cracks is discussed in section 3.4), it was obvious that further testing needed to be performed at a much higher stress range so that the fatigue lives of the specimens could be compared within the finite-life region of the AASHTO S-N diagram. For the next control specimen, the nominal weld toe stress range was increased to 96.5 MPa (14.0 ksi). This specimen also reached over two million cycles without cracking. Finally, the third control specimen was cycled at a nominal weld toe stress range of 138 MPa (20.0 ksi) and developed a fatigue crack in less than a million cycles.

After this test, it was thought that the remainder of testing could proceed at a nominal weld toe stress range of 138 MPa (20.0 ksi). However, the next specimen tested, which was a specimen treated with UIT, achieved five million cycles with no indications of cracking. At that point it was agreed upon by the KU research team

and the KDOT project monitor to set a final stress range at which the remaining tests would be performed and define a run-out point at which fatigue tests for the improved specimens would be stopped. The final weld toe stress range selected was 193 MPa (28.0 ksi). This final stress range was used for the remaining two UIT specimens and all of the BOLT and UIT/BOLT specimens. One-hundred ninety-three MPa (28.0 ksi) proved to be a sufficient stress range in that most of the improved specimens failed in a timely manner. A discussion of the possible reasons why the specimens outperformed the AASHTO fatigue curves is included in Section 4.1.1. A summary of the various stress ranges that testing was performed at is shown in Figures 3.7 and 3.8 in SI and U.S. Customary units, respectively. Notice that the final stress range chosen was larger than the constant amplitude fatigue threshold for a Category A detail, which meant that the testing program had the ability to detect potential improvements in fatigue categorization up to and including Category A details.

In the course of selecting the final stress range, all three of the control specimens were tested at stress ranges less than 193 MPa (28.0 ksi), leaving no control specimens to be tested at the final stress range. Therefore, three new control specimens were fabricated by the same fabricator that produced the 12 original specimens. Upon visual inspection, the fillet welds on the new control specimens appeared to be slightly smaller, less consistent, and of lower overall quality than the welds on the 12 original specimens. Therefore, one of these additional control specimens was tested at a nominal weld toe stress range of 138 MPa (20.0 ksi) and the results were compared to the fatigue life of the original control specimen that was tested at a stress range of 138 MPa (20.0 ksi). This was done to ensure that the original and additional control specimens demonstrated similar fatigue behavior. The other two additional control specimens were tested at 193 MPa (28 ksi), bringing the number of specimens tested at 193 MPa (28 ksi) to 10 and total number of specimens tested to 15.

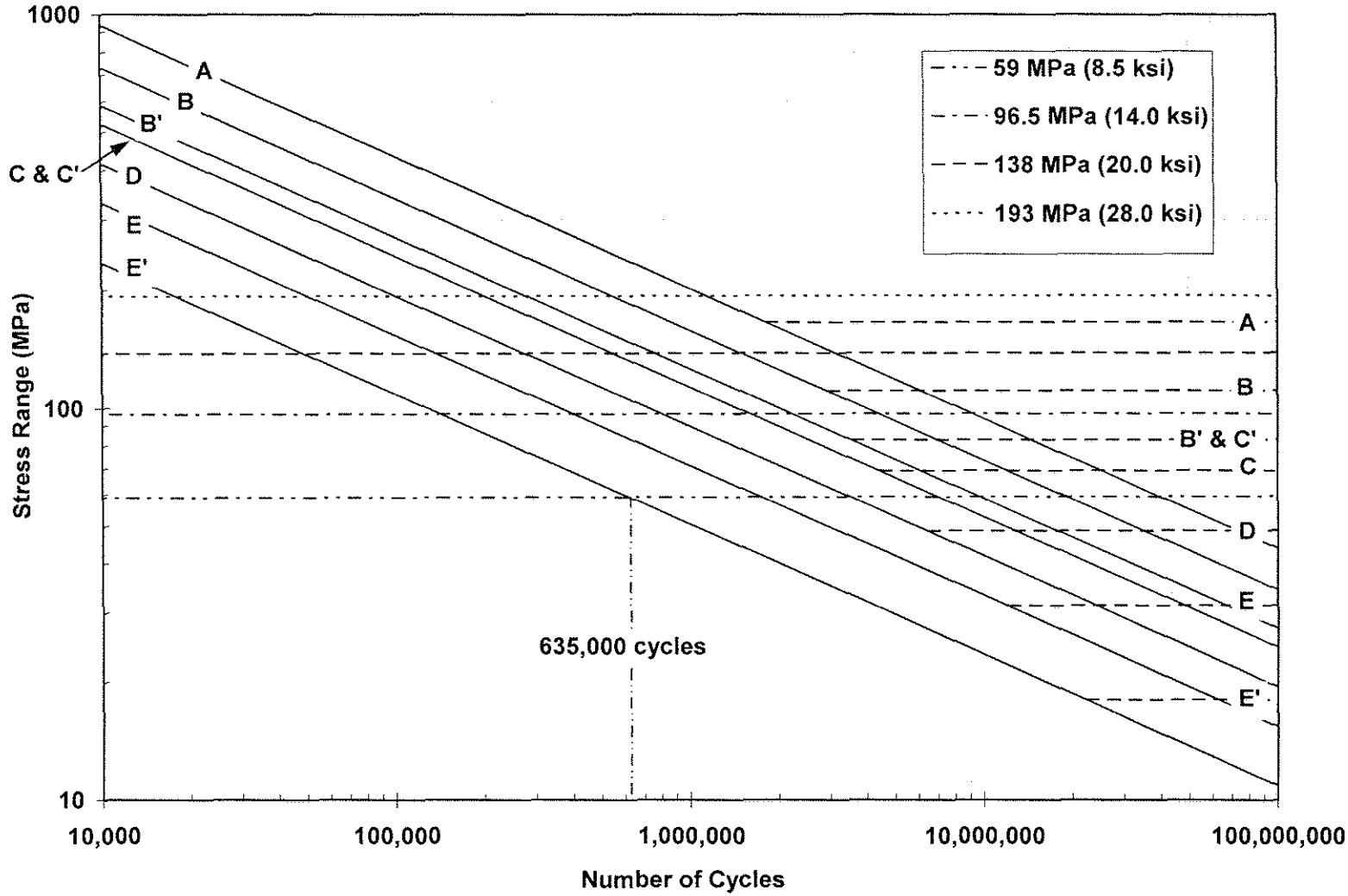

Figure 3.7. Nominal weld toe stress ranges at which fatigue testing was performed (SI).

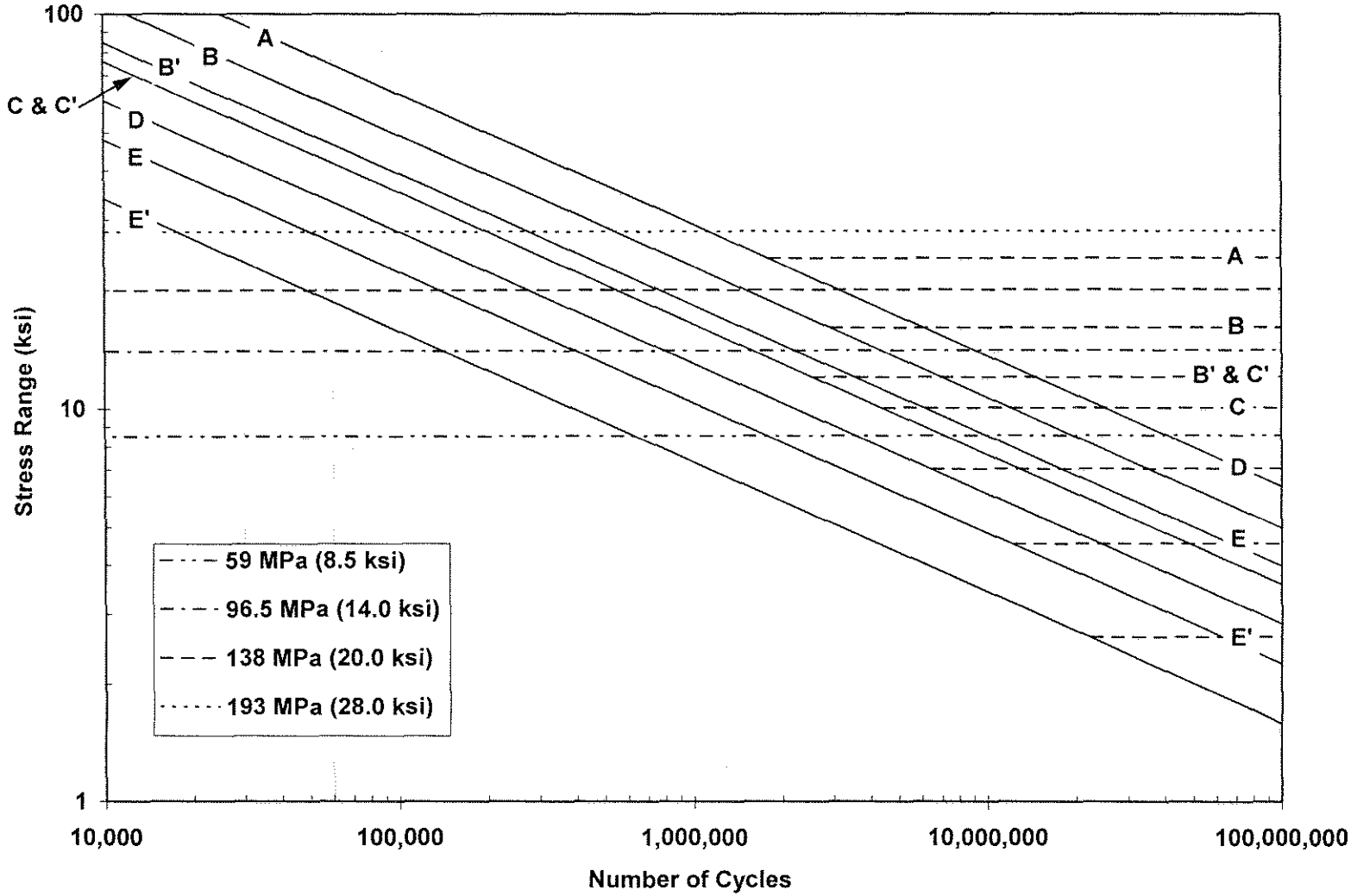

Figure 3.8. Nominal weld toe stress ranges at which fatigue testing was performed (U.S. Customary).

3.2.3 Loading Method

The primary variable of importance that needed to be controlled during each fatigue test was the tensile stress range at the toes of the transverse fillet welds connecting the coverplates to the flanges. The toes of the transverse fillet welds will be referred to as simply the "weld toes" in the following discussion. Through basic principles of static equilibrium, the required stress range at the weld toes could be translated into the required load range to be applied to the specimen by the testing machine during fatigue testing. Of course, this transformation depended on the method used to load a specimen.

Initially, it was thought that the simplest and most logical method to load a specimen would be to subject the ends of the flange to axial tension. By controlling the axial load range applied to the flange, the tensile stress range at the weld toes, which was equal to the axial load range divided by the cross-sectional area of the flange, could also be controlled. However, problems with this loading method were discovered after performing a finite element analysis of an axially loaded specimen. The primary problem uncovered during the analysis was that the specimen was found to deflect laterally while being loaded, causing significant bending-related stresses in the specimen. Upon investigation, it was determined that the lateral deflection was caused by the change in location of the specimen's elastic neutral axis in the coverplated region of the specimen. When the flange was axially loaded, the elastic neutral axis in the coverplated region (which was shifted toward the coverplated side of the flange) sought to align itself with the elastic neutral axis at the ends of the flange, causing the middle portion of the specimen to deflect laterally. The lateral deflection calculated by the finite element analysis was large enough to cause the surface of the coverplate to be in compression. Considering these results, it was determined that loading the flanges axially would not produce desirable specimen behavior and a new means of loading the specimens was devised.

It was determined that the best way to achieve the desired tensile stress range at the weld toes was to subject the specimens to three-point-bending. This method of loading was chosen because large tensile stresses could be achieved at the weld toes by applying relatively small loads to the three-point-bending frame. Unlike axial loading, where the maximum achievable weld toe stress was limited by the testing machine's load capacity, three-point-bending provided the capability to stress the weld toes well past the yield point of the steel when only a fraction of the testing machine's load capacity was applied to the bending frame. Three-point-bending was also used because the specimens could be subjected to a simple, linear moment gradient that facilitated the calculation of applied load range required to produce a desired weld toe stress range.

After selecting three-point-bending as the preferred method for fatiguing the specimens, a three-point-bending frame compatible for use with the testing machine had to be fabricated. The frame consisted of an upper and a lower component that were attached to the crossheads of the testing machine. The lower portion of the bending frame was fabricated from a 1520 mm (60.0 in.) length of HSS 127×127×9.5 (HSS 5.00×5.00×0.38) steel tube of an unknown grade that was left over from previous research done at the KU structures laboratory. This tube was used because it was rigid enough to minimize frame deflections during testing and light enough to be lifted into the testing machine without special equipment.

To transfer forces to the specimens, round steel bars measuring 127 mm (5.00 in.) long and 50.8 mm (2.00 in.) in diameter were mounted to each end of the tube. The center-to-center spacing of the round bars, and thus the span length for bending frame, was 1118 mm (44.00 in.). Since the specimens had to be loaded into the bending frame with their coverplated sides facing downward, the round bars were mounted up off the top surface of the tube several inches to allow ample room for specimen deflection and to provide access to the weld toes for crack inspection. This

was achieved by welding each round bar to the end of a flat steel bar having dimensions PL 25.4×127×76.2 (PL 1.00×5.00×3.00). The opposite end of the flat bar was then welded to another flat steel bar oriented orthogonal to the first bar and having dimensions PL 25.4×127×152 (PL 1.00×5.00×6.00). The purpose of the second flat bar was to distribute loads over a larger surface area of the tube, thus reducing local bearing stresses in the tube.

To secure the tube assembly to the lower crosshead during testing, a flat steel bar having dimensions PL 25.4×102×241 (PL 1.00×4.00×9.50) was attached to the center of the tube so that 114 mm (4.50 in.) of the bar protruded from the bottom of the tube. The bar was attached to the tube by cutting 25.4×102 mm (1.00×4.00 in.) slots in the top and bottom walls of the tube and inserting the bar through the bottom slot until the leading edge of the bar was nearly flush with the top outer surface of the tube. The bar was then fillet welded to the top and bottom surfaces of the tube. The bar was attached to the top and bottom surfaces of the tube rather than simply welding a short length of bar to the bottom of the tube to reduce the stress that each weld would be subjected to during testing, thereby greatly increasing the fatigue life of the tube assembly. During testing, the tube rested on the surface of the lower crosshead and the protruding portion of the bar was clamped by the crosshead's hydraulic wedge grips.

The upper portion of the three-point-bending frame consisted of a PL 25.4×102×241 (PL 1.00×4.00×9.50) steel bar with a 127 mm (5.00 in.) long, 50.8 mm (2.00 in.) diameter round steel bar welded to one end. Approximately 114 mm (4.5 in.) of the bar was inserted into the grips of the testing machine's upper crosshead and clamped by the hydraulic wedge grips. During fatigue testing, the curved surface of the round bar provided the third point of load application at the midpoint of the specimen.

Attached to this upper portion of the bending frame was an apparatus designed to maintain the alignment of the testing machine's lower crosshead during testing. This alignment apparatus was necessary because although the testing machine's upper crosshead was fixed against rotation, the lower crosshead was attached to the freely rotating actuator. The apparatus also prevented the specimens from falling off the lower portion of the load frame when they fractured. The apparatus consisted of a 304.8 mm (12.00 in.) length of HSS 127×127×9.5 (HSS 5.00×5.00×0.38) steel tube with 25.4×102 mm (1.00×4.00 in.) slots cut into the top and bottom faces at the center of the tube. At each end of this tube, 381 mm (15 in.) lengths of HSS 25.4×25.4×6.4 (HSS 1.00×1.00×0.25) steel tube were welded to the front and back faces of the larger tube so that 254.0 mm (10.00 in.) of the smaller tubes protruded vertically from the bottom face of the larger tube. This apparatus was then attached to the upper portion of the bending frame by inserting the PL 25.4×102×241 (PL 1.00×4.00×9.50) flat bar through the slots cut in the apparatus until the bottom face of the apparatus was in contact with the round bar. The top and bottom faces of the apparatus were then welded to the bar. During testing, the protruding portions of the four 25.4 mm (1.00 in.) square tubes fit snugly around the lower HSS 127×127×9.5 (HSS 5.00×5.00×0.38) tube and prevented the lower portion of the bending frame and lower crosshead from rotating. At the outset of testing, it was obvious that the frictional forces between a specimen and the three load points were large enough to prevent the lower crosshead from rotating, thus eliminating the need for the alignment apparatus. Therefore, the protruding 25.4 mm (1.00 in.) tubes were bent outward slightly so they wouldn't rub against the lower portion of the bending frame. The geometry and dimensions of the three-point-bending frame are shown in Figure 3.9. This figure also shows the orientation of a specimen in the bending frame.

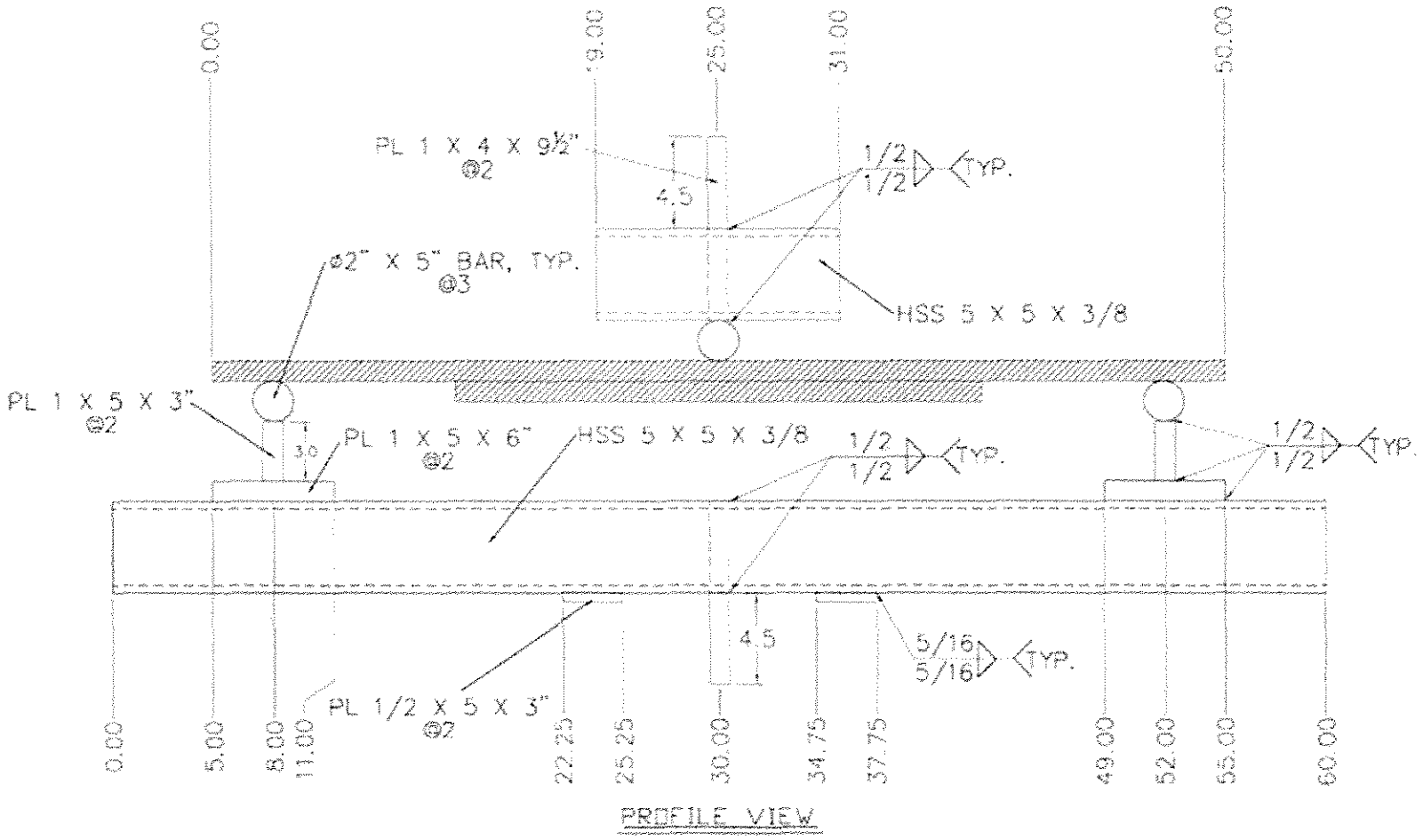

Figure 3.9. Geometry and Dimensions of three-point-bending frame (U.S. Customary units).

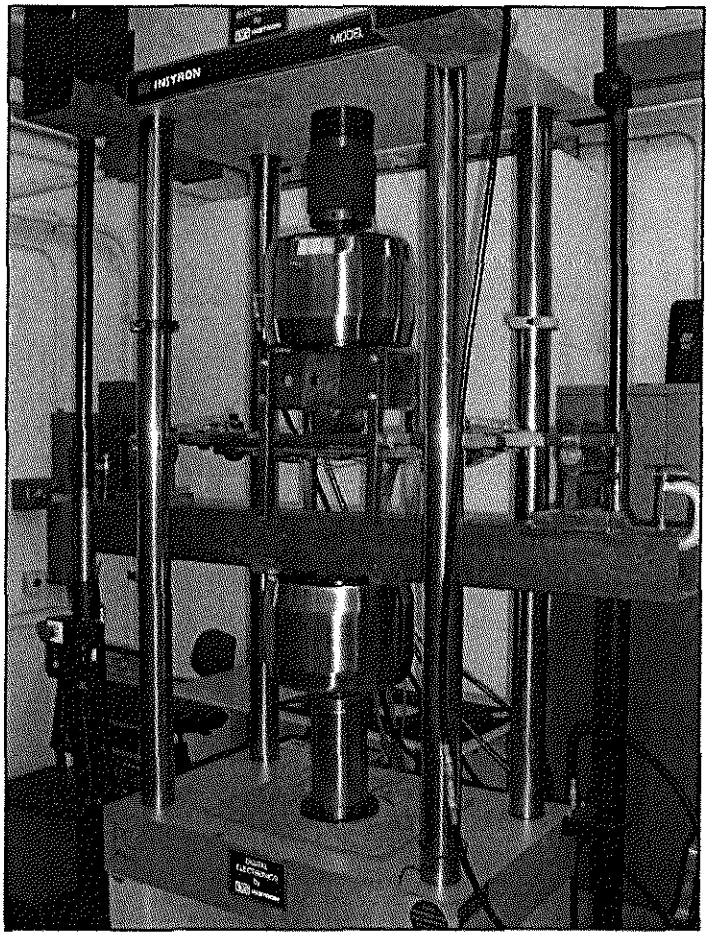

Figure 3.10. Three-point-bending frame with specimen installed.

The bending frame with a specimen installed is shown in Figure 3.10. Other safety devices were also incorporated into the bending frame to prevent a specimen from falling out during testing. One such device was a retainer that was clamped to the lower portion of the bending frame at each end of a specimen to prevent the specimen from moving longitudinally during testing. The retainers were fabricated from thin steel bars and clamped to the bending frame with C-clamps. The other safety devices employed were retainers that were attached to the sides of the round bars on the lower portion of the bending frame. The purpose of these retainers was to prevent a specimen from moving in the transverse direction during testing. These retainers consisted of short segments of steel bar welded to flat washers. During

testing, the transverse retainers were attached to the bending frame by inserting bolts through the flat washers and threading the bolts into holes that were drilled and tapped into the sides of the round bars. Figure 3.11 shows a view of one end the bending frame with both the longitudinal and transverse retainers installed. Although the retainers were used during all of the tests, the frictional forces between the specimens and the three load points proved to be large enough to prevent the specimens from moving during testing. Thus, none of the retainers actually touched the specimens during testing.

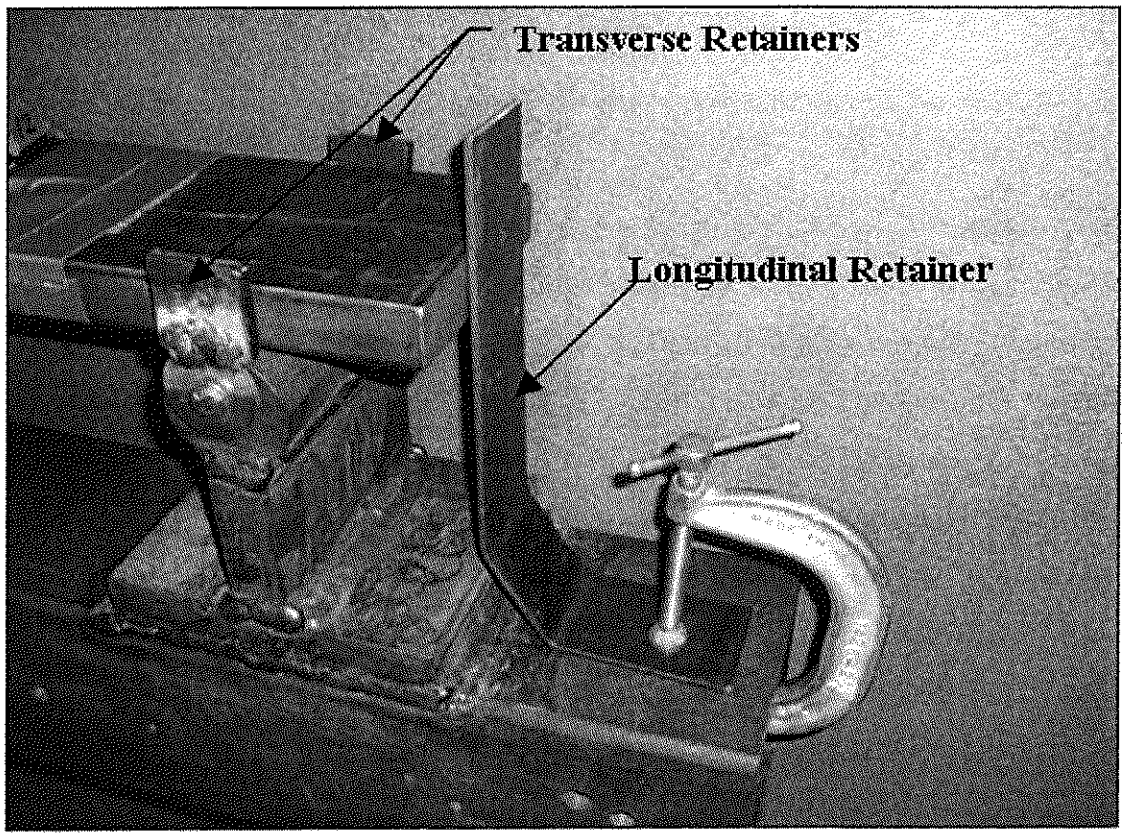

Figure 3.11. Retainers used to restrain fatigue specimen under cyclic loading.

3.2.4 Testing Machine

The testing machine used to perform all tests for this project was an Instron model 1334 closed-loop servohydraulic testing system. As shown in Figure 3.10, this

testing system consisted of a four-column, free standing load frame supporting a movable upper crosshead and a lower actuator with a range of motion of ±76.2 mm (±3.00 in.). The load frame had a static rating of ±489 kN (±110 kips) and a fatigue rating of ±240 kN (±55 kips). The actuator was powered by a remote high pressure hydraulic power supply. The hydraulic power supply furnished hydraulic fluid to the servohydraulic actuator at an operating pressure of 20 MPa (3000 psi) and was rated at 10 gallons per minute flow. Hydraulic pressure was created by an electric motor driving a water-cooled, positive displacement pump within the hydraulic power supply. The load frame's crosshead lifts, crosshead clamps, and wedge grips were also operated by the hydraulic power supply. Movement of the bottom-mounted hydraulic actuator was controlled by a detached servovalve mounted to a manifold. The servovalve regulated fluid flow to the actuator as a function of the electrical control signal from the controller.

The testing machine included a linear variable differential transducer (LVDT) integrated with the actuator as well as an internal load cell installed in the upper crosshead. Data from both the LVDT and load cell was read by the controller and used to control the motion of the actuator during operation. Both the LVDT and the load cell were tested for accuracy, calibrated, and certified by an Instron representative immediately prior to the start of the testing program and once toward the end of the program.

All functions of the model 1334 testing machine were regulated by an Instron model 8800D controller. The controller was added to the testing machine immediately prior to the start of this testing program and replaced the outdated original Instron controller. The model 8800D controller is compatible with single-axis servohydraulic testing machines and is capable of controlling actuator movement in position, load, and two strain modes. Only the load and position modes were used as active channels during this project. Notable features of the 8800D controller used

during this testing program were the Amplitude Control feature and the Analog Output feature. The Amplitude Control feature monitored feedback from the active channel of the system in real-time during testing and appropriately amplified the command signal to the servovalve. In doing this, the controller was able to automatically maintain the desired value for the active channel throughout a test. The Analog Output feature allowed the controller to transform the load and position data measured by the load cell and LVDT into output voltages. Thus, by connecting coaxial cables from the controller to analog channels of a separate data acquisition system, the load and position of the actuator could be recorded by the data acquisition system.

Standard equipment accompanying this controller included an 8800 operator panel and the FastTrack console. All functions of the controller could be accessed through either the operator panel or the FastTrack console, which was a user interface installed on an accompanying PC. For this project, the FastTrack console was used to control the system at all times because the FastTrack console was integrated with the software program used to create the loading protocol and monitor the waveform during testing.

For this project, the loading protocol applied to the specimens was created using the WaveMaker-Editor software program. This program created block files that were loaded into the controller to regulate the actions of the actuator during a test. For each block created in WaveMaker-Editor, the waveform parameters for that block as well as any data sampling, data storage, and event detection parameters were entered. To execute the block files created by WaveMaker-Editor, the WaveMaker-Runtime program was used. This program provided a user interface for controlling, monitoring, and modifying the progress of each fatigue test. The WaveMaker-Runtime interface included continuously updating graphs of actuator position versus time, load cell reading versus time, and load cell reading versus actuator position. A

real-time track of the active channel, which was the load channel, was also part of the interface. A sample screenshot of the WaveMaker-Runtime user interface is shown in Figure 3.12. This figure shows the WaveMaker-Runtime interface in the middle of the figure and the live displays integrated with the FastTrack console at the top of the figure. One important feature of the WaveMaker-Runtime application was that all of the menus of the FastTrack console were available while testing was in progress. During a test, the minimum load, maximum load, frequency, manual signal amplification, event detectors, and amplitude control features could all be accessed and easily modified.

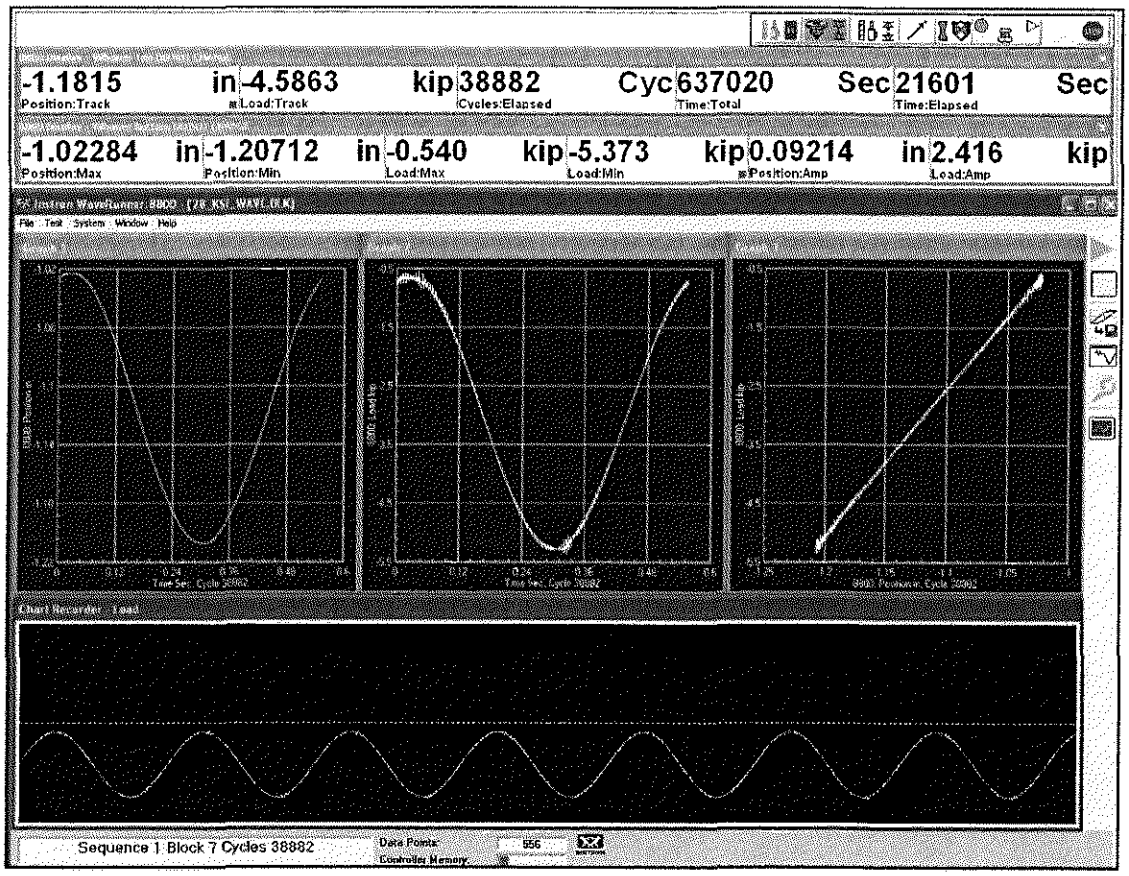

Figure 3.12. WaveMaker-Runtime user interface.

During each fatigue test, data from the testing machine's LVDT and load cell was recorded and stored in a Microsoft Excel file by the 8800D controller. As previously mentioned, the type of data and frequency at which data was stored was established when writing the block files using the WaveMaker-Editor program. For this project, data was sampled from both the LVDT and the load cell at a frequency of 2000 hz and recorded for every 50^{th} cycle. Every 50^{th} cycle, the minimum and maximum load measured by the load cell as well as position measured by the internal LVDT were recorded. In this manner, only four data points were generated every 50^{th} cycle, resulting in a manageable amount of data to be stored and analyzed. By subtracting the minimum load and position recorded from the maximum load and position recorded, respectively, the cyclic load and cyclic displacement of a specimen could be determined. This data was used to compare the behavior of the different specimen types as well as monitor for changes in the behavior of a given specimen throughout a test. As will be discussed in section 3.4.3, cyclic data was used to detect crack propagation and growth in the specimens.

3.2.5 Test Parameters

3.2.5.1 Waveform

During fatigue testing, movement of the actuator was regulated by the controller using data measured by the testing machine's internal load cell. By activating the controller's Amplitude Control feature, the controller monitored feedback signals from the testing machine's load cell and applied an appropriate amplification to the command signal given to the actuator to accurately maintain the amplitude and path of the waveform. All specimens tested in this program were subjected to a waveform that followed a sinusoidal load path from a minimum applied load to a maximum applied load. The primary parameters that were inputted into the WaveMaker-Editor software to define the waveform were the waveform shape, minimum load, maximum load, and loading frequency.

3.2.5.2 Applied Load Range

The first step in defining the parameters that controlled the waveform during testing was to determine the load range corresponding to the desired stress range at the weld toe. To determine the required load range, the required moment range at the weld toe was first calculated from the flange section properties. The equation used to calculate the required moment range was $M_{req}=\sigma I/y$, where σ was the desired stress range at the weld toe, I was the moment of inertia of the flange, and y was the neutral axis depth in the flange. Using the linear moment gradient imposed by the 3-point bending frame, the required load range was then calculated from the required moment range. The equation used to calculate the required load range was $P_{req}=2M_{req}/x$ where x was the distance from the transverse weld toe to the nearest outer load point of the three-point-bending frame. Sample calculations for determining the applied load range corresponding to a desired weld toe tensile stress range can be found in the Appendix H. A summary of the nominal weld toe stress ranges and the corresponding applied load ranges that were used during testing is found in Table 3.2.

Table 3.2. Applied load ranges corresponding to nominal weld toe stress ranges.

Nominal Weld Toe Stress Range, MPa (ksi)	Applied Load Range kN (kips)
59 (8.5)	6.530 (1.468)
96.5 (14.0)	10.75 (2.417)
138 (20.0)	15.36 (3.453)
193 (28.0)	21.50 (4.835)

3.2.5.3 Load Ratio

Once the load range was calculated for a desired weld toe stress range, the maximum and minimum applied loads corresponding to the peaks and troughs of the sinusoidal waveform had to be determined. Along with the waveform shape and the loading frequency, the minimum and maximum applied loads were the primary inputs when defining a load-controlled, sinusoidal waveform in Wavemaker. According to

the AASHTO specification (AASHTO 2004), only the stress range, not the maximum and minimum stress, affects the fatigue life of a weldment. Therefore, any combination of maximum and minimum stress that results in the desired stress range at the weld toe could theoretically be applied to the specimens. This means that any corresponding minimum and maximum applied loads could be used for the waveform.

However, recent research (Roy et al. 2003; Koenigs et al. 2003) suggests that UIT is the most effective at extending the fatigue life of a weld detail when the stress ratio, r (ratio of minimum applied stress to maximum applied stress), is at a minimum. It is important to note that the minimum and maximum stresses used in determining the stress ratio are measured relative to the stress in the weld detail at the instant UIT is performed. Therefore, adjusted minimum and maximum stresses equal to the actual minimum and maximum stresses minus the stress during UIT treatment must be used when determining the stress ratio. In an effort to determine the greatest possible improvement caused by UIT, and to simulate loading conditions of actual UIT-treated bridge details, all specimens tested in this project were tested at a constant stress ratio of 0.1, which is considered to be a small stress ratio. Since the specimen weld toes were treated with UIT while under no load, the minimum and maximum stresses applied during testing did not need to be adjusted when calculating the stress ratio. Typically, UIT is performed on a detail of an assembled structure where all self-weight and permanent dead loads have been applied. Therefore, the adjusted minimum stress at the treated detail is approximately zero and the load ratio is also very nearly zero.

Once the required load range was determined, the minimum and maximum loads were calculated using the load ratio. For a constant load ratio of 0.1, the equation used to calculated the minimum load was $P_{min} = (1/9)P_{range}$, where P_{range} was the required load range. The maximum load range was then calculated using the

equation $P_{max} = P_{min} + P_{range}$. Sample calculations for determining the minimum and maximum applied load for a required load range and a load ratio can be found in the Appendix A. A summary of the minimum and maximum loads applied to the specimens tested at various nominal weld toe stress ranges is shown in Table 3.3.

Table 3.3. Summary of minimum and maximum applied cyclic loads.

Nominal Weld Toe Stress Range, MPa (ksi)	Applied Load Range, kN (kips)	Maximum Applied Load, kN (kips)	Minimum Applied Load, kN (kips)
59 (8.5)	6.530 (1.468)	0.726 (0.163)	7.256 (1.631)
96.5 (14.0)	10.75 (2.417)	1.19 (0.269)	11.95 (2.686)
138 (20.0)	15.36 (3.453)	1.71 (0.384)	17.07 (3.837)
193 (28.0)	21.50 (4.835)	2.39 (0.537)	23.90 (5.372)

3.2.5.4 Loading Frequency

The final parameter that defined the sinusoidal waveform being applied to the specimens was the rate at which the specimens were cycled, referred to as the "loading frequency" and measured in cycles/second. It was found that the loading frequency was limited by the method chosen to load the specimens. Because the specimens were being bent about their weak axis during three-point-bending, the deflection of the lower portion of the bending frame with respect the upper portion of the bending frame was rather large. This large deflection translated into a relatively large range of actuator movement of nearly 5 mm (0.2 in.) at the final stress range. Thus, the loading frequency had to be held at a relatively small value to allow the hydraulic pump to accommodate the large actuator deflection. At nominal weld toe stress ranges of 8.5 and 14 ksi, a loading frequency of 5 Hz could be maintained. At a weld toe stress range of 20 ksi, the frequency had to be dropped to 3.0 Hz. At the final weld toe stress range of 28 ksi, the maximum loading frequency at which the hydraulic pump could maintain a pressure of 17 MPa (2400 psi) required to operate the crosshead clamps and wedge grips was 1.8 cycles/second. At frequencies higher

than this value, the crosshead clamps would eventually unlock and the controller would end the fatigue test. Therefore, all specimens subjected to 28 ksi nominal weld toe stress range were tested at 1.8 cycles/second until the onset of rapid fatigue crack propagation. This frequency resulted in the completion of 155,500 cycles in a 24-hour period. Once a specimen began to deflect severely due to advanced crack propagation, the loading frequency was slowed to 1.5 cycles/second for the duration of the test to maintain the required hydraulic pressure.

3.3 FATIGUE TESTING INSTRUMENTATION

3.3.1 Strain Gages

Actual stresses in the specimens were measured using an array of strain gages. The strain gages used were Vishay Micro-Measurements uniaxial strain gages having the designation WK-06-250BG-350. The conductive foil used in these gages was a nickel-chromium alloy called K-alloy, which is a modified Karma alloy in self-temperature-compensated form. This alloy was chosen because of its excellent fatigue life of 10^7 cycles at 2000 με and its good stability (Vishay 2007a). The carrier matrix or backing of the gages was a fully encapsulated, glass-fiber-reinforced epoxy phenolic resin. This backing provides outstanding performance over a wide range of temperatures (-233°C to +288°C (-452°F to +550°F)) and has a maximum elongation of 2%. The maximum specified elongation for each gage as a whole was ±1.5%. The foil grid used in the gages had an active gage length of 6.35 mm (0.250 in.) and a grid width of 3.18 mm (0.125 in.). The overall gage dimensions were 13.2×5.59 mm (0.520×0.220 in.). The gages had a resistance of 350.0 Ohms ± 0.3%, a gage factor of 2.03 ± 1.0%, and a transverse sensitivity of -4.4% ± 0.2% (Vishay 2007b). Each gage also had high-endurance leadwires pre-soldered to the grid by the manufacturer. This option was chosen so that soldering directly to the gages was not necessary, eliminating the possibility of fatiguing a soldered connection to failure during testing. Complete specifications for the gage used can be found in Appendix F.

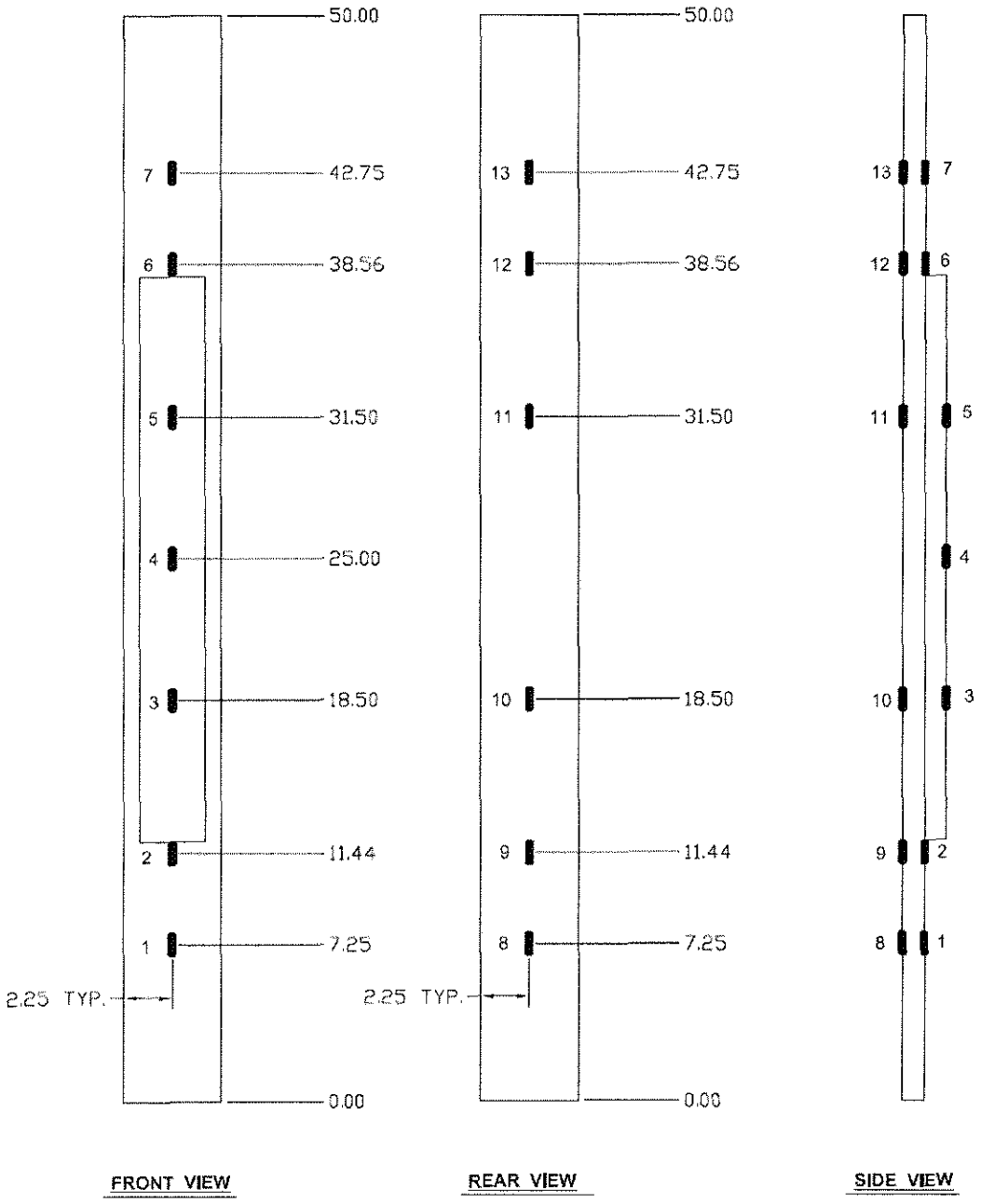

Figure 3.13. Strain gage locations.

To obtain a thorough portrait of strains, each fatigue specimen was fitted with 13 of the strain gages described above, placed at locations shown in Figure 3.13. All gages were placed with their centerlines aligned with the longitudinal centerline of the specimen. As Figure 3.13 shows, the gages were placed symmetrically about the transverse centerline of each specimen. This was done to ensure that the specimen was being loaded symmetrically, i.e. gages one and seven would show identical strains if being loaded symmetrically. Also, Figure 3.13 shows that at every gage location, there is a gage on both the front and back of the specimen. This was done so that a profile of the neutral axis location could be determined throughout the length of the member.

3.3.2 Strain Gage Temperature Effects

Whenever strain gages are used, close attention must be paid to the harmful effects of ambient temperature and changes in ambient temperature on the performance of the strain gages. In general, changes in temperature cause the material that a gage is bonded to and the gage itself to expand or contract, causing an actual temperature-induced strain in the gage. In addition, the resistance properties of the foil used in the gage change as the temperature changes, resulting in spurious apparent strain in the gage. As mentioned earlier, the gages used in for this project are self-temperature-compensating (S-T-C), meaning that the effects of temperature can be neglected under most conditions. This is possible because the metallurgical properties of K-alloy gages are such that this alloy can be processed to minimize the thermal output over a wide temperature range when bonded to test materials with thermal expansion coefficients for which they are intended. This is demonstrated by Figure 3.14, which shows the variation in thermal output of K-alloy with temperature (Vishay 2007c). Note that when near room temperature (+24°C (+75°F)), the thermal output for K-alloy is very negligible. The S-T-C of the gages used for this project was 06 ppm/°F (parts per million per degree Fahrenheit), which is an alternate

notation used to express the coefficient of thermal expansion of the gage. The corresponding coefficient of thermal expansion for carbon steel is 6.7 ppm/°F, which matches the S-T-C of the gage quite well.

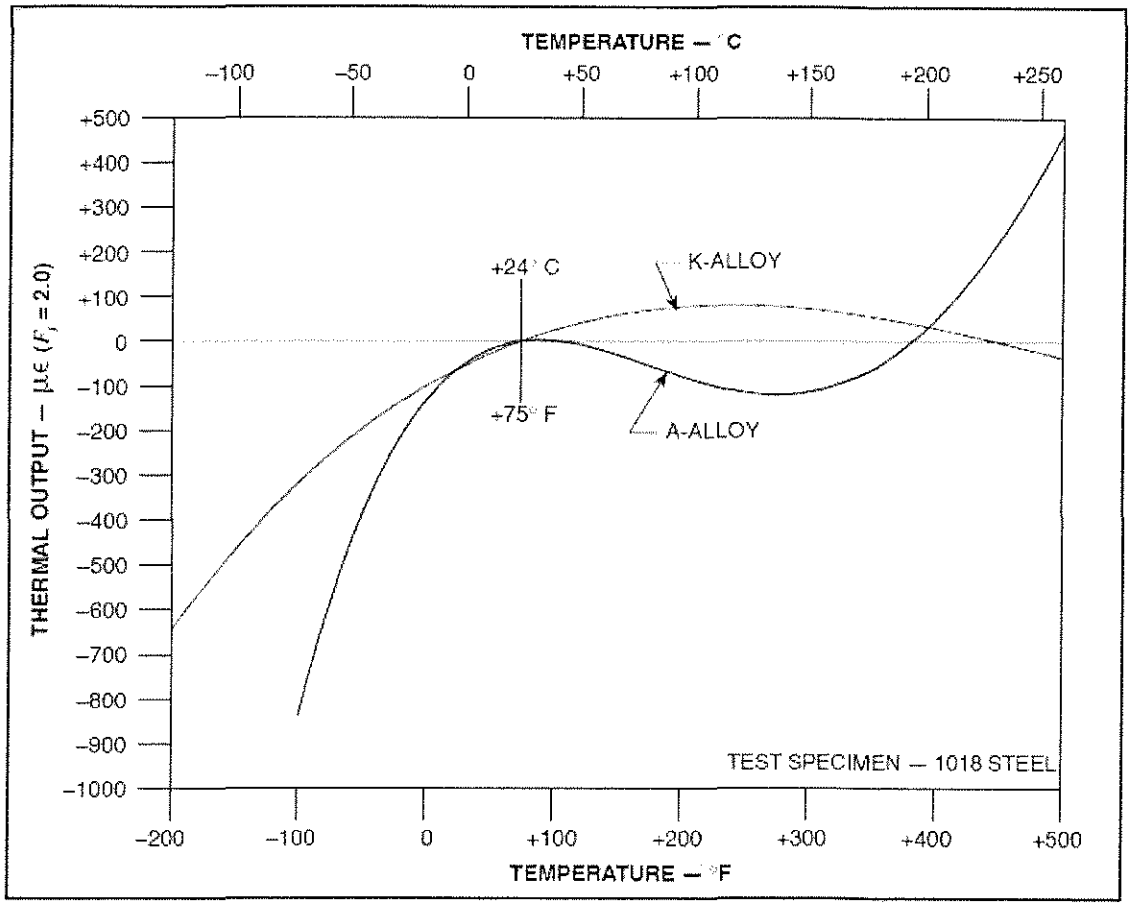

Figure 3.14. Thermal output variation in temperature for self-temperature-compensated K-alloy strain gages (Vishay 2007c).

Another advantage of K-alloy gages is that the gage factor changes very little with changes in temperature. As Figure 3.15 shows, the gage factor for a K-alloy gage changes linearly with temperature changes. For S-T-C of 06, the gage factor changes by a mere 1.0% ± 0.2% per 100°C (212°F) (Vishay 2007c). Since testing for this project was performed at approximately 23°C (73°F), changes in gage factor as well as thermal output of the gages could safely be neglected.

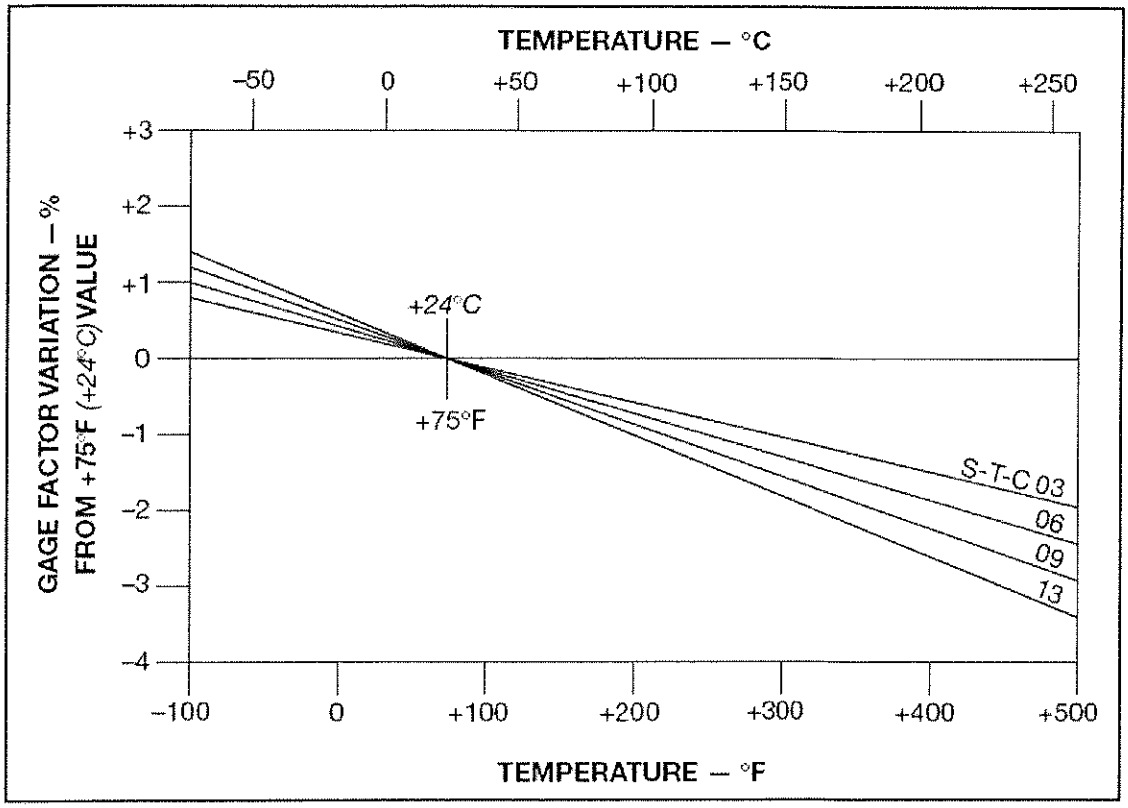

Figure 3.15. Variation of K-alloy gage factor with temperature (Vishay 2007c).

3.3.3 Strain Gage Installation

3.3.3.1 Surface Preparation

The first and most important step in the strain gage installation process is surface preparation. Proper surface preparation is necessary to produce a chemically clean surface having appropriate roughness, alkalinity, and layout lines. The surface preparation was performed in accordance to Vishay Micro-Measurements Application Note B-129-8 (Vishay 2005a).

Following the procedure recommended by this Application Note, all surfaces of a specimen were first thoroughly degreased to remove oils, greases, organic contaminants, and soluble chemical residues. Degreasing was achieved by spraying CSM-2 (an aerosol degreasing solvent) on all surfaces, and wiping dry with a clean cotton cloth.

After degreasing, the specimen surface was abraded in the vicinity of each strain gage location to remove the mill scale from the base metal and to produce a surface texture suitable for strain gage bonding. At a given gage location, the mill scale was removed from an area approximately 38 mm (1.5 in.) long by 25 mm (1.0 in.) wide using a Dremel rotary tool with a tapered grinding stone bit. An ideal surface texture was then achieved using silicon-carbide sandpaper. First, the surface was wet-sanded for several minutes using 220-grit sandpaper and liberal amounts of M-Prep Conditioner A. Conditioner A is a water-based, mildly acidic surface cleaning solution that, when used during wet-sanding, accelerates the cleaning process and acts as a gentle etchant. After thorough wet-sanding, the surface was rinsed with several drops of Conditioner A and wiped dry using gauze sponges. When wiping the surface, a clean gauze sponge was started in the middle of the abraded area and pulled toward the edge, then repeated for the other half of the treated area using a new clean gauze sponge. This was done to ensure that no contaminants from the surrounding surface were pulled into the abraded area. The wet-sanding procedure described above was then repeated using 320-grit sandpaper until a smooth surface free of flaws was produced. The surface was then rinsed with Conditioner A and wiped dry with gauze sponges to complete the surface abrading process.

To facilitate accurate placement of a given strain gage, a pair of crossed layout lines were then burnished into the abraded surface at the point where the strain measurement was to be made. The pair of layout lines consisted of one line oriented in the direction of strain measurement and the other line oriented perpendicular to the first line. These lines were then used as reference lines when placing the strain gage. Burnishing the layout lines into the surface was achieved by lightly pulling a ballpoint pen across the surface. Lines were burnished, rather than scored or scribed, to avoid introducing stress concentrations in the material at the layout line locations.

To achieve a chemically clean surface at a given gage location, several drops of Conditioner A were applied to the abraded surface. The surface was then scrubbed with wooden, cotton-tipped applicators until a clean tip was no longer discolored during scrubbing. Care was taken to ensure that the surface remained wet during scrubbing and that the Conditioner A was not allowed to dry on the surface. Once it was deemed chemically clean, the surface was wiped dry using gauze sponges as described above.

Finally, M-Prep Neutralizer 5A was used to restore the neutral alkalinity of the surface, which was left in an acidic state from the Conditioner A. At a given gage location, Neutralizer 5A was applied liberally and the surface was scrubbed with a wooden, cotton-tipped applicator for approximately one minute. When neutralized, the surface was wiped dry using gauze sponges as described above. Since a fully-prepared surface may become contaminated very quickly by the ambient environment, care was taken to apply a strain gage to a prepared surface within minutes of neutralizing.

3.3.3.2 Strain Gage Application

The application of strain gages to the prepared surface was performed in accordance to Vishay Micro-Measurements Instruction Bulletin B-127-14 (Vishay 2005b). Since the reliability and longevity of the bond between a strain gage and the base material depends heavily on the chemical cleanliness of both the gage and the base material, care was taken throughout the gage application process to avoid touching the gage or prepared surface. To achieve a chemically clean surface from which to handle the strain gages, the lid of an acrylic strain gage case was scrubbed with a wooden, cotton-tipped applicator and a liberal amount of Conditioner A. The lid was dried with gauze sponges, neutralized with Neutralizer 5A, and dried again with gauze sponges. This process was repeated between every strain gage application to maintain chemical cleanliness.

To begin the strain gage application process, a strain gage was first transferred from the manufacturer's envelope to the cleaned gage case lid. To avoid contamination, the gage was transferred by grasping by the leadwires using a pair of tweezers. The gage and two bondable terminals were placed bond-side-down on the lid. The bondable terminals were manufactured by Vishay Micro-Measurements and each consisted of a copper solder tab with a polyimide film backing. The terminals were placed on either side of the strain gage at locations convenient for leadwire attachment.

To transfer the gage and terminals to the specimen surface, a 150 mm (6.0 in.) length of M-Line PCT-2A cellophane tape was laid over the gage and terminals and rubbed against the lid to adequately adhere the top side of the gage and terminals to the tape. One end of the tape was then slowly pulled up and away from the gage at a 45° angle with respect to the lid until the entire length of tape was removed from the lid. This shallow angle was maintained to prevent damage to the gage resulting from excessive bending during removal from the lid. The gage was then placed onto the specimen surface, taking care to align both the longitudinal and transverse triangular alignment marks on the gage (see Figure 3.16) with the layout lines burnished into the specimen surface. Once properly aligned, the tape was rubbed thoroughly against the specimen to ensure that the position of the gage would not shift during bonding.

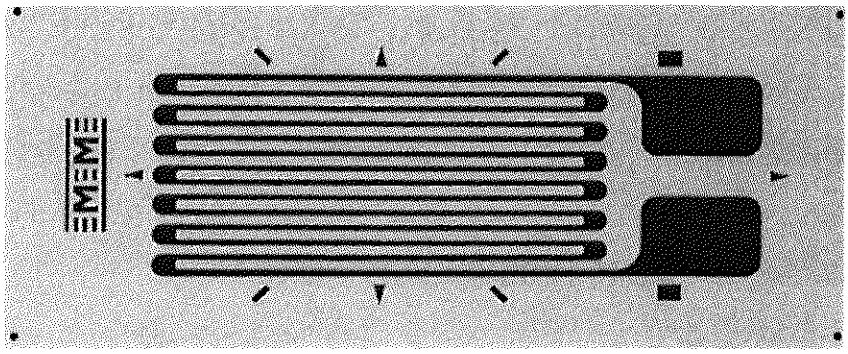

Figure 3.16. Micro-Measurements strain gage WK-06-250BG-350 (Vishay 2007b).

To prepare the gage and terminals for bonding to the surface, the end of the cellophane tape that was on the opposite side of the gage from the leadwires was slowly pulled up and away form the gage at a 45° angle with respect to the surface. The tape was lifted until it was free from the specimen approximately 8 mm (0.3 in.) beyond the far edge of the gage. The free end of the tape was then folded back and stuck to the specimen to expose the bonding surfaces of the gage and terminals. To improve the reactivity rate and effectiveness of the adhesive during bonding, M-Bond 200 Catalyst C was applied to the bonding surfaces of the gage and terminals. A very thin, uniform coat of catalyst was achieved by first dipping the brush in the bottle then stroking the brush against the inside neck of the bottle 10 times before swabbing the bonding surfaces with the brush.

After allowing the catalyst to dry for one minute, the tucked-under end of the tape was lifted from the specimen and held in place while one drop of M-Bond 200 adhesive was applied to the junction between the tape and specimen at the opposite end of the tape. Immediately after applying the adhesive, the free end of the tape was rotated back to its original position and held just above the surface. While holding the free end of the tape taut, a gauze sponge was firmly wiped over the top of the tape, starting at the side of the gage where the adhesive was applied and ending at the opposite end of the gage. Constant, firm pressure was then applied directly over the gage and terminals for one minute to allow the adhesive to adequately cure. After no less that two additional minutes, the bond between the gage and surface was strong enough to remove the cellophane tape. To remove the tape, one end of the tape was lifted and peeled back directly over itself at a 180° angle with respect to the surface until the entire piece of tape was free. At this point, the strain gage was ready to be soldered to the leadwires.

3.3.3.3 Wire Preparation

In conforming to the wiring schematic accompanying the data acquisition system, three-conductor shielded cable manufactured by Belden was used to connect the strain gages to the data acquisition system. Each conductor of the cable consisted of 22 American Wire Gauge (AWG) stranded, tinned copper wire with red, black, or clear polyethylene insulation. The three conductors were twisted and wrapped with Beldfoil® aluminum foil shielding and an accompanying 22 AWG stranded, un-insulated, tinned copper drain wire. The bundle of conductors and shielding was covered in a flexible polyvinyl chloride jacket for protection. Approximately 6100 mm (240 in.) of cable was needed to connect each strain gage to the data acquisition system's connection board.

To prepare one end of a cable to be soldered to a strain gage, 51 mm (2.0 in.) of the PVC jacket, aluminum shielding, and drain wire were stripped from the insulated conductors using a utility knife. After being untwisted and straightened, the three conductors were placed beside one another on a piece of scrap iron. A hot soldering iron was then laid across the conductors 25 mm (1.0 in.) from the end, causing the insulation to melt at that location. The insulation remaining at the ends of the conductors was then stripped by pulling firmly on the ends of the insulation, thus exposing 25 mm (1.0 in.) of bare stranded wire for each conductor. To accommodate soldering of the conductors to the strain gage leadwires, a single strand of bare wire was isolated and pulled at a 90° angle with respect to the other strands for the black and red conductors only. The remaining strands of the red conductor were then twisted together. The remaining strands of the black conductor were twisted with all of the strands of the clear conductor, forming a single, twisted bundle of strands. Each of the two twisted conductor ends was then tinned with solder to produce a formable solid conductor and trimmed to a length of 3.2 mm (0.13 in.) beyond the

start of the insulation using a wire cutter. The solder specifications and tinning procedure are discussed in the "Soldering" section of this chapter.

To prepare the other end of the cable to be connected to the data acquisition system, 76 mm (3.0 in.) of the PVC jacket and aluminum shielding were stripped from the insulated conductors and drain wire using a utility knife. Approximately 6.4 mm (0.25 in.) of insulation was then removed from the ends of the conductors using a wire stripper, and the exposed strands were twisted together. To facilitate quick and reliable connections to the connection board, spade terminals were fastened to the ends of the three conductors and the drain wire using crimping pliers.

3.3.3.4 Wire Soldering

Each strain gage was electrically connected to a 6100 mm (240 in.) cable by soldering the leadwires of the strain gage to the prepared end of a cable. Soldering was performed using a Vishay Micro-Measurements Mark VII Soldering Station, lead-free flux, and solder purchased from Vishay Micro-Measurements. The solder was an alloy consisting of tin and silver and had a melting temperature of 221°C (430°F). This solder was chosen primarily for its good mechanical fatigue properties, but also for its excellent strength and superior electrical conductivity. Soldering was performed following the procedure specified by Vishay Micro-Measurements Application Note TT-609 (Vishay 2007d).

Short circuiting of a strain gage caused by multiple wires contacting the specimen surface was prevented by adhering drafting tape to the specimen adjacent to the gage and terminals. Next, the solder tabs of the terminals were tinned to ensure rapid surface wetting and good heat transfer during the soldering operation. The first step of the tinning process was to apply a small amount of flux to each terminal using a brush. This was done to remove oxidation from the terminals and facilitate the flow of solder from the soldering iron to the terminals. After the soldering iron was allowed to heat to 221°C (430°F), the tip of the iron was wiped against a moist

sponge, and a small amount of solder was melted onto the tip of the iron. The tip was then lightly pressed against a terminal to transfer the solder onto the terminal. Additional solder, if needed, was added directly from the spool onto the terminal to form a smooth hemispherical dot of solder. This tinning process was also used to tin the exposed ends of the conductors in the cables as discussed previously.

With all components tinned, the two conductors from a cable were then soldered to the terminals. To attach a conductor to a terminal, the 3.2 mm (0.13 in.) exposed end of the conductor was first bent down approximately 45°. The end was then placed in contact with the tinned terminal while the tip of the soldering iron was pressed against the terminal. Once the solder on the terminal had melted, the iron was removed and the conductor was held in place until the solder cooled and hardened.

To complete the electrical connection between the strain gage and the cable, the gage leadwires were tied and soldered to the isolated wire strands of the conductors. To connect a pair of leadwires to an isolated strand, the two leadwires attached to one end of the strain gage circuit were first separated from the two wires attached to the other end. A small loop was formed in the pair of leadwires using tweezers, and the end of the strand from the conductor was inserted into the loop. Both ends of the loop were pulled carefully to form a knot around the strand. A small amount of solder was then applied to the knot to ensure a reliable electrical connection.

After a strain gage was soldered, a liberal amount of Vishay Micro-Measurements M-Coat A polyurethane coating was brushed over the gage. Once dry, this coating provided mechanical protection and electrical insulation for the gage. To prevent the cables from pulling on the terminals excessively during testing, each cable was secured to the specimen a short distance from its corresponding strain gage using bondable cable tie anchors and cable ties. As a final means of protecting the

strain gages during testing, each gage was covered by one or two pieces of duct tape prior to the start of testing. A complete strain gage installation, prior to the application of M-Coat A polyurethane coating and protective duct tape, is shown in Figure 3.17.

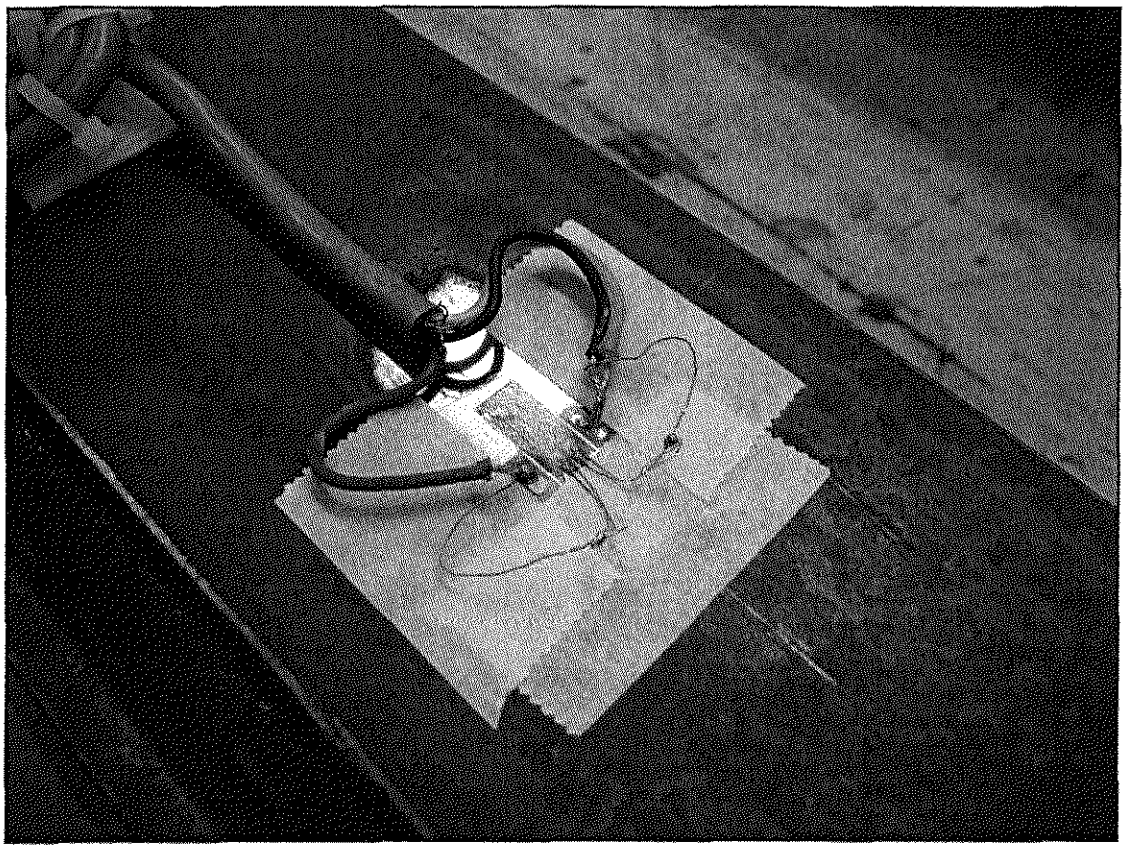

Figure 3.17. Strain gage installation (M-Coat A polyurethane and duct tape not shown).

3.3.4 Data Acquisition

3.3.4.1 WaveBook Data Acquisition System

Data from the strain gages were read and recorded using an IOTech WaveBook data acquisition system. The WaveBook is a portable data acquisition system capable of simultaneously recording up to 24 channels of strain input and eight channels of analog input. WaveBook features WaveView software, which is a

user-friendly, PC-based interface. Using WaveView, strain from multiple channels as well as analog signals from multiple channels could be monitored in real-time using the Scope feature or recorded to a text file using the Direct-to-Disk feature. To ease the connection of strain gage leadwires to the WaveBook, a plywood board with 13 sets of quick-connect terminal strips was fabricated. By permanently connecting the WaveBook input cables to the terminal strips, the strain gage leadwires could be quickly connected to the terminal strips to interface with the WaveBook. Figure 3.18 shows all components of the data acquisition system.

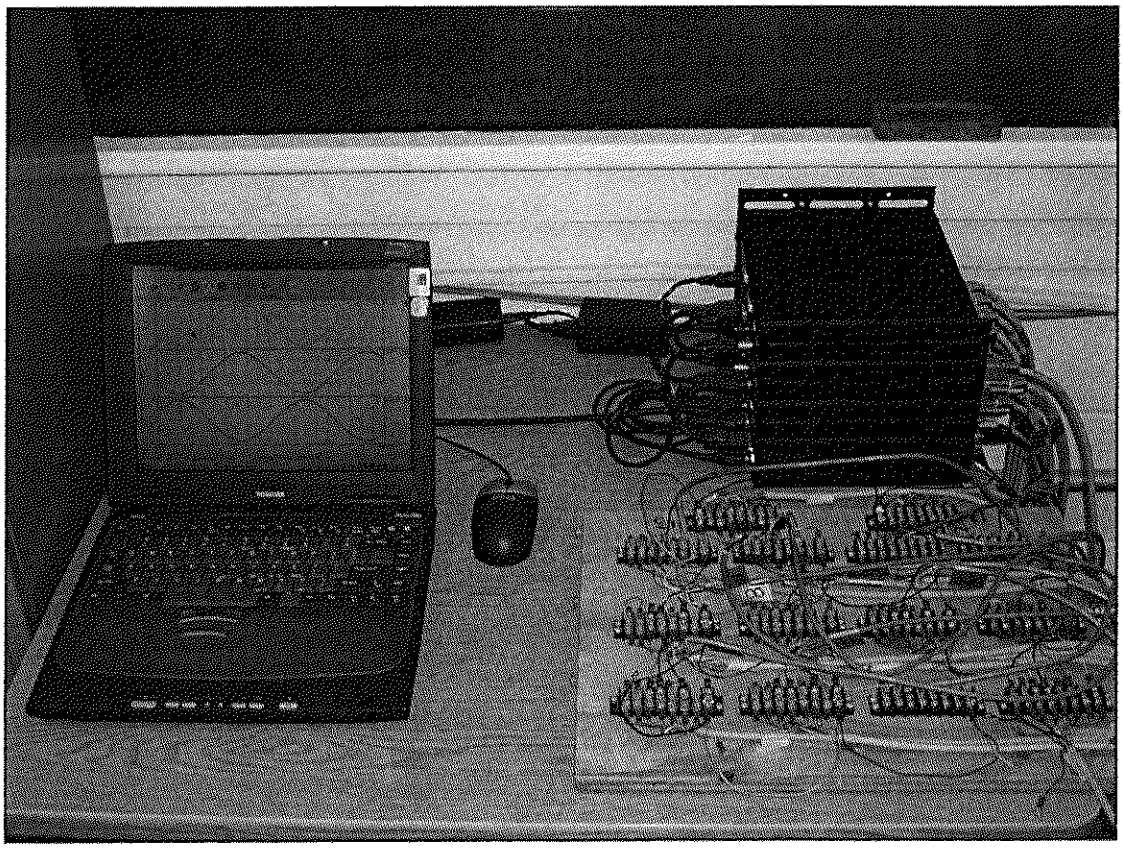

Figure 3.18. WaveBook data acquisition system components.

The WaveBook was capable of measuring strains using 1/4, 1/2, or full internal Wheatstone bridge circuits. For this testing program, the strain measured by

the gages was determined using 1/4 bridge Wheatstone bridge circuits having three 350Ω internal resistors and an excitation voltage of 10 volts. A large excitation was used to increase the sensitivity of the gages. As each gage was strained, the change in voltage measured across the Wheatstone bridge was correlated to the change in resistance of the gage using the shunt calibration method. The shunt calibrations were performed using WaveBook's internally supplied shunt resistances of 34.65 kΩ. Calibration was performed automatically using the WaveView strain gage calibration interface. The changes in resistance calculated for the strain gages were correlated to the strains in the gages using a gage factor of 2.03 provided by Vishay Micro-Measurements. Because three-conductor strain gage leadwires were used, the Wheatstone bridge circuits used in the WaveBook compensated for the effects of leadwire resistance. Since only 6100 mm (240 in.) lengths of leadwires were used, the effects of leadwire resistance could have been neglected regardless of whether or not compensation was employed.

3.3.4.2 Recorded Data

For each specimen, data was recorded using the WaveBook for all 13 strain gages as well as analog load and position inputs from the 8800D controller as discussed in section3.2.4. Since analyzing strain gage data was a very labor intensive and time consuming activity, data was recorded only once each day, corresponding to one reading per 150,000 cycles of testing. When recording strain, data from the strain gages was sampled at a frequency of 2000 cycles/second for a period of two seconds. This allowed approximately 3.5 fatigue cycles to be recorded. The data was then used to plot microstrain versus time for all of the strain gages, load versus time for the analog load input, and position versus time for the analog position input using Microsoft Excel. The average strain range was then determined for each gage by averaging the maximum and minimum strains recorded for the gage and calculating the difference of the averages. As will be discussed later in this chapter and later

chapters, the average strain ranges were then used to compare the behavior predicted by finite element models and theoretical models to the measured behavior, to monitor the initiation and propagation of fatigue cracks, and to ensure that the specimens were being loaded symmetrically. In addition to the regular data recorded by the WaveBook, data was also recorded during static stiffness tests as will be discussed in section 3.4.2.

3.4 FATIGUE CRACK DETECTION

3.4.1 Dye Penetrant

As each specimen was being tested, the fillet welds near the ends of the coverplate were routinely visually inspected for the presence of cracks using a Zyglo® Penetrant Kit manufactured by the Magnaflux Corporation. The penetrant kit contained a hand-held ultraviolet light, a fluorescent dye penetrant, a developer, and a cleaner/remover. The aerosol type dye penetrant, developer, and cleaner/remover were chosen for use over the liquid type to accommodate overhead application of these products. The dye penetrant was a water-insoluble penetrant that fluoresced a bright greenish-yellow color when exposed to ultraviolet radiation. This penetrant was ideal for detecting fatigue cracks because it was highly penetrative and very sensitive to narrow or shallow cracks.

At the outset of testing, it was determined that a procedure for detecting cracks differing from that published by the manufacturer gave the clearest and earliest indication of the presence of a crack. Therefore, a modified procedure incorporating only some of the features of the Zyglo kit was used to detect cracks during testing. When performing the modified dye penetrant inspection procedure, the testing machine remained cycling at the normal test load range for the duration of the inspection. The inspection process began by cleaning the weld and adjacent areas with the cleaner/remover, which contained the solvent naphtha. The cleaner/remover was sprayed onto the weld, wiped off with a paper towel, and allowed to dry for

several seconds. Once the surface was dry, the area to be inspected was sprayed thoroughly with dye penetrant. The dye penetrant was left on the surface for several seconds to allow full penetration of the dye into any cracks. All dye penetrant remaining on the surface was then removed as effectively as possible using a paper towel. At this point, the procedure used during testing differed from the manufacturer's procedure in that the developer was not used. Instead, the ultraviolet light was held next to the weld and fatigue cracks were easily distinguished by pumping or surging of the dye penetrant into and out of the cracks. To aid in the inspection for surging under ultraviolet light, a hand-held magnifying glass with a focal length of about 51 mm (2.0 in.) was used. This method proved to be very effective at detecting even small cracks having a surface length less than 1.6 mm (0.063 in.).

The modified method for detecting cracks was chosen over the manufacturer's method because use of the developer required that all penetrant be completely removed from the surface prior to applying the developer. This was easily achieved for any flat, smooth surfaces. However, rough or irregular surfaces, such as those present at fillet welds, trapped sufficient amounts of developer in non-cracked surface deformations to cause false crack indications once the developer was applied. Using the modified method allowed cracks to be indicated effectively without the total removal of penetrant from the surface. Using the modified crack detection method had another advantage over using the manufacturer's recommended procedure in that the fatigue test did not have to be stopped to inspect for cracks using the modified method.

3.4.2 Static Stiffness Testing

In addition to using dye penetrant, a second technique was employed to detect the onset of weld toe cracking and to monitor crack propagation during fatigue testing of each specimen. This technique involved periodically subjecting a specimen to

static load tests. The primary objective of each static load test was to measure the specimen's overall resistance to bending under an applied static load. This resistance to bending was referred to as the "static stiffness" of a specimen. Theoretically, a decrease in the static stiffness of a non-yielding specimen held at a constant temperature could only be caused by a reduction in the effective cross-sectional area of the specimen. For the specimens used in this project, a decrease in the effective cross-sectional area was the result of a growing fatigue crack. Therefore, a decrease in the measured static stiffness of a specimen was taken as a direct indication of fatigue crack growth.

Before a static stiffness test could be performed on a specimen, the fatigue test being performed had to be stopped. In an effort to minimize disruptions to fatigue testing, static stiffness tests were performed only once daily for the UIT and UIT/BOLT specimens and every 20,000 cycles until crack initiation for the CONTROL and BOLT specimens. After CONTROL and BOLT specimens experienced crack initiation, static stiffness tests were performed once daily for the remainder of the fatigue test. Each static stiffness test was performed by controlling the load applied to the same three-point-bend configuration used for the fatigue tests. A load of 2.23 kN (0.500 kips) was first applied to the specimen and maintained for 5 seconds. The load was then ramped slowly to 24.47 kN (5.500 kips) over the next 60 seconds, resulting in a static loading rate of 0.371 kN/sec (83.3 lbs/sec). After maintaining 24.47 kN (5.500 kips) for 5 seconds, the static stiffness test was completed and the regular fatigue test was resumed. Throughout each static test, the position of the actuator and load applied by the actuator were measured by the testing machine's LVDT and load cell, respectively, and recorded by the controller's internal data acquisition system. Data was recorded at a frequency of 100 data points per second.

To determine the value of static stiffness for each static stiffness test, a graph of applied load versus absolute actuator position for the load ramp (excluding the first and last 10 seconds of the ramp) was plotted using Microsoft Excel. A linear trend line was then calculated and plotted using Excel's trend line generator. The value of the static stiffness was considered to be equal to the slope of that trend line, having units of kN/mm (kips/in.). Multiple static stiffness values determined in this manner were then plotted against the fatigue cycle at which each stiffness test was run to monitor changes in the static stiffness for each specimen throughout testing. Crack initiation was generally indicated by a series of similar stiffness values followed by a series of decreasing stiffness values. Acceleration or deceleration in crack propagation rates could also be determined by examining these plots. Sample plots of static stiffness as well as results of static stiffness tests are presented and discussed in section 4.5

In addition to recording data from the testing machine's LVDT and load cell, strain measurements were also recorded for the array of strain gages during static stiffness testing. This data provided a means to monitor changes in the deflected shape of a specimen caused by the formation of fatigue cracks. For each of the 13 strain gages, microstrains were recorded by the WaveBook at a frequency of 100 data points per second for the duration of the stiffness test.

From the strain data recorded during a load ramp (excluding the first and last 10 seconds of the ramp), a graph of microstrain versus absolute crosshead position was plotted for each strain gage using Microsoft Excel. A linear trend line was then calculated and plotted using Excel's trend line generator. The slope of this line was termed the "normalized microstrain" of the gage and had units of $\mu\varepsilon$/in. The normalized microstrain of a gage quantified the local rate of strain in the material at the location of that gage as the specimen underwent deflection. The deflected shape, or mode shape, of a specimen was approximated by simultaneously analyzing the

normalized microstrain for all 13 gages along the length of the specimen. Theoretically, the mode shape of an uncracked specimen would remain the same throughout the duration of a fatigue test. Thus, the values of normalized microstrain for all of the strain gages would remain constant until the initiation of fatigue cracking. Once fatigue cracks formed in a specimen, the mode shape of the specimen would be altered and the values of normalized microstrain for the gages would be changed. Therefore, fatigue crack initiation and propagation could be predicted by monitoring changes in the normalized microstrain for the strain gages. Results related to this monitoring technique are presented in section 4.5.

3.4.3 Dynamic Monitoring

For each specimen, fatigue crack initiation and growth were also monitored using data taken from the testing machine's load cell and internal LVDT during cyclic loading. As mentioned earlier in this chapter, the minimum and maximum position of the actuator as well as minimum and maximum load applied by the actuator were recorded by the controller's internal data acquisition system every 50^{th} cycle. For each recorded cycle, the cyclic displacement corresponding to the difference between the maximum and minimum actuator position was then calculated. Similarly, the load range corresponding to the difference between the maximum and minimum load applied by the actuator was also calculated for each recorded cycle. A measure of the overall resistance of a specimen to bending under dynamic loading, hereby referred to as the "dynamic stiffness" of a specimen, was calculated by dividing the load range by the cyclic displacement for each recorded cycle. The units of measure for the dynamic stiffness of a specimen were kN/mm (kips/inch).

Similar to the static stiffness discussed previously, the dynamic stiffness of a non-yielding specimen held at a constant temperature could only be decreased by reducing the effective cross-sectional area at any point in the specimen. For the

specimens used in this project, a reduction in the effective cross-sectional area was caused by fatigue crack growth. Therefore, a decrease in the dynamic stiffness was a direct indication of fatigue crack growth. By recording and monitoring changes in the dynamic stiffness of a specimen throughout the duration of a fatigue test, the initiation and propagation of fatigue cracks could be predicted. Performing dynamic stiffness measurements had an advantage over performing static stiffness measurements in that crack initiation and growth could be monitored continuously rather than periodically. In addition, recording the dynamic stiffness data did not require the fatigue test to be stopped.

In addition to the data taken by the testing machine's LVDT and load cell, cyclic strain values measured by the 13 strain gages and recorded by the WaveBook data acquisition system were also used to monitor fatigue crack initiation and propagation. As discussed earlier in this chapter, a two-second period of cyclic strain data was recorded at a frequency of 2000 data points per second once a day throughout the duration of each fatigue test. This data was used to calculate an average cyclic strain range for each strain gage under fatigue loading. These average cyclic strain ranges were not only used to calculate the cyclic fatigue stress ranges at the gage locations, but they were also used to detect the presence of fatigue cracks by monitoring changes in the cyclic strain ranges throughout a fatigue test.

3.5 TENSILE TESTING

Tensile testing of coupons cut from fatigue specimens was performed to determine the material properties of the A36 steel used to fabricate the specimens. Material properties of interest were yield strength and modulus of elasticity. Both of these material properties were used to define the material when creating finite element models (see Chapter 5). The modulus of elasticity was also used to determine stresses in fatigue specimens from measured strains (see Chapter 4). Other

material properties determined during fatigue testing were tensile strength and elongation.

Tensile testing was performed in accordance to American Society for Testing and Materials (ASTM) test designation E 8 (ASTM 2001). Following guidelines prescribed in test designation E 8, tensile coupons were machined from the mid-depth of the ends of the flanges. Machining was performed by Rice Precision Manufacturing in Baldwin City, Kansas. Figure 3.19 shows the dimensions of the tensile coupons. A total of 16 tensile specimens were machined from two control specimens after the specimens were fatigue tested. Fourteen of the specimens were tension tested to failure and the remaining two specimens were left untested for comparison.

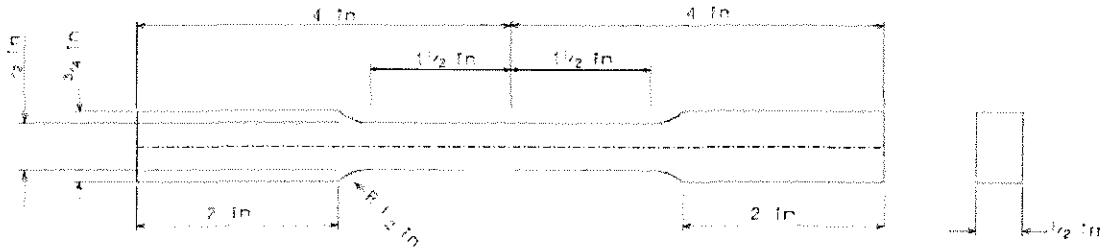

Figure 3.19. Tensile specimen dimensions.

Prior to tensile testing, the width and thickness at the center of the reduced section were measured using a digital caliper that was accurate to 0.01 mm (0.0005 in.). For each measurement, the dimension was measured five times, averaged, and rounded to the nearest 0.03 mm (0.001 in.) per test specification E 8. Also prior to testing, gage lengths were lightly punched into the surface of the reduced section to measure elongation after the completion of each tensile test. To mark the gage lengths, the same digital caliper was used to mark distances of 25.40 mm (1.000 in.) and 38.10 mm (1.500 in.) on each side of the specimen centerline using a pencil. The marks closer to the centerline formed a 50.80 mm (2.000 in.) primary gage length to be used in determining elongation. The marks farthest from the centerline formed a

76.20 mm (3.000 in.) secondary gage length to be used in determining elongation if the fracture occurred outside the primary gage length. These marks were made permanent by lightly punching the specimen surface at each mark.

In accordance with test designation E 8, the specimens were tested under position-controlled crosshead movement. Up to first yielding, the rate of crosshead separation was maintained at 0.25 mm/min (0.010 in./min) to provide a loading rate between the specified limits of 68.9 and 689 MPa/min (10,000 and 100,000 psi/min). After yielding, the rate of crosshead separation was increased to 13 mm/min (0.50 in./min) to provide a loading rate between the specified limits of 0.05 and 0.5 mm/mm length of reduced section/min (0.05 and 0.5 in./in. length of reduced section/min). This rate was maintained until specimen failure.

Throughout each fatigue test, load and position data were recorded by the controller. Additionally, extension data was measured by an Epsilon model 3542-0200-050-ST axial extensometer. This extensometer has a gage length of 50 mm (2 in.) and can measure extension from -10% strain to +50% strain. The working temperature range of this extensometer is -40°C to 100°C (-40°F to 210°F). This extensometer exceeds ASTM class B-1 requirements for accuracy, making it a acceptable for use in determining material properties per ASTM test designation E 8. A specification sheet as well as a certification sheet for this extensometer is shown in Appendix E.1. Data recorded by the load cell and extensometer was used to generate stress-strain curves for each specimen to determine material properties.

After test completion, the two halves of a specimen were fitted together and the distance between the original gage length punch marks was measured using the same digital caliper. This data was then used to determine the elongation of the specimen.

CHAPTER 4 EXPERIMENTAL RESULTS

4.1 FATIGUE LIFE

In this section, the experimentally-determined fatigue lives of 15 specimens are presented and compared to each other as well as to the AASHTO (2004) design equation (Eqn. 3.1) and corresponding S-N diagram. The fatigue lives to crack initiation reported correspond to the number of cycles elapsed prior to the visual detection of a fatigue crack through the use of the modified dye penetrant method as described in section 3.4.1. For reasons discussed in section 4.3.1, the dye penetrant crack detection method proved to be the most reliable and consistent method to detect the onset of fatigue cracking. The fatigue lives to failure reported correspond to the number of cycles elapsed before a specimen could no longer carry the applied load as a result of advanced fatigue crack growth.

4.1.1 Fatigue Life for Preliminary Specimens

As discussed in section 3.2.2, a number of specimens were tested at a nominal weld toe stress range of either 58.6, 96.5, or 138 MPa (8.50, 14.0, or 20.0 ksi) before a final stress range of 193 MPa (28.0 ksi) was chosen for the remainder of the specimens. All specimens tested at a nominal weld toe stress range less than 193 MPa (28.0 ksi) will henceforth be referred to as "preliminary specimens," and the results of fatigue tests performed on these specimens will be discussed in this section. The fatigue lives to crack initiation for all preliminary specimens are shown on the S-N diagrams in Figure 4.1 (SI units) and Figure 4.2 (U.S. Customary units) and summarized in Table 4.1. The S-N diagrams also show lines corresponding to the fatigue lives predicted by the AASHTO fatigue design equation (Eqn. 3.1) for the various fatigue categories.

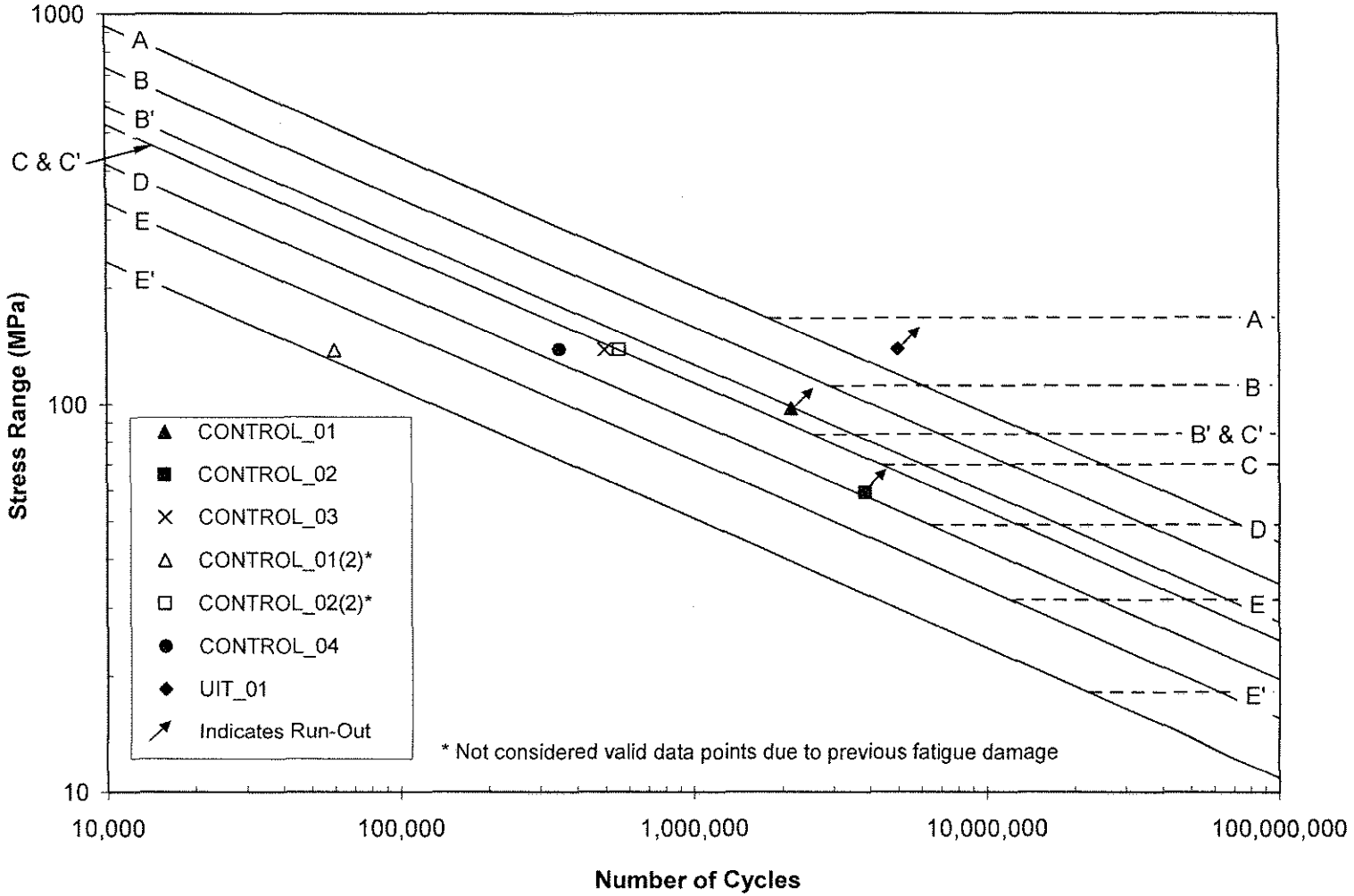

Figure 4.1. S-N diagram showing the results of preliminary testing and the AASHTO fatigue curves (SI).

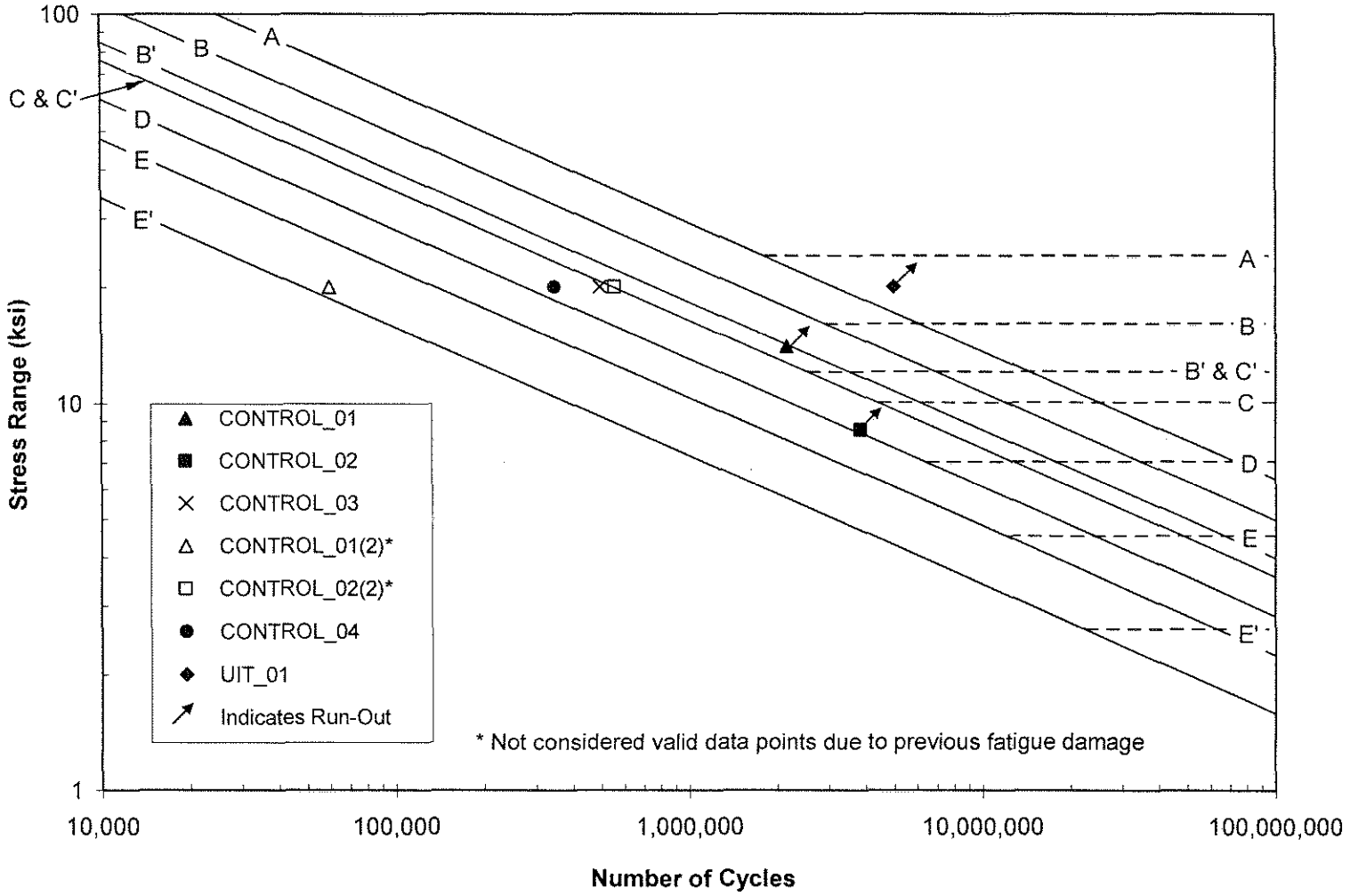

Figure 4.2. S-N diagram showing the results of preliminary testing and the AASHTO fatigue curves (U.S. Customary).

Table 4.1. Fatigue test results for preliminary specimens.

Specimen	Stress Range, MPa (ksi)	Cycles to Initiation	Cycles to Failure
CONTROL_01	96.5 (14.0)	2,160,000 *	Not Achieved
CONTROL_02	58.6 (8.50)	3,850,000 *	Not Achieved
CONTROL_03	138 (20.0)	500,000	Not Achieved
CONTROL_01(2)	138 (20.0)	60,000 **	Not Achieved
CONTROL_02(2)	138 (20.0)	520,000 **	Not Achieved
CONTROL_04	138 (20.0)	350,000	Not Achieved
UIT_01	138 (20.0)	5,000,000 *	Not Achieved
* Achieved run-out			
** Not considered valid data points due to previous fatigue damage			

4.1.1.1 Test Results for Preliminary Specimens

The first specimen to be fatigue tested was CONTROL_02. This specimen was tested at a nominal weld toe stress range of 58.6 MPa (8.50 ksi). Since failure was predicted to occur by Eqn. 3.1 at 635,000 cycles at this stress range, a run-out point was not defined prior to testing this specimen. After the specimen was cycled for 3,850,000 cycles without initiation of a crack, which was six times longer than predicted, it was declared that the specimen had achieved run-out. In an attempt to ensure that the next specimen tested, CONTROL_01, would develop a crack in a timely manner, the nominal weld toe stress range was increased to 96.5 MPa (14.0 ksi). Prior to testing this specimen, a run-out point of 2,000,000 cycles was defined. After achieving 2,160,000 cycles without initiation of a crack, this specimen was also declared to have achieved run-out. However, it must be noted that the crack inspection procedure using dye penetrant had not yet been fully optimized for these first two specimens. The procedure used to detect cracks for these specimens followed the manufacturer's procedure of using the developer in addition to the penetrant. As discussed in section 3.4.1, use of the developer may have caused small fatigue cracks to be misinterpreted as weld surface flaws. As a result, either of these specimens may have actually developed small fatigue cracks without being detected.

This potential occurrence, however, does not seem to be justified by data recorded by the controller. The controller data, although also not fully optimized for these early tests, did not indicate definite development of a crack in either of these specimens. As discussed later in this section, both of these specimens were later cycled at a nominal weld toe stress range of 138 MPa (20.0 ksi) and inspected for cracks using the more accurate modified dye penetrant detection procedure. Since no cracks were found in either specimen at the outset of testing at 138 MPa (20.0 ksi), it can be stated with certainty that neither specimen achieved fatigue crack initiation the first time it was tested.

After specimen CONTROL_01 achieved run-out, it was decided to increase the nominal weld toe stress range for the next specimen, CONTROL_03, to 138 MPa (20.0 ksi). For the first 930,000 cycles, visual crack inspection was performed using the manufacturer's dye penetrant procedure, thus masking any small fatigue cracks. At 930,000 cycles, the modified dye penetrant method of crack detection described in section 3.4.1 was employed for the first time, indicating the presence of a crack 6.4 mm (0.25 in.) in length at the center of the weld toe. This rather large crack size indicated that crack initiation had taken place earlier than 930,000 cycles but was not detected because of shortcomings in the manufacturer-prescribed dye penetrant detection method. In light of this, the fatigue life for this specimen was estimated by examining trends in data recorded by the controller, as will be discussed in section 4.3.1. The fatigue life to crack initiation for this specimen was determined to be approximately 500,000 cycles. This was one of only four specimens for which controller data was used to determine fatigue initiation life. The remainder of the specimens were examined for cracks using the modified dye penetrant method and their fatigue lives to crack initiation were based on the findings of those examinations.

To determine the effectiveness of the modified dye penetrant method at detecting small cracks, both of the previously tested control specimens, CONTROL_02 and CONTROL_01, were retested at a nominal weld toe stress range of 138 MPa (20.0 ksi). These specimens were designated CONTROL_01(2) and CONTROL_02(2). At the outset of testing these two specimens, it was understood that since they were both previously tested at stress ranges greater than the constant-amplitude fatigue threshold for a Category E' specimen of 18 MPa (2.6 ksi) (AASHTO 2004), these specimens had already endured unknown amounts of accumulated fatigue damage. Correspondingly, their fatigue lives to crack initiation when cycled at a stress range of 138 MPa (20.0 ksi) were expected to be less than that of CONTROL_03, which was 500,000 cycles. The main goal of testing these specimens was to become familiar with and test the effectiveness of the modified dye penetrant method, not to evaluate their fatigue lives.

The number of cycles to crack initiation for CONTROL_01(2) and CONTROL_02(2) was 60,000 and 520,000, respectively. Although data points for these two specimens are shown on Figures 4.1 and 4.2, it is noted that these results are affected by previous fatigue damage and do not represent the fatigue lives of undamaged control specimens subjected to a stress range of 138 MPa (20.0 ksi). From testing these two specimens, it was found that surface fatigue cracks could be visually detected using the modified dye penetrant method when they reached approximately 1.6 mm (0.063 in.) in length. The ability to detect cracks of this size was determined to be adequate for defining crack initiation.

Since CONTROL_03 developed a fatigue crack at 500,000 cycles, it was thought that the retrofitted specimens would each develop fatigue cracks in a finite number of cycles (less than 2,000,000) if they were subjected to a nominal weld toe stress range of 138 MPa (20.0 ksi). To test this hypothesis, one of the UIT-treated specimens, UIT_01, was cycled at a stress range of 138 MPa (20.0 ksi). Run-out was

declared when that specimen reached 5,000,000 cycles without detection of crack initiation.

Although this run-out value was ten times longer than the fatigue life of CONTROL_03, the goal of the project was to quantify improvement in fatigue life caused by the improvement methods. Therefore, it was deemed imperative that as many specimens as possible develop fatigue cracks in a finite number of cycles. After meeting with the KDOT project monitor, it was decided to once again increase the nominal weld toe stress range at which the specimens would be tested. It was determined that all further tests would be performed at this final weld toe stress range of 193 MPa (28.0 ksi) and run-out would be defined at a later time if necessary.

As discussed in section 3.2.2, one of the additional control specimens, CONTROL_04, was tested in fatigue at a nominal weld toe stress range of 138 MPa (20.0 ksi) to ensure that the three additional control specimens would behave similarly to the original specimens. CONTROL_04 cycled for 350,000 cycles before developing a fatigue crack. This value was 25% lower than the fatigue life of CONTROL_03, which was the original control specimen tested at 138 MPa (20.0 ksi). One possible explanation for the shorter fatigue life of specimen CONTROL_04 was that the welds on the three additional specimens appeared to be of lower quality than the welds on the original specimens, as discussed in section 3.2.2. Although the percent difference between the fatigue lives of the original and additional control specimens was significant, it was considered to be acceptable given the general variability inherent in fatigue testing. Thus, the fatigue lives of the two additional control specimens tested at a nominal weld toe stress range of 193 MPa (28.0 ksi) were considered to be valid data points and were compared to the fatigue lives of the retrofitted specimens tested at a stress range of 193 MPa (28.0 ksi) without adjustment. In the course of testing all preliminary specimens, none of the specimens reached fatigue failure.

4.1.1.2 Comparison of Preliminary Specimen Results to AASHTO Equations

As evident from Figures 4.1 and 4.2, the fatigue lives of all preliminary specimens exceeded the fatigue life predicted by the AASHTO fatigue design equation (Eqn. 3.1) for a Category E' detail by a large margin. Of the four preliminary control specimens, the two specimens not achieving run-out failed after exceeding the AASHTO Category D design curve. CONTROL_02 and CONTROL_01 achieved Category D and Category C classification, respectively, before run-out was declared. As stated earlier, CONTROL_01(2) and CONTROL_02(2) were not valid data points and did not display fatigue behavior representative of undamaged control specimens. The preliminary specimen treated with UIT achieved AASHTO Category B classification in the infinite-life region of the S-N diagram (for Category B details) before run-out was declared.

To gain an understanding of why the preliminary control specimens outperformed the AASHTO fatigue design equation for a Category E' detail by a large margin, it was first necessary to examine how the AASSHTO design equations were determined. The AASHTO fatigue curves were constructed from the results of numerous fatigue tests performed over a period of several decades, starting in the 1960's, on full-scale bridge girders employing various weld details (Barsom and Rolfe 1999). For each of the geometries tested, it was found that the presence of gouges and weld-imperfection stress raisers in a detail decreased the fatigue life of that detail. Consequently, significant variability in fatigue-life data was obtained for details having identical geometry but containing different size imperfections. In one study, the longest fatigue life obtained for a certain detail was about four times longer than the same detail that exhibited the shortest life (Barsom and Rolfe 1999). To ensure that an adequate margin of safety was incorporated into the fatigue design of bridges, the AASHTO design equation for each detail category was written so that it corresponded to the 95% confidence limit for 95% survival of all details included that

category. Thus, the AASTHO design equation for a given category roughly estimates the fatigue life of a detail having the worst possible weld quality. As noted in section 3.1.2, the fillet welds on the specimens tested in the current project were determined to be at least average quality if not better. Given the strong correlation between weld quality and fatigue life, the fact that the specimens outperformed the AASHTO Category E' design curve by a significant margin may be explained by the high quality of the welds alone.

The continuum of detail geometries tested during the development of the AASHTO fatigue specification was divided into eight categories (A, B, B', C, C', D, E, and E'). Naturally, a variance in stress concentration severity exists within each category as result of varying detail geometry. As stated above, the AASHTO design curve for each category was drawn so that it corresponded to the 95% confidence limit for 95% survival of all details included that category. Thus, the AASTHO design curve for a given category roughly corresponds to the detail having the most severe geometry within the category in addition to the lowest weld quality. Details having the least severe geometry within a category would be expected to outperform the AASHTO design curve for that category. Since the coverplates on the specimens tested in the current program were only slightly thicker than the 20 mm (0.80 in.) limit separating Category E' coverplate details from Category E coverplate details (AASHTO 2004), the specimens had less severe geometry than other Category E' details having thicker coverplates that were tested when developing the Category E' design curve. The specimens should have outperformed the AASHTO Category E' design curve on that basis alone. The combination of high relative weld quality and low relative detail severity accounts for the specimens' long fatigue lives and their outperforming the AASHTO Category E' design curve.

4.1.2 Fatigue Life for Control Specimens

The two remaining control specimens to be tested at a nominal weld toe stress range of 193 MPa (28.0 ksi) were CONTROL_05 and CONTROL_06. CONTROL_05, being the first control specimen tested at a stress range of 193 MPa (28.0 ksi), was expected to cycle for at least 100,000 cycles prior to crack initiation. Thus, the specimen was visually inspected for cracks using dye penetrant at 20,000 cycles and not inspected again until 125,000 cycles. When the specimen was inspected at 125,000 cycles, the presence of cracks over 51 mm (2.0 in.) in length at both transverse welds indicated that crack initiation had occurred much earlier than expected. Similar to CONTROL_03, the fatigue life to crack initiation for this specimen had to be estimated by examining trends in the data recorded by the controller (see section 4.3). By examining controller data, it was concluded that crack initiation had occurred at approximately 80,000 cycles. Taking into consideration the short fatigue life obtained by CONTROL_05, CONTROL_06 was visually inspected using dye penetrant at frequent intervals until crack initiation. From interpolating the results of dye penetrant inspections performed at 40,000 and 60,000 cycles, it was determined that crack initiation criteria were met at approximately 50,000 cycles for CONTROL_06.

The average of the fatigue lives of these two specimens was 65,000 cycles, and the percent difference between the fatigue lives was 38%. For typical fatigue testing of weldments, it is ideal to select a stress range so that all specimens are allowed to cycle for at least 100,000 cycles prior to crack initiation as suggested by the S-N diagram presented in the AASHTO specification. Unfortunately, the large improvement in fatigue life displayed by the preliminary UIT specimen dictated that the fatigue lives of the control specimens had to be very short if the retrofitted specimens were to fail in a finite number of cycles. Although an average fatigue life of 65,000 cycles was not ideal, it was an accurate measure of the fatigue life of the

control specimens when tested at a stress range of 193 MPa (28.0 ksi) and will be used to compare the performance of the control specimens to the retrofitted specimens.

CONTROL_05 cycled for a total of 290,000 cycles until it reached failure as previously defined. The resulting propagation life of this specimen, defined as the difference between the fatigue life to initiation and the fatigue life to failure, was 210,000 cycles. Due to time limitations, CONTROL_06 was not cycled to ultimate failure, and was removed from the testing machine after 280,000 cycles. Crack locations and propagation behavior for these and all other specimens are discussed in section 4.2.

4.1.3 Fatigue Life for Bolted Specimens

All three of the bolted specimens were tested at a nominal weld toe stress range of 193 MPa (28.0 ksi). BOLT_01, being the first specimen tested at a stress range of 193 MPa (28.0 ksi), was expected to cycle for a least a few hundred thousand cycles prior to crack initiation. Similar to CONTROL_01, BOLT_01 was inspected for cracks using dye penetrant at the start of testing and not again until 90,000 cycles had elapsed. When inspected at 90,000 cycles, a shallow crack measuring 6.4 mm (0.25 in.) in length was detected at the transverse weld toe, indicating that crack initiation had taken place shortly before the specimen was inspected. Once again, trends in the data recorded by the controller were used to estimate the fatigue life to initiation for the specimen. By examining controller data, it was estimated that crack initiation for BOLT_01 occurred at approximately 80,000 cycles.

Given the short fatigue life achieved by BOLT_01, the two remaining bolted specimens were inspected for cracks every 20,000 cycles until fatigue crack initiation. After initiation, they were inspected once daily for the remainder of the test. BOLT_02 was found to have extremely small fatigue cracks less than 1.6 mm (0.063

in.) in length when inspected using dye penetrant at 40,000 cycles and a larger crack measuring 6.4 mm (0.25 in.) in length when inspected at 60,000 cycles. These results suggest that the fatigue life to crack initiation for BOLT_02 was approximately 50,000 cycles. When BOLT _03 was inspected at 75,000 cycles, it had developed a 6.4 mm (0.25") crack in one of the welds toes, indicating that initiation had taken place just prior to inspection. Since the specimen was found to have no cracks when it was inspected at 60,000 cycles, it was determined that the fatigue life to crack initiation of BOLT_03 was 70,000 cycles.

The rounded average of the fatigue lives of the three bolted specimens was 70,000 cycles. The range of the fatigue lives was 30,000 cycles and the percent difference in fatigue life between the specimen with the shortest fatigue life and the specimen with the longest fatigue life was 38 %. Similar to the results of the control specimens, the average fatigue life of the bolted specimens was shorter than the ideal minimum for a fatigue test of 100,000 cycles. However, the bolted specimens displayed a relatively narrow range of fatigue life, indicating that the true behavior of bolted specimens tested at 193 MPa (28.0 ksi) was measured in this experiment.

All three of the Bolted specimens were tested to failure as previously defined. BOLT_01 failed at 530,000 cycles, BOLT_02 failed at 300,000 cycles, and BOLT_03 failed at 400,000 cycles, resulting in an average of 410,000 cycles to failure. The range in the number of cycles to failure was 130,000 cycles and the percent difference in the number of cycles to failure between the specimen with the longest failure life and the shortest failure life was 25%. Most importantly, the length of the propagation life of each specimen appeared to be directly correlated to the length of the initiation life of that specimen. BOLT_01, BOLT_02, and BOLT_03 had propagation lives of 450,000 cycles, 250,000 cycles, and 330,000 cycles, respectively. Although the propagation lives for the three specimens were not equal, they were all between 5.7 and 6.7 times longer than their respective initiation lives.

With only three specimens tested, this occurrence may have been a coincidence. However, these results suggest that a weld detail having a given geometry and high weld quality will not only have a longer fatigue life to crack initiation than a detail having identical geometry and poor weld quality, but it will also have a somewhat slower rate of crack propagation. This phenomenon may possibly be due to initiation and propagation of cracks at multiple locations in a weld of poor quality as opposed to initiation and propagation of cracks at limited locations in a weld of high quality. Since the stress range driving crack growth would be identical for the two cases presented, the individual cracks in high quality and poor quality welds would propagate at equal rates once initiated. However, the presence of numerous and intersecting cracks in a weld of poor quality may have an aggregate effect and decrease the overall propagation life of the weld.

4.1.4 Fatigue Life for Specimens Treated with UIT

Two specimens treated with UIT were tested at a nominal weld toe stress range of 193 MPa (28.0 ksi). As discussed in section 4.1.1, the third UIT-treated specimen, UIT_01, was tested at a stress range of 138 MPa (20.0 ksi). The first of these two specimens to be tested, UIT_02, fatigued for 1,300,000 cycles before a crack was detected visually using dye penetrant. The second specimen, UIT_03, fatigued for 2,100,000 cycles before a crack was detected. The average of the fatigue lives to crack initiation of these two specimens was 1,700,000 cycles. Although the fatigue lives of these two specimens seem very different from each other, the percent difference between the fatigue lives of the two specimens was 38%. This is the same percent difference reported for both the control specimens and the bolted specimens tested at a stress range of 193 MPa (28.0 ksi).

Unfortunately, time limitations did not allow either of the specimens treated with UIT to achieve fatigue failure. Both specimens, however, were tested well past the point of crack initiation to collect data on crack propagation behavior. Specimen

UIT_02 was allowed to cycle for 1,650,000 cycles after crack initiation and specimen UIT_03 was allowed to cycle for 2,290,000 cycles after initiation. As will be discussed in sections 4.2 and 4.3, the specimens treated with UIT displayed greatly retarded crack propagation rates and peculiar propagation behavior compared to the control specimens.

4.1.5 Fatigue Life for Combination Specimens

All three of the specimens treated with UIT and pretensioned bolts, referred to as combination specimens, were tested at a nominal weld toe stress range of 193 MPa (28.0 ksi). The fatigue life to crack initiation of the first of these specimens to be tested, UIT/BOLT_01, was determined using data recorded by the controller because the ultraviolet light used to detect cracks with dye penetrant was being repaired at the time of crack initiation. When the ultraviolet light was repaired and the specimen was inspected at 750,000 cycles, a fatigue crack greater than 25 mm (1.0 in.) in length was already present in one of the welds. By examining trends in controller data (see section 4.3), the fatigue life to crack initiation was estimated to be 550,000 cycles for UIT/BOLT_01. The fatigue lives of the other two combination specimens were determined by visual inspection using dye penetrant. UIT/BOLT_02 developed a fatigue crack at 1,070,000 cycles and UIT/BOLT_03 developed a fatigue crack at 1,370,000 cycles. The rounded average of the fatigue lives to crack initiation of these three specimens was 1,000,000 cycles. The range in fatigue life to crack initiation was 820,000 cycles and the percent difference between the specimen with the shortest life and the specimen with the longest life was 60%. Obviously, there was much more scatter in the results for the combination specimens than for any of the other three specimen types. The fatigue lives of UIT/BOLT_02 and UIT/BOLT_03 were in close agreement while the fatigue life of UIT/BOLT_01 was substantially different (55% lower than the average of the fatigue lives of UIT/BOLT_02 and UIT/BOLT_03). Additional tests of this specimen type would be necessary to

determine if specimen UIT/BOLT_01 was an outlier. Since there were only three specimens, it had to be considered a valid data point.

One of the three combination specimens was allowed to cycle until fatigue failure. This specimen, UIT/BOLT_01, failed at 2,410,000 cycles. The resulting propagation life of the specimen was 1,860,000 cycles. The other two combination specimens were allowed to cycle well past the point of crack initiation, but the tests were ended before fatigue failure was achieved. UIT/BOLT_02 was allowed to cycle for 790,000 cycles past initiation and UIT/BOLT_03 was allowed to cycle for 450,000 cycles past initiation.

4.1.6 Fatigue Life Comparison

The fatigue lives to crack initiation for all specimens tested at 193 MPa (28.0 ksi) are summarized in Table 4.2 and shown on S-N diagrams in Figure 4.3 (SI units) and Figure 4.4 (U.S. Customary units). The S-N diagrams also show lines corresponding to the fatigue lives predicted by the AASHTO fatigue design equation (Eqn. 3.1) for the various fatigue categories.

Table 4.2. Test results for specimens tested at a stress range of 193 MPa (28.0 ksi).

Specimen	Stress Range, MPa (ksi)	Cycles to Initiation	Average Cycles to Initiation	Cycles to Failure
CONTROL_05	193 (28.0)	80,000	65,000	290,000
CONTROL_06	193 (28.0)	50,000		Not Achieved
BOLT_01	193 (28.0)	80,000	70,000	530,000
BOLT_02	193 (28.0)	50,000		300,000
BOLT_03	193 (28.0)	70,000		400,000
UIT_02	193 (28.0)	1,300,000	1,700,000	Not Achieved
UIT_03	193 (28.0)	2,100,00		Not Achieved
UIT/BOLT_01	193 (28.0)	550,000	1,000,000	2,400,000
UIT/BOLT_02	193 (28.0)	1,070,000		Not Achieved
UIT/BOLT_03	193 (28.0)	1,370,000		Not Achieved

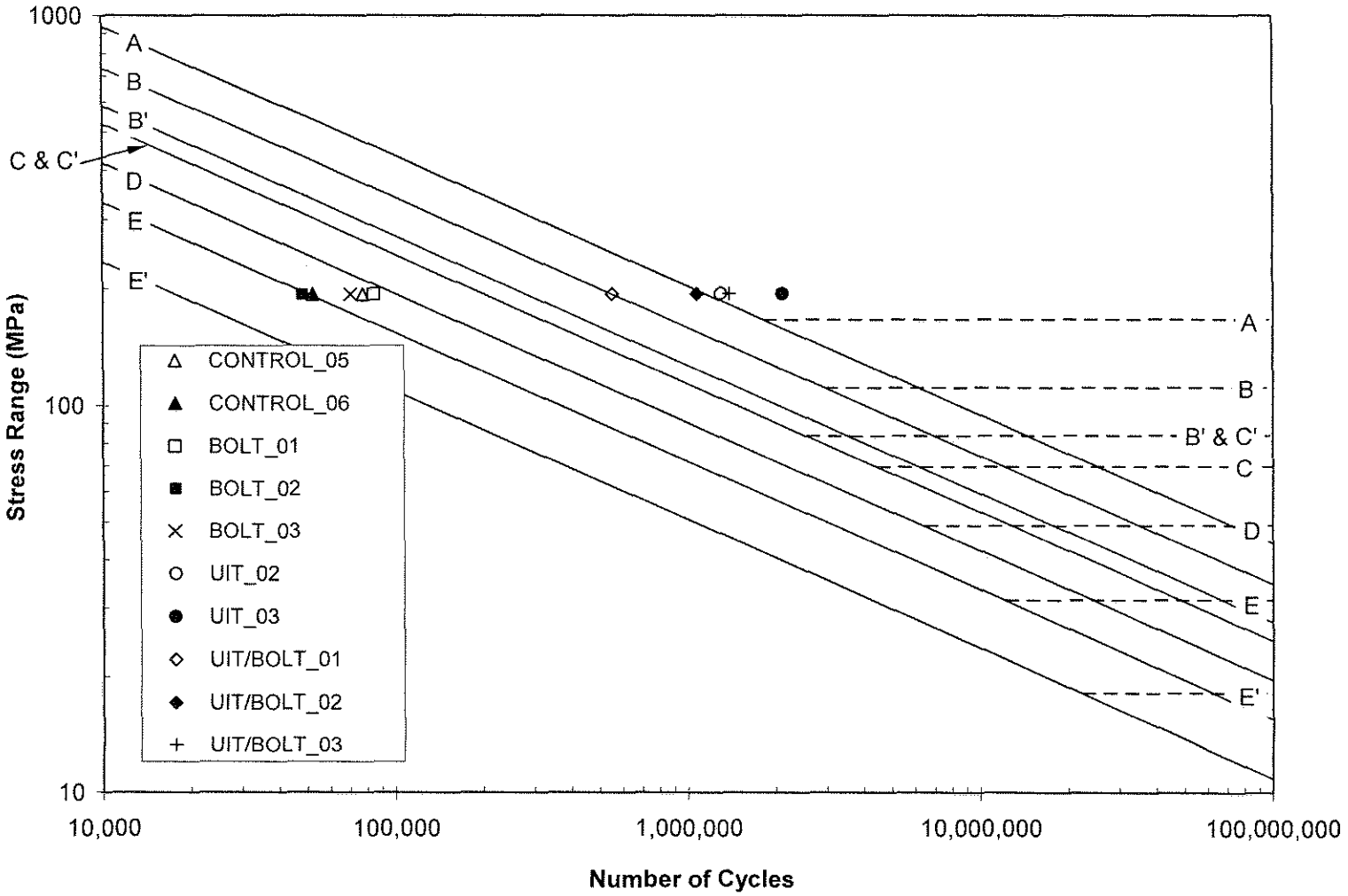

Figure 4.3. S-N diagram showing the results for specimens tested at 193 MPa (SI).

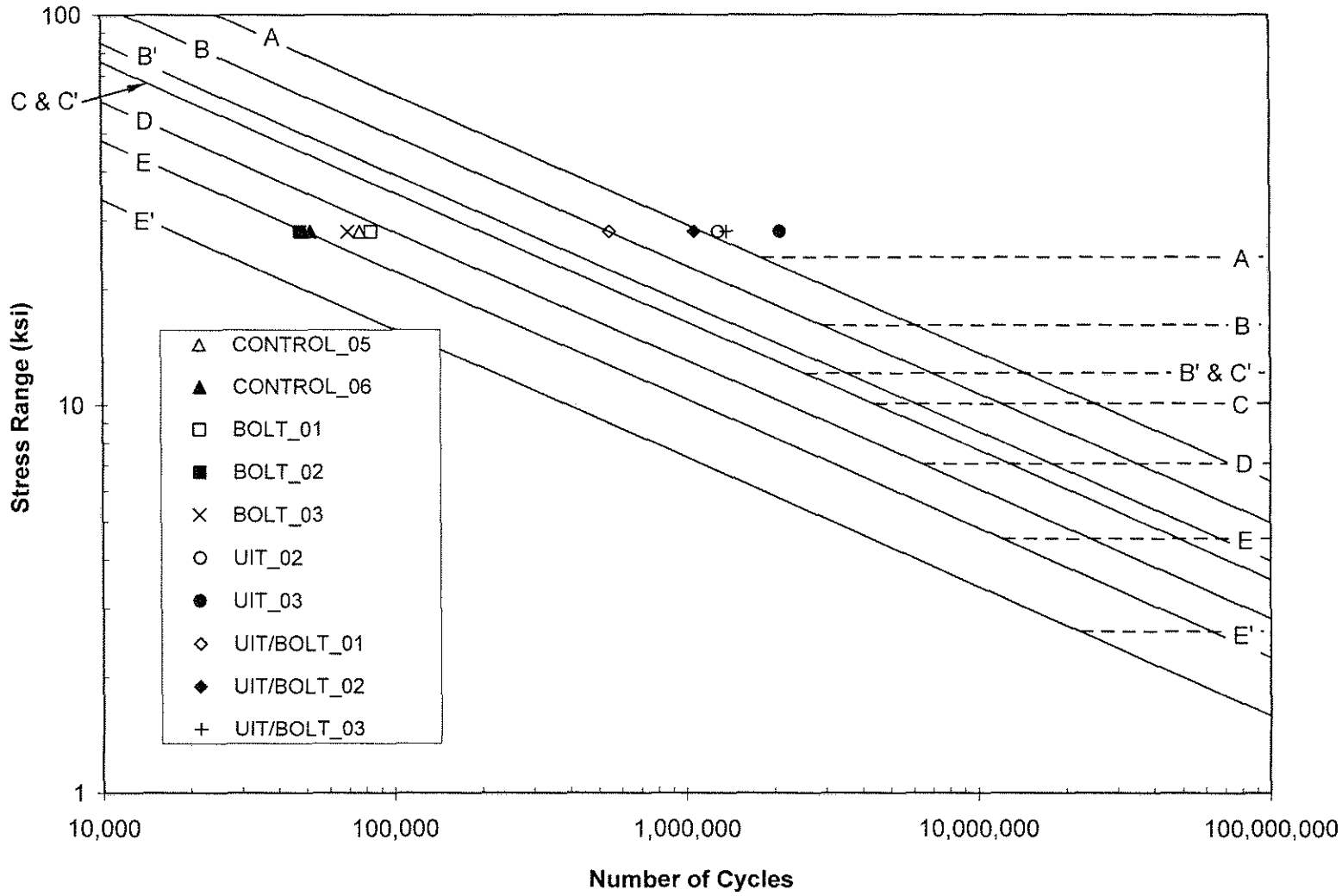

Figure 4.4. S-N diagram showing the results for specimens tested at 28 ksi (U.S. Customary).

4.1.6.1 Bolted Specimens versus Control Specimens

It is clear from the fatigue life data that treating the weld toes with UIT had a very profound effect on improving the fatigue lives of the weld details while adding bolts to the coverplate ends did not. The difference in average fatigue life between bolted specimens and control specimens was only 5,000 cycles, or 7%, indicating that adding bolts to the coverplate ends had a negligible effect on enhancing fatigue life when the specimens were subjected to a weld toe stress range of 193 MPa (28.0 ksi). However, a difference in performance between the two specimen types may have been masked because both types displayed short fatigue lives. If the control and bolted specimens had been allowed to fail at higher numbers of cycles by testing at a lower stress range, a difference in fatigue performance between the two specimen types, although likely to be small, may have become apparent. As discussed previously, testing at a lower stress range was not possible due to the large improvement in fatigue life caused by UIT.

Regardless of the exact effect coverplate bolting had on fatigue life improvement, the bolted specimens did not achieve the significant improvement in fatigue life that would qualify coverplate bolting as an effective fatigue life enhancement method. Suggested explanations as to why coverplate bolting was ineffective address the hypotheses presented in section 2.4 regarding the effects that adding bolts would have on the state-of-stress in the weld. One hypothesis presented was that adding a pretensioned bolt near a coverplate end would induce a compressive stress in the transverse weld, thus reducing the residual tensile stress in the weld. As will be discussed in section 5.4, a finite element analysis of a bolted specimen revealed that adding a pretensioned bolt to the end of coverplate actually induced tensile stresses in the transverse weld. This result suggested that the fatigue lives of the bolted specimens were likely worsened by the stress field resulting from the pretension forces. However, it must be noted that the specimens tested for this project were free to expand and contract as the coverplate bolts were pretensioned.

On actual bridge girders, restraint from the girder web would not allow free expansion of the flange and coverplate as the bolts were pretensioned. Thus, the stress field induced in the specimens may not have been an accurate representation of the stress field that would be induced in actual girder coverplates. The restraint in actual girders may cause the induced stresses in the transverse weld to be compressive.

The other hypothesis presented regarding the effects of coverplate bolting was that the bolt would transfer forces developed in the specimen flange to the coverplate by means of friction between the plates, thus reducing the amount of force that would be transferred through the weld. Obviously, the amount of force that the friction connection transferred was small and did not affect the stress in the weld during loading.

4.1.6.2 Specimens Treated with UIT versus Control Specimens

Treating weld toes with UIT had a very positive effect on fatigue life enhancement. At a nominal weld toe stress range of 193 MPa (28.0 ksi), the average fatigue life of specimens treated with UIT was more than 25 times longer than the average fatigue life of control specimens. UIT_02, which was the lowest-performing specimen treated with UIT, outperformed CONTROL_05, which was the highest-performing control specimen, by more than 16 times. The significant difference in fatigue life between the control specimens and the specimens treated with UIT suggests that UIT is a very effective fatigue life enhancement method when properly employed.

4.1.6.3 Combination Specimens versus Specimens Treated with UIT

Specimens having coverplate bolts in addition to being treated with UIT did not show an improvement in fatigue life over specimens treated with UIT alone. Therefore, no positive aggregate effect resulting from bolting and treating with UIT was observed. Relative to the performance of specimens treated with UIT alone,

adding bolts to specimens treated with UIT actually decreased the fatigue performance. At a nominal weld toe stress range of 193 MPa (28.0 ksi), the average fatigue life of combination specimens was 41 % lower than the average fatigue life of specimens treated with UIT alone. The highest-performing combination specimen had a fatigue life roughly equal to the fatigue life of the lowest-performing specimen treated with UIT alone. These data suggest that adding coverplate bolts to the specimens had a detrimental effect on fatigue life enhancement. As discussed earlier, this negative effect was not apparent on the untreated bolted specimens compared to the control specimens because of the short fatigue lives of these specimen types. The decrease in fatigue life for the combination specimens compared against fatigue lives of UIT-treated specimens was most likely a result of the tensile stress induced in the weld from the addition of the bolt as predicted by the finite element model (see section 5.3). It should be noted that, theoretically, if the coverplate bolts had been pretensioned prior to treatment with UIT, the tensile stress induced in the weld during bolting would have been removed by the UIT treatment. If that were the case, the bolted specimens treated with UIT would have likely performed very similarly to the specimens treated with UIT alone. Therefore, performing UIT before pretensioning the bolts was a conservative consideration in this experimental design.

4.1.6.4 Comparison to AASHTO Fatigue Equations

The fatigue lives of all specimens tested at a nominal weld toe stress range of 193 MPa (28.0 ksi) are compared to the AASHTO fatigue design equation (Eqn. 3.1) graphically on the S-N diagrams shown in Figures 4.3 (SI) and 4.4 (U.S. Customary). As shown in these figures, all control and bolted specimens achieved AASHTO Category E detail classification. Two of these specimens, CONTROL_06 and BOLT_02, had fatigue lives identical to that predicted by the AASHTO fatigue life equation for a Category E detail at a stress range of 193 MPa (28.0 ksi). Given the high weld quality and relatively less severe geometry of these specimens (see section

4.1.1.2), Category E is a logical and appropriate level of performance for these E' details. Both specimens treated with UIT performed as well as AASHTO Category A details. Category A is the most fatigue-resistant detail defined by AASHTO and has a fatigue resistance equivalent to that of an un-welded flat plate. Compared to control specimens, specimens treated with UIT improved by six AASHTO categories. Combination specimens performed slightly worse than specimens treated with UIT alone, achieving AASHTO Category B levels of performance for two of the details and Category A performance for the third. Although these specimens improved over the control and bolted specimens by at least five AASHTO categories, the majority of combination specimens were one category worse than the specimens treated with UIT alone.

4.2 FATIGUE CRACK BEHAVIOR

4.2.1 Crack Initiation Locations

As testing progressed, it became obvious that fatigue cracks initiated at predictable locations on the transverse welds for each of the four specimen types. The following sections discuss typical crack locations for each specimen type and present possible explanations for these crack locations.

4.2.1.1 Initiation Locations for Control Specimens and Bolted Specimens

Much like the fatigue performances of the two specimen types, the fatigue crack initiation locations for control specimens and bolted specimens were not significantly different. For all six control specimens and all three bolted specimens, fatigue cracks initiated at the toes of the transverse fillet welds on the base-metal (flange plate) side of the weld. This typical crack initiation location is shown for a bolted specimen in Figure 4.5. When the photograph in Figure 4.5 was taken, the fatigue crack had propagated along the entire length of the weld toe.

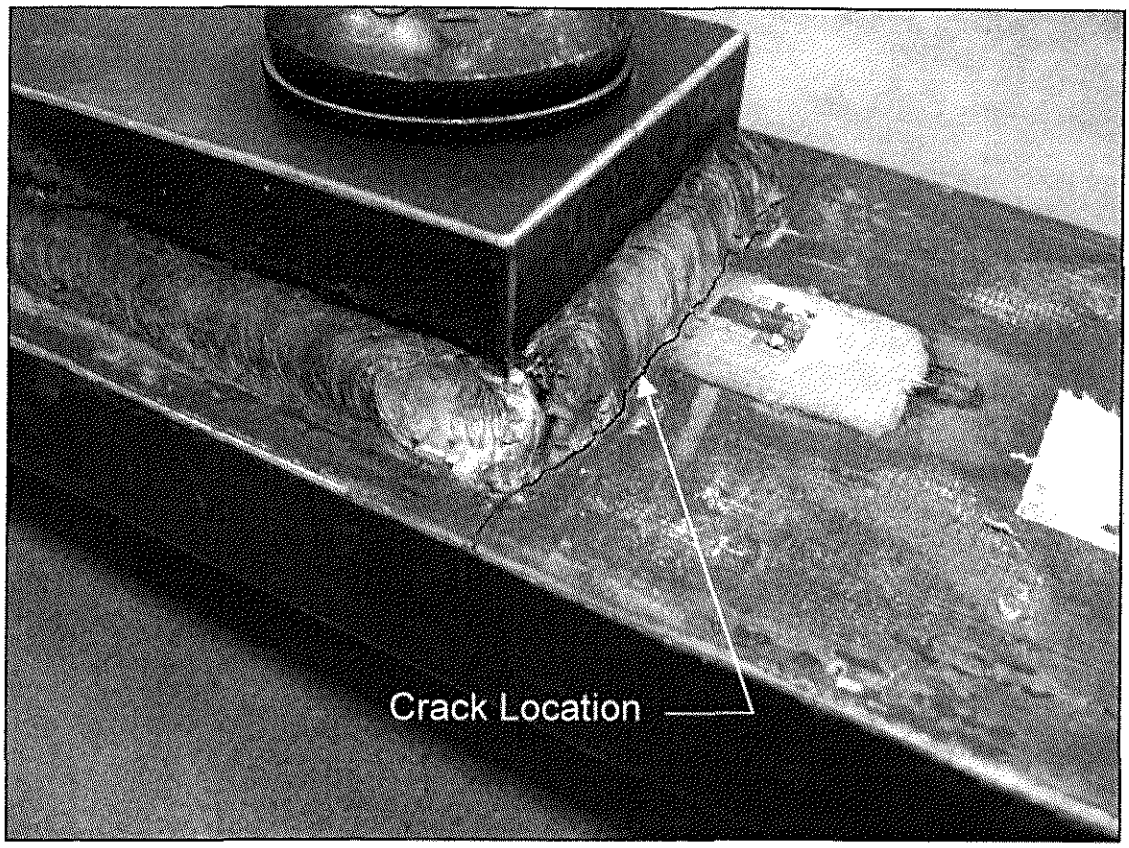

Figure 4.5. Weld toe crack in a bolted specimen.

For control specimens and bolted specimens, fatigue cracks initiated at either the center of the transverse weld toe or at one of the ends of the transverse weld toe. The distribution of cracks forming at these locations was evenly distributed and showed no correlation to specimen type. As a finite element analysis of a control specimen indicated (see Chapter 5), the region having the highest concentration of stress when loaded was the center of the weld toe. This suggests that all cracks should have initiated near the centers of the weld toes. However, weld interfaces existed at both ends of all transverse welds because longitudinal welds were ended and transverse welds were started at these locations during fabrication. Therefore, small discontinuities or stress concentrations may have been introduced at the ends of the transverse weld toes. The location of fatigue crack initiation for these two

specimen types was likely governed by the severity of the imperfections or stress concentrations introduced at the ends of the transverse weld. Specimens having more severe imperfections or stress concentrations at the weld interfaces likely formed cracks near the ends of the weld toes whereas specimens having less severe imperfections or stress concentrations at the weld terminations likely formed cracks near the center of the weld toes. Additionally, some specimens appeared to be slightly warped or twisted as a result of uneven weld heating. Due to warping, some specimens came in contact with only one side of the loading round at each end of the bending frame during loading. Loading a specimen in this manner may have resulted in a higher stress concentration at one end of the transverse weld toe on each side of the coverplate rather than at the center, thus causing the ends of the welds to crack.

Control specimens and bolted specimens displayed an even distribution regarding the end of the coverplate to develop a fatigue crack first. Of the nine specimens, the first fatigue crack initiated on the end of the bending frame labeled "END A" twice, the end of the bending frame labeled "END B" three times, and both ends of the bending frame simultaneously three times. As discussed above, initiation for CONTROL_05 was determined using data recorded by the controller and it could not be determined which side formed a fatigue crack first because both sides were cracked when the modified dye penetrant procedure was employed for the first time.

The crack-initiation distribution discussed above accounts for the fact that the lower portion of three-point-bending frame was removed from the actuator halfway through the testing program to repair a fatigue crack that had formed in the tube. When the bending frame was reinstalled, it was unintentionally oriented opposite from its original orientation. For the purposes of tracking crack initiation, the sides of the bending frame labeled "END A" and "END B" prior to removal were still referred to as END A and END B after being reinstalled. Thus, cracks forming on a given side of a specimen did not necessarily coincide to cracks forming on END A or END

B of the bending frame. The even distribution suggests that the specimens were loaded symmetrically by the three-point-bending frame. Data recorded by the array of strain gages (see section 4.4) also supports this claim.

4.2.1.2 Initiation Locations for UIT Specimens and Combination Specimens

Similar to the relationship between control specimens and bolted specimens, fatigue cracks formed at identical locations on the transverse fillet welds of specimens treated with UIT and combination specimens. Two specimens treated with UIT and all three combination specimens developed fatigue cracks in the throats of the transverse fillet welds, approximately halfway between the weld toe adjacent to the flange and the weld toe adjacent to the coverplate. As discussed previously, UIT_01 was tested at a lower nominal stress range and did not develop fatigue cracks. This typical crack initiation location is shown for a specimen treated with UIT in Figure 4.6. In this photograph, the crack is indicated by the fluorescence of dye penetrant absorbed by the crack and exposed to ultraviolet light. When this photograph was taken, the crack had propagated to a length of approximately 51 mm (2.0 in).

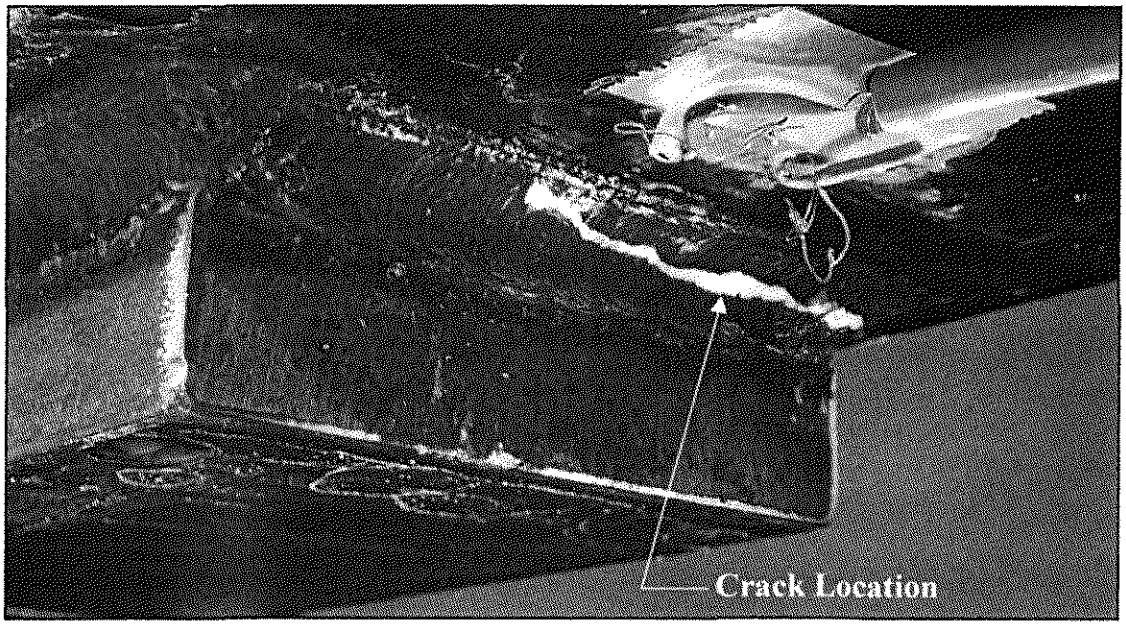

Figure 4.6. Weld throat crack on a specimen treated with UIT.

Unlike control specimens and bolted specimens, none of the cracks that formed in the throats of the UIT-treated specimens or the combination specimens initiated near the centers of the transverse welds. Rather, all cracks initiated near the ends of the transverse welds. In some cases, cracks formed across the interface between longitudinal and transverse welds despite additional treatment with UIT at the interface. An example of this additional treatment at an interface is shown in Figure 3.3. In none of the specimens did cracks initiate anywhere along the weld toes. This was likely due to the combined effects of large compressive stresses and improved geometry caused by UIT treatment in the immediate vicinity of the weld toes.

Obviously, once the weld toes were eliminated as primary crack initiation sites, the next most vulnerable locations were the weld throats near the ends of the transverse welds. Cracks may have initiated at these locations rather than at the centers of the weld throats for reasons similar to those presented for control specimens and bolted specimens. If large enough flaws in the weld throat were introduced when one weld was stopped and the next weld was started, treating that area with UIT would relax the residual stresses around the flaws but would not remove the flaws. This may have caused the interface region to be more susceptible to cracking than the center. Additionally, warping in the specimens may have caused the ends of the transverse welds to be more greatly stressed than the centers of the welds during loading.

Crack initiation did not show a preference for either end of the bending frame for the specimens treated with UIT or combination specimens. Of the five specimens that developed fatigue cracks, three had first crack initiation on END A of the bending frame, one had first crack initiation on END B of the bending frame, and one developed cracks on both ends simultaneously. This data does not show significant

evidence of preference toward one side, indicating that the specimens were symmetrically loaded by the bending frame.

4.2.2 Crack Propagation Behavior

Crack propagation behavior was determined by measuring surface lengths of cracks as they propagated in the specimens as well as monitoring trends in data recorded by the controller throughout each fatigue test. Because the three-dimensional behavior of crack propagation could not be accurately captured by measuring surface lengths of cracks, monitoring trends in data recorded by the controller was the primary means by which crack propagation was monitored. The analysis and interpretation of this data as it relates to fatigue crack growth is discussed in section 4.3. The behavior of crack propagation for the four specimen types fell into two categories: specimens displaying a crack propagation plateau and specimens not displaying a crack propagation plateau.

4.2.2.1 Specimens Not Displaying a Crack Propagation Plateau

All control specimens and all bolted specimens were placed in the category of specimens not displaying a crack propagation plateau. After initiation, cracks in these specimens propagated at exponentially increasing rates until fatigue failure was achieved. For each of these specimens, a fatigue crack initiating at the weld toe propagated along the entire length of the transverse weld toe while advancing into the base metal of the flange at the same time. All cracks propagated into the flange in a direction orthogonal to the longitudinal axis of the flange. When a crack reached a critical depth into the flange, the flange would fail by yielding of the reduced flange cross section under the applied bending moment. A sudden, fracture-type failure typical of fatigue failure did not occur. A typical failure of this type is shown for CONTROL_05 in Figure 4.7.

Although crack propagation behavior of control specimens and bolted specimens was similar, the propagation lives of bolted specimens appeared to be significantly

longer than those of control specimens. The average of the crack propagation lives for the bolted specimens was 410,000 cycles, which was 120,000 cycles, or 41 %, longer than the propagation life of CONTROL_05, the only control specimen to be tested to failure. A possible explanation for this phenomenon may have been that as cracks began to propagate through the welds in the bolted specimens, the bolts began transferring larger portions of the force to the coverplate, thus slowing the propagation of cracks. Although additional data regarding the propagation lives of control specimens would have to be obtained to prove that a difference between the propagation lives of these specimen types exists, these results suggest that adding a pretensioned bolt to the end of a coverplate may enhance the propagation life of the transverse weld detail.

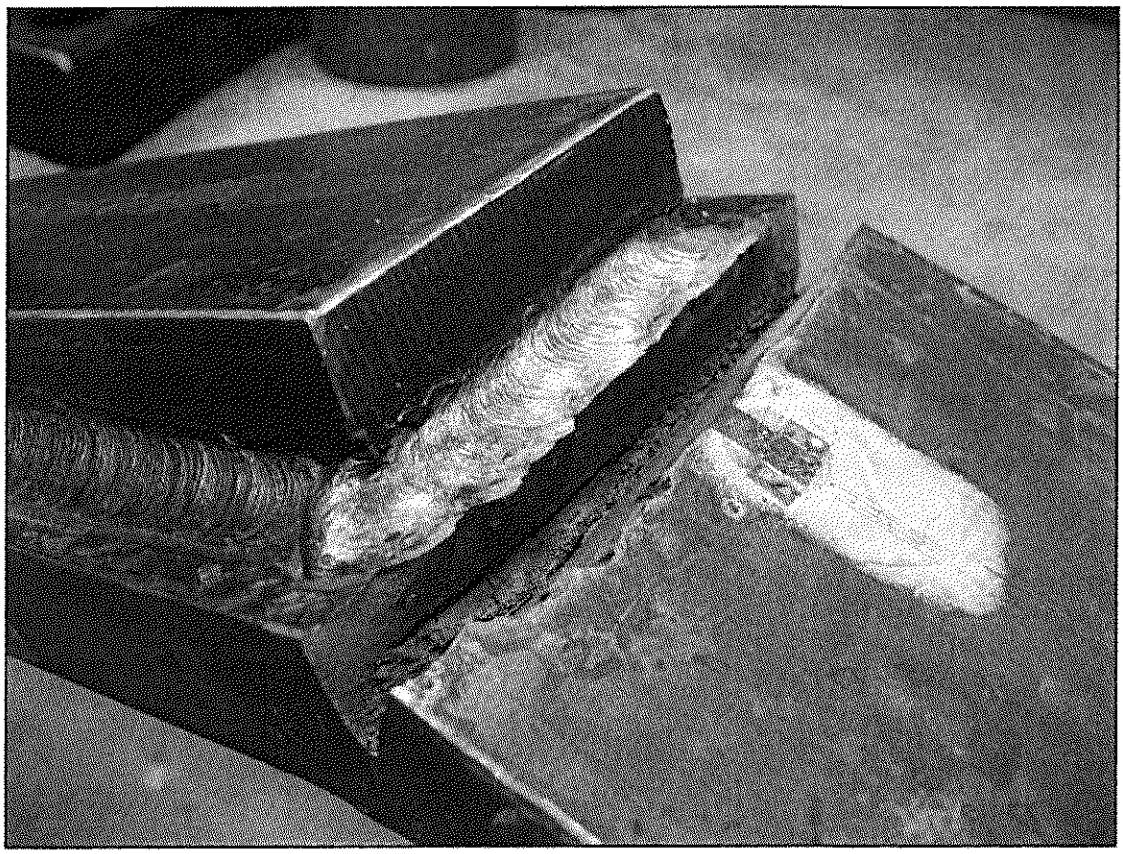

Figure 4.7. Fatigue failure of a control specimen.

4.2.2.2 Specimens Displaying a Crack Propagation Plateau

All combination specimens and both specimens treated with UIT that developed cracks were placed in the category of specimens displaying a crack propagation plateau. After initiation, cracks in these specimens began to propagate at exponentially increasing rates. On the surface of a weld, a crack initiating at the weld throat near one end of a transverse weld would propagate across the entire length of the transverse weld throat. At each end of the transverse weld, the crack would then propagate around the corner of the fillet weld, moving along the longitudinal weld and toward the flange at an angle of approximately 45°. The crack would then begin to propagate into the base metal of the flange, advancing in a direction orthogonal to the longitudinal axis of the flange. A typical crack in a specimen displaying a propagation plateau is shown in Figure 4.8. Because UIT _03 was not tested to failure, the crack shown in Figure 4.8 was mechanically opened after testing to expose the crack surfaces.

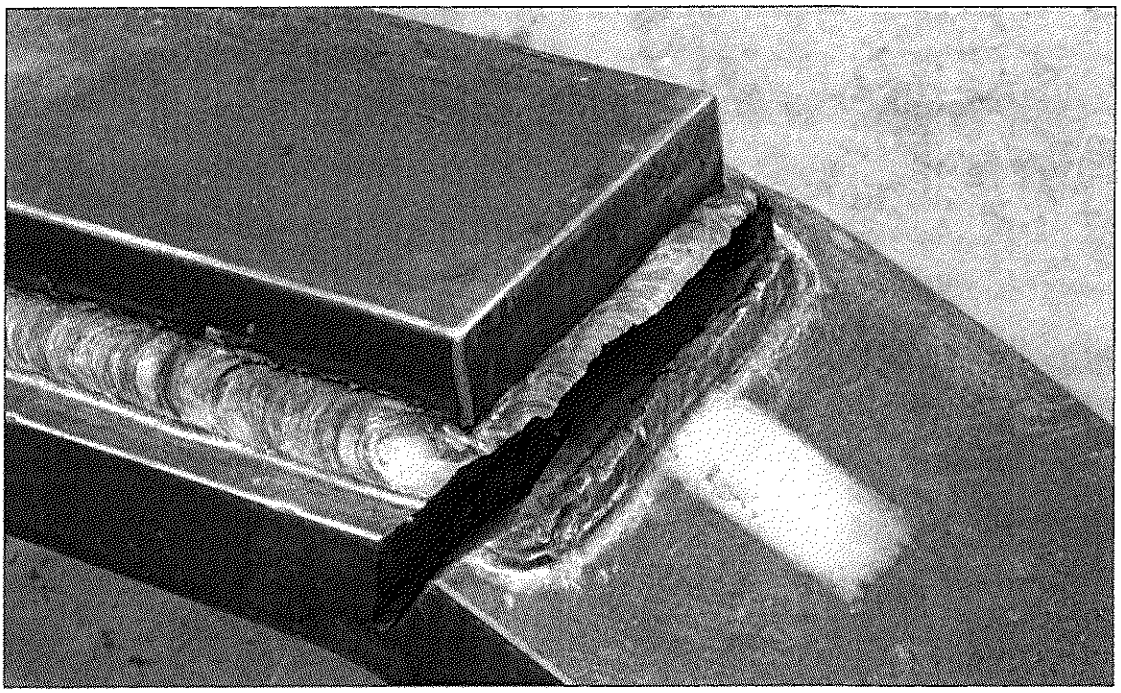

Figure 4.8. Crack propagation in specimen UIT_03.

For all specimens displaying a propagation plateau, the rate of crack propagation through the flange slowed considerably at some point after cracking in the flange had begun. Once this propagation plateau was reached, a crack would propagate through the flange at a slow, constant rate. The crack growth rate during this last phase of propagation was so slow that the test of UIT_03 had to be ended due to time limitations even though the specimen had a crack deeper than 13 mm (0.50 in.) in its flange.

Since it was possible to monitor crack growth at the weld surface only, it could not be determined if cracks in these specimens initiated at the weld root or at the throat of the weld surface. Visually examining the failure surfaces after test completion did not lead to the determination of the initiation site either.

The only deviation from this propagation behavior occurred during testing of UIT/BOLT_01. At the weld surface of this specimen, a crack initiating in the weld throat near one end of a transverse weld propagated across the weld throat for a portion of the length of the transverse weld, then changed direction and propagated along the treated weld toe for the remainder of the length of the transverse weld. The crack then propagated through the weld throat and into the flange in a manner similar to that of the other specimens displaying crack propagation plateaus. It could not be determined if initiation in this specimen occurred at the weld throat or the weld root. Regardless of the crack propagation path, this specimen had a well-defined propagation plateau and achieved a long crack propagation life. The crack pattern for this specimen is shown in Figure 4.9. It must also be noted that the fatigue tests of UIT/BOLT_02 and UIT/BOLT_03 were ended shortly after crack initiation and very little propagation data was recorded for either specimen.

The fatigue crack propagation lives of specimens treated with UIT and combination specimens could not be compared because no specimens treated with UIT and only one combination specimen achieved total failure. However, it was

evident that these specimen types had much longer propagation lives than control specimens. UIT/BOLT_01 had a propagation life of 1,860,000 cycles, while UIT_02 and UIT_03 each cycled for more than 1,500,000 cycles after crack initiation before run-out was declared. When this data was compared to the propagation life of specimen CONTROL_05 of 290,000 cycles, it was evident that treatment with UIT not only increased the initiation lives of the specimens, but it also substantially improved the propagation performance as well.

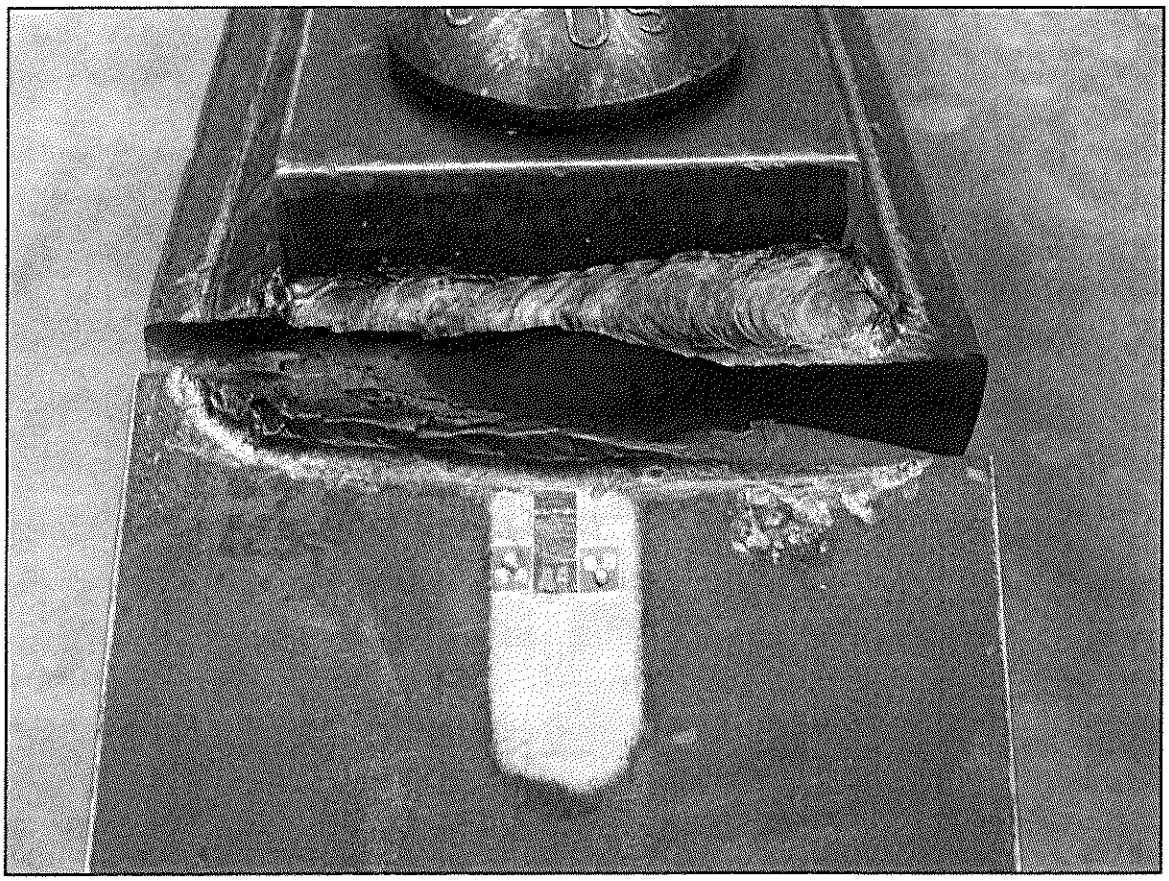

Figure 4.9. Fatigue failure of specimen UIT/BOLT_01.

4.3 FATIGUE DATA RECORDED BY THE CONTROLLER

As discussed in section 3.4.3, the dynamic stiffness of each specimen was monitored during fatigue testing by periodically recording the actuator's minimum

and maximum position and applied load. By monitoring changes in dynamic stiffness throughout each fatigue test, initiation and propagation behavior of fatigue cracks was determined. To illustrate how dynamic stiffness data was interpreted, Figures 4.10 through 4.13 show plots of dynamic stiffness versus number of cycles for one specimen from each of the four specimen types. Each of these specimens was determined to have behavior representative of its specimen type. Indicated on each plot is the fatigue initiation life of that specimen, determined using either the dye penetrant crack detection method or the dynamic stiffness crack detection method as indicated. Plots of dynamic stiffness versus cycle for all specimens are found in Appendix A.

4.3.1 Crack Initiation Determined by Dynamic Stiffness Data

As discussed in section 3.4.3, growth of a fatigue crack in a specimen was expected to cause a decrease in dynamic stiffness recorded by the controller. As Figures 4.10 through 4.13 indicate, dynamic stiffness generally began to decrease at some point after crack initiation. After analyzing dynamic stiffness data recorded for the preliminary specimens, it was thought that monitoring changes in dynamic stiffness could be used as the primary method to determine the point of fatigue crack initiation for all specimens. Changes in dynamic stiffness recorded for the preliminary specimens that developed fatigue cracks (see Appendix A) appeared to accurately predict the onset of fatigue cracking. However, while testing specimens at a nominal weld toe stress range of 193 MPa (28.0 ksi), problems with this crack detection method became apparent.

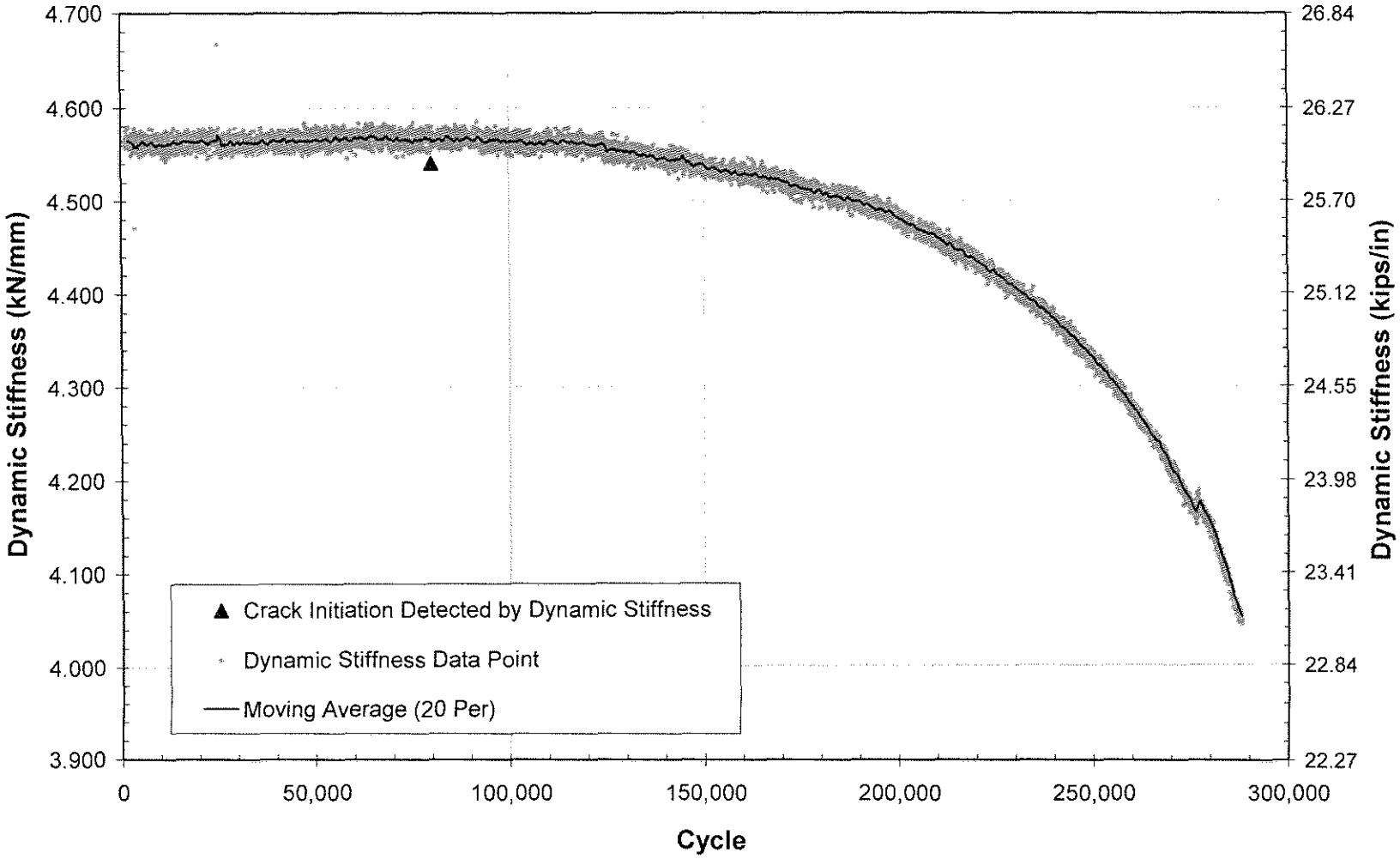

Figure 4.10. Dynamic stiffness versus cycle for specimen CONTROL_05.

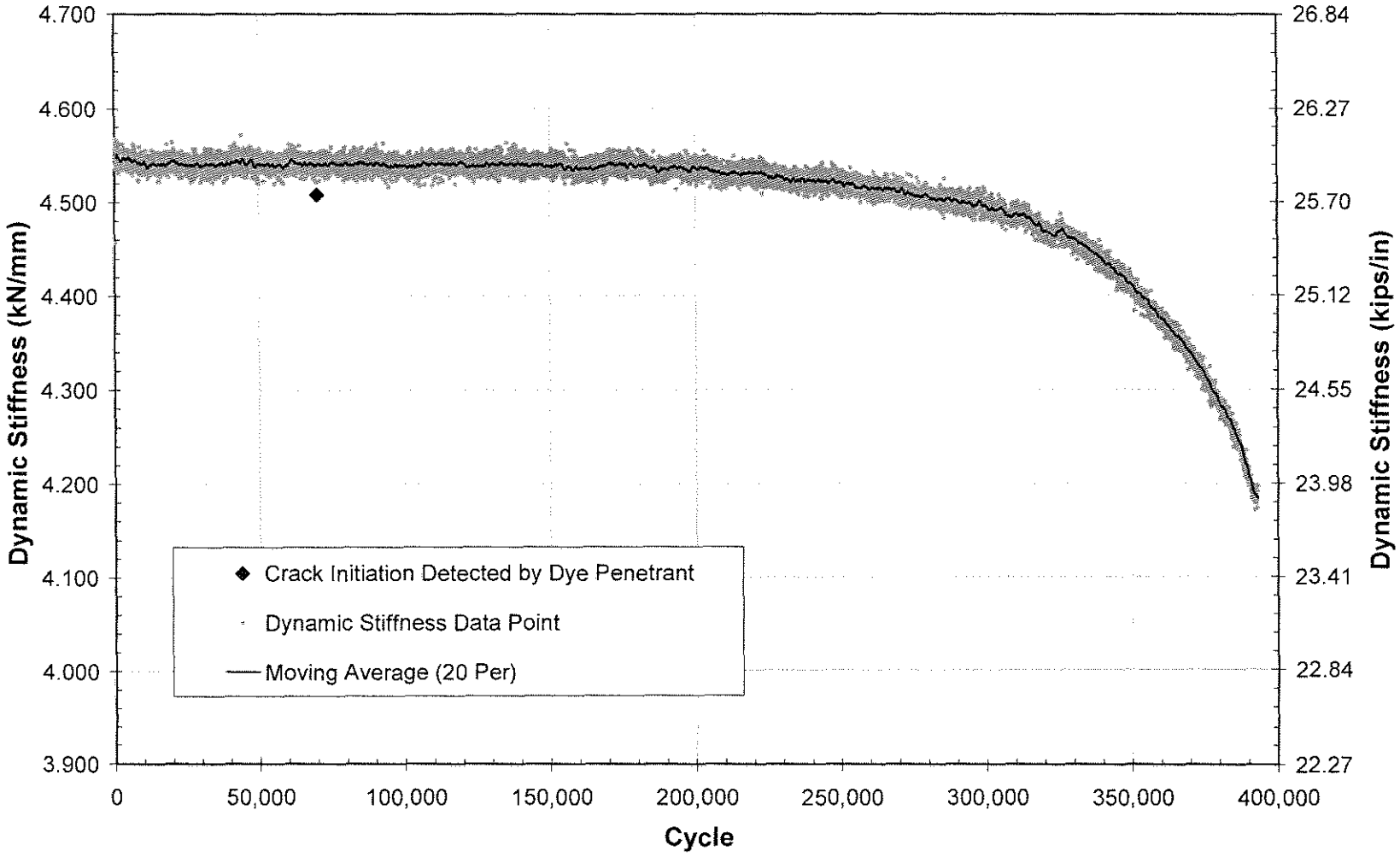

Figure 4.11. Dynamic stiffness versus cycle for specimen BOLT_03.

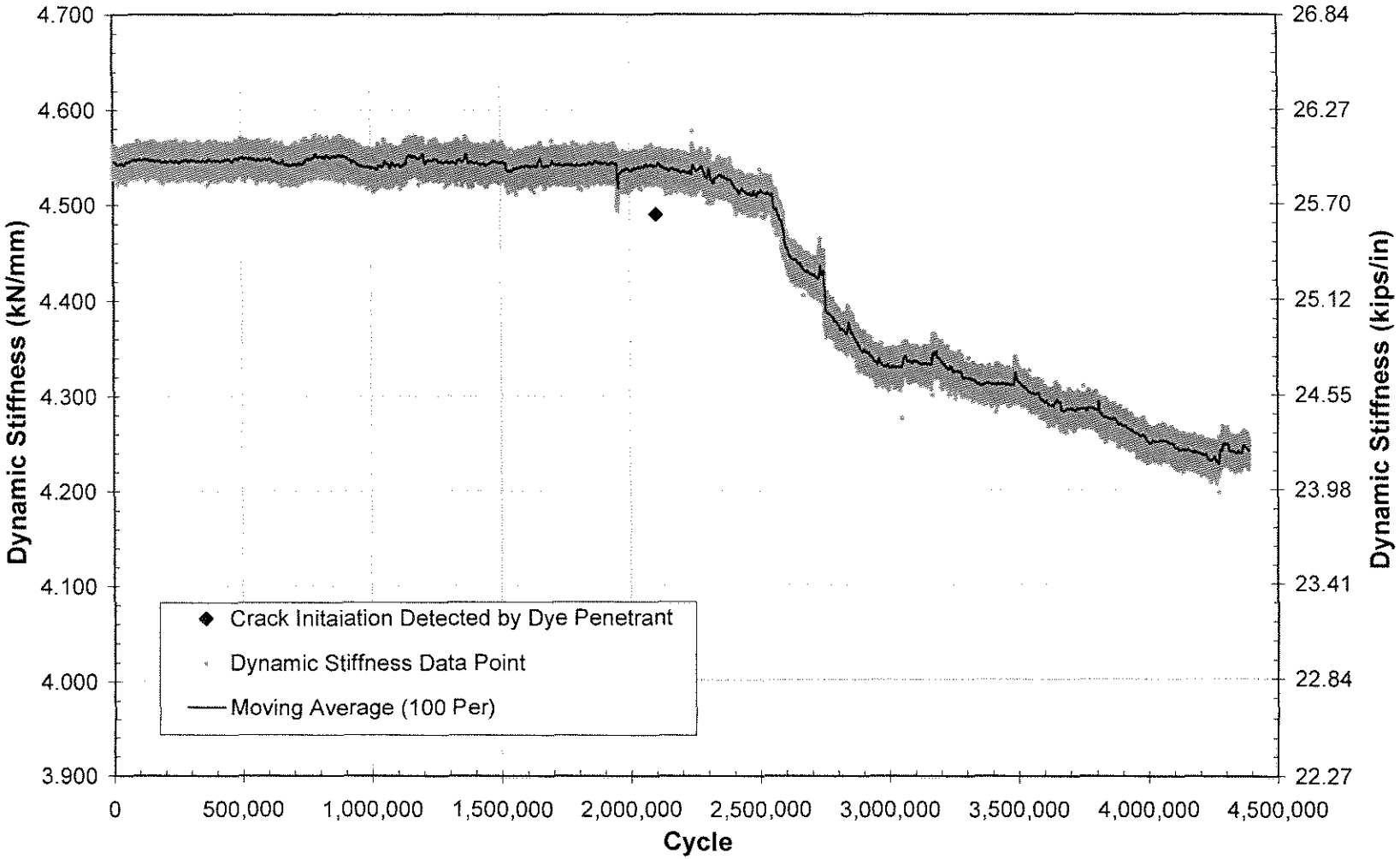

Figure 4.12 Dynamic stiffness versus cycle for specimen UIT_03.

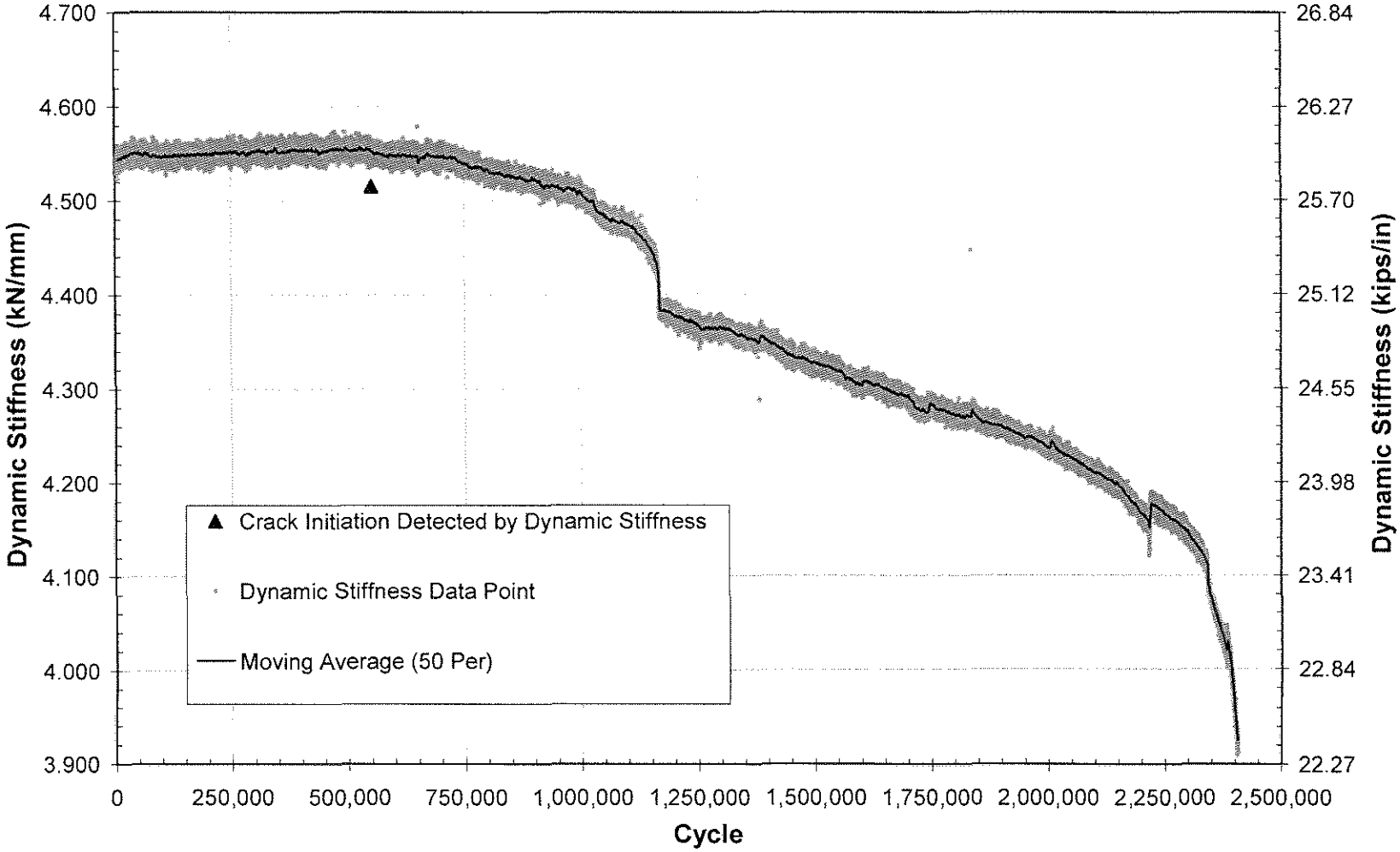

Figure 4.13. Dynamic stiffness versus cycle for specimen UIT/BOLT_01

First, the decrease in dynamic stiffness of a specimen did not perfectly coincide with visual crack detection. Generally, dynamic stiffness did not begin to decrease until about 100,000 cycles after crack initiation detected using dye penetrant. An example of this behavior is shown for BOLT_03 in Figure 4.11. For this specimen, a fatigue crack was detected visually using dye penetrant at 70,000 cycles, but the dynamic stiffness of the specimen did not begin to decrease until approximately 150,000 cycles. The shorter lag between initiation and decreased dynamic stiffness for CONTROL_05 shown in Figure 4.10 illustrates that the lag was not constant and could not be anticipated during physical testing. For specimens having short fatigue lives, this degree of sensitivity to crack initiation was inadequate. However, as shown in Figures 4.12 and 4.13, this same degree of sensitivity was deemed adequate for specimens having long fatigue lives because a lag of 100,000 cycles from initiation to detection was a short period of time relative to the total lives of the specimens. For instance, a lag of 100,000 cycles was only 5% of the initiation life of specimen UIT_03, whereas the same lag was 143% of the initiation life of specimen BOLT_03. For all combination and UIT-treated specimens, a lag of 100,000 cycles was equal to a range of 5% to 18% of the initiation lives of these specimens. Had all specimens tested for this project achieved longer fatigue lives, the sensitivity of the dynamic stiffness crack detection method would have been adequate.

A second problem with the dynamic stiffness crack detection method was inconsistency in the data. For some fatigue tests, considerable amounts of drift in the data made it difficult to discern crack initiation from drift. Sizable shifts in dynamic stiffness also occurred when a fatigue test was stopped to perform a static stiffness test and then restarted shortly thereafter. On the plots of dynamic stiffness versus cycle, these shifts are indicated by spikes in the moving average curves. Because of these drawbacks, and because fatigue crack initiation could be acceptably determined

using the modified dye penetrant method, monitoring changes in dynamic stiffness was not used as the primary method to determine crack initiation.

Despite visual detection being the preferred method of crack detection, fatigue crack initiation was determined by monitoring changes in dynamic stiffness for three of the specimens tested at a nominal weld toe stress range of 193 MPa (28.0 ksi), as discussed in section 4.1. This method was used to detect initiation only because the dye penetrant method was either not used frequently enough to determine initiation (CONTROL_05 and BOLT_01), or the ultraviolet light source was being repaired at the time of crack initiation (UIT/BOLT_01). For these specimens, fatigue crack initiation was defined as the point at which dynamic stiffness began to decrease. As evident from the preceding discussion, crack initiation in these specimens may have actually taken place somewhat earlier than this point. However, given the variability in the lag between initiation and reduced dynamic stiffness, it was impossible to estimate how much earlier initiation occurred. Defining crack initiation at the start of dynamic stiffness reduction was the only option and was considered to be adequate for these three specimens. For these three specimens, plots of dynamic stiffness versus number of cycles showing the point at which crack initiation was defined are shown in Figures 4.10 and 4.13 for CONTROL_05 and UIT/BOLT_01, respectively. A similar plot for BOLT_01 is shown in Appendix A.

4.3.2 Crack Propagation Determined by Dynamic Stiffness Data

As cracks propagated in the specimens, the advancing crack tip was generally somewhere inside either the transverse weld or the flange. Therefore, the position of a crack tip, the shape of a crack, or the direction of crack propagation could not always be determined by measuring crack lengths at the surface of a specimen. Because the complex three-dimensional propagation of fatigue cracks in specimens could not be adequately understood by measuring crack surface lengths, dynamic stiffness data was used as the primary means to monitor fatigue crack propagation

behavior. The slope of a plot of dynamic stiffness versus number of cycles for a specimen was directly related to the fatigue crack growth rate in the specimen. A zero slope correlated to no crack growth, a constant negative slope correlated to a constant crack growth rate, and an exponentially decreasing slope correlated to an exponentially increasing crack growth rate.

Through the analysis of dynamic stiffness data, it was discovered that all specimens treated with UIT (both combination and UIT alone) displayed crack propagation plateaus. As illustrated by Figures 4.12 and 4.13, the dynamic stiffness of each of these specimens decreased exponentially after crack initiation, indicating that fatigue cracks in these specimens propagated at exponentially increasing rates after crack initiation. As the dynamic stiffness of each specimen approached asymptotic behavior, the propagation rate slowed abruptly. After that point, the dynamic stiffness continued to decrease slowly at a constant rate, indicating slow fatigue crack growth in a specimen. As shown in Figure 4.13, the dynamic stiffness of specimen UIT/BOLT_01 eventually began to decrease at an exponential rate once again very near failure. It is assumed that other specimens displaying crack propagation plateaus would have displayed similar behavior had they been tested to failure. The reasons why these specimens displayed a crack propagation plateau could not be determined with certainty. Because the location of a crack tip within a specimen at the onset of a propagation plateau was unknown, the mechanisms by which crack growth was slowed could not be hypothesized.

As illustrated by Figures 4.10 and 4.11, specimens that were not treated with UIT (control and bolted specimens) did not display crack propagation plateaus. The dynamic stiffness of each of these specimens decreased exponentially until specimen failure, indicating exponentially increasing growth rate during propagation. This behavior is typical of fatigue crack propagation and was anticipated for all of the specimens.

4.4 STRAIN GAGE RESULTS FOR FATIGUE TESTS

During each fatigue test, an array of 13 strain gages attached to the specimen surface measured induced strains at locations along the specimen shown in Figure 3.17. Strains measured by the strain gages were recorded by the WaveBook data acquisition system shown in Figure 3.12. During fatigue testing, strain was periodically recorded for a two-second duration at a sampling rate of 2000 Hz. The purpose of sampling for a short duration at a high frequency was to enable a thorough analysis of a few fatigue cycles assumed to be representative of all fatigue cycles at that point in the fatigue test. All strain data recorded during fatigue testing was plotted and analyzed using Microsoft Excel. A plot of microstrain versus time is shown in Figure 4.14 for strain gage one and strain gage eight on UIT/BOLT_03. Because this data was taken at approximately 300,000 cycles past the start of fatigue testing, the strains recorded represent the behavior of an uncracked combination specimen. A sample plot of strains recorded during fatigue testing is shown for each strain gage location in Appendix B. Sample strains for every gage location on every specimen are not shown because strain data recorded at a given strain gage location varied little among the specimens, as will be discussed in section 4.4.1.

The plot of microstrain versus cycle for the strain gages shown in Figure 4.14 is representative of the quality of data recorded for all but two of the specimens tested at a nominal weld toe stress range of 193 MPa (28.0 ksi). As evident from Figure 4.14, noise, or scatter, in the strain data recorded for these specimens was less than 20 microstrain. However, strains measured for the preliminary specimens were much noisier, having a scatter band on the order of 100 microstrain. The large reduction in noise was achieved when all equipment was powered by an uninterruptible power supply (UPS) having multiple electrical filters. This is evidence that most of the noise in the data was caused by electrical noise in the wiring of the laboratory.

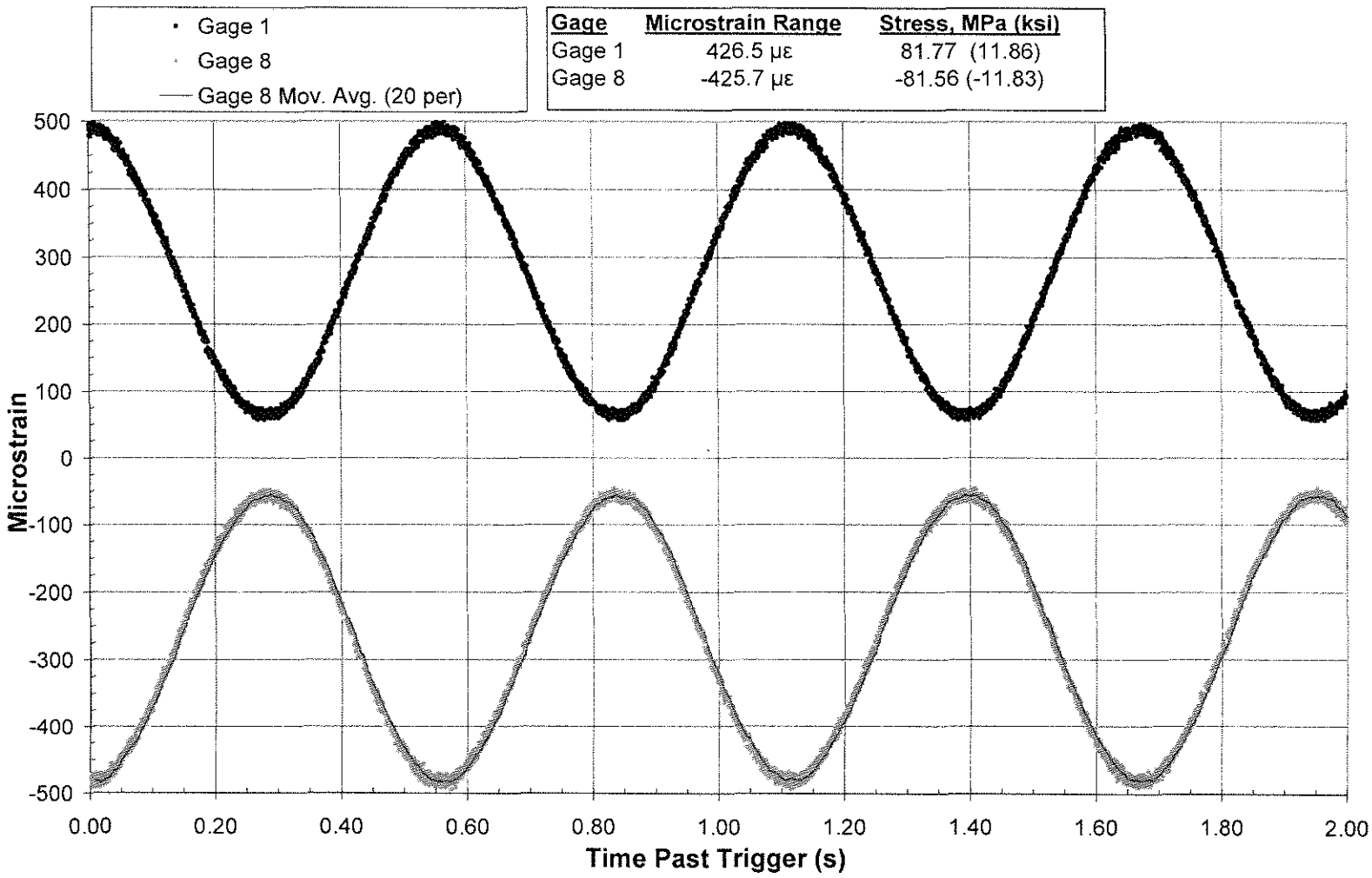

Figure 4.14. Microstrain versus time for strain gage 1 and strain gage 8 on specimen UIT/BOLT_03 at 294,000 cycles.

Another source of noise for the preliminary specimens was radio frequency (RF) interference from fluorescent lighting and machinery in adjacent laboratories. This noise was reduced for the specimens tested at 193 MPa (28.0 ksi) by ensuring that one end of the aluminum shielding in each of the cables attaching a strain gage to the WaveBook was grounded properly. This insured that all RF interference attacking the cables was properly drained through the ground wire of the laboratory's electrical wiring.

The large difference in the amounts of noise between data taken for the preliminary specimens and data taken for the specimens tested at a stress range of 193 MPa (28.0 ksi) illustrates the significant effect that interference can have on test results and demonstrates the importance of taking the necessary precautions to eliminate as much interference as possible. Because of large amounts of noise in the data taken for preliminary specimens, the strain ranges measured for these specimens were not considered to be accurate and were not compared to any other data. Additionally, the first two specimens tested at a stress range of 193 MPa (28.0 ksi) were tested before the UPS was added to the system. Strain data taken for these two specimens, BOLT_01 and UIT_02, also displayed large scatter and consequently were not used for comparison.

4.4.1 Stress Range Comparisons Using Strain Gage Data

Strain gage data was recorded during fatigue tests primarily as a means to compare theoretical stress ranges in the specimens under a given load range to actual stress ranges induced in the specimens under the same applied load range. Actual stress ranges in the specimens were determined using strain data recorded as discussed in the previous section. For each two-second sample recorded, a plot of microstrain versus time was generated for each strain gage, as shown in Figure 4.14. A curve representing a moving average of 20 data points was then fitted to the data for each strain gage. The moving average curves were removed from Figure 4.14 to

better show the data points. The microstrain range for each gage was then determined by taking the average of the points of maximum strain achieved by the moving average curve minus the average of the points of minimum strain achieved by the moving average curve. Using this method, the calculated microstrain range represented an average microstrain range of the three cycles recorded. The microstrain range for a gage was then used to calculate the stress range at that gage by multiplying the microstrain range by the modulus of elasticity of the steel, which was determined to be 191,000 MPa (27,800 ksi) as will be discussed in section 4.6.3. For a given specimen, the stress range calculated for each strain gage was found to fluctuate very little prior to crack initiation. The average of the stress ranges calculated for a strain gage prior to crack initiation could be compared to the theoretical stress range for that location. The average stress ranges prior to crack initiation for all but two specimens tested at a stress range of 193 MPa (28.0 ksi) are summarized in Table 4.3 for strain gages on the tensile side of the specimens and in Table 4.4 for strain gages on the compressive side of the specimens.

The two specimens tested at a weld toe stress range of 193 MPa (28.0 ksi) that are not included in Table 4.3 are specimens BOLT_01 and UIT_02. As mentioned previously, these specimens were tested prior to the addition of the UPS to the system and the strains recorded for these specimens were not considered sufficiently accurate. Each entry in Tables 4.3 and 4.4 represents the average of the stress ranges calculated for all two-second samples taken prior to crack initiation for a given strain gage on a given specimen. Although it is not evident from Table 4.3, the variation in strain range and corresponding variation in stress range prior to crack initiation for a given strain gage on a given specimen was found to be very small. In most of the specimens, the strain range calculated for a given strain gage for any two-second sample did not differ from the average strain range by more than two microstrain.

Table 4.3. Average stress ranges prior to crack initiation for gages 1 through 7.

Specimen	Average Stress Range Prior to Fatigue Crack Initiation, MPa (ksi)			
	Gage 1	**Gage 2**	**Gage 3**	**Gage 4**
CONTROL_05	83.98 (12.18)	184.5 (26.75)	104.1 (15.10)	142.4 (20.66)
CONTROL_06	81.79 (11.86)	175.3 (25.43)	103.0 (14.94)	140.8 (20.43)
BOLT_02	83.64 (12.13)	183.9 (26.67)	103.5 (15.01)	142.6 (20.69)
BOLT_03	81.89 (11.88)	175.0 (25.38)	103.1 (14.96)	141.5 (20.53)
UIT_03	83.92 (12.17)	176.8 (25.64)	104.9 (15.21)	144.0 (20.89)
UIT/BOLT_01	83.93 (12.17)	176.3 (25.57)	104.6 (15.18)	144.0 (20.88)
UIT/BOLT_02	82.66 (11.99)	165.1 (23.95)	103.3 (14.99)	142.5 (20.67)
UIT/BOLT_03	82.00 (11.89)	173.0 (25.09)	103.5 (15.01)	141.1 (20.47)
Average	**82.98 (12.03)**	**176.2 (25.56)**	**103.8 (15.05)**	**142.4 (20.65)**
Standard Deviation	0.9285 (0.1347)	5.735 (0.8317)	0.6586 (0.0955)	1.122 (0.1627)
Theoretical	**94.44 (13.70)**	**186.1 (26.99)**	**116.7 (16.92)**	**165.6 (24.02)**
Percent Difference	**-12.14 %**	**-5.310 %**	**-11.07 %**	**-14.02 %**
Specimen	**Gage 7**	**Gage 6**	**Gage 5**	
CONTROL_05	81.81 (11.87)	175.9 (25.52)	103.6 (15.03)	
CONTROL_06	79.86 (11.58)	175.9 (25.52)	103.3 (14.99)	
BOLT_02	82.61 (11.98)	174.9 (25.37)	103.5 (15.01)	
BOLT_03	80.52 (11.68)	183.7 (26.64)	103.1 (14.95)	
UIT_03	82.85 (12.02)	172.3 (24.99)	104.7 (15.18)	
UIT/BOLT_01	83.96 (12.18)	172.0 (24.94)	104.3 (15.12)	
UIT/BOLT_02	83.44 (12.10)	171.8 (24.92)	102.5 (14.87)	
UIT/BOLT_03	81.73 (11.85)	169.7 (24.62)	102.0 (14.80)	
Average	**82.10 (11.91)**	**174.5 (25.31)**	**103.4 (14.99)**	
Standard Deviation	1.315 (0.1907)	4.027 (0.5841)	0.8013 (0.1162)	
Theoretical	**94.44 (13.70)**	**186.1 (26.99)**	**116.7 (16.92)**	
Percent Difference	**-13.07 %**	**-6.221 %**	**-11.39 %**	

Table 4.4. Average stress ranges prior to crack initiation for gages 8 through 13.

Specimen	Average Stress Range Prior to Fatigue Crack Initiation, MPa (ksi)		
	Gage 8	**Gage 9**	**Gage 10**
CONTROL_05	-83.10 (-12.05)	-158.9 (-23.05)	-84.48 (-12.25)
CONTROL_06	-82.42 (-11.95)	-155.4 (-22.54)	-84.94 (-12.32)
BOLT_02	-83.05 (-12.05)	-157.0 (-22.77)	-85.12 (-12.34)
BOLT_03	-81.57 (-11.83)	-154.6 (-22.43)	-84.39 (-12.24)
UIT_03	-82.87 (-12.02)	-159.6 (-23.15)	-85.20 (-12.36)
UIT/BOLT_01	-82.59 (-11.98)	-155.6 (-22.56)	-84.66 (-12.28)
UIT/BOLT_02	-81.52 (-11.82)	-153.0 (-22.19)	-84.05 (-12.19)
UIT/BOLT_03	-81.94 (-11.88)	-155.6 (-22.57)	-84.78 (-12.30)
Average	**-82.38 (-11.95)**	**-156.2 (-22.66)**	**-84.70 (-12.29)**
Standard Deviation	0.5957 (0.0864)	2.060 (0.2988)	0.3640 (0.0528)
Theoretical	**-94.44 (-13.70)**	**-186.1 (-26.99)**	**-95.98 (-13.92)**
Percent Difference	**-12.77 %**	**-16.07 %**	**-11.75 %**
Specimen	**Gage 13**	**Gage 12**	**Gage 11**
CONTROL_05	-82.25 (-11.93)	-155.7 (-22.59)	-84.26 (-12.22)
CONTROL_06	-81.76 (-11.86)	-157.2 (-22.80)	-84.16 (-12.21)
BOLT_02	-83.24 (-12.07)	-155.8 (-22.60)	-84.25 (-12.22)
BOLT_03	-81.90 (-11.88)	-156.6 (-22.72)	-84.06 (-12.19)
UIT_03	-81.77 (-11.86)	-158.9 (-23.04)	-84.04 (-12.19)
UIT/BOLT_01	-81.89 (-11.88)	-155.5 (-22.55)	-84.38 (-12.24)
UIT/BOLT_02	-82.74 (-12.00)	-152.8 (-22.17)	-83.53 (-12.11)
UIT/BOLT_03	-81.03 (-11.75)	-153.1 (-22.20)	-83.53 (-12.11)
Average	**-82.07 (-11.90)**	**-155.7 (-22.58)**	**-84.03 (-12.19)**
Standard Deviation	0.6300 (0.0914)	1.879 (0.2725)	0.3059 (0.0444)
Theoretical	**-94.44 (-13.70)**	**-186.1 (-26.99)**	**-95.98 (-13.92)**
Percent Difference	**-13.10 %**	**-16.34 %**	**-12.45 %**

As evident from the small standard deviation listed for each gage location in Tables 4.3 and 4.4, specimen type did not affect the induced stress range at a given strain gage location. Thus, the overall response of a specimen to an applied load was

not changed by adding coverplate bolts or performing UIT. For purposes of comparing measured stress ranges to theoretical stress ranges, the average stress ranges calculated for all specimens at a given strain gage location were averaged. This overall average, indicated in bold lettering in Tables 4.3 and 4.4, represents the average stress range at a given strain gage location prior to crack initiation, regardless of specimen type. The overall average stress range at each gage location was then compared to the theoretical stress range for that location.

The theoretical stress range calculated for each strain gage location is listed in bold lettering in Tables 4.3 and 4.4. The relationship between the load range applied to the three-point-bend frame and the resulting theoretical induced stress ranges at strain gage locations is discussed in section 3.2.5.2. Sample calculations for the transformation of applied load range into theoretical stress range at strain gage locations are shown in Appendix H. Percent differences between the measured and theoretical stress ranges for all gage locations are listed in bold lettering in Tables 4.3 and 4.4. As indicated in these tables, the measured stress range at each gage location was lower than the theoretical stress range for that location. The percent difference between measured and theoretical stress range ranged from -5.31 % to -16.3 %, and the average percent difference was 12.0%. For gage locations other than the front or back side of the weld toe, the percent difference ranged from approximately -11% to -13%. At the weld toe, the stress concentration caused gages two and six to have a decreased percent difference while the resulting lack of stress on the back side of the flange caused gages nine and twelve to have an increased percent difference. After analyzing all data, it was determined that the actual stresses induced in the specimens were approximately 12% lower than the theoretical nominal stresses.

One possible explanation as to why there was a systematic difference in stress range relates to the method by which the testing machine loaded the specimens. While loading the specimens in fatigue, the Adaptive Control feature of the controller

amplified the signal to the actuator so that the largest and smallest loads measured by the testing machine's load cell corresponded to the maximum and minimum desired loads entered by the user into the loading protocol. However, the measurements made by the load cell had inherent noise typical of any strain gage. The maximum and minimum loads measured by the load cell, therefore, represented the upper and lower bounds of the scatter band of the data rather than the actual applied load range. This phenomenon is demonstrated for specimen UIT/BOLT_03 in Figure 4.15.

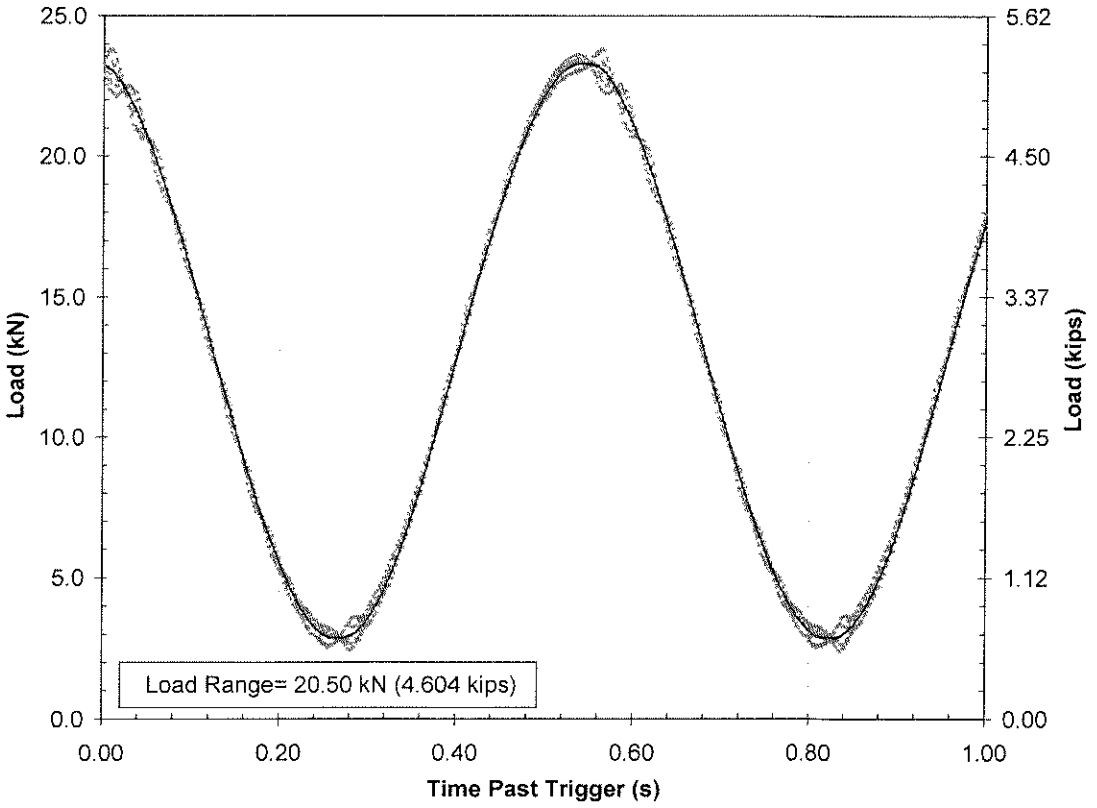

Figure 4.15. Load data measured by load cell for specimen UIT/BOLT_03.

Figure 4.15 shows data recorded by the load cell for a period of one second. The black line drawn on the gray data points represents a moving average of 5 data points. This moving average curve eliminated the noise in the load cell data and was a better representation of the actual load range that was applied to the specimen. Although the difference between the largest and smallest data points shown on Figure

4.14 was likely very close to the desired load range of 21.50 kN (4.835 kips), the difference between the maximum and minimum points on the moving average curve was only 20.50 kN (4.604 kips) as indicated on Figure 4.14. This is a difference of approximately 5%. Although a 5% difference between actual and desired applied load may not alone have caused a 12% difference between measured and theoretical stress range, it did likely contribute significantly to the difference.

Another aspect that may account for the difference between the measured and theoretical stress ranges was the method used to calculate the theoretical stress ranges. In calculating the theoretical stress ranges, the specimen was assumed to be in frictionless contact with the bending frame. This assumption allowed a simple bending moment diagram to be determined for the specimen. In reality, friction between the specimens and the points of load application on the bending frame may have caused the specimens to behave as if they were pinned to the bending frame on each end. If the specimens did behave as though pinned, axial forces may have developed in specimens and reduced the bending moments. This behavior was investigated further by comparing finite element models of specimens having pinned ends with models having rollers. These analyses are discussed in section 5.2.

4.4.2 Fatigue Crack Detection Using Strain Gage Data

After the quality of the strain data was enhanced by adding the UPS to the system, it was noticed that changes in the stress ranges measured by the strain gages adjacent to the weld toes (gages two and six) took place once a crack initiated in a specimen. This phenomenon was the result of a change in the stress path in the vicinity of the weld due to the discontinuity introduced by the fatigue crack. The changes in stress range measured by these gages are illustrated by the behavior of strain gage two and strain gage six for specimen UIT_03, shown in Figure 4.16. In Figure 4.16, each data point represents the stress range calculated for a two-second sample of strain data as discussed previously.

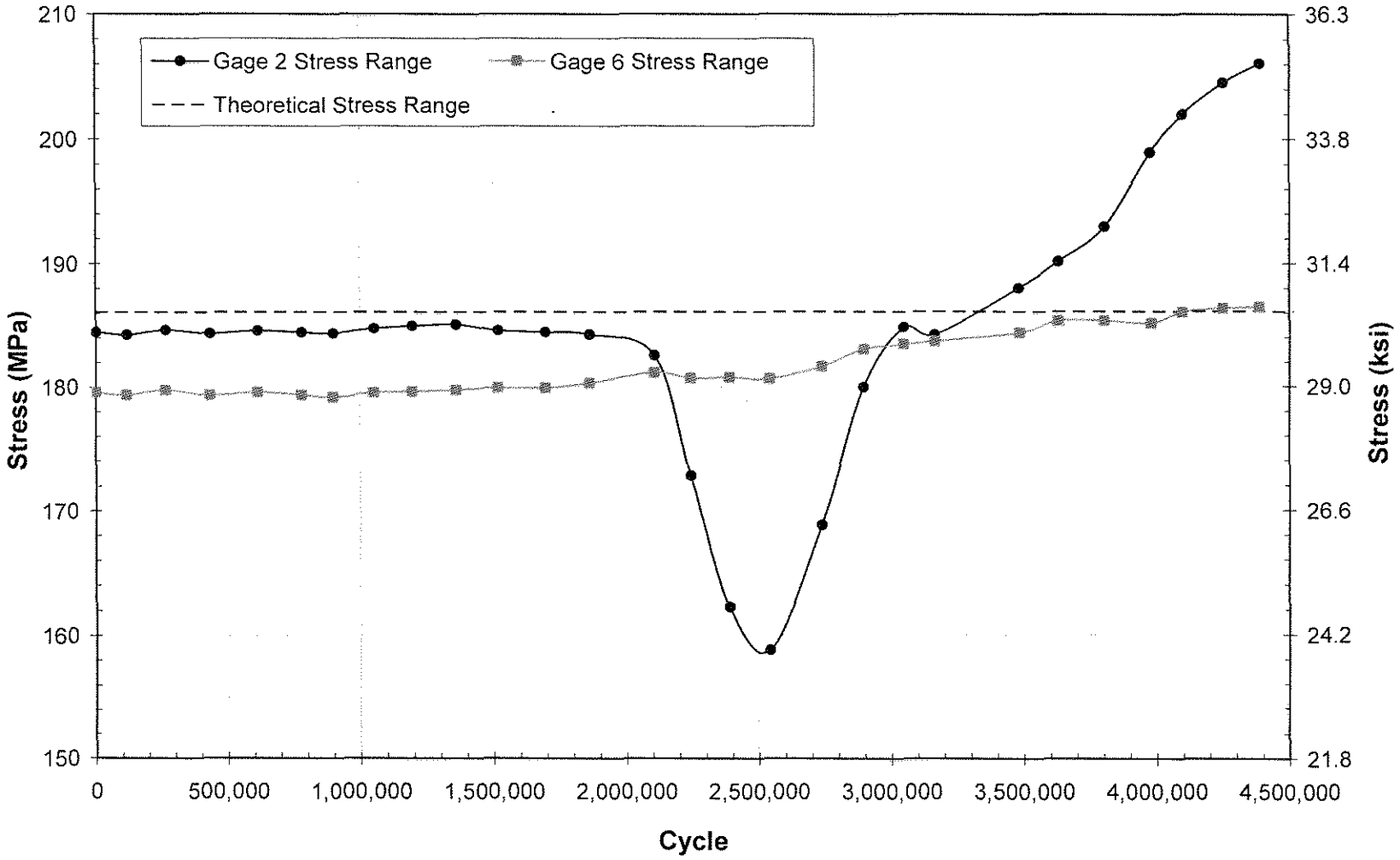

Figure 4.16. Stress ranges recorded for strain gages two and six during fatigue testing of UIT_03.

Plots similar to Figure 4.16 for strain gages two and six for all specimens can be found in Appendix D. Using the modified dye penetrant method, crack initiation for specimen UIT_03 was determined to have occurred at 2,100,000 cycles. At initiation, this specimen developed fatigue cracks in both transverse welds simultaneously. As discussed previously and illustrated in Figure 4.16, the stress range measured for each gage prior to fatigue crack initiation showed little deviation. However, as shown in Figure 4.16, when a crack formed in a transverse weld, the stress measured by the strain gage adjacent to that weld either decreased or increased noticeably. Much like the crack detection method using controller data, it was thought that this crack detection method using strain gage data could be used as the primary crack detection method. However, shortcomings in this method became apparent for some of the specimens.

The first shortcoming in the strain gage crack detection method was variability in the behavior of the measured stress range at crack initiation. This variability is demonstrated by the two strain gages shown in Figure 4.16. Although fatigue cracks in the welds adjacent to each of the gages developed in the weld throat near one end of the transverse weld, gage six showed an increase in stress range while gage two showed a decrease in stress range. This difference in behavior was likely due to the way in which each fatigue crack propagated after initiation. The crack near gage two quickly propagated across the entire length of the transverse weld throat while the crack near gage six propagated slowly toward the longitudinal weld. Also, the reason why the stress range measured by gage two changed from a decreasing trend to an increasing trend during crack propagation could not be explained. Similar variant behavior was found in other specimens, as shown in Appendix D.

A second shortcoming in the strain gage crack detection method was the subtlety with which the stress range changed at crack initiation for some of the strain gages. While about half of the strain gages at the weld toes showed a decisive change

in stress range at crack initiation, the other half showed little change. This behavior is illustrated in Figure 4.16. The stress range measured by gage two sharply declined at crack initiation while the stress range measured by gage six increased only slightly. For all specimens, this difference in behavior was likely a result of the location of crack initiation as well as the propagation behavior of each crack. As shown in Appendix D, changes in stress range at crack initiation measured by other strain gages were even more subtle than that of gage six in Figure 4.16. Because of these disadvantages, the strain gage crack detection method was not used as the primary crack detection method. However, it should be noted that strain gage data could be used to detect crack initiation for a fatigue testing program if the location of crack initiation and the behavior of crack propagation were well known for the specimens being tested.

4.5 STATIC STIFFNESS TEST RESULTS

As discussed in detail in section 3.4.2, static stiffness tests were performed for each specimen tested at a nominal weld toe stress range of 193 MPa (28.0 ksi) to detect the onset of fatigue cracking and to monitor fatigue crack propagation. Static stiffness tests were not performed for preliminary specimens. During each static stiffness test, the load applied to the bending frame and the position of the actuator were recorded by the testing machine's controller. Strains measured by the array of strain gages were also recorded by the WaveBook data acquisition system. Data recorded by both the controller and the WaveBook was used in an attempt to detect crack initiation and monitor crack propagation.

4.5.1 Static Stiffness Data Recorded by the Controller

During each static stiffness test, the load applied to the three-point-bending frame and the position of the actuator were recorded by the controller at a sampling rate of 100 Hz. To measure the stiffness of the specimen during loading, the applied load was plotted against the position of the actuator using Microsoft Office Excel

2003 software. An automatic linear regression was performed by Excel to generate a linear trend line for the data. The slope of this trend line, having units of kN/mm (kips/in) was recorded as the static stiffness of the specimen for that static stiffness test. An example of the analysis of data from a single static stiffness test is shown in Figure 4.17 for specimen CONTROL_06. In Figure 4.17, the equation of the trend line is shown in SI units on the left side of the trend line and U.S. Customary units on the right side of the trend line.

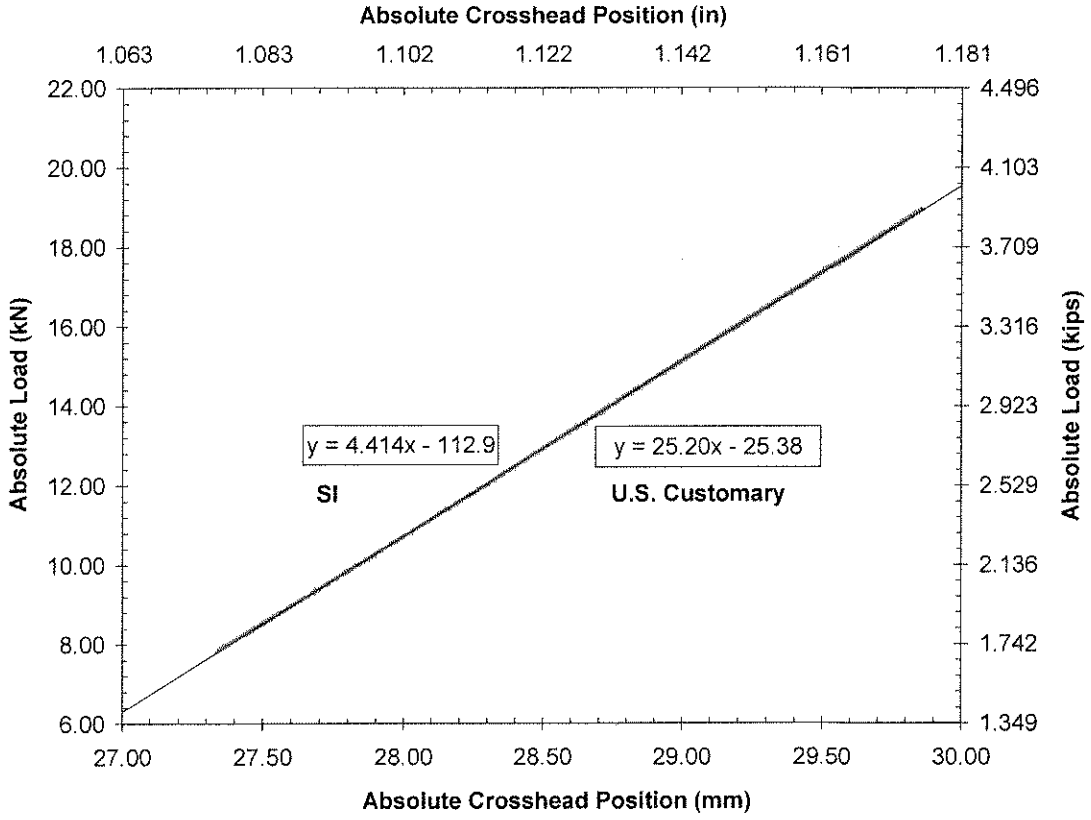

Figure 4.17. Static stiffness test results for specimen CONTROL_06 at 40,000 cycles.

For each specimen, the results of all static stiffness tests were plotted against the cycle at which each test was performed to detect crack initiation and to monitor crack propagation. Plots of static stiffness versus number of cycles are shown in

Figures 4.18 and 4.19 for specimens BOLT_02 and UIT_03, respectively. The plot of static stiffness versus number of cycles for specimen BOLT_02 was considered to be representative of the plots for all specimens displaying short fatigue lives (control specimens and bolted specimens). The plot of static stiffness versus number of cycles for specimen UIT_03 was considered to be representative of the plots for all specimens displaying long fatigue lives (combination specimens and UIT-treated specimens). Plots of static stiffness versus number of cycles for all specimens for which stiffness tests were performed can be found in Appendix C.

As illustrated by these two figures, the shape of the curve of static stiffness versus cycle for a given specimen type was very similar to the shape of the curve of dynamic stiffness versus cycle for the same specimen type. The static stiffness recorded during each static stiffness test was conceptually equivalent to the dynamic stiffness recorded during fatigue testing. Static stiffness tests were performed in addition to measuring dynamic stiffness because static stiffness tests could be performed under controlled, repeatable conditions. Because of the level of control that existed for the static stiffness tests, it was thought that these tests would be more precise and more sensitive to changes in specimen behavior than dynamic stiffness. However, as illustrated by Figures 4.18 and 4.19, the results of static stiffness tests displayed precision and sensitivity to crack initiation roughly equivalent to that of dynamic stiffness measurements.

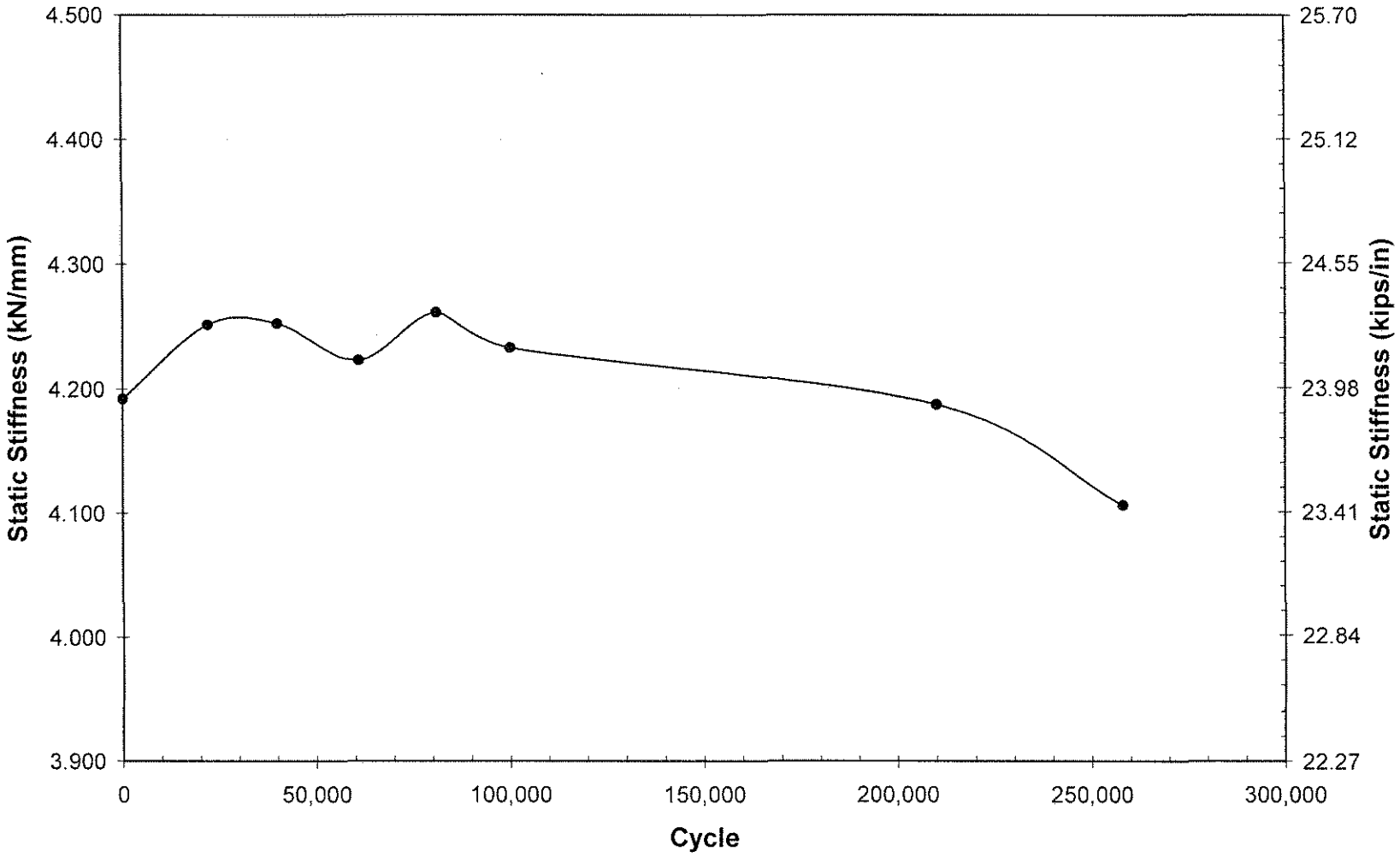

Figure 4.18. Static stiffness versus cycle for specimen BOLT_02.

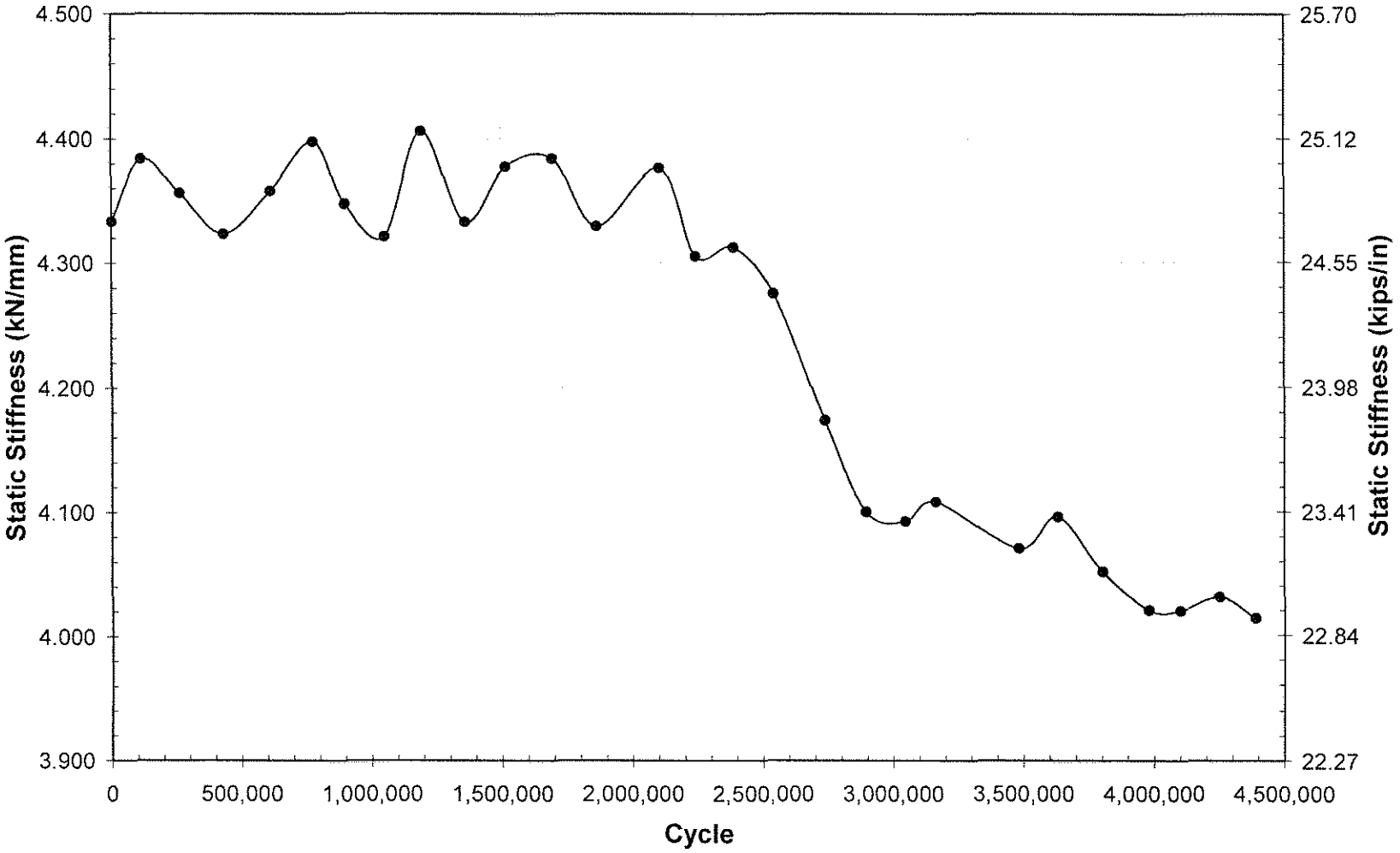

Figure 4.19. Static stiffness versus cycle for specimen UIT_03

The degree of sensitivity to fatigue crack initiation displayed by the static stiffness crack detection method is illustrated for specimen BOLT_02 in Figure 4.18. Although this specimen developed a fatigue crack at 50,000 cycles, the static stiffness did not begin to decrease until after at least 100,000 cycles, resulting in a minimum lag of 50,000 cycles. This value was similar to the lag found using the dynamic stiffness crack detection method. For specimens having short fatigue lives, this degree of sensitivity to crack initiation was inadequate. However, as shown in Figure 4.19, this same degree of sensitivity was adequate for specimens having long fatigue lives because a lag of 50,000 cycles from initiation to detection was a short period of time relative to the lives of the specimens. Had all specimens tested for this project achieved longer fatigue lives, the sensitivity of this crack detection method would have been adequate.

The precision of the static stiffness crack detection method proved to be worse than that of the dynamic stiffness crack detection method. As shown in Figure 4.19, the width of the scatter band of the static stiffness data was approximately 0.1 kN/mm (0.6 kips/in). As shown in Figures 4.10 through 4.13, this value was twice as large as the width of the scatter band for dynamic stiffness data of 0.05 kN/mm (0.3 kips/in). In general, the static stiffness crack detection method and the dynamic stiffness crack detection method proved to be equivalently effective at detecting fatigue crack initiation. Because both of these methods were less effective than the modified dye penetrant crack detection method, neither was chosen as the primary crack detection method.

4.5.2 Static Stiffness Data Measured by the Strain Gages

As discussed in section 3.4.2, strain data recorded during static stiffness testing was also analyzed in an attempt to detect fatigue cracks. This method of detecting fatigue cracks had multiple shortcomings and, therefore, was abandoned as a method to determine fatigue crack initiation. The shortcomings in this detection

method were similar to those discussed in section 4.4.2 and included: varying strain behavior in response to crack formation, lack of sensitivity to crack initiation, and subtly in changing strain behavior.

4.6 TENSILE TEST RESULTS

Tension testing of 14 tensile coupons was performed according to ASTM test designation E 8 (ASTM 2001). Of the 14 tests, the results of three were considered to be invalid due to slippage of the extensometer on the specimen surface prior to first yielding. It was determined that extensometer slippage, rather than grip slippage, had occurred by analyzing plots of load versus position recorded by the controller for these three specimens. Plots of extension recorded by the extensometer versus position recorded by the controller were also analyzed for comparison. Because plots of load versus position for these three specimens were quite linear prior to first yielding, it was determined that grip slippage had not occurred. Plots of extension versus position indicated a non-linear relationship between extension and position, indicating that the extensometer was slipping along the surfaces of these three specimens prior to first yield. Per section 7.14.7 of ASTM test designation E 8, all results for these specimens were discarded due to a malfunction in the testing equipment. Stress-strain diagrams for these three specimens can be found in Appendix E.

The remaining 11 specimens displayed model tension test behavior. A summary of the modulus of elasticity, yield strength, tensile strength, and elongation of each specimen is shown in Table 4.5. A view of a typical ductile failure is shown for one of the specimens in Figure 4.20. Figure 4.21 shows the fracture locations for all 14 specimens. Figures 4.22 and 4.23 show plots of stress versus strain over two strain ranges for a typical specimen.

Table 4.5. Summary of results for tensile specimens.

Specimen	Modulus of Elasticity, MPa (ksi)	Yield Strength, MPa (ksi)	Tensile Strength, MPa (ksi)	Elongation, %
T1	195,000 (28,300)	308 (44.6)	495 (71.8)	37.0
T2	192,000 (27,800)	301 (43.6)	494 (71.6)	40.5
T3	179,000 (26,000)	321 (46.5)	493 (71.5)	38.0
T4	204,000 (29,600)	314 (45.6)	493 (71.5)	38.5
T5	184,000 (26,700)	314 (45.5)	493 (71.5)	39.0
T6	195,000 (28,200)	296 (43.0)	489 (70.9)	37.0
T7	188,000 (27,300)	326 (47.3)	492 (71.3)	37.5
T8	194,000 (28,100)	317 (46.0)	493 (71.5)	39.0
T9	189,000 (27,400)	329 (47.7)	494 (71.6)	37.5
T10	197,000 (28,500)	315 (45.7)	493 (71.5)	38.5
T12	189,000 (27,500)	301 (43.7)	485 (70.4)	36.5
Average	**191,000 (27,800)**	**313 (45.4)**	**492 (71.4)**	**38.1**
Range	25,000 (3,600)	33.0 (4.70)	10.0 (1.40)	4.00
Standard Deviation	6,430 (913)	10.1 (1.45)	2.69 (0.374)	1.10

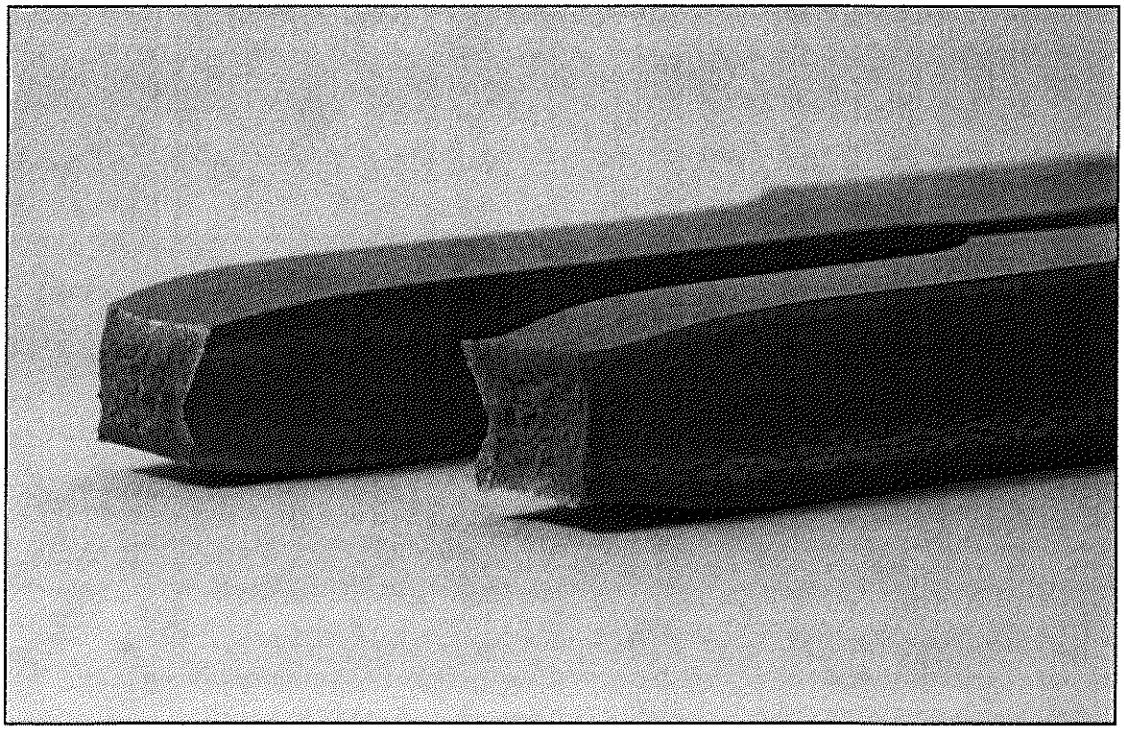

Figure 4.20. Ductile failure surface of a tensile specimen.

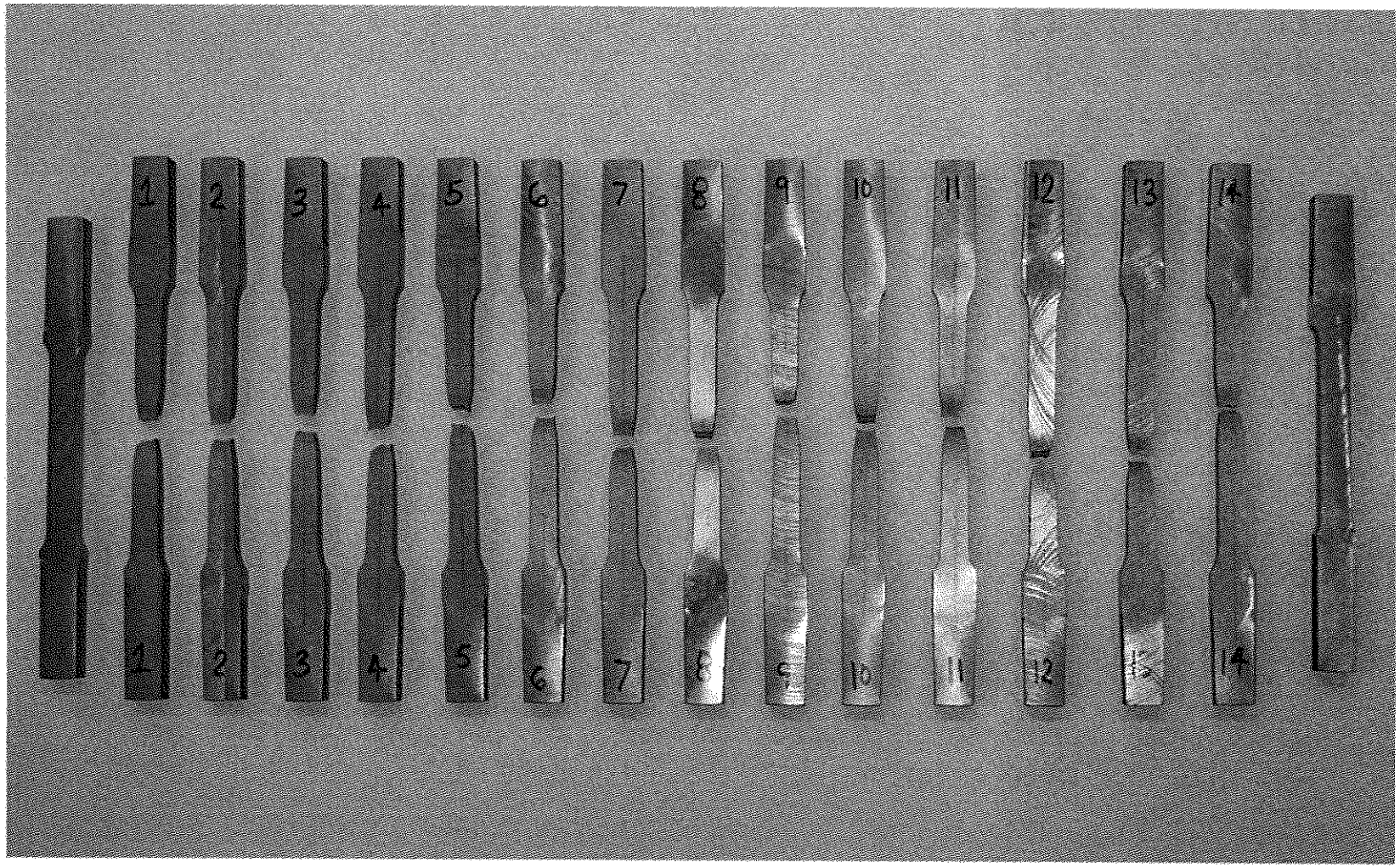

Figure 4.21. Fracture locations for all tensile specimens.

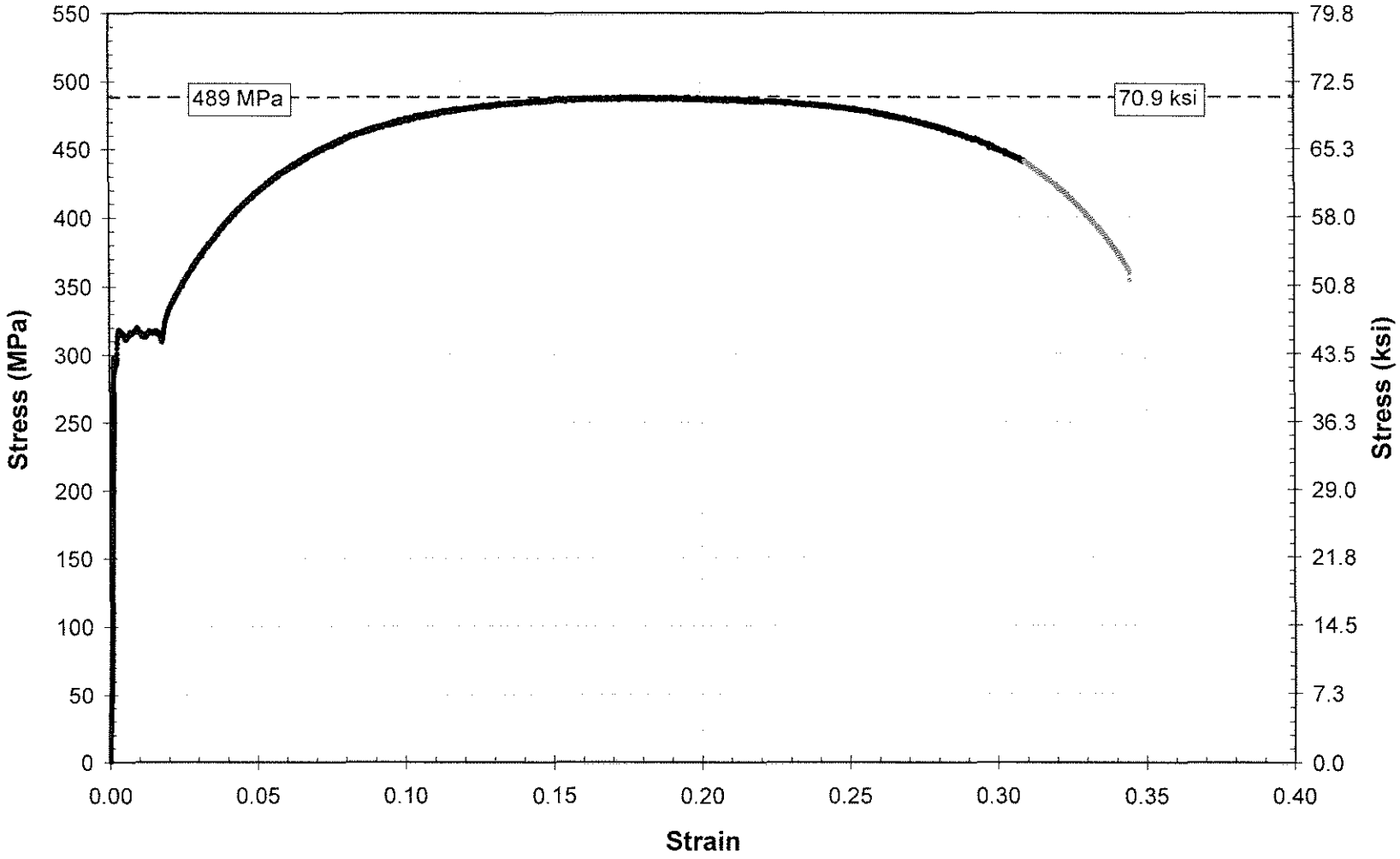

Figure 4.22. Stress versus strain plot used to determine tensile strength for specimen T6.

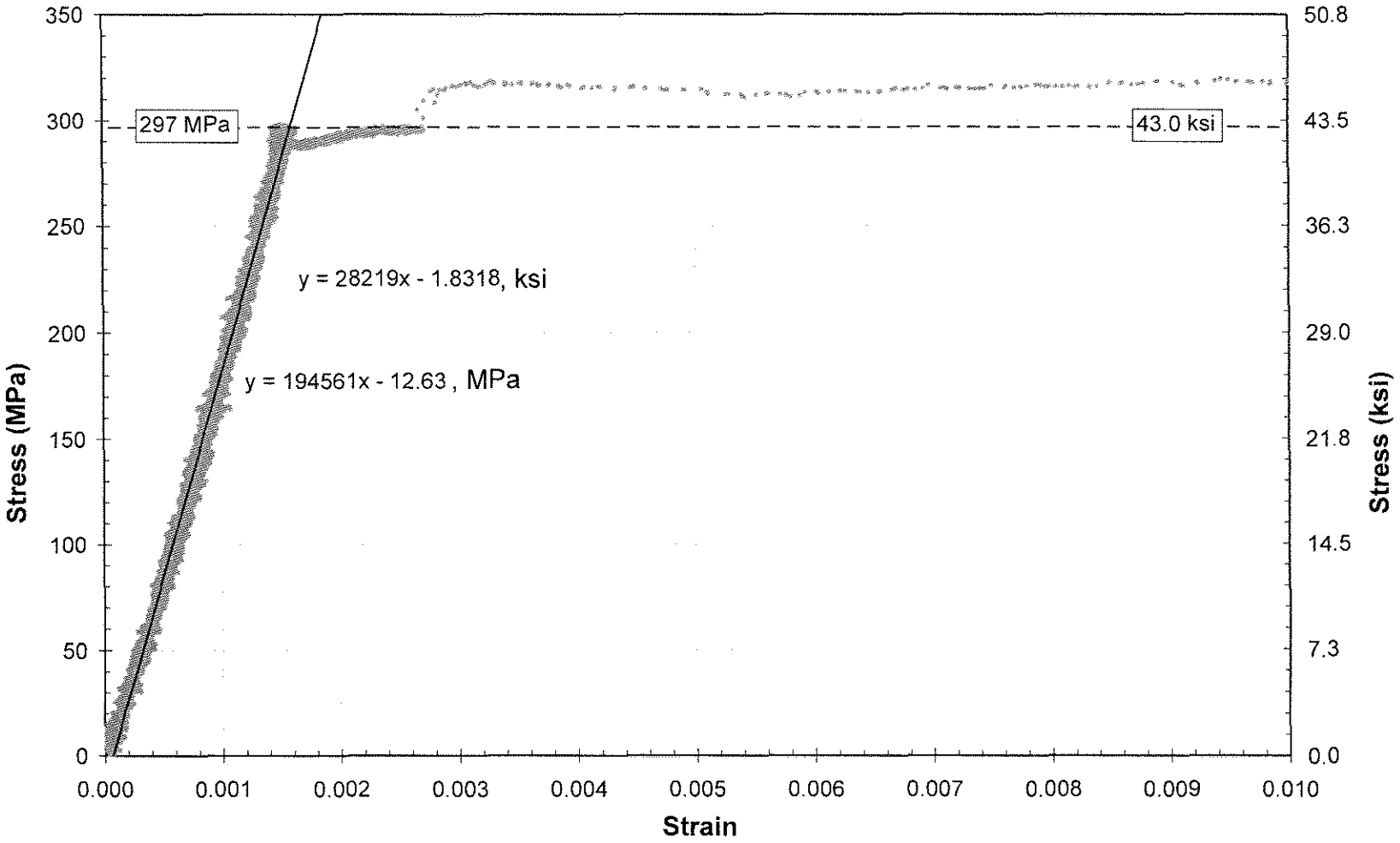

Figure 4.23. Stress versus strain plot used to determine yield strength and modulus of elasticity for specimen T6.

4.6.1 Yield Strength

At the outset of tensile testing, it was calculated that a rate of crosshead separation of 0.13 mm/min (0.0050 in/min) would result in a rate of stress application between 68.9 and 689 MPa/min (10,000 psi/min and 100,000 psi/min), which is the stress rate prior to first yield required by section 7.6.3.2 of ASTM specification E 8. Results for the first two specimens tested, T1 and T2, showed that this rate of crosshead separation only provided 39.6 MPa/min (5,750 psi/min) and 47.7 MPa/min (6,920 psi/min) for these two specimens, respectively. Since these rates of stress application were outside the ASTM standard, the rate of crosshead separation was increased to 0.25 mm/min (0.010 in/min) for the remaining specimens. At this rate of crosshead separation, the resulting rate of stress application for the remaining specimens ranged from 88.9 to 105 MPa/min (12,900 to 15,200 psi/min) and averaged 100 MPa/min (14,500 psi/min). Therefore, the remaining specimens were tested within the ranges specified by specification E 8 prior to first yield.

Per section 7.7.3 of ASTM specification E 8, the autographic diagram method was used to determine the yield strength of the tensile specimens rather than the offset method. Use of this method was suggested by Note 33 of the specification. This note states that when the offset method is used to calculate the yield strength of a material exhibiting discontinuous yielding and yield point elongation, force fluctuations in the plateau region where the offset intersects the stress-strain curve may significantly affect the measured yield strength. Therefore, the offset method is best suited for materials displaying continuous yielding and having no yield point elongation, whereas the autographic diagram method is best suited for materials displaying discontinuous yielding and yield point elongation (possessing a well-defined yield plateau). As illustrated from by Figure 4.23, the tensile specimens tested for this project displayed discontinuous yielding and yield point elongation. Using the autographic diagram method, the yield strength of the specimens was determined by

recording the stress corresponding to the maximum force at the onset of discontinuous yielding. Therefore, the yield strengths reported for the specimens correspond to the upper yield strength as defined in the specification. The determination of yield strength using the autographic diagram method is illustrated by Figure 4.23. As evident from this figure, the yield strength corresponds to the maximum stress achieved by the stress-strain curve prior to discontinuous yielding. Plots of stress versus strain used to determine the yield strength for all tensile specimens are shown in Appendix E.2.

The yield strengths calculated for all tensile specimens are summarized in Table 4.5. As shown in Table 4.5, the average yield strength of the specimens was 313 MPa (45.4 ksi) and the standard deviation in yield strength was 10.1 MPa (1.45 ksi). As expected, the average yield strength for the specimens was greater than the minimum yield strength of 248 MPa (36.0 ksi) required for A36 steel.

4.6.2 Tensile Strength

Per section 7.10 of ASTM specification E 8, tensile strength was determined by dividing the maximum force measured by the load cell by the original cross-sectional area of the specimen being tested. As illustrated by Figure 4.22, the tensile strength of a specimen corresponded to the apex of the stress-strain curve during the strain hardening phase of loading. The tensile strength calculated for each specimen is reported in Table 4.5. As shown in Table 4.5, the average tensile strength for the specimens was 492 MPa (71.4 ksi). The standard deviation for the tensile strength of the specimens was 2.69 MPa (0.374 ksi). The average tensile strength for the specimens was greater than the minimum of 400 MPa (58.0 ksi) required for A36 steel. Plots of stress versus strain displaying the tensile strengths of the specimens are shown in Appendix E.3.

4.6.3 Modulus of Elasticity

For each specimen, the modulus of elasticity was determined by analyzing the linear portion of a plot of stress versus strain obtained from a tension test. Plots of stress versus strain for the linear portion of loading were constructed using Microsoft Excel. An example of a plot of stress versus strain for the linear portion of loading is shown for specimen T6 in Figure 4.23. The modulus of elasticity of a specimen was determined using Excel's automatic linear regression feature. Using this feature, a linear trend line was calculated for all data points recorded before the onset of yielding. The slope of this line was then automatically calculated by Excel and displayed on the stress-strain diagram. The slope of this trend line was assumed to be equal to the modulus of elasticity the specimen for which the stress-strain diagram was drawn. The modulus of elasticity for each specimen is reported in Table 4.5. As shown in Table 4.5, the average modulus of elasticity for the 11 specimens was 191,000 MPa (27,800 ksi). The standard deviation for the modulus of elasticity of the specimens was 6,430 MPa (913 ksi). The average modulus of elasticity calculated for the tensile specimens was somewhat lower than the value of 200,000 MPa (29,000 ksi) commonly used in the analysis and design of steel structures. However, this occurrence is not entirely unusual. Plots of stress versus strain for the linear portion of loading and the corresponding trend lines used to determine modulus of elasticity are shown for all specimens in Appendix E.2.

4.6.4 Elongation

For each of the tensile tests, the extensometer was removed from the specimen after the tensile strength was achieved but prior to fracture. This was done to avoid damaging the extensometer. As illustrated by Figure 4.22, the point at which the extensometer was removed from a specimen corresponds to the end of the black data points on a plot of stress versus strain. Subsequent data points on a plot of stress versus strain were calculated using the load and position data recorded by the testing

machine's load cell and internal LVDT, respectively. These data points appear gray on the plots of stress versus strain (see Appendix E.3). From this data, strain was calculated by dividing the change in position measured by the internal LVDT by the original length of the specimen's reduced section of 76 mm (3.0 in.). Since each specimen was gripped closer towards the ends of the specimen than the start of the reduced section, using the original length of the reduced section to determine strain was an oversimplification and led to a change in behavior on the stress-strain curve when the extensometer was removed. For most of the tensile specimens, the portion of the stress-strain curve determined using controller data was shifted relative to the stress-strain curve calculated using the extensometer. The excellent fit of the two curves shown in Figure 4.22 was not characteristic of the majority of the specimens. However, this secondary stress-strain data was obtained only for the purpose of completing the stress-strain curve and was not used to determine any of the engineering properties of the tensile specimens. Thus, conformance to the ASTM specification was maintained for the tensile testing. Plots of stress versus strain showing the secondary stress-strain curves for all specimens are shown in Appendix E.3.

Because the extensometer was removed prior to fracture, percent elongation for the specimens was calculated rather than percent elongation at fracture (see section 7.11.5.2 of ASTM specification E 8). Per section 7.11.2 of ASTM specification E 8, the two halves of each specimen were fitted together after fracture to determine the percent elongation. For each specimen, the distance between the original 50.8 mm (2.00 in) gage length punch marks was measured to the nearest 0.3 mm (0.01 in) using the same digital caliper that was used to measure the original gage length. The elongation was then calculated and reported to the nearest tenth of a percent. The percent elongation for each specimen is reported in Table 4.5. As shown in Table 4.5, the average percent elongation for the 11 specimens was 38.1%

(51mm (2.0 in) gage length). The standard deviation for the elongation of the specimens was 1.10%. The average elongation for the tensile specimens was much larger than the minimum elongation of 21% (51mm (2.0 in) gage length) required for A36 steel.

CHAPTER 5 FINITE ELEMENT ANALYSIS

Three finite element analyses were performed as supplements to the fatigue tests completed for this research project. The objectives of these analyses were to (1) investigate the reduced (compared to theoretical) average stress ranges measured by the strain gages, (2) determine the frictional characteristics between a specimen and the bending frame, and (3) examine changes in the state-of-stress in the transverse weld as a result of adding a pretensioned bolt to the end of a coverplate. The first two objectives were achieved by generating and comparing the results of two finite element models while the latter of these goals was achieved by generating and analyzing a single model.

5.1 MODEL PARAMETERS

All finite element models were generated using ABAQUS/CAE software Version 6.6.1 and solved using ABAQUS/Standard software. The results of these analyses were analyzed and interpreted using ABAQUS/Viewer software. The two models created to complete objectives one and two listed previously were identical in all respects except for boundary conditions. These two models will henceforth be referred to as "bending models". The third model differed in geometry and will henceforth be referred to as the "bolted model". Model parameters for these two model types will be discussed individually.

5.1.1 Bending Model Parameters

To achieve objectives one and two listed above, it was desired to accurately model the fatigue specimens tested for this project and subject the models to the load that was theoretically calculated to produce a nominal weld toe stress range of 193 MPa (28.0 ksi) in the specimens. To enable the use of a fine element mesh while maintaining a sufficiently low number of elements to allow each model to solve in a timely manner, only half of a specimen was modeled. Because the specimen geometry was symmetric about the centerline, one half of the specimen was

eliminated from the model and boundary conditions simulating that half of the model were imposed on the cross-sectional surface at the centerline. The imposed boundary conditions simulating the removed half of the model are discussed later in this section. Figure 5.1 shows the completed meshed bending model.

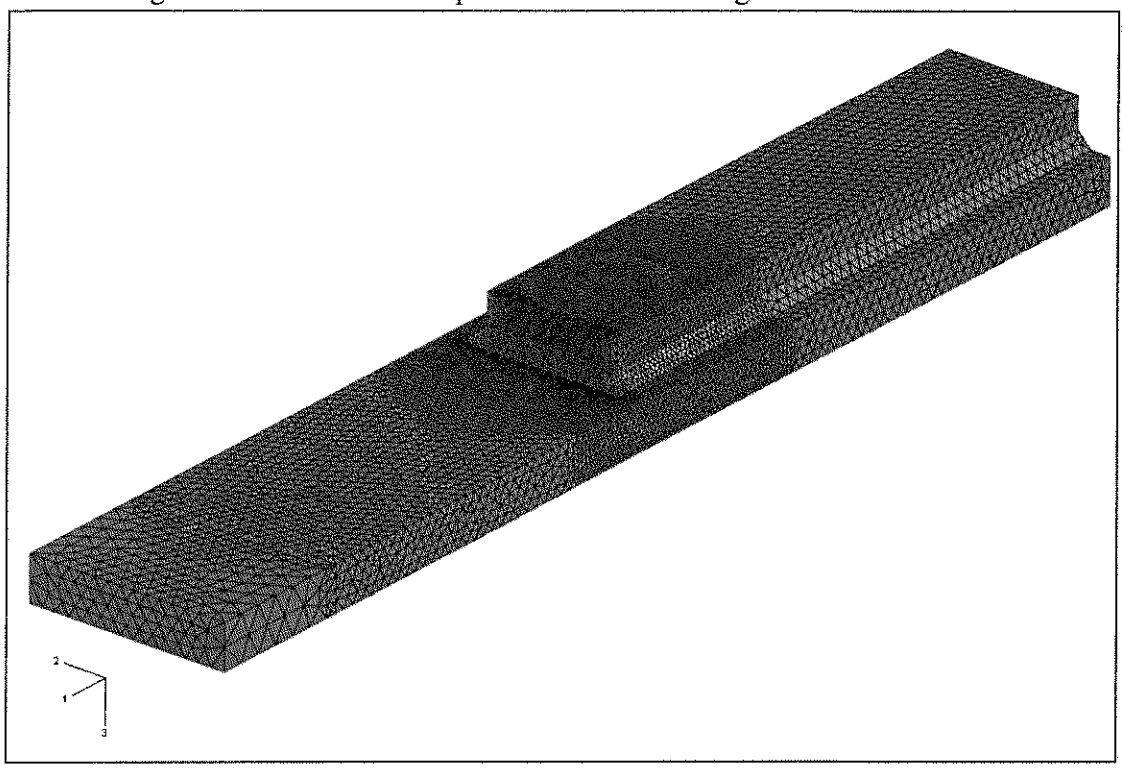

Figure 5.1. Isotropic view of the final meshed bending model.

Rather than constructing the bending model from separate parts and connecting the parts using tie constraints, equations, or another connection technique, it was decided that the entire specimen half would be modeled as a single three-dimensional part. This was done to avoid variability in force transfer and contact behavior that occasionally occurs when connecting parts of a model using these connection techniques. By modeling a single part, all forces were transferred through the model by shared element nodes, ensuring accurate force transfer. Since the actual specimens had an interface between the flange and the coverplate and were, therefore, not a continuous solid, a slit measuring 76.20 mm (3.000 in) wide × 0.03 mm (0.001

in) high × 330.20 mm (13.000 in) deep was cut into the center of the model to simulate the surfaces of the flange and coverplate. Because of the very shallow height of the slit, the two surfaces created by this slit, although not initially in contact, came in contact as soon as load was applied to the model and simulated the contact between the flange and coverplate of the fatigue specimens. An exposed view of this slit visible at the centerline cross-section is shown in Figure 5.2.

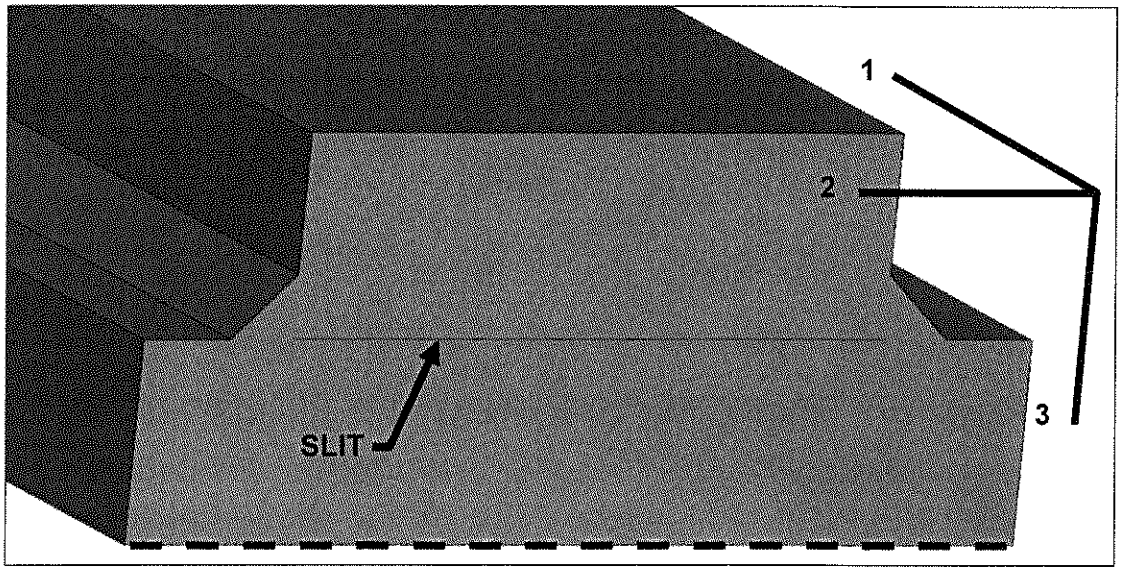

Figure 5.2. Exposed cross-section at centerline of specimen for ABAQUS models.

The material properties used for the bending models were those determined by the tension testing discussed in sections 3.5 and 4.6. The modulus of elasticity used for the models was 191,000 MPa (27,800 ksi). Since strains much larger than the strain at the yield point of the material were not expected, a perfectly elastoplastic material model was used, ignoring the effects of strain hardening. The yield strength used for the models was 313 MPa (45.4 ksi), as determined from tension testing. The commonly accepted Poisson's ratio for steel of 0.3 was also used.

Contact properties were defined for the two surfaces of the slit representing the flange and coverplate contact surfaces. For behavior normal to the surfaces, hard,

true surface-to-surface contact was chosen. Thus, planes defined by nodal positions of one surface were not allowed to pass through planes defined by the nodal positions of the other surface. For tangential behavior between the surfaces, friction coefficients were defined. The commonly accepted static and dynamic coefficients of friction of 0.74 and 0.57, respectively, for steel-to-steel contact were used. The normal and tangential contact parameters used for the bending models allowed the slit to accurately simulate the behavior of the flange-coverplate interface in the fatigue specimens.

Elements sizes, locations, and types were defined for the bending models through the process of meshing. At the onset of meshing, it was deemed desirable to strictly control the positions and sizes of all elements in the mesh. This was done so that fine meshes, corresponding to small element sizes, could be used at locations of high stress concentration and coarse meshes, corresponding to large element sizes, could be used at locations of low stress concentration. Therefore, an attempt was made to control the position of every node in the model. The meshed bending model resulting from this process is shown in Figure 5.3. An enlarged view showing the mesh near the transverse weld is shown in Figure 5.4.

The strictly-controlled meshing process was very laborious and required the use of hundreds of model partitions. The reason for this laboriousness was the means by which ABAQUS/CAE assigns element nodes to model locations. Using ABAQUS/CAE, the user cannot define the actual locations of nodes. Rather, the user defines the positions of "seeds" along edges of a region of the model, then ABAQUS/CAE automatically meshes that region, attempting to match nodal locations to the seed locations as best as possible. Unfortunately, when a moderately-sized, complex-shaped region of a model is meshed automatically, ABAQUS/CAE does a poor job of honoring seed locations. Therefore, the model had to be partitioned into many small regions to control the exact locations of the nodes.

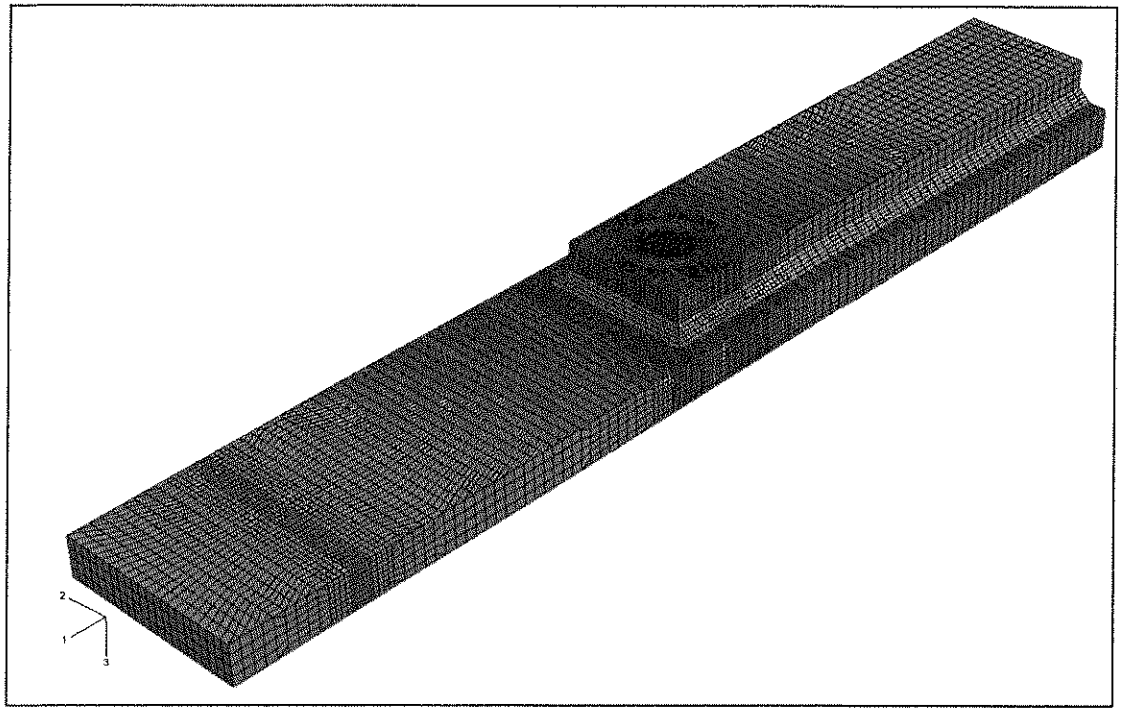

Figure 5.3. Preliminary mesh for the bending model.

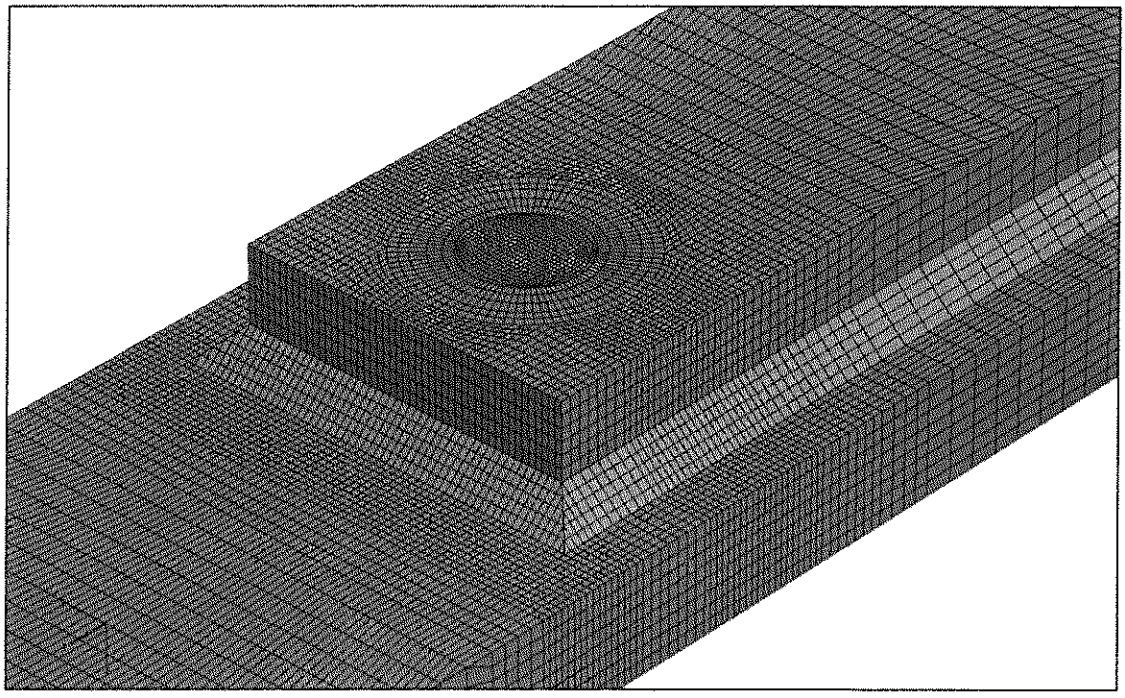

Figure 5.4. Preliminary mesh at the weld toe of the bending model.

When the bending model was meshed in this manner, care was taken to ensure that an identical mesh could be produced for the bolted model to be completed later. Because the bolted model required that a cylindrical bore be cut through the flange and coverplate (see section 5.1.2), a cylindrical surface was partitioned in the bending model near the transverse weld, as shown in Figure 5.4. This was done so that for the bolted model, the material and corresponding mesh inside the cylindrical surface could be easily removed and the remainder of the mesh would be identical to the bending model. However, when meshing the bolted model, it was found that ABAQUS/CAE would not allow hexahedral elements to be placed adjacent to the free surface of the bore. Only tetrahedral elements were allowed. Since the triangular faces of tetrahedral elements could not be used adjacent to the rectangular faces of hexahedral elements, the entire bolted model had to be meshed using tetrahedral elements to avoid using tie constraints or other incompatible meshing procedures. Because it was desired to have identical meshes for the bending and bolted models, the bending model had to be meshed using only tetrahedral elements as well. Therefore, the strictly controlled mesh created for the bending model was abandoned and that mesh will henceforth be referred to as the preliminary mesh.

To mesh the bending model using tetrahedral elements, the model was partitioned into only a few large sections. For the sections where the mesh was to be finer, such as at the weld toe, the centerline, and points of load application, edge seeds were placed more closely than at sections where the mesh was to be less dense. This method of meshing proved to be vastly simpler than the method used to produce the preliminary mesh. As shown in Figure 5.1, this less-controlled method of meshing produced a symmetric mesh that was much finer at regions of high stress concentration than regions of low stress concentration. Figure 5.5 shows an enlarged view of the mesh near the transverse weld.

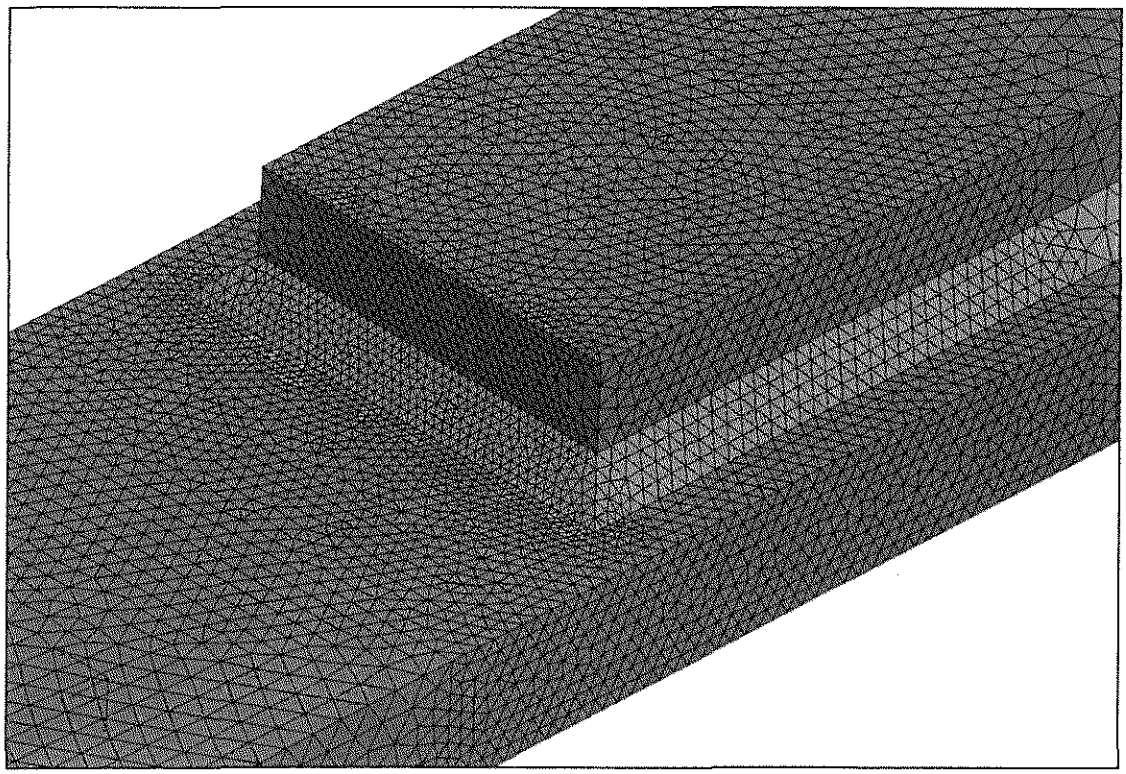

Figure 5.5. Final mesh at the weld toe of the bending model.

The tetrahedral elements comprising the transverse weld and adjacent regions had edge lengths of approximately 1.6 mm (0.063 in) while elements in areas of low stress concentration had edge lengths of approximately 6.25 mm (0.250 in). Smaller element sizes were used at the weld toe and other areas of stress concentration because stresses at those regions were expected to fluctuate greatly over very short distances in the model. Small elements were required if these stress fluctuation were to be accurately measured in these regions. Using larger elements at regions of high stress concentration and large stress fluctuation would have likely resulted in a reduction of resulting peak stresses at these regions. Considering the difference in time it took to generate the preliminary and final meshes, coupled with the fact that the two resulting meshes were equal in quality, it was determined that the less-controlled meshing technique was more efficient and, hence, preferred over the preliminary meshing procedure. All tetrahedral elements used for the final mesh

were 3-dimensional, 4-node standard stress elements from the ABAQUS/Standard element library, labeled C3D4. No wedge or hexahedral elements were used. Both of the bending models had identical meshes. Each mesh was comprised of 47,499 nodes and 244,782 elements.

For both bending models, the theoretical load required to induce a nominal weld toe stress range of 193 MPa (28.0 ksi) was applied over a surface area 114.3 mm (4.500 in) long × 6.35 mm (0.250 in) wide at a distance of 76.20 mm (3.000 in) from the end of the flange. Since only half of a specimen was modeled, half of the theoretical load range, or 10.75 kN (2.417 kips) was applied over this area. At a stress ratio of 0.1, this load range translated into a maximum applied load of 11.95 kN (2.686 kips) and a minimum applied load of 1.20 kN (0.269 kips). The maximum load applied over the area described resulted in an applied pressure of 16.46 MPa (2.387 ksi), and the minimum load applied over the area described resulted in an applied pressure of 1.65 MPa (0.239 ksi). Since an elastoplastic material model was used, the material in the model underwent non-linear deformation at regions of high stress concentration. Because of this nonlinear behavior, each bending model had to be solved once with the maximum load applied and once with the minimum load applied. Stress and deflection ranges were then calculated by subtracting the stresses and deflections under minimum load from the stresses and deflections under maximum load. Had an elastic material model been used rather than an elastoplastic material model, the stress and deflection ranges could have been determined by simply applying the load range of 10.75 kN (2.417 kips) to the flange.

For both of the bending models, the boundary conditions at the centerline of the specimen were identical. To simulate the contact between the specimen and the middle loading point on the three-point-bending frame, the bottom edge of the flange at the specimen centerline was fixed against translation in all three directions. This edge is indicated by the dashed black line in Figure 5.2. This edge was also fixed

against rotation in two direction vectors: (1) parallel to axis one shown in Figure 5.2 and (2) parallel to axis three shown in Figure 5.2. The edge remained free to rotate about axis two shown in Figure 5.2. Therefore, this edge was fixed against translation in three directions and rotation in two directions, similar to the actual fatigue specimen loading conditions (assuming high frictional forces existed). To simulate the half of the specimen that was removed from the model, the entire cross-sectional surface at the specimen centerline, as shown in Figure 5.2, was fixed against translation parallel to axis one shown in Figure 5.2. This simple boundary condition provided restraint equivalent to what the other half of the specimen would have provided, but still allowed Poisson effects to take place in the material.

The third boundary condition applied to the bending models simulated contact between the specimen flange and the outside load point on the three-point-bending frame. This boundary condition differed for the two models. The first model, labeled the "roller" model, was not restrained at the point of load application. By applying no boundary conditions, the end of the flange was free to translate in directions perpendicular to axes three and one, as shown in Figure 5.2. Although also free to translate in a direction perpendicular to axis two, the symmetry of the model and applied loads prevented deflection in this direction. By applying no boundary conditions, a perfectly frictionless roller was simulated for this model. In theory, this model was expected to develop nominal stresses (away from stress concentrations) similar to the nominal stresses calculated theoretically.

The second model, labeled the "pinned" model, was restrained in direction parallel to axis one at the point of load application, as shown in Figure 5.2. This boundary condition allowed the end of the flange to translate freely in a direction parallel to axis three, but remain constant in a direction parallel to axis one. By applying this boundary condition, a perfectly pinned connection between the flange and the bending frame was simulated. This connection allowed the flange to rotate

freely, identical to a pinned connection. The stresses and deflections calculated for these two models were compared to stresses and deflections calculated for the fatigue specimens to not only determine why the nominal specimen stresses were approximately 12% less than theoretically expected, but to also determine if the contact between the specimens and bending frame behaved as pinned, frictionless, or somewhere in between.

5.1.2 Bolted Model Parameters

As mentioned in the previous section, most of the parameters entered for the bolted model were identical to those of the bending models. An identical modulus of elasticity, Poisson's ratio, and elastoplastic material model was used. The slit created to simulate the interaction between the contact surfaces of the flange and coverplate had the same dimensions and the same contact interaction properties as the bending models. Identical solution parameters were also used when solving with ABAQUS/Standard.

The only differences between the bolted model and the bending models were specimen geometry, applied loads, and boundary conditions. The geometry of the bolted model was identical to the geometry of the bending models except that a 25.40 mm (1.000 in) diameter cylinder of material was removed from the flange and coverplate near the transverse weld. Reflecting what was done by the fabricators for the actual fatigue specimens, the center of this bore was placed a distance of 31.75 mm (1.250 in) from the end of the coverplate. The resulting mesh was very similar to that of the bending specimens, except that elements at the location of the bore were removed and some elements adjacent to the bore were adjusted. The completely meshed bolted specimen is shown in Figure 5.6. An enlarged view of the mesh near the transverse weld is shown in Figure 5.7. Element sizes in regions of high and low stress concentration were the same as the element sizes in corresponding regions for the bending models. The mesh for bolted model was comprised of 45,771 nodes and

234,381 elements. These quantities were slightly lower than those of the bending models due to the elements that were removed at the bore location. The same element type, C3D4, was used for the tetrahedral elements.

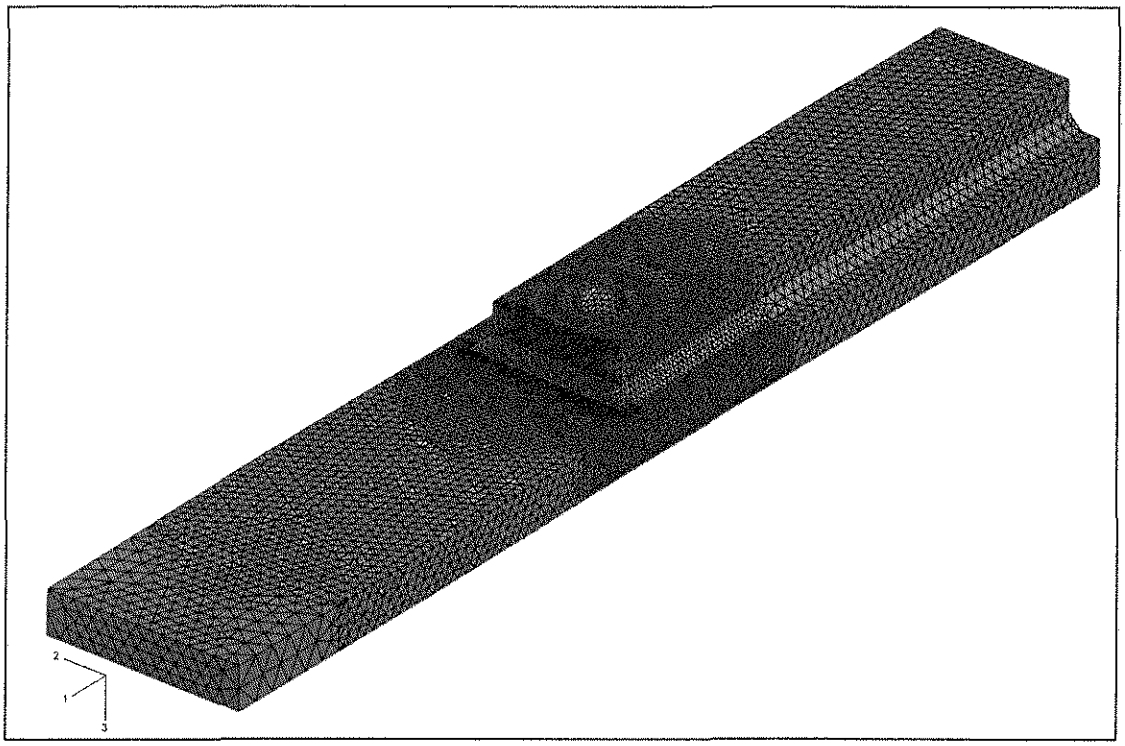

Figure 5.6. Isotropic view of the final meshed bolted model.

The largest difference between the bolted model and the bending models was the manner in which the models were loaded. For the bolted model, the load applied to the flange by the bending frame was removed. Instead, circular pressure loads concentric with the bore were applied to the top of the coverplate and the bottom of the flange. These loads simulated the forces applied to a specimen when a bolt was pretensioned. By subjecting the model to pretension forces only, the goal was to determine the changes in the state-of-stress at the weld toe caused by the bolt. The gross diameter of the loaded area on each side of the specimen was 50.80 mm (2.000 in), reflecting the actual diameters of both the washer and the bolt shoulder used for

the specimens. By subtracting the area of the bore from the gross area of the loaded surface, the net area over which the pressure force was distributed was 1520 mm^2 (2.356 in^2) on each face of the specimen. Because the specified pretension force in each bolt was 226.9 kN (51.00 kips) (AISC 2005), the resulting pressure force applied to each face of the specimen wasc149.24 MPa (21.645 ksi).

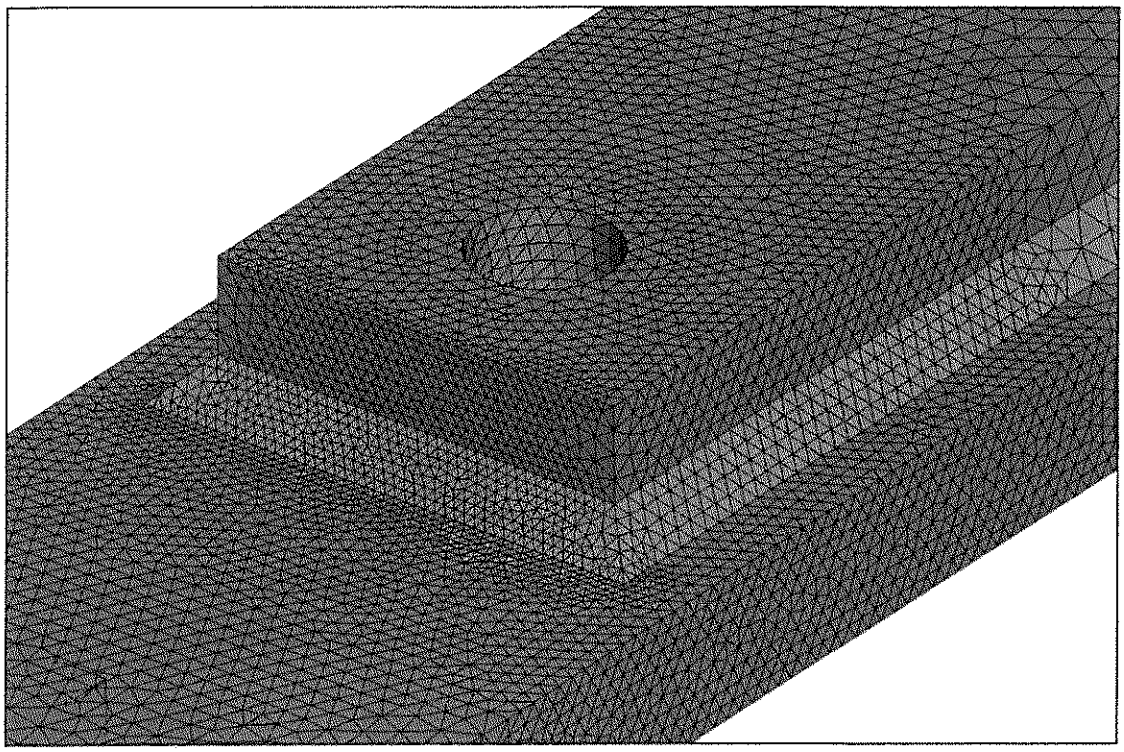

Figure 5.7. Final mesh at the weld toe of the bolted model.

The boundary conditions used to constrain the bolted model were identical to the boundary conditions used to constrain the roller model. These boundary conditions allowed the bolted specimen to expand and contract freely under the applied pretension pressures. As discussed briefly in Chapter 4, a model allowing free expansion may not have accurately simulated the behavior of a highly constrained flange on an actual girder. However, the model did accurately simulate the behavior of the fatigue specimens tested for this project. Because the goal of this

model was to simulate the behavior of the fatigue specimen, a model allowing free expansion was used.

5.2 COMPARISON OF BENDING STRESS RANGES

To compare bending stresses calculated for both bending models, each model had to be solved once with the maximum load applied and once with the minimum load applied. The results of these four solutions were then used to compare the roller model and pinned model stress ranges to each other, to the average stress ranges measured by the strain gages, and to theoretical nominal stress ranges.

5.2.1 Von Mises Stresses

The most general way to compare the resultant stresses for two finite element models was to compare the resultant three-dimensional states-of-stress in the models. For the bending models, this was done by comparing Von Mises stress, which is a measure of the magnitude of the three-dimensional state of stress at a given point. Although Von Mises stress does not indicate the magnitudes or orientations of the individual principal stresses, it does quantify the degree to which a material is being stressed three-dimensionally. The Von Mises stresses under maximum load are displayed for the roller and pinned models in Figures 5.8 and 5.9, respectively. Enlarged views of the transverse weld region for the roller and pinned models are shown in Figures 5.10 and 5.11, respectively. For the latter two figures, the model was also sectioned longitudinally at the centerline so the Von Mises stresses in the material could be seen as well. The legend for all four figures is shown in Figure 5.12. Also, all element edges have been removed from the four figures to better show the stress contours.

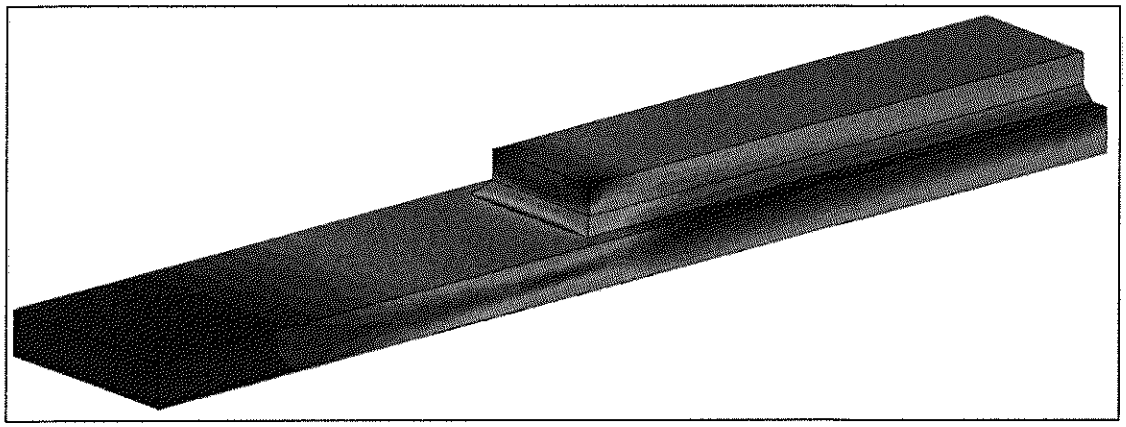

Figure 5.8. Von Mises stresses at the surface of the roller model.

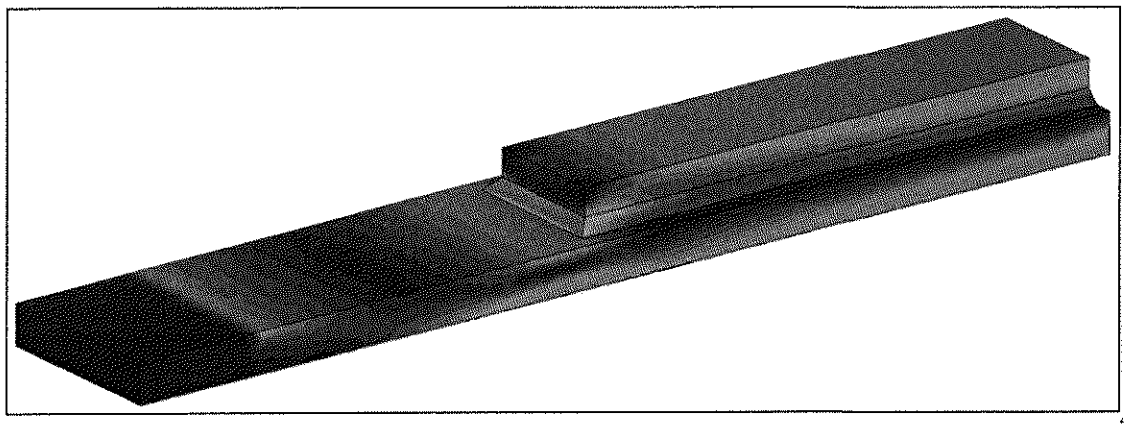

Figure 5.9. Von Mises stresses at the surface of the pinned model.

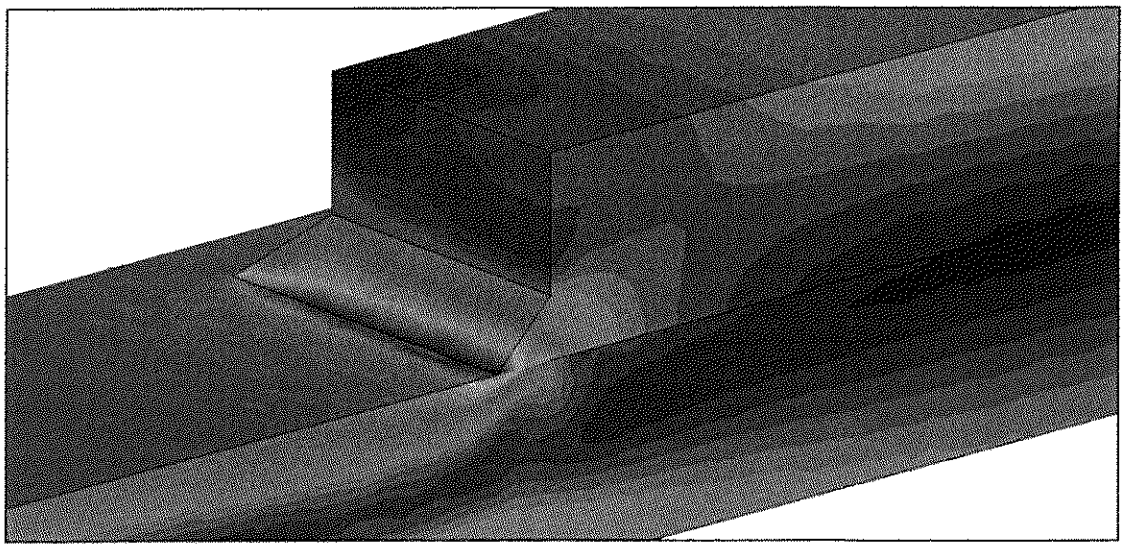

Figure 5.10. Cross-section at the weld showing Von Mises stresses for the roller model.

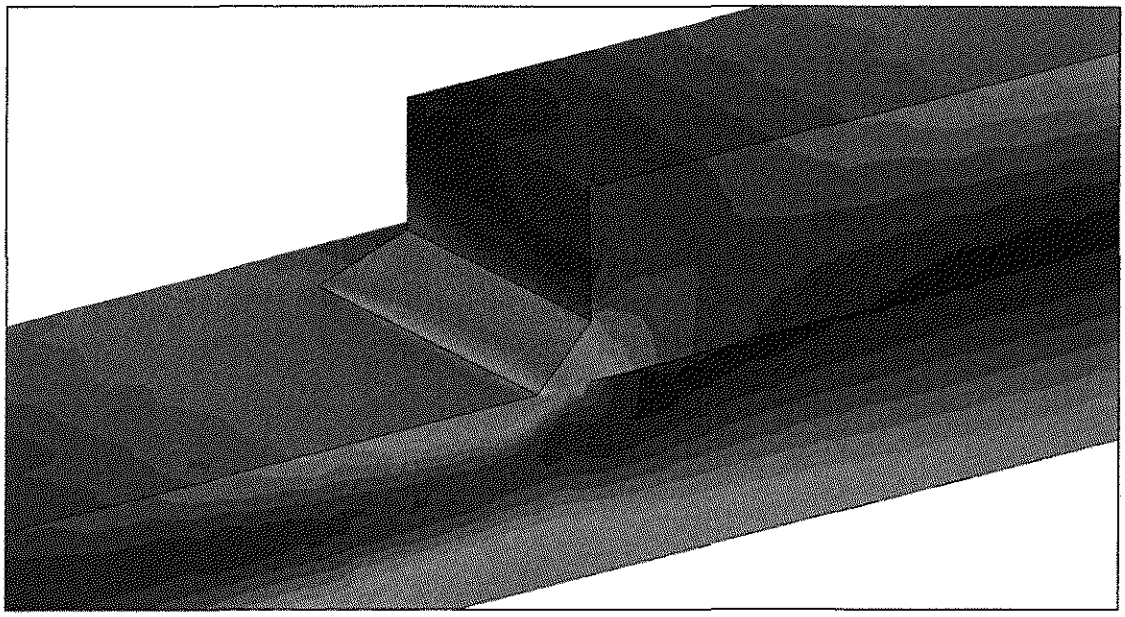

Figure 5.11. Cross-section at the weld showing Von Mises stresses for the pinned model.

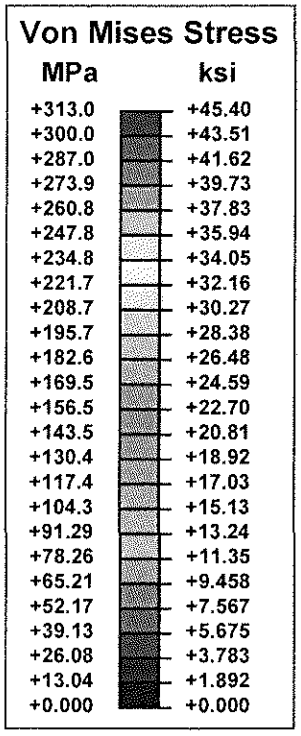

Figure 5.12. Contour legend for Figures 5.8 through 5.11

By comparing Figures 5.8 and 5.9, it was evident that differences in boundary conditions for the two bending models primarily affected the stresses in the end of the flange and in the transverse weld region. The coverplated portions of the models, away from the coverplate ends, appeared to have very similar Von Mises stresses at all locations. By comparing Figures 5.10 and 5.11, it was evident that the roller model had a larger and more intense area of stress concentration at the weld toe than did the pinned model. With the maximum load applied, the roller model had a relatively large area at a Von Mises stress of 313 MPa (45.4 ksi), indicating plastic yielding, while the pinned model did not reach the yield strength at any point. A possible explanation for this difference in behavior is discussed in section 5.3. Although figures showing the Von Mises stress contours under the minimum applied load are not shown, the stress contours for these models had patterns similar to those for the models subjected to the maximum applied load. The magnitudes of the Von Mises stresses for these models were approximately one tenth the magnitudes of the stresses for the models subjected to the maximum load. The largest Von Mises stress encountered under the minimum load occurred at the toe of the transverse weld for the roller model and had a value of approximately 45 MPa (6.5 ksi).

As evident from Figures 5.8 and 5.9, the Von Mises stresses in the flange were very different for the two models. Because Von Mises stresses do not differentiate between compression and tension, it was difficult to determine the cause of these differences in stress. Therefore, an alternate measure of stress had to be examined for both models to determine the reasons for these differences in Von Mises stress. The alternate measure of stress and the probable causes of the differences in stress in the ends of the flange are discussed in section 5.3.2.

5.2.2. Model Comparison to Experimental and Theoretical Stresses

To compare the results of the two finite element models to the experimentally determined stress ranges and the theoretical stress ranges, stresses parallel to the

longitudinal axis (axis one in Figure 5.2) of the specimen had to be recorded at the surfaces of the two models. Stresses in the direction of axis one, labeled "S11 stresses" had to be recorded for the models because this was the direction in which the strain gages measured strains on the fatigue specimens. This was also the direction in which the theoretically calculated stresses acted.

To record S11 stresses for each bending model, the contours of the model were set to indicate S11 stresses. A path was then drawn along the centerline of the top of the model and another path was drawn along the centerline of the bottom of the model. Along each of these paths, S11 stresses at the intersections of the path with the element edges were recorded. At each intersection, the un-deflected position along axis one (from the free edge of the flange) was recorded as the independent variable and the S11 stress was recorded as the dependent variable. S11 stresses are shown for the models subjected to the maximum load in Figures 5.13 and 5.14 for the roller and pinned models, respectively. Figures 5.15 and 5.16 show the stress contours on the outside surface of the flange for the roller and pinned models, respectively. In these figures, black dashed lines show the surface paths along which S11 stresses were recorded. The legend for these figures is shown in Figure 5.17.

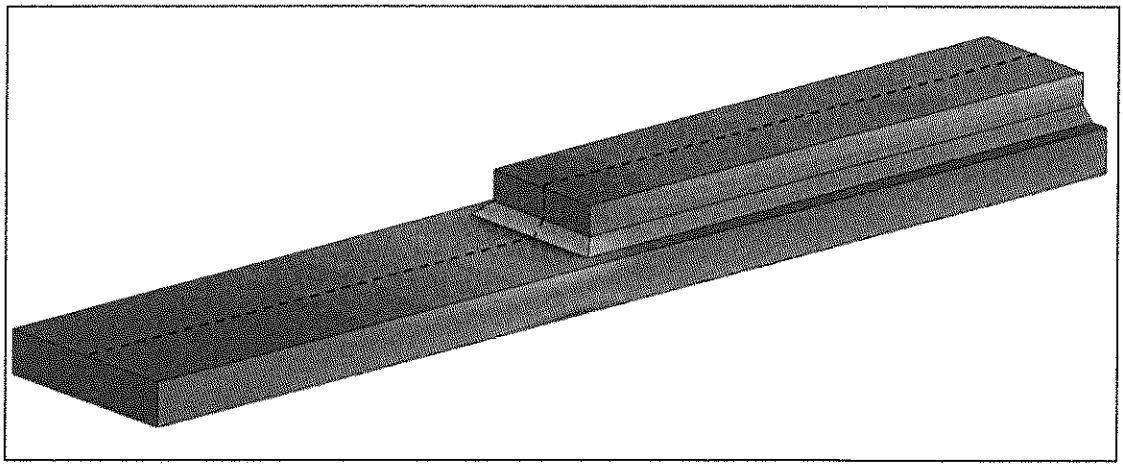

Figure 5.13. S11 stresses for the roller model at maximum load.

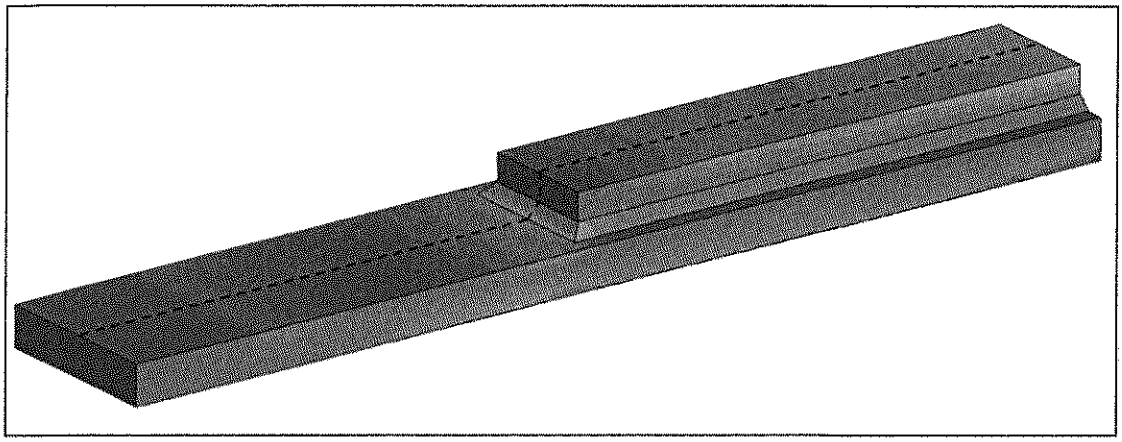

Figure 5.14. S11 stresses for the pinned model at maximum load.

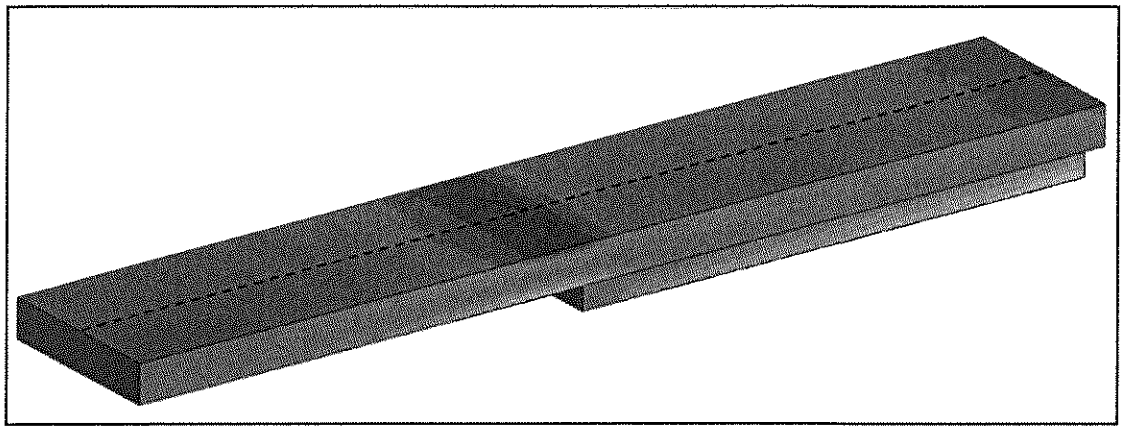

Figure 5.15. S11 stresses on the flange surface for the roller model at maximum load.

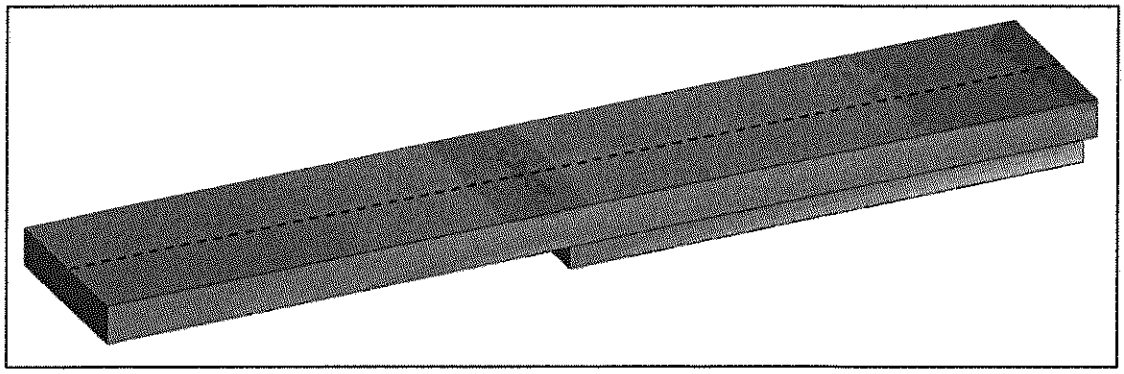

Figure 5.16. S11 stresses on the flange surface for the pinned model at maximum load.

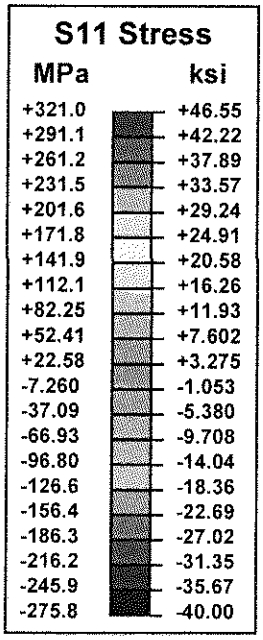

Figure 5.17. Contour legend for Figures 5.13 through 5.16

S11 stresses under the minimum applied load are not shown for either model. S11 stress ranges along the paths shown in Figures 5.13 through 5.16 were calculated by subtracting the S11 stresses for the model subjected to the minimum load from the S11 stresses for the model subjected to the maximum load. The S11 stress ranges along each path were then compared to each other, the theoretical stress range, and the experimentally determined stress ranges by plotting all data using Microsoft Excel. These plots are shown in Figures 5.18 and 5.19. Figure 5.18 shows all stresses along the centerline of the coverplated side of the flange. Figure 5.19 shows all stresses along the centerline of the face of the flange without the coverplate. The average strain gage stresses shown in these figures were determined using the results of Tables 4.3 and 4.4. Key points on the curves shown in Figures 5.18 and 5.19 are summarized in Tables 5.1 and 5.2, respectively. These tables show the stress range calculated by each of the four methods at every strain gage location. The percent differences listed in these tables are with respect to the theoretical stresses.

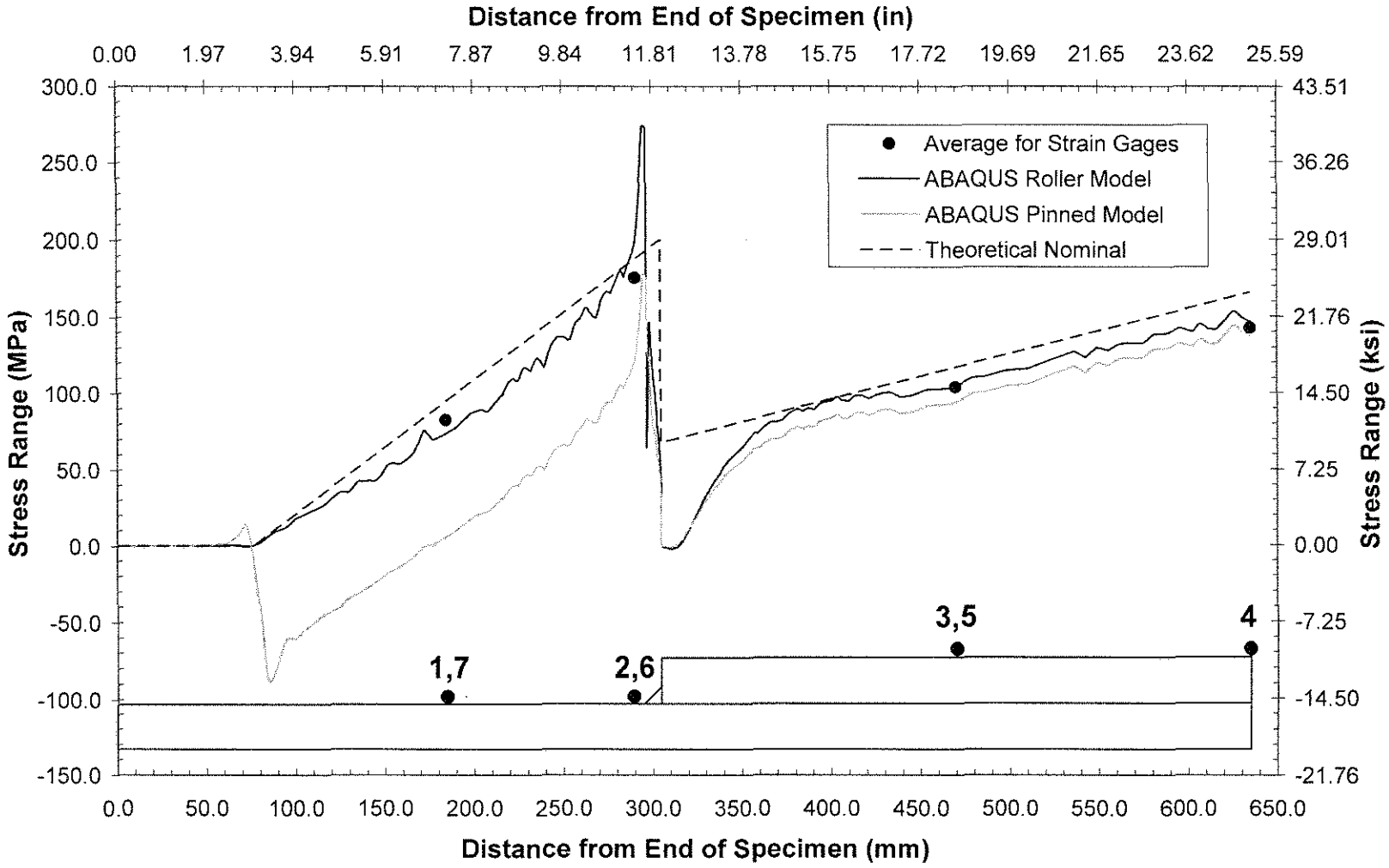

Figure 5.18. Stress range along upper surface of specimen, determined by ABAQUS models, strain gages, and theory.

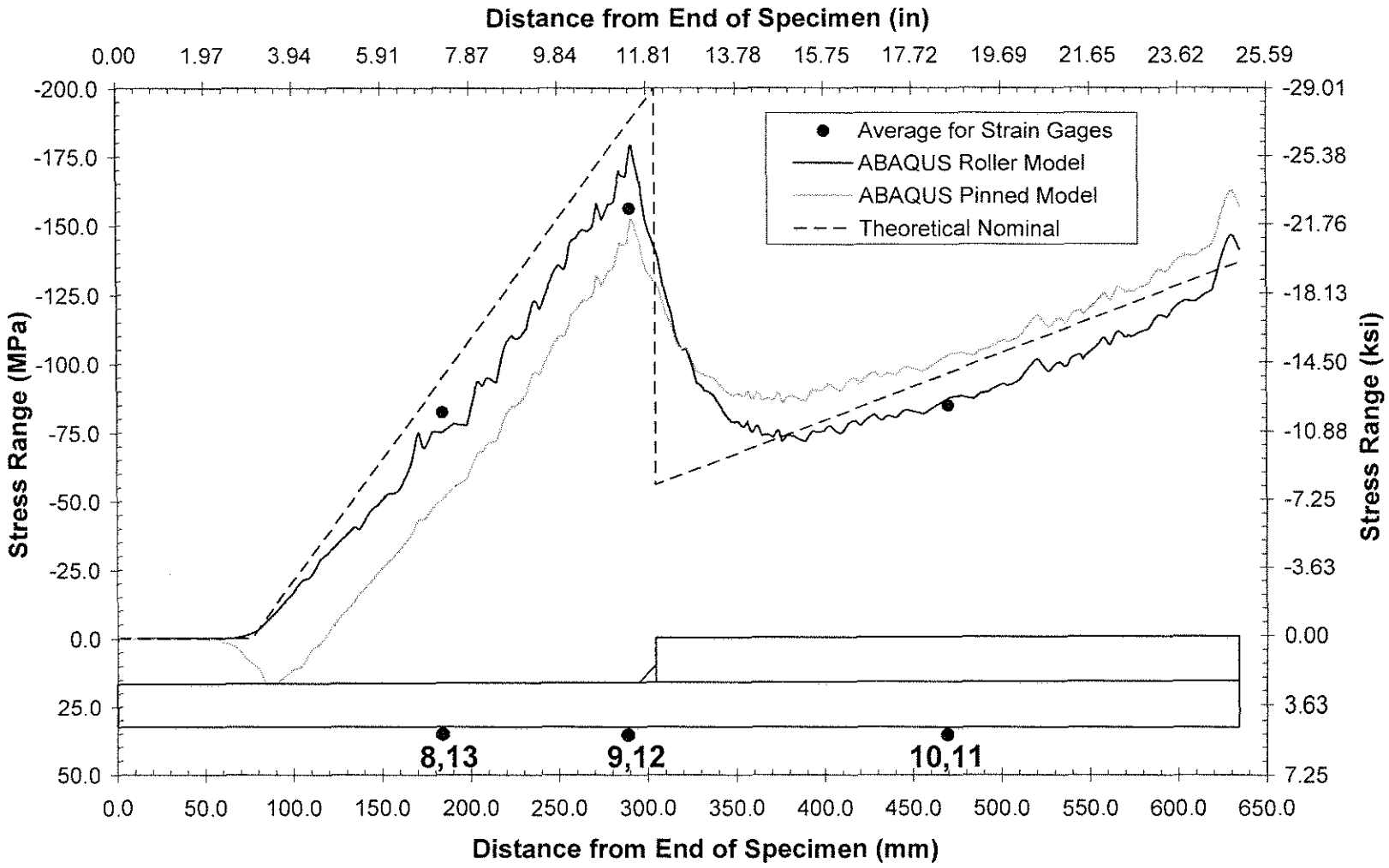

Figure 5.19. Stress range along lower surface of specimen, determined by ABAQUS models, strain gages, and theory.

Table 5.1. Summary of calculated stress ranges at strain gage locations.

	Strain Gage Location			
	1,7	**2,6**	**3,5**	**4**
Distance from End of Specimen, mm (in)	184 (7.25)	290.5 (11.44)	469.9 (18.50)	635.0 (25.00)
Theoretical Stress Range, MPa (ksi)	94.44 (13.70)	187.5 (27.19)	116.7 (16.92)	165.6 (24.02)
Experimentally Determined Stress Range, MPa (ksi)	82.54 (11.97)	175.4 (25.43)	103.6 (15.03)	142.4 (20.65)
% Difference from Theory	**-12.60**	**-6.479**	**-11.21**	**-14.02**
Stress Determined from Roller Model, MPa (ksi)	73.61 (10.68)	198.1 (28.73)	104.5 (15.15)	146.7 (21.28)
% Difference from Theory	**-22.06**	**5.662**	**-10.47**	**-11.42**
Stress Determined from Pinned Model, MPa (ksi)	5.3 (0.77)	120.7 (17.50)	94.08 (13.64)	137.2 (19.90)
% Difference from Theory	**-94.41**	**-35.63**	**-19.37**	**-17.14**

Table 5.2. Summary of calculated stress ranges at strain gage locations.

	Strain Gage Location		
	8,13	**9,12**	**10,11**
Distance from End of Specimen, mm (in)	184 (-7.25)	290.5 (-11.44)	469.9 (-18.50)
Theoretical Stress Range, MPa (ksi)	-94.44 (-13.70)	-187.5 (-27.19)	-95.97 (-13.92)
Experimentally Determined Stress Range, MPa (ksi)	-82.23 (-11.93)	-156.0 (-22.62)	-84.37 (-12.24)
% Difference from Theory	**-12.93**	**-16.83**	**-12.09**
Stress Determined from Roller Model, MPa (ksi)	-75.24 (-10.91)	-168.4 (-24.42)	-85.35 (-12.38)
% Difference from Theory	**-20.34**	**-10.20**	**-11.07**
Stress Determined from Pinned Model, MPa (ksi)	-50.5 (-7.32)	-143.9 (-20.87)	-101.0 (-14.64)
% Difference from Theory	**-46.53**	**-23.26**	**5.203**

By examining Figures 5.18 and 5.19, it is evident that the stresses calculated for the roller model were lower than the theoretical nominal stresses along the entire length of the specimen except near the transverse weld. The stresses calculated for the pinned model were lower than the theoretical nominal stresses as well as the roller model stresses everywhere along the length of the specimen with the exception of the bottom of the flange in the coverplated region. In this region, the stresses calculated for the pinned model were larger than the stresses calculated for the roller model as well as the theoretical stresses. The specific differences in stress for both models at strain gage locations are shown in Tables 5.1 and 5.2.

The fact that stresses calculated by both models were generally lower than theoretical stresses may explain why the stresses determined experimentally using strain gage data were lower than the theoretical stresses. Assuming the behavior of the specimens was accurately simulated by either bending model (or an alternate model with intermediate boundary conditions between the two models), the specimens would not have been expected to achieve the theoretical stresses.

Because the stress ranges measured by the roller model and the strain gages were very similar (see Tables 5.3 and 5.4) and generally lower than the theoretical stress ranges, it was determined that the theoretically calculated stress ranges were errant. Obviously, one or more of the assumptions used when calculating the theoretical stresses was incorrect. Some assumptions made when calculating the theoretical stresses included: (1) material behavior was linear-elastic, (2) plane sections remained plane, (3) pure bending stresses were the only stresses induced in the specimens, and (4) supports were perfectly frictionless. Obviously, the actual supports had an unknown amount of friction present (thought to be small as will be discussed in section 5.3). However, support friction was not included in the roller model, and this model had stress ranges systematically lower than theoretically

stresses. Therefore, the assumption that the supports were frictionless likely did not cause the theoretical stresses to be errant.

Each of the other three assumptions listed previously made have deviated from the actual characteristics of the models and specimens. Obviously, the assumption that the material was linear-elastic was untrue. As shown in Figure 5.10, a region of plastic deformation occurred at the weld toe of the roller model. Plastic deformation also likely occurred at the weld toes in the specimens. However, it cannot be stated with certainty what effect, if any, this plastic deformation had on the stress distribution. In the coverplated region of the specimens (or models), plane sections may not have remained entirely plane due to the discontinuity of the cross section at the flange-coverplate interface. The assumption that the specimens (or models) were in pure bending may not have been true near the transverse weld region due to concentration of stress in the weld. The aggregate affects of these small deviations from the assumptions, although not easily quantifiable, likely caused the theoretically calculated stresses to differ from those calculated by the finite element models and the strain gages.

Lastly, the 5% difference in load range applied to the specimens compared to theoretical load range (see section 4.1.1) was likely not the cause of the differences in stresses between the specimens and theory. This is because both bending models had the theoretical loads applied, and these models showed systematically lower stress ranges compared to theoretical stress ranges.

5.3 Roller Model Behavior versus Pinned Model Behavior

5.3.1 Determination of Bending frame friction characteristics

To determine the frictional characteristics between the fatigue specimens and the three-point-bending frame, the stress range curves for the roller and pinned models shown in Figures 5.18 and 5.19 were compared to the average stress ranges calculated for each of the strain gage locations. As shown by these figures, the

average experimental stress range calculated for four of the seven strain gage locations was between the roller curve and the pinned curve. The other three average experimental stress ranges that were not between the two curves were all closer to the roller curve than the pinned curve. These observations suggest that contact between the specimen and the bending frame was between perfectly frictionless and perfectly pinned, but the behavior was much more closely simulated by the perfectly frictionless model. This claim is also supported by the data shown in Tables 5.3 and 5.4.

Table 5.3. Comparison of model stresses to strain gage stresses for gages 1 through 7.

	Strain Gage Location			
	1,7	**2,6**	**3,5**	**4**
Distance from End of Specimen, mm (in.)	184.2 (7.25)	290.5 (11.44)	469.9 (18.50)	635.0 (25.00)
Experimentally Determined Stress Range, MPa (ksi)	82.54 (11.97)	175.4 (25.43)	103.6 (15.03)	142.4 (20.65)
Stress Determined from Roller Model, MPa (ksi)	73.61 (10.68)	198.1 (28.73)	104.5 (15.15)	146.7 (21.28)
% Difference from Experimental	**-10.82**	**12.98**	**0.83**	**3.02**
Stress Determined from Pinned Model, MPa (ksi)	5.3 (0.77)	120.7 (17.50)	94.08 (13.64)	137.2 (19.90)
% Difference from Experimental	**-93.61**	**-31.17**	**-9.19**	**-3.63**

Table 5.4. Comparison of model stresses to strain gage stresses for gages 8 through 13.

	Strain Gage Location					
	8,13		**9,12**		**10,11**	
Distance from End of Specimen, mm (in.)	184	(-7.25)	290.5	(-11.44)	469.9	(-18.50)
Experimentally Determined Stress Range, MPa (ksi)	-82.23	(-11.93)	-156.0	(-22.62)	-84.37	(-12.24)
Stress Determined from Roller Model, MPa (ksi)	-75.24	(-10.91)	-168.4	(-24.42)	-85.35	(-12.38)
% Difference from Experimental	**-8.506**		**7.965**		**1.163**	
Stress Determined from Pinned Model, MPa (ksi)	-50.5	(-7.32)	-143.9	(-20.87)	-101.0	(-14.64)
% Difference from Experimental	**-38.59**		**-7.731**		**19.67**	

Similar to Tables 5.1 and 5.2, these tables show the stress ranges calculated by the roller and the pinned models at every gage location, in addition to the stresses determined using strain gage data. Tables 5.3 and 5.4 differ from Tables 5.1 and 5.2 in that the percent differences listed for the roller and pinned models are with respect to the experimentally determined stresses rather than the theoretical stresses. Therefore, the percent differences listed in Tables 5.3 and 5.3 offer a means to quantitatively compare the roller and pinned model curves to the experimental data. These tables show that at six of the seven strain gage locations, the absolute percent difference for the roller model was smaller than the absolute percent difference for the pinned model. The other strain gage location (location 9,12) had essentially the same absolute percent difference for both models. Because Tables 5.3 and 5.4 are simply numerical interpretations of Figures 5.18 and 5.19, the data presented by these

tables also support the argument that the roller model more accurately simulated specimen behavior.

Another means by which the frictional behavior between the specimens and the bending frame was compared was through the analysis of deflection data. In addition to the S11 stresses, deflections parallel to axis three shown in Figure 5.2 were recorded along the paths shown in Figures 5.13 through 5.16 for both bending models. As expected, the deflections of the top surface and bottom surface of each model were very nearly identical. Therefore, only the deflections on the side of the model with the coverplate were recorded.

Ideally, the deflections of the bending models would have been compared to the deflections of the specimens at multiple locations along the length of a specimen. However, deflection data at multiple locations was not recorded when the specimens were subjected to a nominal weld toe stress range of 193 MPa (28.0 ksi). Therefore, the only deflection data recorded at a stress range of 193 MPa (28.0 ksi) was the range of movement of the actuator measured by the testing machine's internal LVDT. This deflection, with an adjustment, was equal to the deflection of the specimen flange at the point of contact with the bending frame relative to the center of the specimen. The adjustment accounted for the deflection of the tube comprising the lower half of the bending frame under the applied load range. Using RISA-3D version 6.0 structural design software, the deflection of the tube at the point of contact with the specimen relative to the middle of the tube was found to be 0.457 mm (0.018 in). The output data from the RISA-3D analysis is shown in Appendix F.

By averaging all differences in position recorded by the controller for specimens tested at a stress range of 193 MPa (28.0 ksi), the average range of movement of the actuator was determined to be 4.70 mm (0.185 in). By subtracting the deflection of the tube from the average range of movement of the actuator, the deflection of the flange at the point of load application with respect to the center of

the specimen was determined to be 4.24 mm (0.167 in). This deflection, and the deflections of the bending models are plotted in Figure 5.20. At the point of load application, the deflection of the roller model was 4.45 mm (0.175 in) and the deflection of the pinned model was 3.91 mm (0.154 in). The roller and bending model deflections were 4.79 % different and -7.78 % different than the deflection of the specimens, respectively.

Figure 5.20 shows that the deflection of the specimens was found to be less than that of the roller model and greater than that of the pinned model, suggesting that the behavior of the specimens was somewhere between perfectly frictionless and perfectly pinned. The lower percent difference between the roller model and the specimen deflection supports the conclusion that the roller model more accurately simulated the behavior of the specimens than the pinned model. Considering the results of the stress comparison as well as the deflection comparison, it was determined that the contact between the three-point-bending frame and the specimen flanges was between perfectly frictionless and perfectly pinned. The data suggest that the contact was much closer to being perfectly frictionless than perfectly pinned, but some friction did occur.

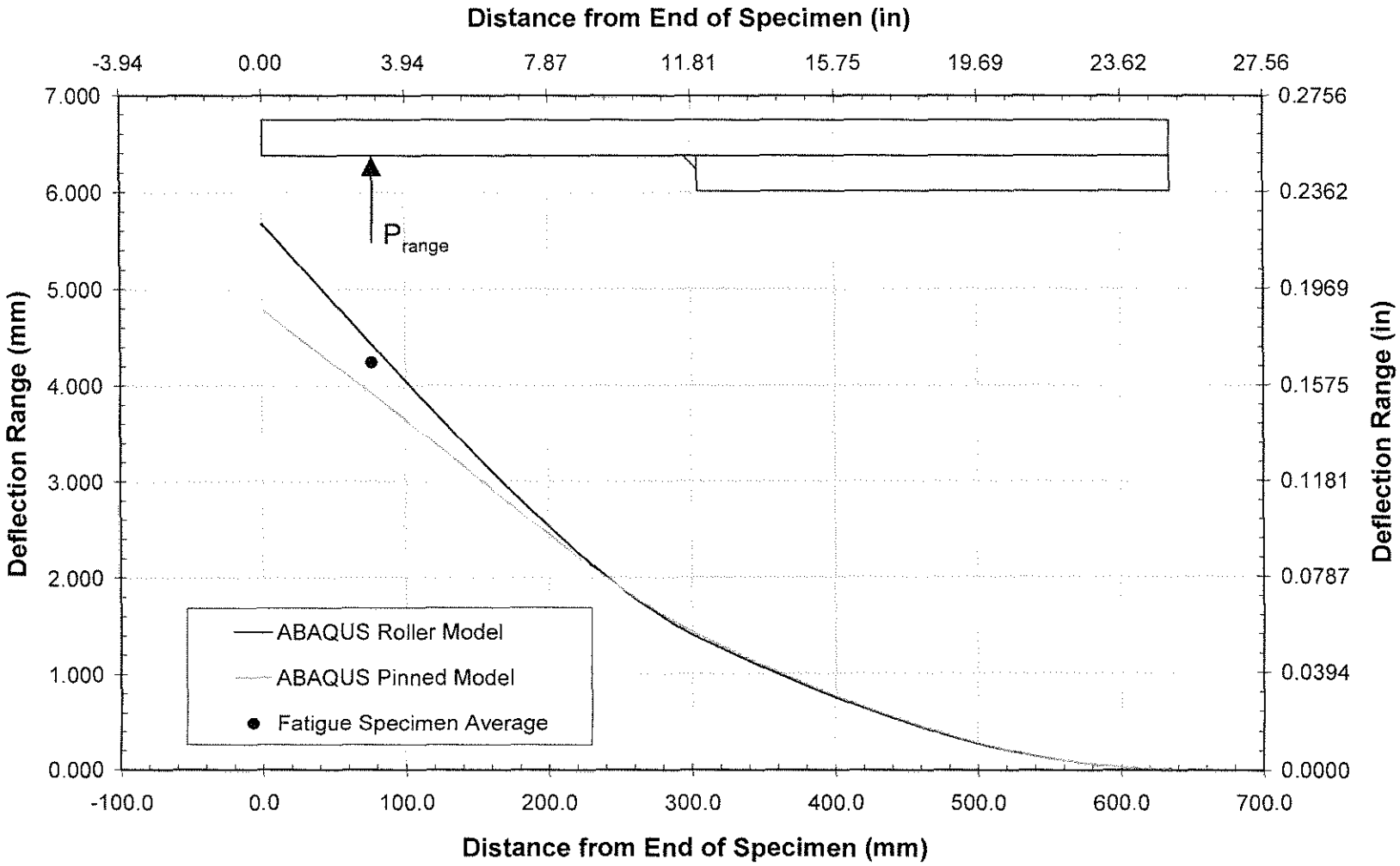

Figure 5.20. Deflections of the bending models and fatigue specimens.

5.3.2. Differences in Roller and Pinned Model Behavior

The cause of the differences in stress range calculated for the roller model and the pinned model can be explained by examining the S11 stresses ranges shown in Figure 5.18 and 5.19 and the longitudinal deflections of the roller model shown in Figure 5.21. Figure 5.21 shows an exaggerated profile of the deflected shape of the roller model with longitudinal deflection contours mapped on the profile. Longitudinal deflections were equivalent to deflections parallel to axis one shown in Figure 5.2. A positive longitudinal deflection corresponded to a deflection toward the free end of the flange.

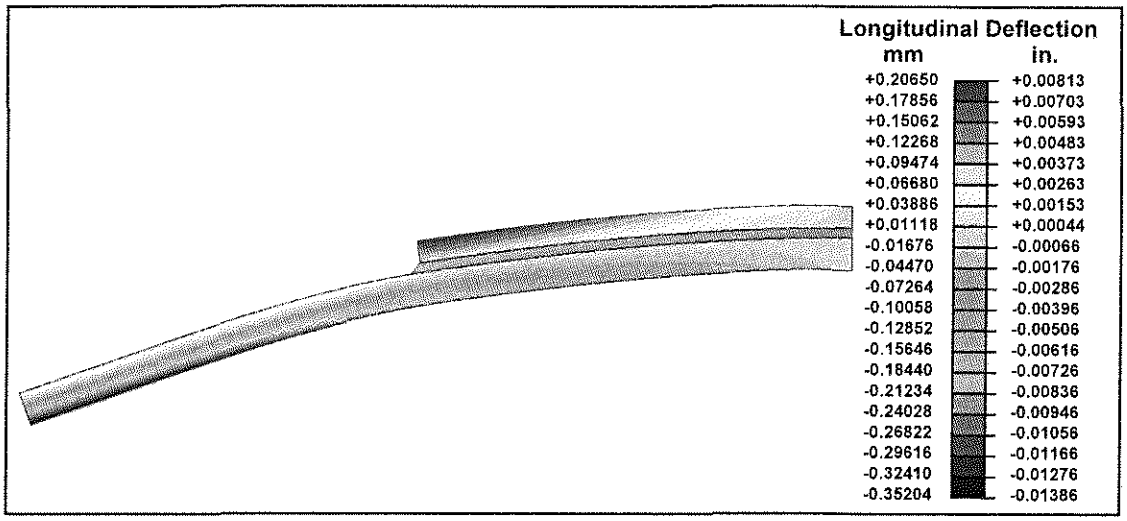

Figure 5.21. Longitudinal deflection of roller model.

As shown in Figure 5.21, the side of the flange to which the load was applied (the top side of the flange shown in Figure 5.20) deflected outward toward the free end of the flange for the roller model. The opposite side of the flange (the bottom side of the flange shown in Figure 5.20) deflected inward away from the free end of the flange for the roller model.

Because the pinned model was restrained from deflecting longitudinally at the point of load application, axial forces were developed in the flange to restrain the deflection. On the side of the flange to which the load was applied, a compressive force was induced in the pinned model to restrain the positive longitudinal displacement. This axial compressive force reduced the tensile bending stresses near this face (coverplate side) of the flange. This behavior is very clearly shown for the pinned model in Figure 5.18. Near the point of load application, where the theoretical tensile bending stress ranges were low, the compressive axial restraining force caused the stresses to be compressive for the pinned model. The relatively constant shift in the curves for the pinned model with respect to the curve for the roller model suggests that the compressive axial restraining force caused a constant reduction in tensile bending stress range at this face of the flange. By examining Figure 5.18, it was determined that the constant reduction in tensile bending stress range at this face was approximately 100 MPa (14.5 ksi). The reduction in the tensile stress range along the entire face of the flange is likely what also caused the reduction in stress concentration at the weld toe of the pinned model compared to the roller model.

On the side of the flange opposite of which load was applied, a tensile force was induced in the pinned model to restrain the negative longitudinal displacement. This axial tensile force reduced the compressive bending stresses near this face (non-coverplated side) of the flange. As shown in Figure 5.19, this axial tensile force caused a relatively constant shift in the curve for the pinned model with respect to the roller model. This indicates that the tensile force caused a constant decrease in the compressive stress range at this face of the flange. By examining the moment curve for the pinned model near the point of load application, it was estimated that the axial tensile restraining forced reduced the compressive stress at the face of the flange by approximately 25.0 MPa (3.63 ksi).

The absolute magnitude of the latter restraining stress was roughly 25% of the restraining stress on the opposite face of the flange of 100 MPa (14.5 ksi). This difference was due to way in which the model was restrained. To accurately simulate the friction between the specimens and the loading frame, the pinned model was restrained in the direction of axis one at the point of load application on the coverplated face of the flange only. The coverplated side of the flange was truly restrained, and thus developed large restraining stresses. The opposite (non-coverplated) face of the flange was not restrained at the point of load application. Therefore, the non-coverplated side of the flange was only partially restrained due to the restraint applied to the opposite face and could deflect longitudinally under load. The longitudinal deflection at the point of load application on this face of the flange did not allow a restraining stress larger than 25.0 MPa (3.63 ksi) to be developed.

5.4 Changes in State-of-Stress Resulting from Pretension Forces

Because the effectiveness of coverplate bolting was highly dependent on whether the stresses induced in the transverse weld were compressive or tensile, Von Mises stresses were not examined when analyzing the bolted model. Rather, the maximum principle stress and stress direction were used to determine the effects of coverplate bolting. The induced maximum principal stresses resulting from the application of pressure forces simulating bolt pretension are shown at the weld toe of the bolted specimen in Figure 5.22. This model had been sectioned at the centerline to show the internal maximum principal stresses.

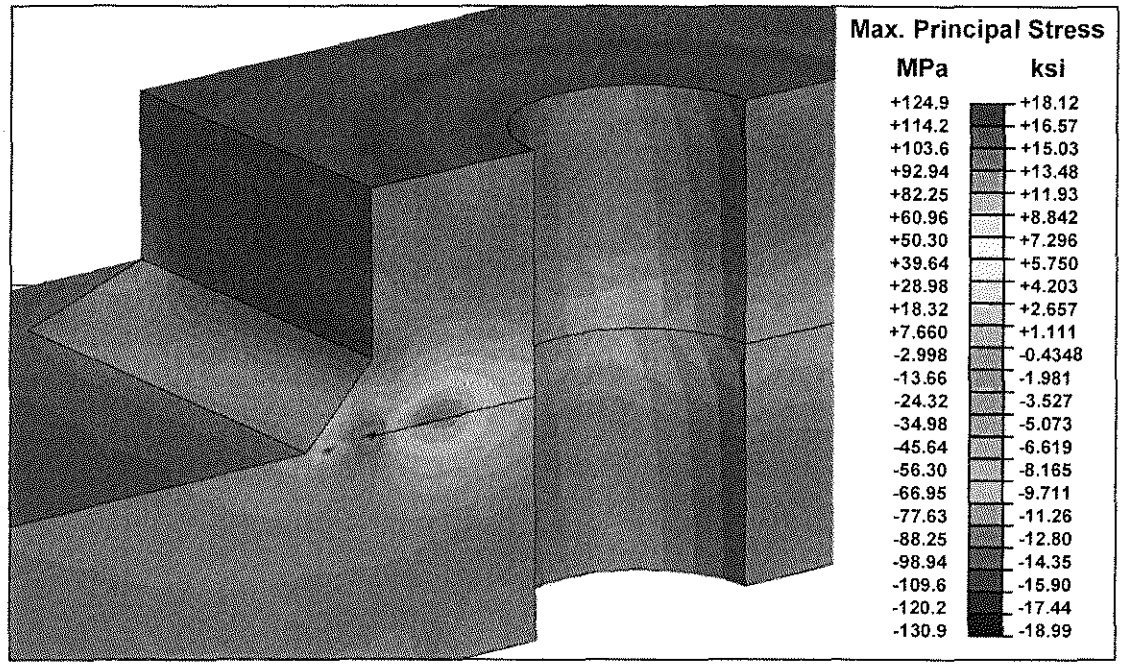

Figure 5.22. Maximum principal stresses resulting from bolt pretension.

As shown in Figure 5.22, the surface of the transverse fillet weld had a tensile principal stress resulting from the application of the pretension forces. The magnitude of this principal stress at the surface of the specimen near the middle of the transverse weld was approximately 55 MPa (8.0 ksi). Upon close examination of the surface of the transverse weld in Figure 5.22, it was noticed that the throat of the weld was slightly more stressed than the weld toe at the center of the weld. Also, the end of the transverse weld seems to be more highly stressed than the middle. This is evident from the very small orange colored region near the end of the weld toe in Figure 5.22 as well as the larger orange colored region where the transverse weld meets the corner of the coverplate in Figure 5.22. These last observations may explain why many of the fatigue cracks in the specimens having bolts (bolted and combination specimens) developed fatigue cracks near the ends of the transverse weld rather than in the center. At the areas near the ends of the transverse welds just discussed, maximum principal tensile stresses of approximately 82.7 MPa (12.0 ksi)

were induced by the addition of the coverplate bolt. These stresses are larger than the maximum principal tensile stress induced at the center of the weld and, thus, may have led to cracks forming near the ends of the transverse welds rather than the centers.

The directions with which the maximum principal tensile stresses at the center of the surface of the transverse weld acted are shown in Figure 5.23. The lengths of the vectors, as well as the sizes of the arrows, illustrate the relative magnitudes of the principal stresses near the center of the weld. As shown in this figure, the maximum principal stresses near the center of the weld acted in a direction nearly parallel to axis three shown in Figure 5.2.

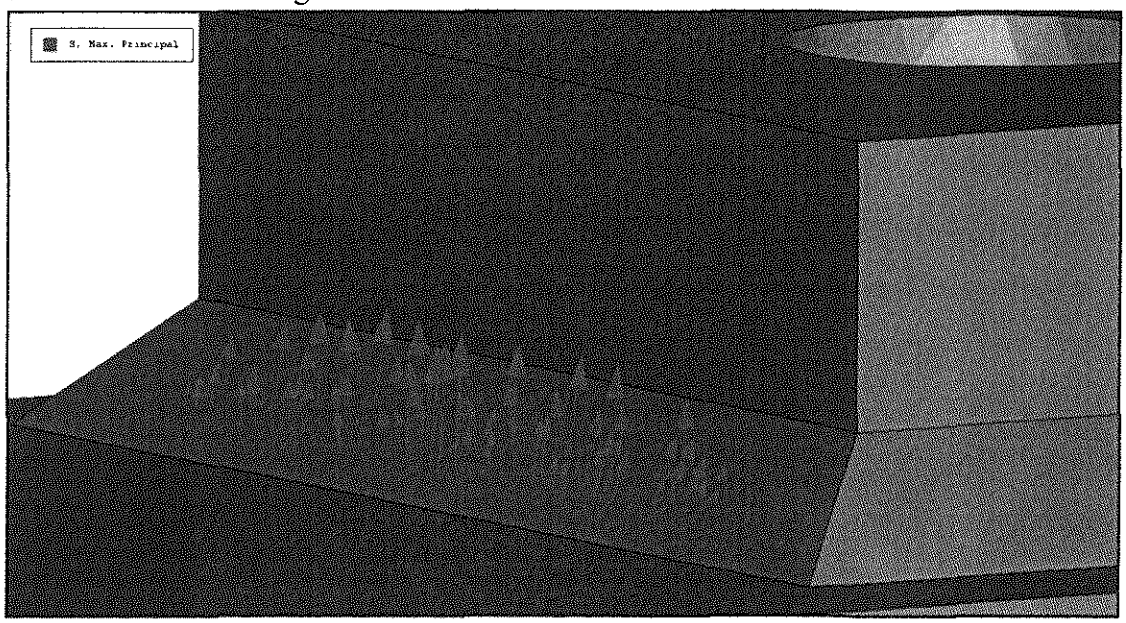

Figure 5.23. Maximum principal stress vectors near the center of the weld toe.

Because maximum principal stresses in the transverse weld were found to be tensile, and because these stresses acted in the direction shown in Figure 5.23, it was determined that the addition of coverplate bolts to the fatigue specimens had a detrimental effect on the state of stress in and near the transverse weld. The additional residual tensile stress in the transverse welds of the specimens as a result of

coverplate bolting may explain why the combination specimens had a shorter average fatigue life than that of the UIT-treated specimens. As discussed in Chapter 4, the difference in fatigue life between the bolted specimens and the control specimens was not clearly indicated because of the short fatigue lives of both of these specimen types. The bolted finite element model suggests that if the control specimens and bolted specimens were tested at a lower stress range, a noticeable difference in fatigue life between the two specimen types would have become apparent.

CHAPTER 6 CONCLUSIONS AND RECOMMENDATIONS

6.1 CONCLUSIONS

6.1.1 Fatigue Life

By comparing the lives of fatigue specimens, it was concluded that treatment of the transverse weld toes with UIT was very effective at enhancing the fatigue lives of the specimens, while adding pretensioned bolts to the ends of the coverplates was not effective (and perhaps damaging) at enhancing the fatigue lives of the specimens. The average fatigue life of specimens treated with UIT and tested at a nominal weld toe stress range of 193 MPa (28.0 ksi) was approximately 25 times longer than the average fatigue life of untreated control specimens. Both control specimens tested at a weld toe stress range of 193 MPa (28.0 ksi) achieved AASHTO Category E detail classification, while both UIT-treated specimens tested at the same stress range outperformed AASHTO Category A detail requirements. Thus, treatment with UIT caused an improvement of six AASHTO fatigue categories.

The average fatigue life for bolted specimens was nearly identical to the average fatigue life for control specimens tested at a weld toe stress range of 193 MPa (28.0 ksi). All control and bolted specimens tested at a weld toe stress range of 193 MPa (28.0 ksi) achieved AASHTO Category E detail classification. Therefore, adding pretensioned bolts to the ends of the coverplates had no effect on the fatigue lives of otherwise untreated specimens. The average fatigue life for combination specimens was 41% lower than the average fatigue life for UIT-treated specimens tested at a weld toe stress range of 193 MPa (28.0 ksi). While all UIT-treated specimens surpassed AASHTO Category A requirements, two of the combination specimens achieved Category B classification while the third combination specimen outperformed Category A detail requirements. Therefore, majority of combination specimens performed one AASHTO fatigue category worse than both UIT-treated specimens tested at a weld toe stress range of 193 MPa (28.0 ksi). These findings

demonstrated that adding pretensioned bolts to the ends of the coverplates had a detrimental effect on the fatigue lives of combination specimens.

Reasons as to why bolted specimens showed no improvement over control specimens and combination specimens showed less improvement that UIT-treated specimens were determined by performing a finite element analysis. From the finite element analysis, it was concluded that tensile stresses, rather than compressive stresses, were induced in the transverse welds as a result of the bolt pretension forces. The addition of tensile stresses to the transverse welds likely caused the bolted and combination specimens to perform equal to or worse than the control and UIT-treated specimens, respectively.

6.1.2 Crack Initiation and Propagation Behavior

All specimens not treated with UIT (control and bolted specimens) developed fatigue cracks at the toes of the transverse welds. In these specimens, cracks initiated at either the center or one of the ends of the transverse weld toe and propagated into the flange in a direction orthogonal to the longitudinal axis of the specimen. Once a crack had initiated in these specimens, the crack growth rate increased exponentially until yielding of the reduced flange section caused failure.

All specimens treated with UIT (UIT and combination specimens) exhibited surface cracks in the transverse weld throat near one end of the transverse weld. On the surface, these cracks propagated along the entire length of the transverse weld throat and into the flange. After a visual inspection, it could not be determined whether cracks in these specimens initiated at the surface of the weld throat or at the weld root. These specimens displayed crack propagation plateaus. At some point during propagation, the exponential crack growth rate would slow considerably. The fatigue crack would then propagate at a slow, constant rate.

6.1.3 Stress Range

Stress ranges along the specimen surfaces were calculated using data recorded from the array of strain gages and the modulus of elasticity determined by testing tensile coupons. The stress ranges at all strain gage locations differed from the theoretical stress ranges at corresponding locations by an average of -12%. All stresses measured experimentally by the strain gages, compressive and tensile, were smaller in magnitude than the corresponding theoretical stresses. However, the magnitudes of the experimentally determined stresses were validated by the results of two finite element analyses.

6.1.4 Crack Detection

During fatigue testing, it was concluded that the most effective method to detect the onset of fatigue crack initiation was the modified dye penetrant method. This method effectively detected the presence of a fatigue crack once it reached a surface length of approximately 1.6 mm (0.063 in). Other less-effective methods employed to detect the onset of fatigue crack initiation were the dynamic stiffness method, the static stiffness method, and strain gage method.

Each of these methods had shortcomings and proved to be less effective at detecting the onset of fatigue cracking than the modified dye penetrant method. Shortcomings in the dynamic stiffness crack detection method included: (1) a lag between visual crack detection and the onset of reduced dynamic stiffness and (2) inconsistency in recorded data, primarily large data shifts. Shortcomings in the static stiffness crack detection method included: (1) a lag between visual crack detection and the onset of reduced static stiffness and (2) a lack of precision in the recorded data. An attempt was also made to determine crack detection by analyzing strain gage data recorded during fatigue tests and static stiffness tests. Shortcomings in this crack detection method included: (1) varying strain behavior in response to crack

formation, (2) lack of sensitivity to crack initiation, and (3) subtlety in changing strain behavior at crack initiation.

6.1.5 Tensile Testing

Based on the results of tensile tests performed in accordance to ASTM test designation E 8, the yield strength of the A36 steel used to fabricate the fatigue specimens was determined to be 313 MPa (45.4 ksi). The tensile strength of the steel was determined to be 492 MPa (71.4 ksi). The elongation of the steel was determined to be 38.1% (51 mm (2.0 in.) gage length). These values of yield strength, tensile strength, and elongation were all greater than the specified minimums of 248 MPa (36.0 ksi), 400 MPa (58.0 ksi), and 21% (51mm (2.0 in) gage length), respectively. By examining the linear portions of stress-strain diagrams for the tensile specimens, the modulus of elasticity of the steel was determined to be 191,000 MPa (27,800 ksi). This value of modulus of elasticity was used to determine the stress ranges at the strain gages. The values of yield strength and modulus of elasticity determined from tensile testing were both used when performing finite element analyses.

6.1.6 Finite Element Analysis

By performing two finite element analyses of a fatigue specimen, it was concluded that the amount of friction between the fatigue specimens and the three-point-bending frame was an intermediate friction between perfectly frictionless (roller) and perfectly pinned. By examining stresses and deflections calculated for the finite element models, it was concluded that friction between the specimens and the bending frame was much closer to perfectly frictionless than perfectly pinned. These two models were also used to further investigate differences between experimental stresses measured by the array of strain gages and theoretical stresses. Because the resulting stress ranges calculated from both finite element models were less than the theoretical stress ranges, the fact that the experimental stress ranges were also lower than the theoretical stress ranges was acceptable, if not expected.

A third finite element analysis was performed to investigate the stresses induced in the weld toes of the specimens as a result of the pretension forces in the bolts. From this analysis, it was concluded that tensile stresses, rather than compressive stresses, were induced in the transverse welds as a result of the pretension forces. The addition of tensile stresses to the transverse welds likely caused the reduction in fatigue life displayed by the combination specimens.

6.2 RECOMMENDATIONS

Considering the results of the fatigue testing program, the application of Ultrasonic Impact Treatment to the toes of transverse fillet welds connecting coverplates to girder flanges is recommended as an effective preventative fatigue life enhancement method for this fatigue-prone detail. Because the mechanisms by which UIT enhances fatigue life are not specific to the geometry of coverplate end details, its use is also recommended for other girder details having fatigue-prone combinations of geometry and stress. The application of UIT to a fatigue-prone detail may improve the fatigue life of the treated detail by up to six AASHTO fatigue categories. However, UIT is not recommended as a fatigue crack repair method. Once a fatigue crack has initiated at a detail, treatment with UIT does not affect the parameters causing continued fatigue crack growth, namely applied stress range and crack geometry.

The proposed modified coverplate bolting procedure is much less effective than the AASHTO coverplate bolting procedure and is not recommended as an effective fatigue life enhancement retrofit for existing coverplate end details. Results of the fatigue testing program showed that adding pretensioned bolts without removing the transverse welds or end portions of the longitudinal welds had either no effect on the fatigue life of the transverse weld detail or a detrimental effect on the fatigue life of the transverse weld detail. However, the effectiveness of the modified coverplate bolting retrofit technique was specific to the geometry of the coverplate

end details. Therefore, the use of pretensioned bolts to enhance the fatigue lives of other common bridge girder details cannot be ruled out based on the findings of this research. Considering the detrimental effects on fatigue life caused by pretensioned bolts for this research program, it is recommended that the effectiveness of pretensioned bolts at enhancing the fatigue lives of other girder details be proven experimentally prior to being employed on existing structures.

Statnikov, E. (2005). "Improvement of quality and reliability of structures by means of UIT Esonix," *IIW Document XIII-2049-05*, International Institute of Welding, Paris, France.

Takamori, H., and Fisher, J.W. (2000). "Tests of large girders treated to enhance fatigue strength." *Transportation Research Record*, 1(1696), 93-99.

Verma, K.K., Statnikov, E.S., and Tehini, L. (2004). "Improving service life of steel bridges, light poles and sign structures through the use of ultrasonic impact treatment (UIT)." *Bridge Maintenance, Safety, Management, and Cost*, Proceedings of the Second International Conference on Bridge Maintenance, Safety, and Management, International Association for Bridge Maintenance and Safety, New York, NY, 443-444.

Vishay Micro-Measurements. (2005a). "Surface preparation for strain gage bonding." *Application Note B-129-8*, Vishay Micro-Measurements, Raleigh, NC.

Vishay Micro-Measurements. (2005b). "Strain gage installations with M-Bond 200 adhesive." *Instruction Bulletin B-127-12*, Vishay Micro-Measurements, Raleigh, NC.

Vishay Micro-Measurements. (2007a). "Strain gage selection: criteria, procedures, recommendation." *Tech Note TN-505-4*, Vishay Micro-Measurements, Raleigh, NC.

Vishay Micro-Measurements. (2007b). "Strain gages and accessories." *Micro-Measurements Product Catalog*, Vishay Micromeasurements, Raleigh, NC.

Vishay Micro-Measurements. (2007c). "Strain gage thermal output and gage factor variation in temperature." *Tech Note TN-504-1*, Vishay Micro-Measurements, Raleigh, NC.

Vishay Micro-Measurements. (2007d). "Strain gage soldering techniques." *Application Note TT-609*, Vishay Micro-Measurements, Raleigh, NC.

Wattar, F., Albrecht, P., and Sahli, A.H. (1985). "End-bolted cover plates." *Journal of Structural Engineering*, 111(6), 1235-1249.

Wright, W. (1996). "Post-weld treatment of a welded bridge girder by ultrasonic impact treatment." *Report*, Federal Highway Administration, September 29, 1996.

APPENDIX A DYNAMIC STIFFNESS PLOTS

This appendix displays plots of dynamic stiffness versus cycle for all fatigue specimens. Data used to calculate dynamic stiffness were measured by the testing machine's internal LVDT and load cell and recorded by the controller. All data were plotted using Microsoft Excel. To display subtle changes in dynamic stiffness as best as possible, each plot shows the narrowest range of dynamic stiffness that the data recorded for that specimen would allow. Therefore, caution must be taken when comparing changes in dynamic stiffness behavior from one plot to another as they may have different vertical scales. Plots are shown in Figures A.1 through A.17.

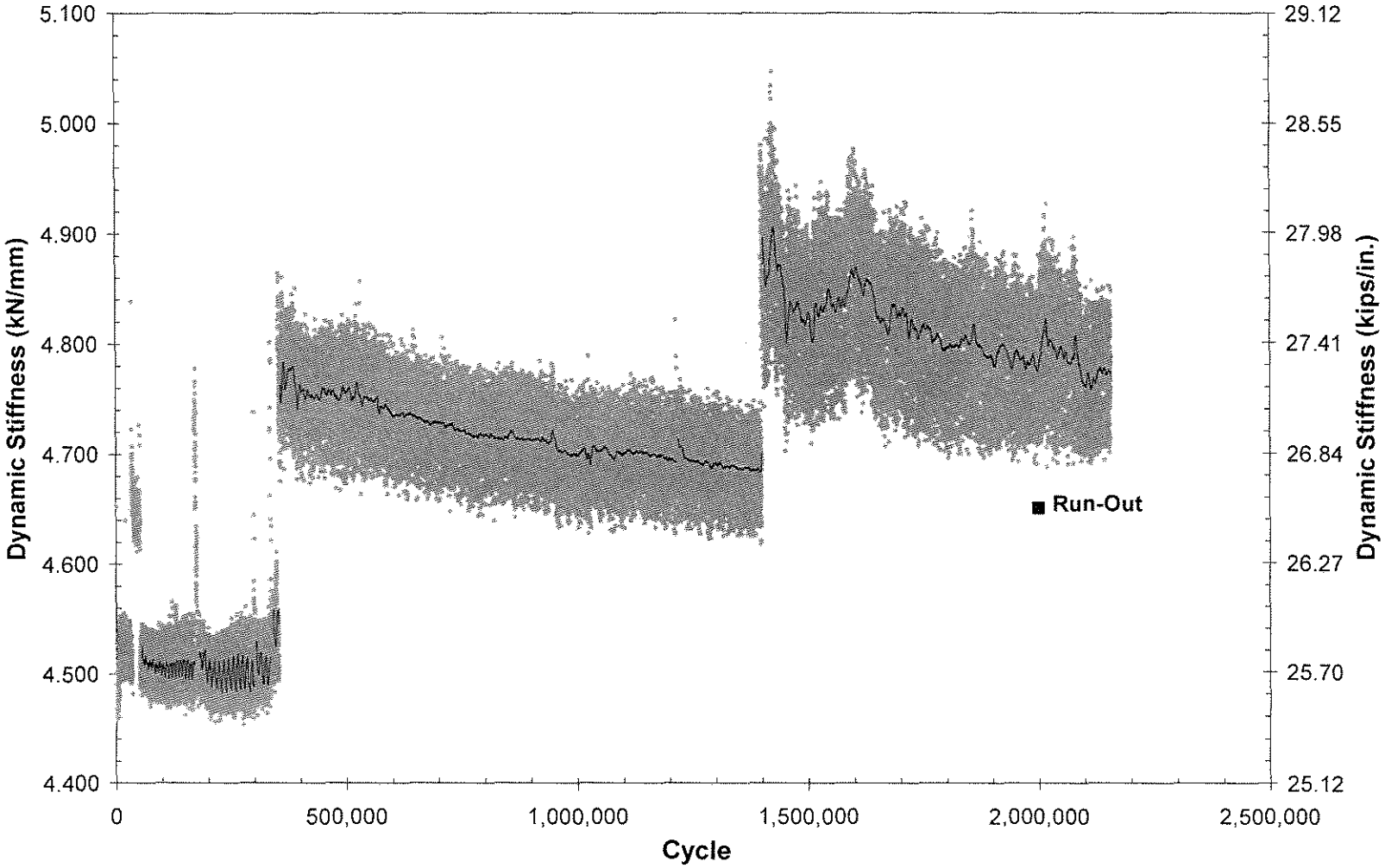

Figure A.1. Dynamic stiffness versus cycle for specimen CONTROL_01.

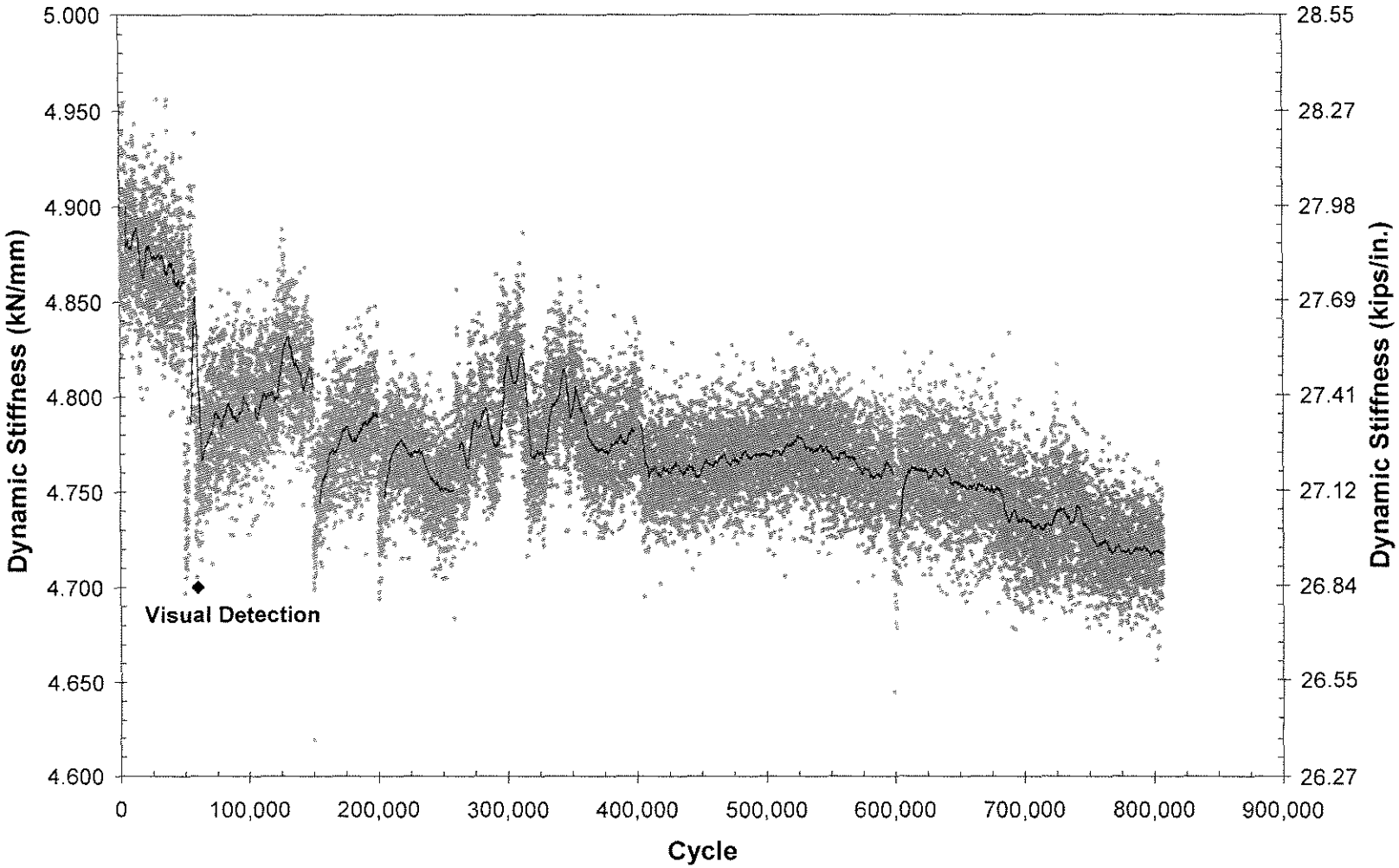

Figure A.2. Dynamic stiffness versus cycle for specimen CONTROL_01 (2).

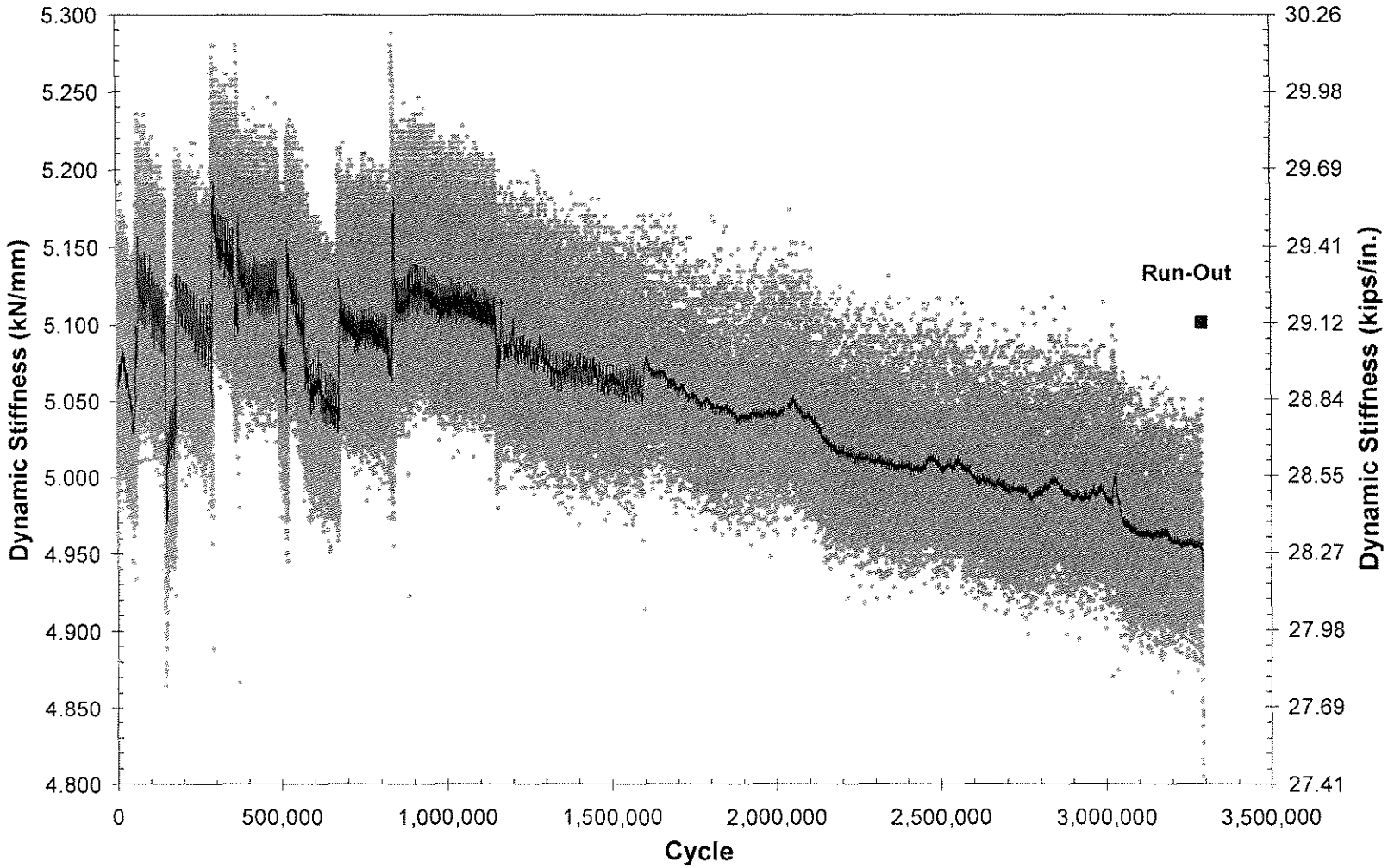

Figure A.3. Dynamic stiffness versus cycle for specimen CONTROL_02.

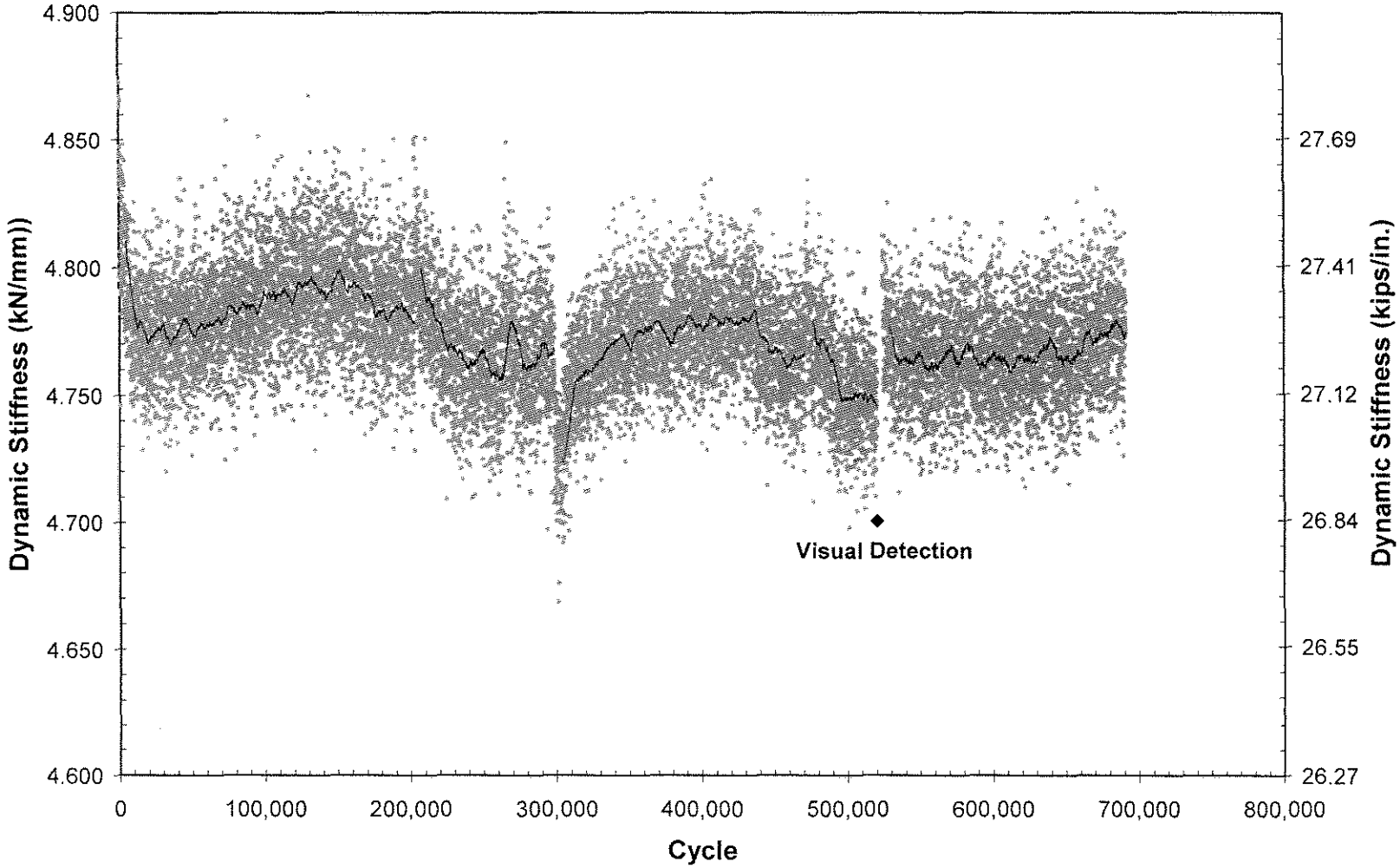

Figure A.4. Dynamic stiffness versus cycle for specimen CONTROL_02(2).

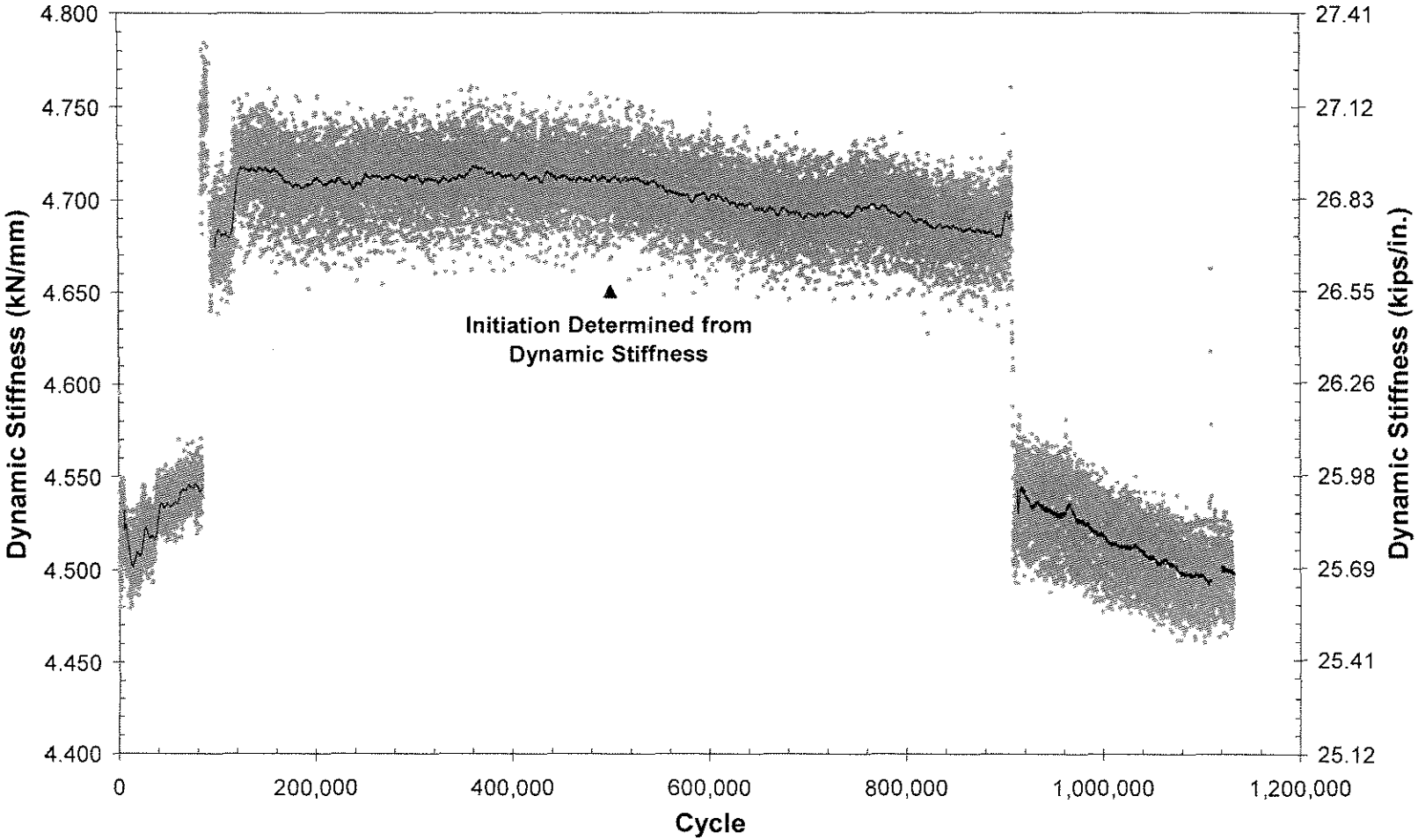

Figure A.5. Dynamic stiffness versus cycle for specimen CONTROL_03.

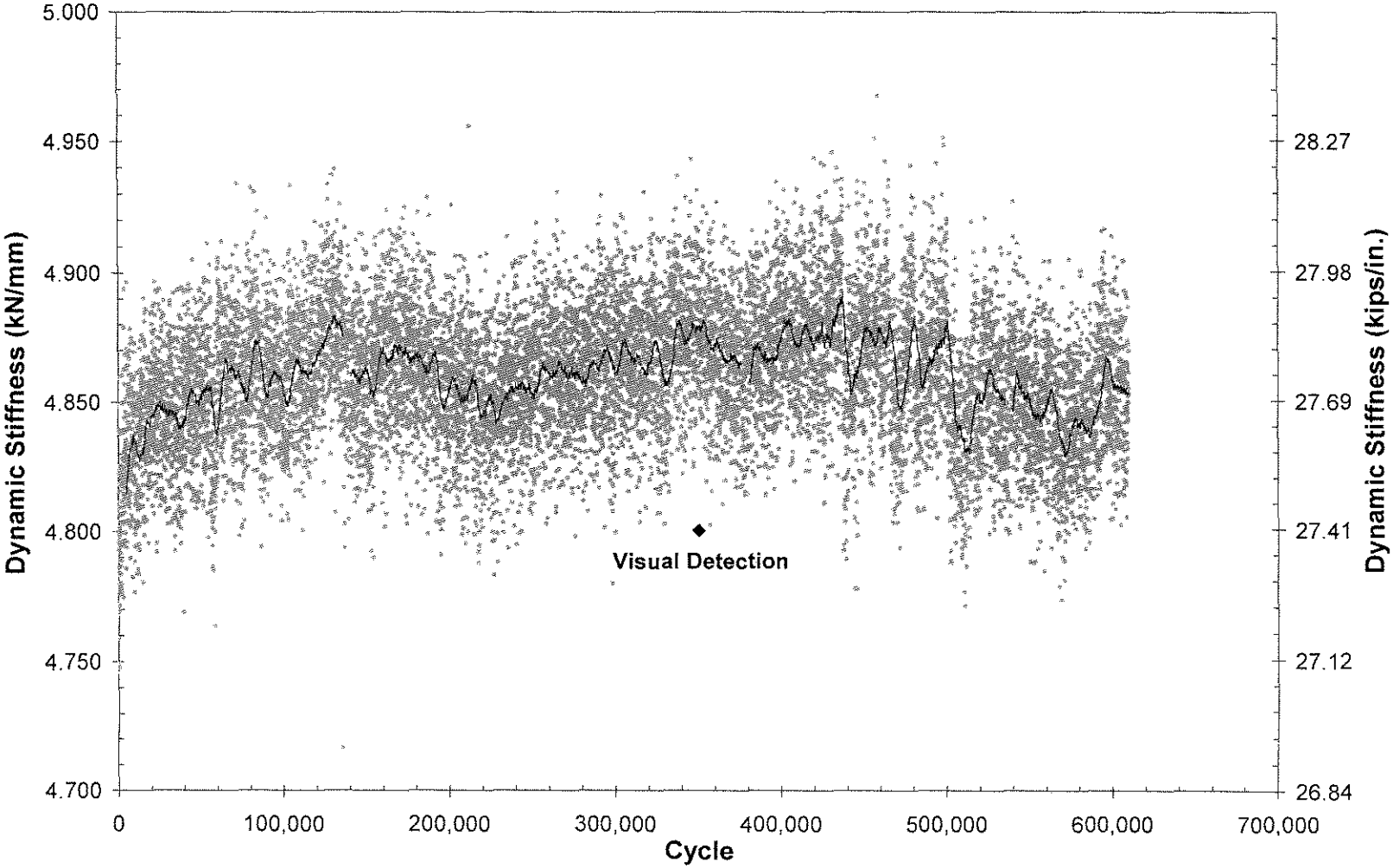

Figure A.6. Dynamic stiffness versus cycle for specimen CONTROL_04.

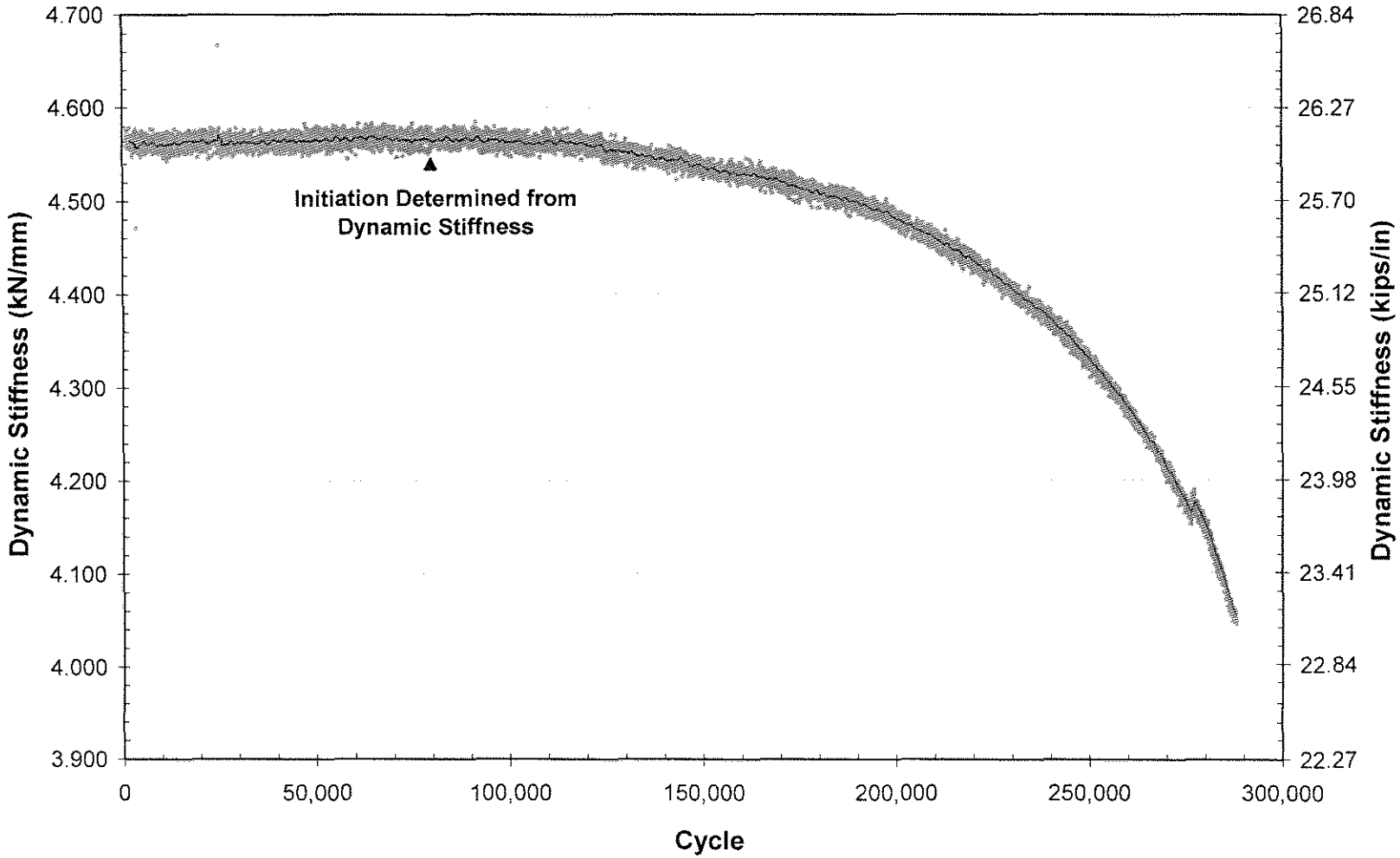

Figure A.7. Dynamic stiffness versus cycle for specimen CONTROL_05.

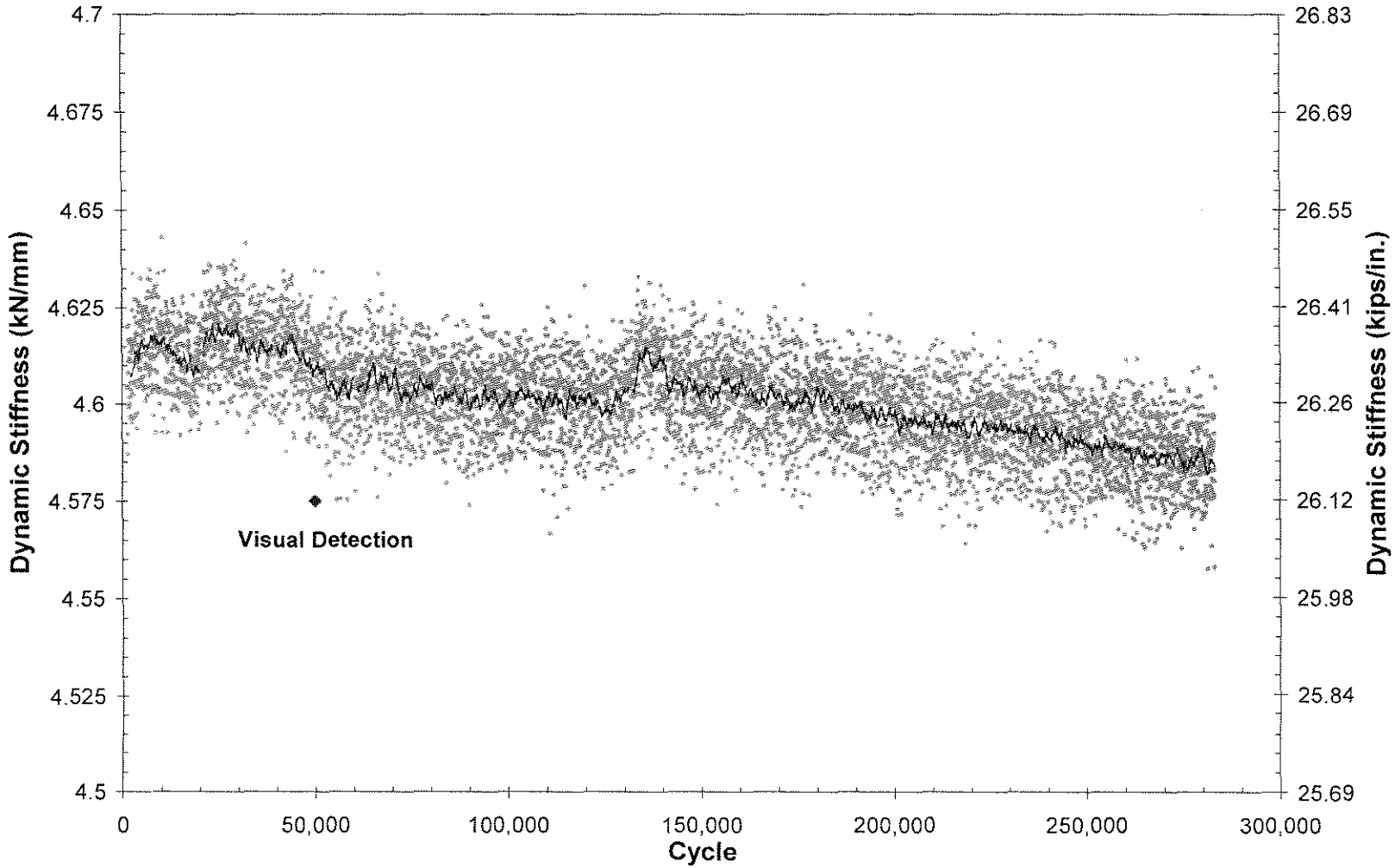

Figure A.8. Dynamic stiffness versus cycle for specimen CONTROL_06.

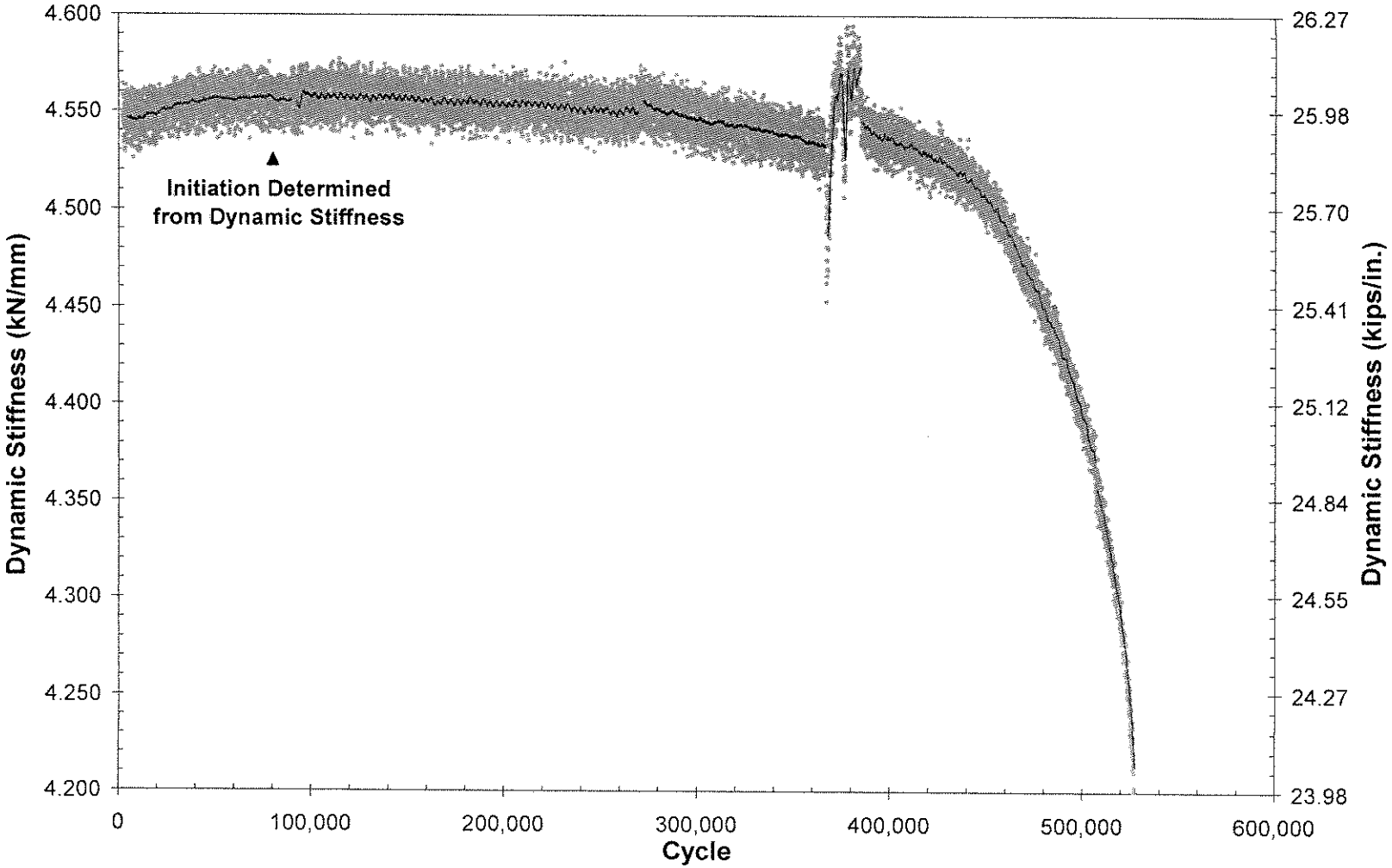

Figure A.9. Dynamic stiffness versus cycle for specimen BOLT_01.

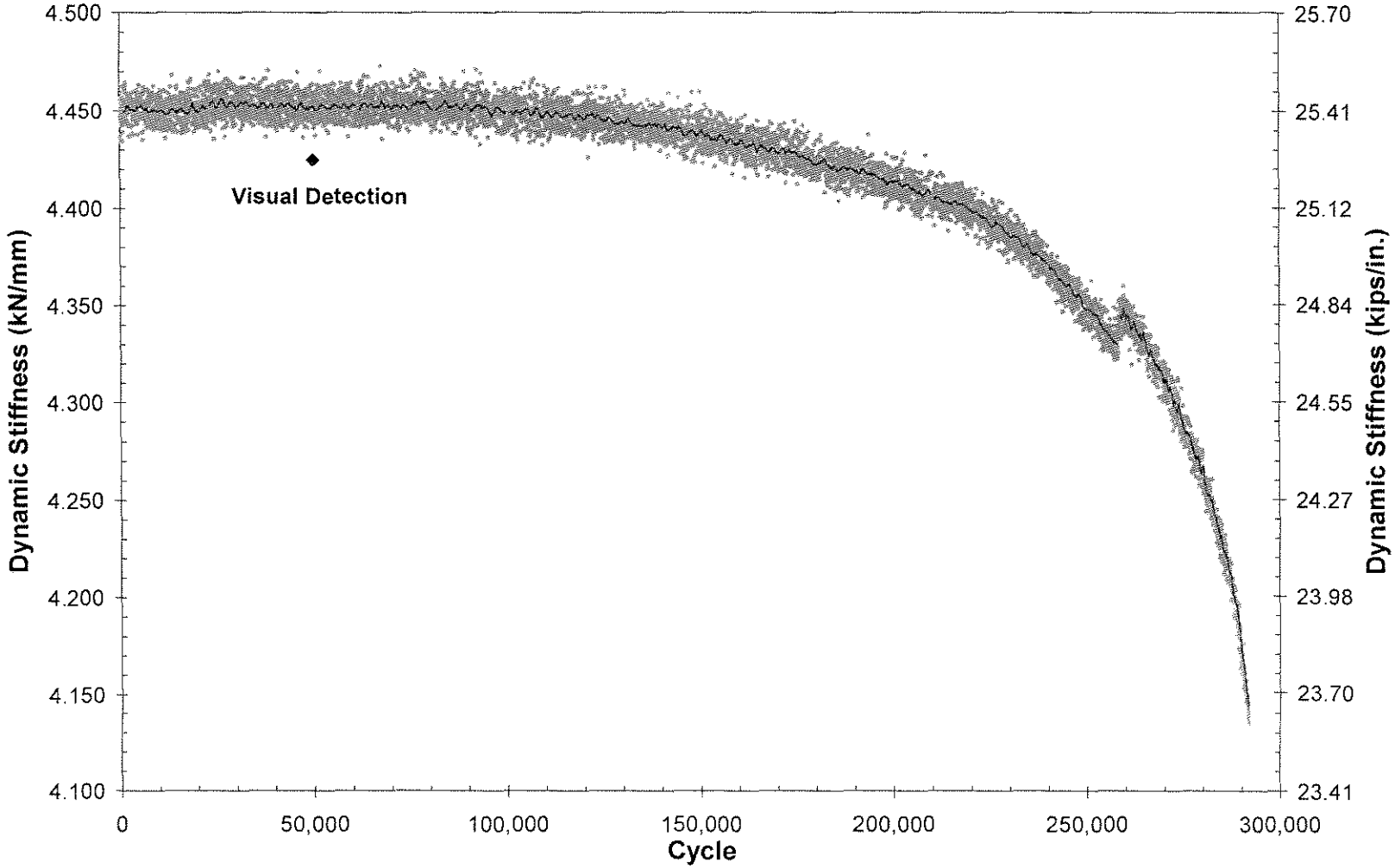

Figure A.10. Dynamic stiffness versus cycle for specimen BOLT_02.

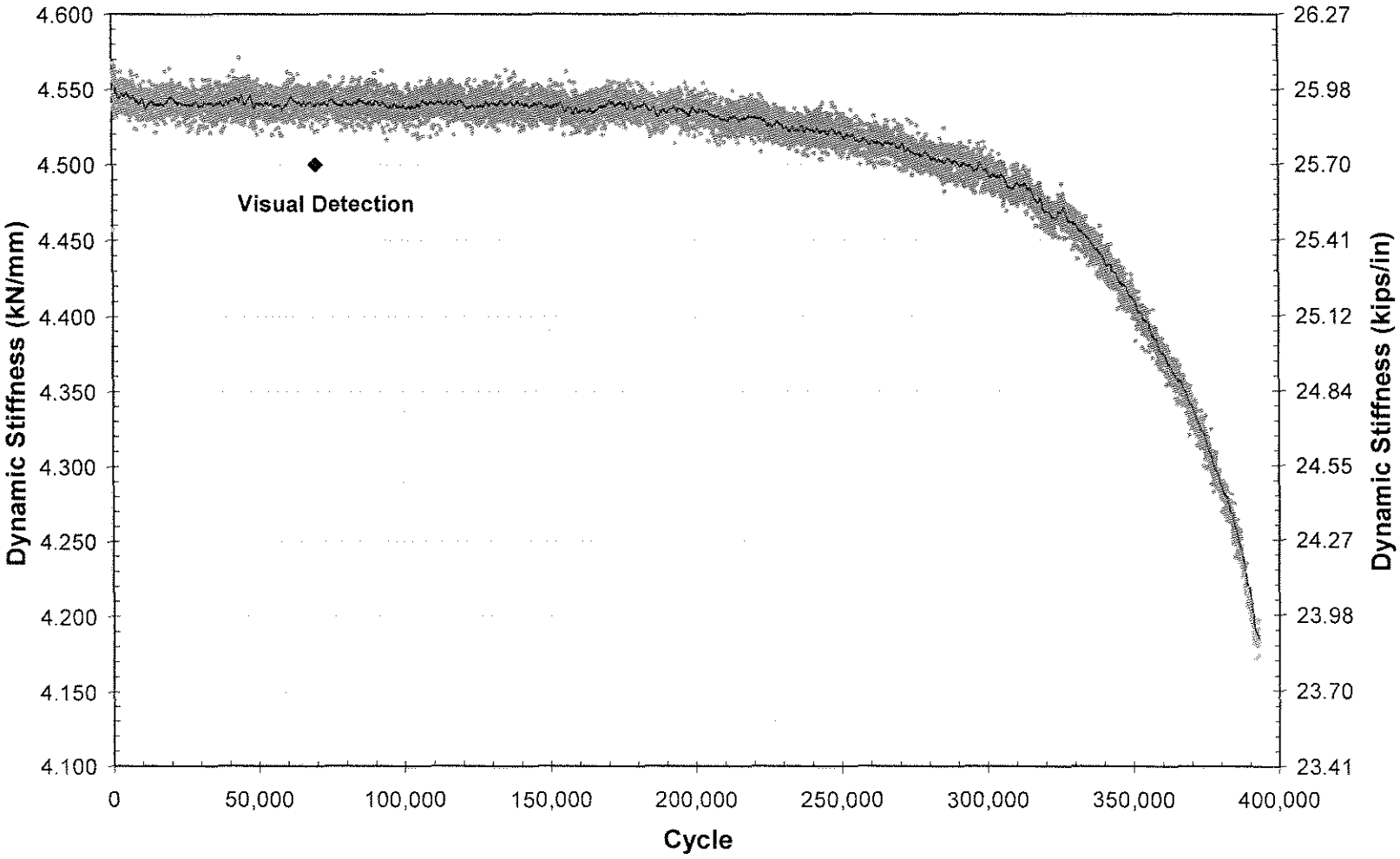

Figure A.11. Dynamic stiffness versus cycle for specimen BOLT_03.

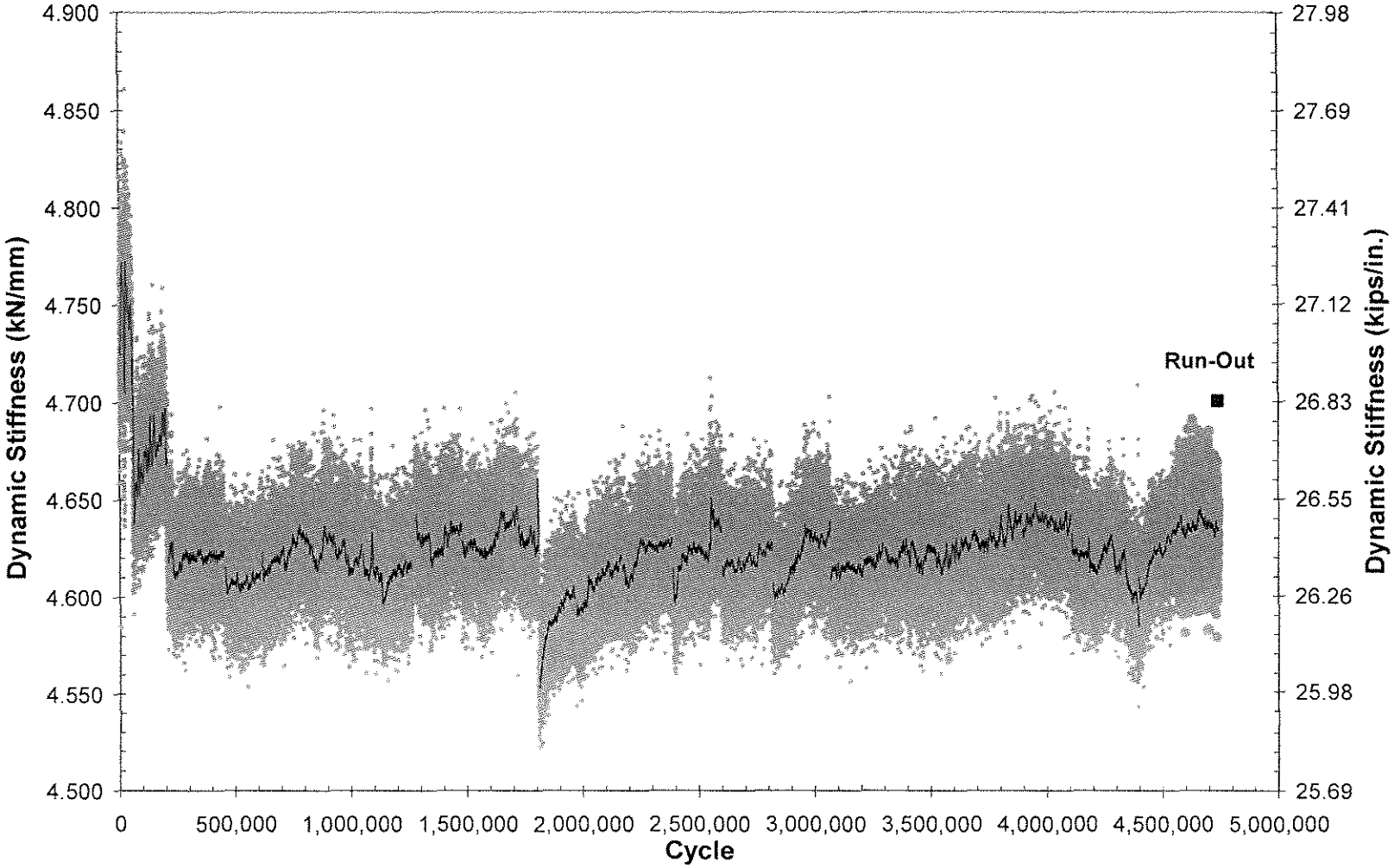

Figure A.12. Dynamic stiffness versus cycle for specimen UIT_01.

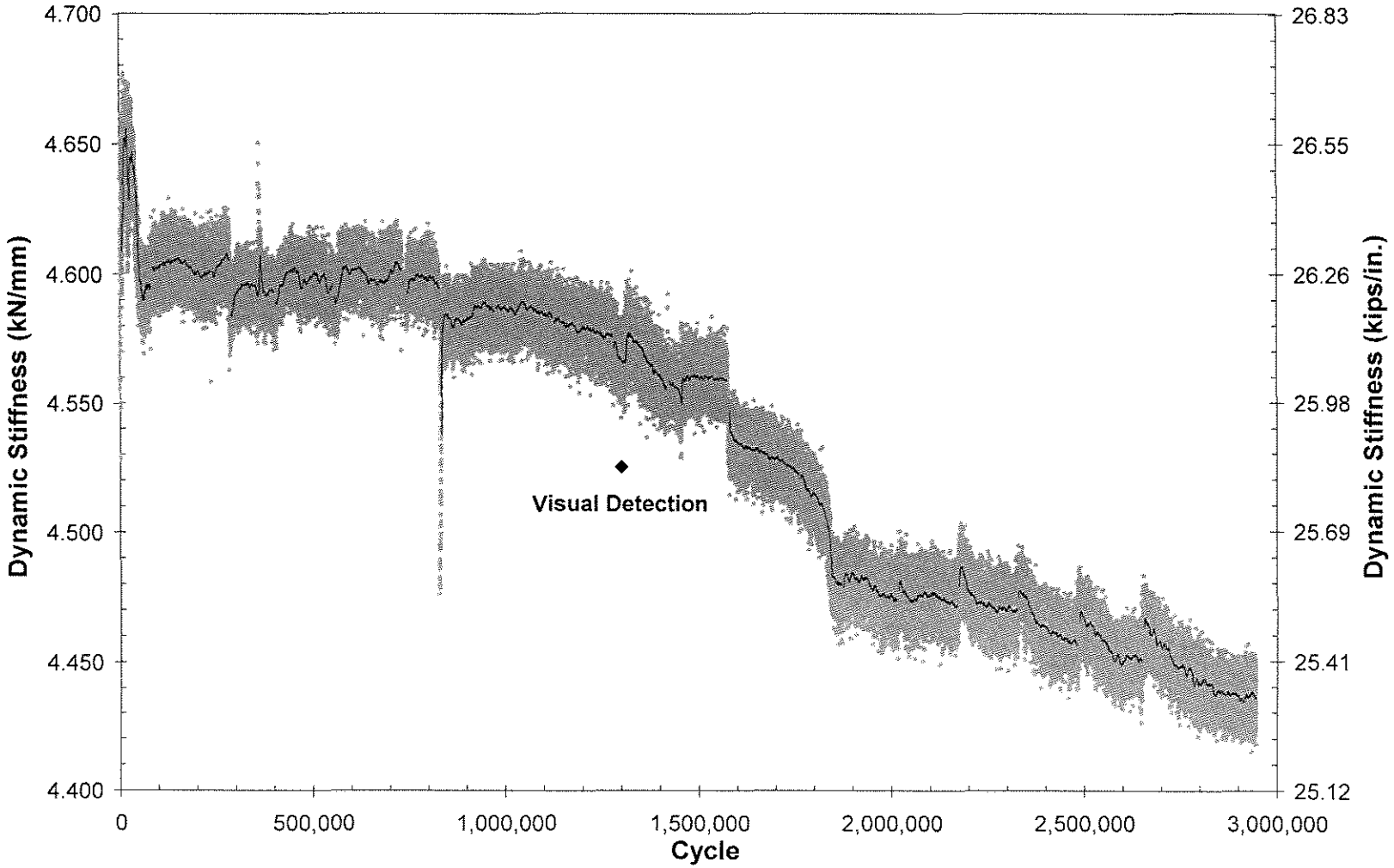

Figure A.13. Dynamic stiffness versus cycle for specimen UIT_02.

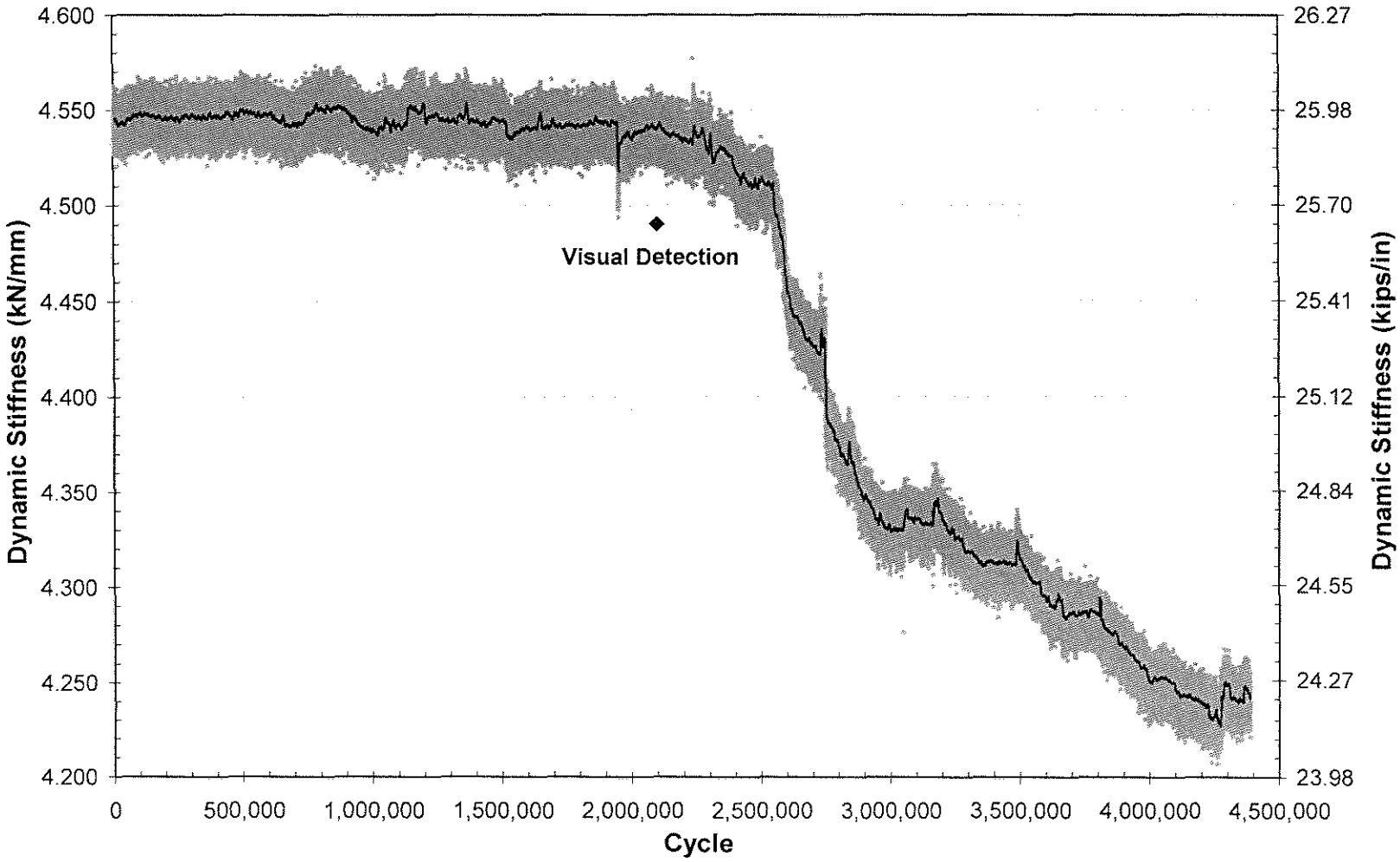

Figure A.14. Dynamic stiffness versus cycle for specimen UIT_03.

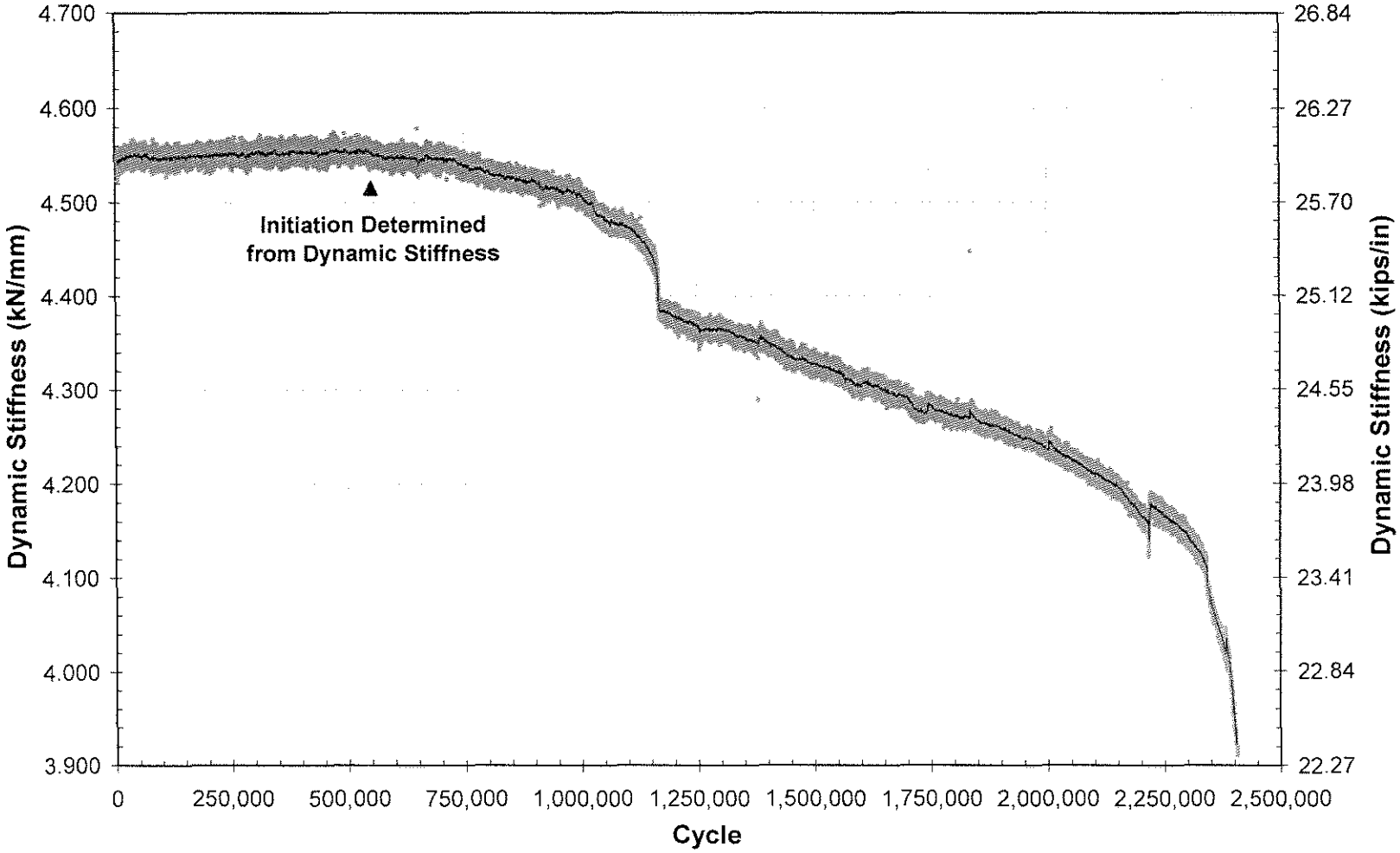

Figure A.15. Dynamic stiffness versus cycle for specimen UIT/BOLT_01.

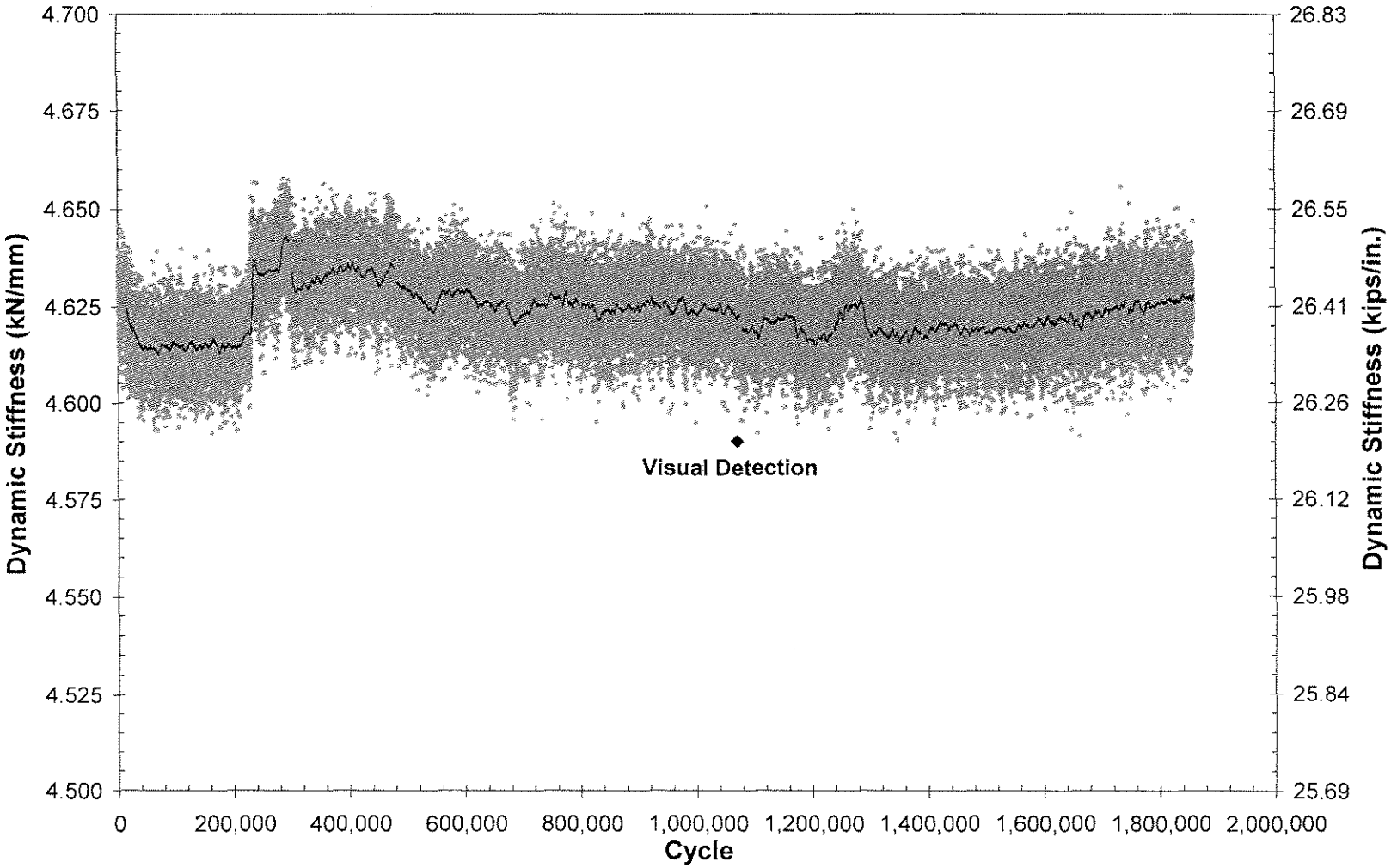

Figure A.16. Dynamic stiffness versus cycle for specimen UIT/BOLT_02.

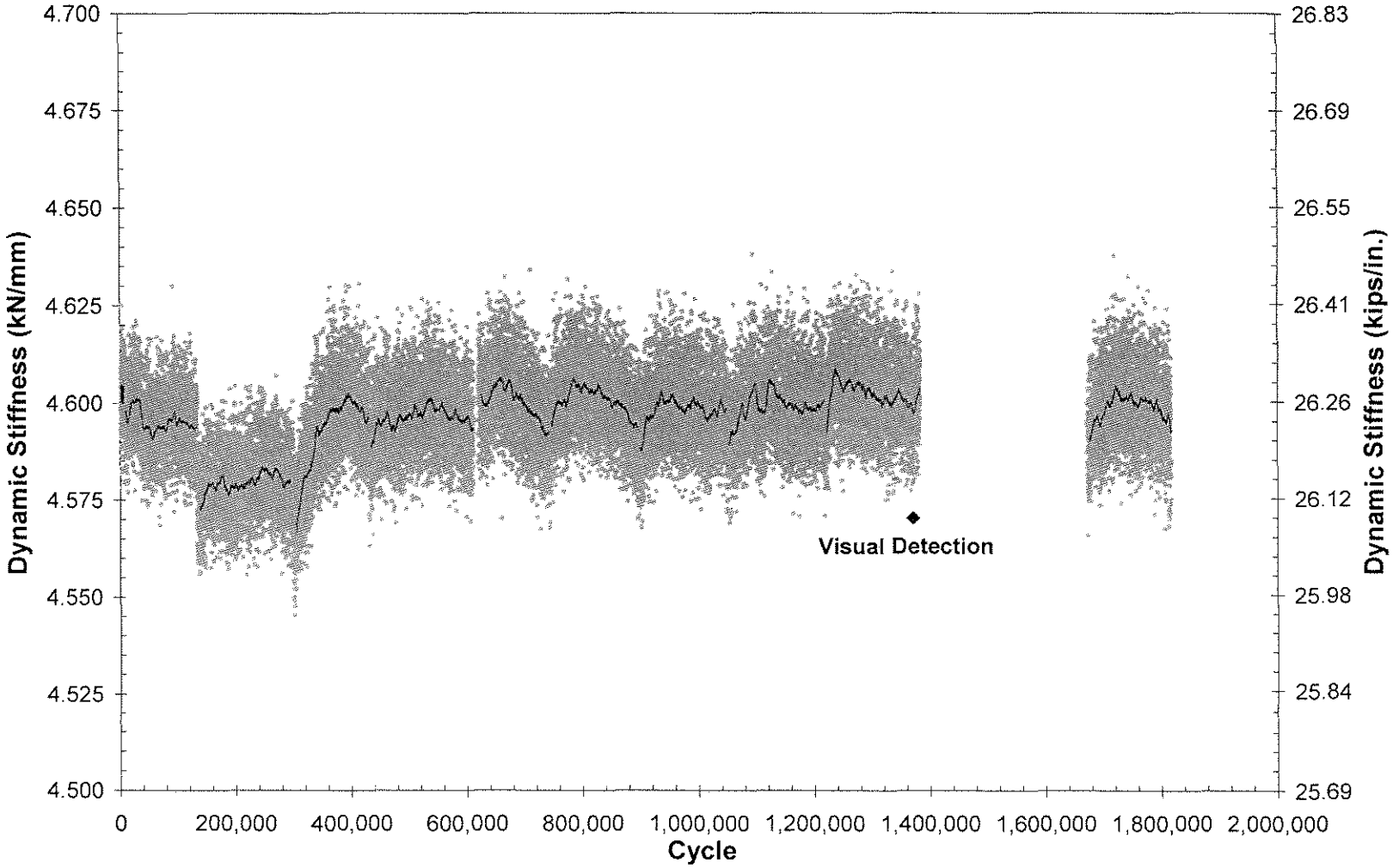

Figure A.17. Dynamic stiffness versus cycle for specimen UIT/BOLT_03.

APPENDIX B MICROSTRAIN PLOTS

This appendix displays plots of microstrain versus time measured by the array of strain gages during fatigue testing. Microstrains were recorded by the WaveBook data acquisition system. Plots were constructed using Microsoft Excel. Each plot shows strains recorded for a time period of two seconds. Because the strain ranges measured for different specimen types did not vary prior to crack formation, plots of recorded strains at each gage location for every specimen type are not shown. Rather, one plot of microstrain versus time is shown for each strain gage location. Specimens for which the plots were constructed were chosen randomly. Plots of microstrain versus time for the array of 13 strain gages are shown in Figures B.1 through B.7.

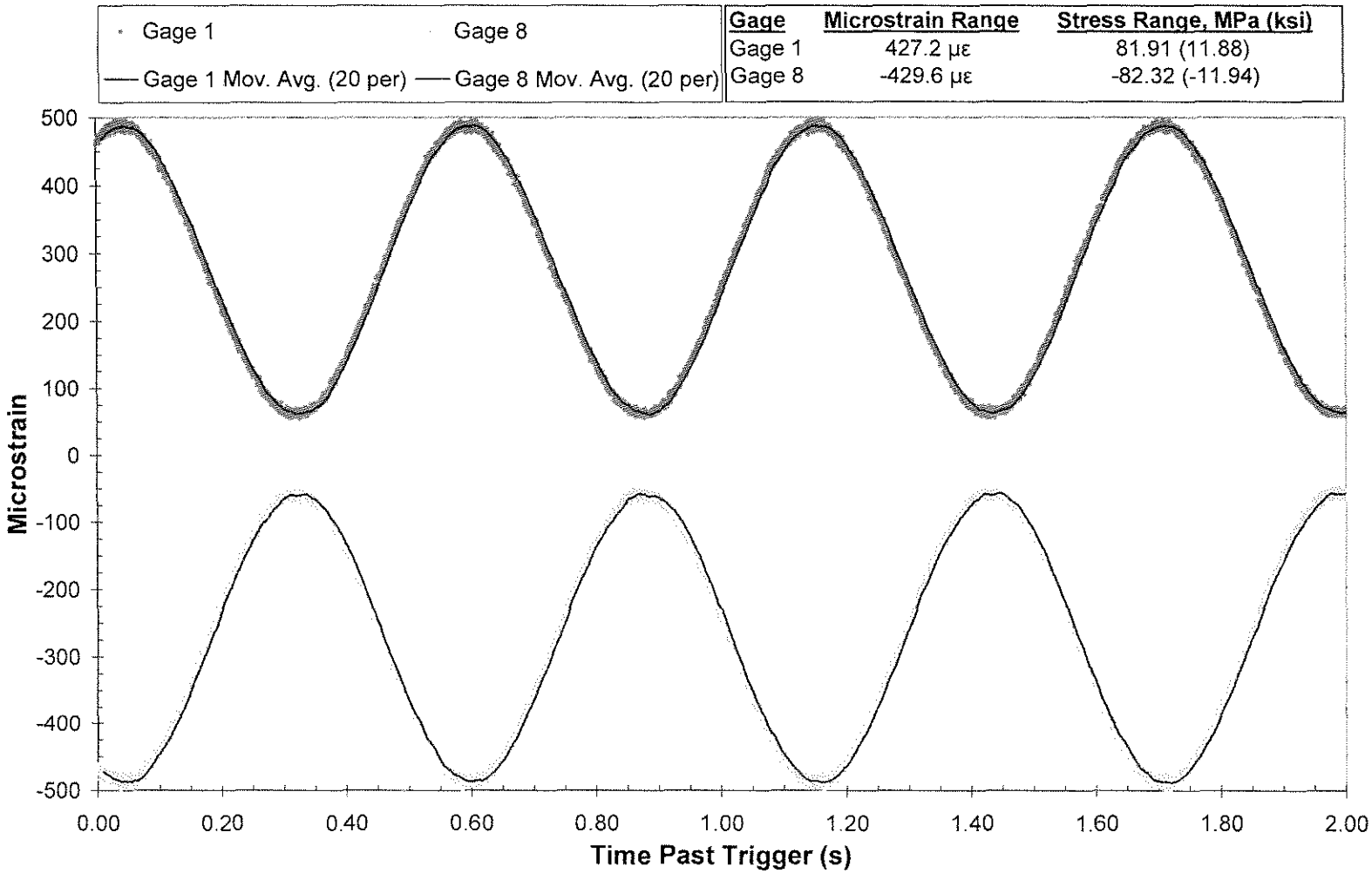

Figure B.1. Microstrain versus time for Gage 1 and Gage 8 on specimen CONTROL_06 at 40,000 cycles.

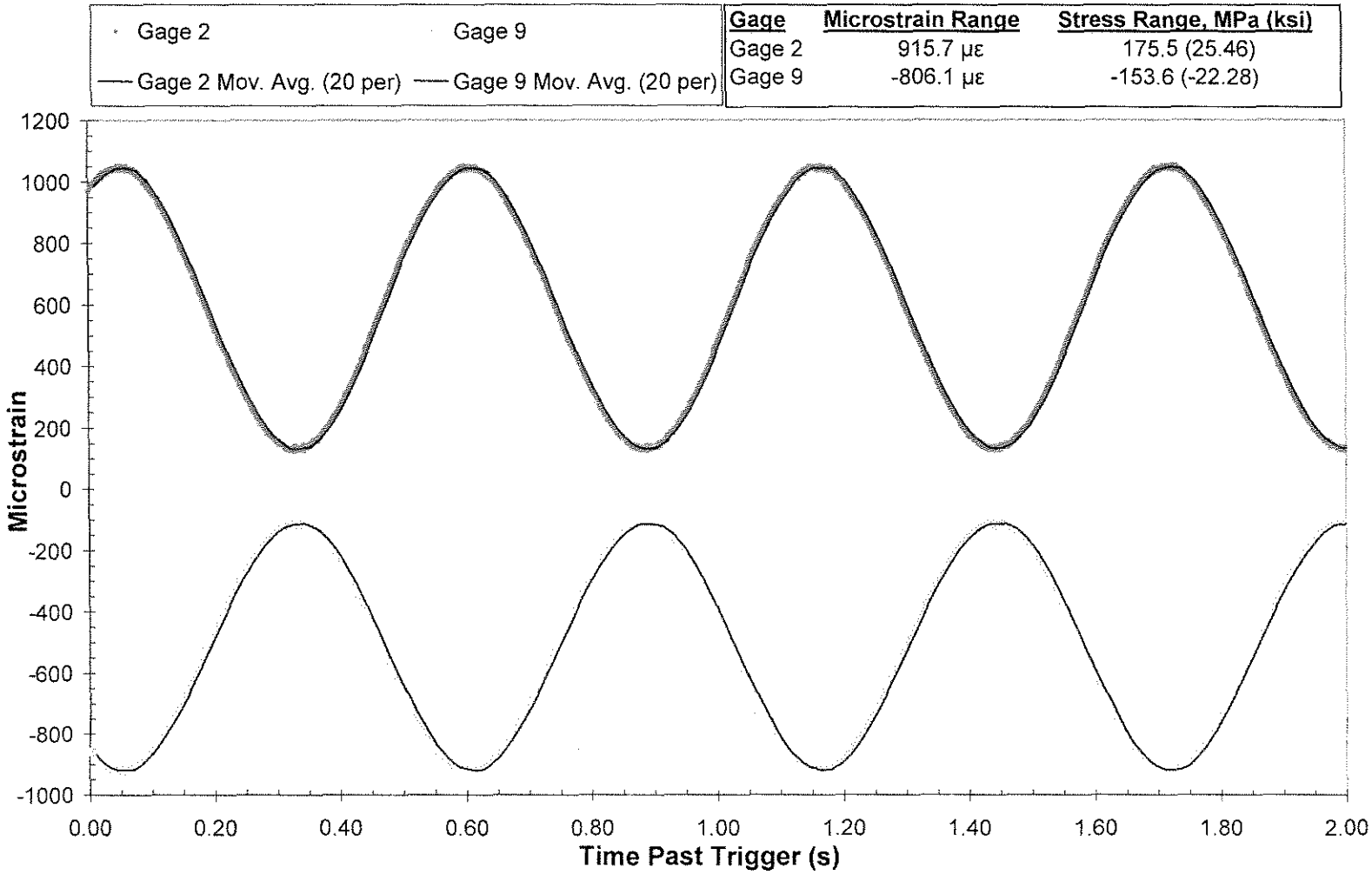

Figure B.2. Microstrain versus time for Gage 2 and Gage 9 on specimen BOLT_03 at 40,000 cycles.

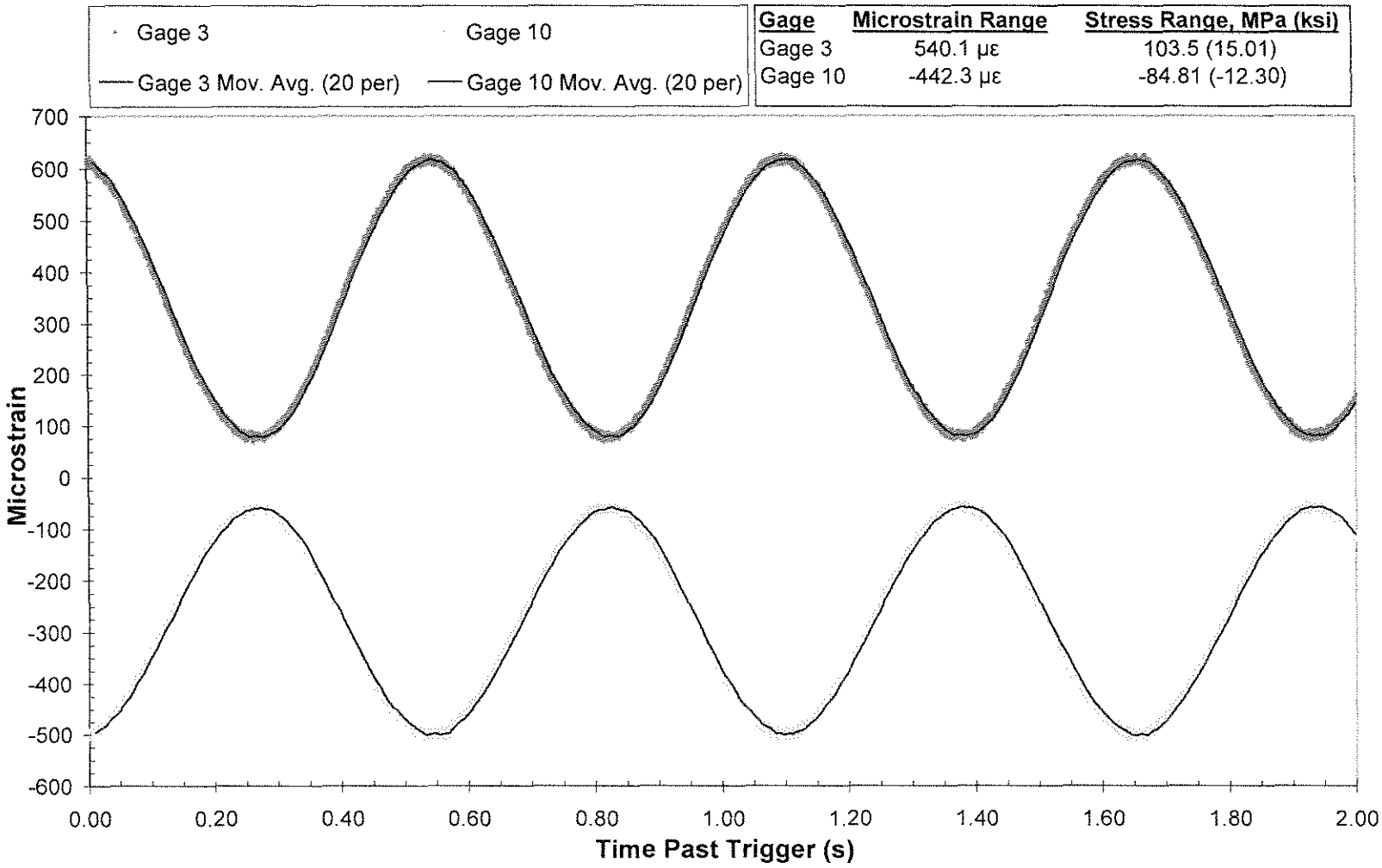

Figure B.3. Microstrain versus time for Gage 3 and Gage 10 on specimen UIT/BOLT_03 at 130,000 cycles.

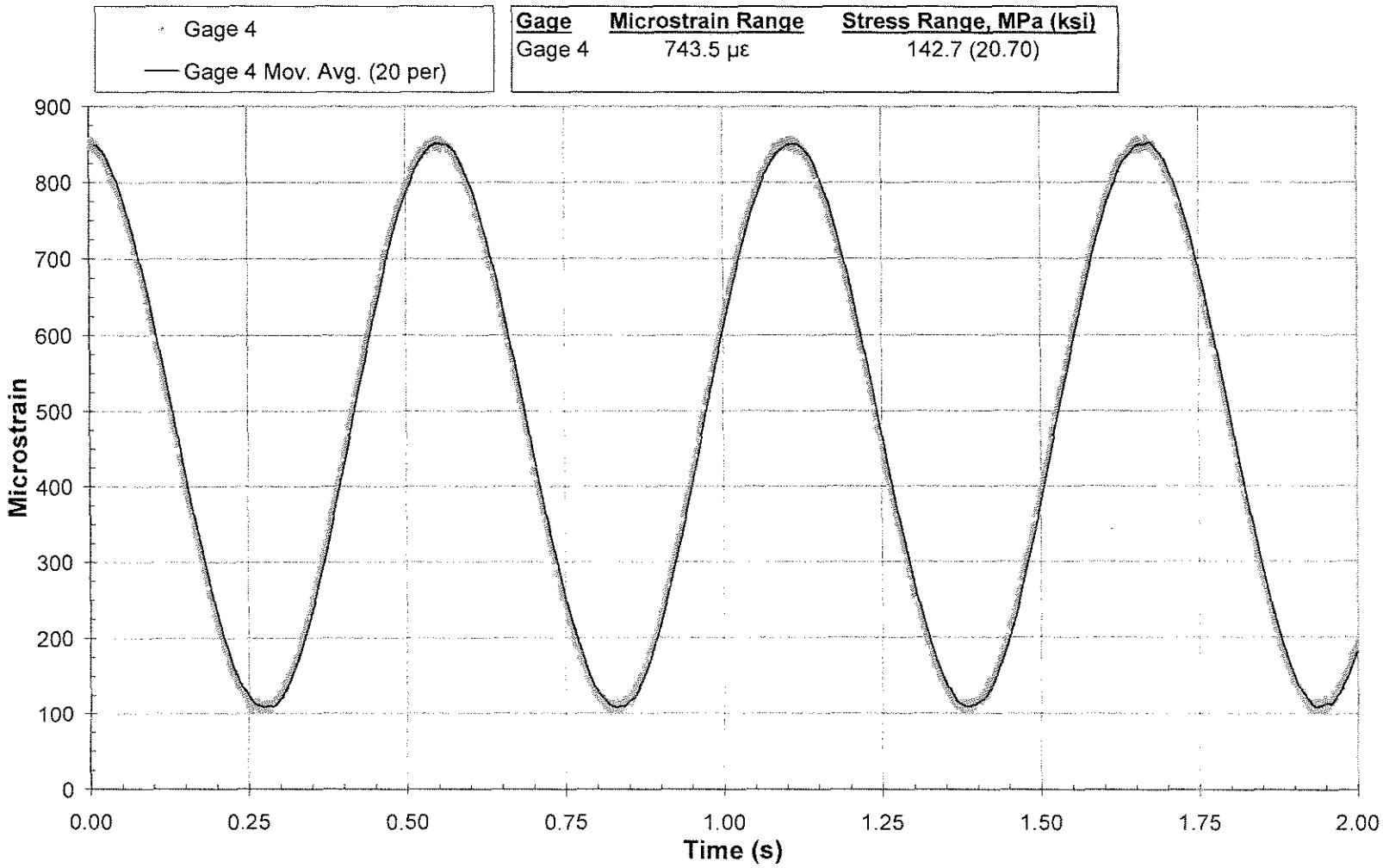

Figure B.4. Microstrain versus time for Gage 4 on specimen UIT/BOLT_02 at 480,000 cycles.

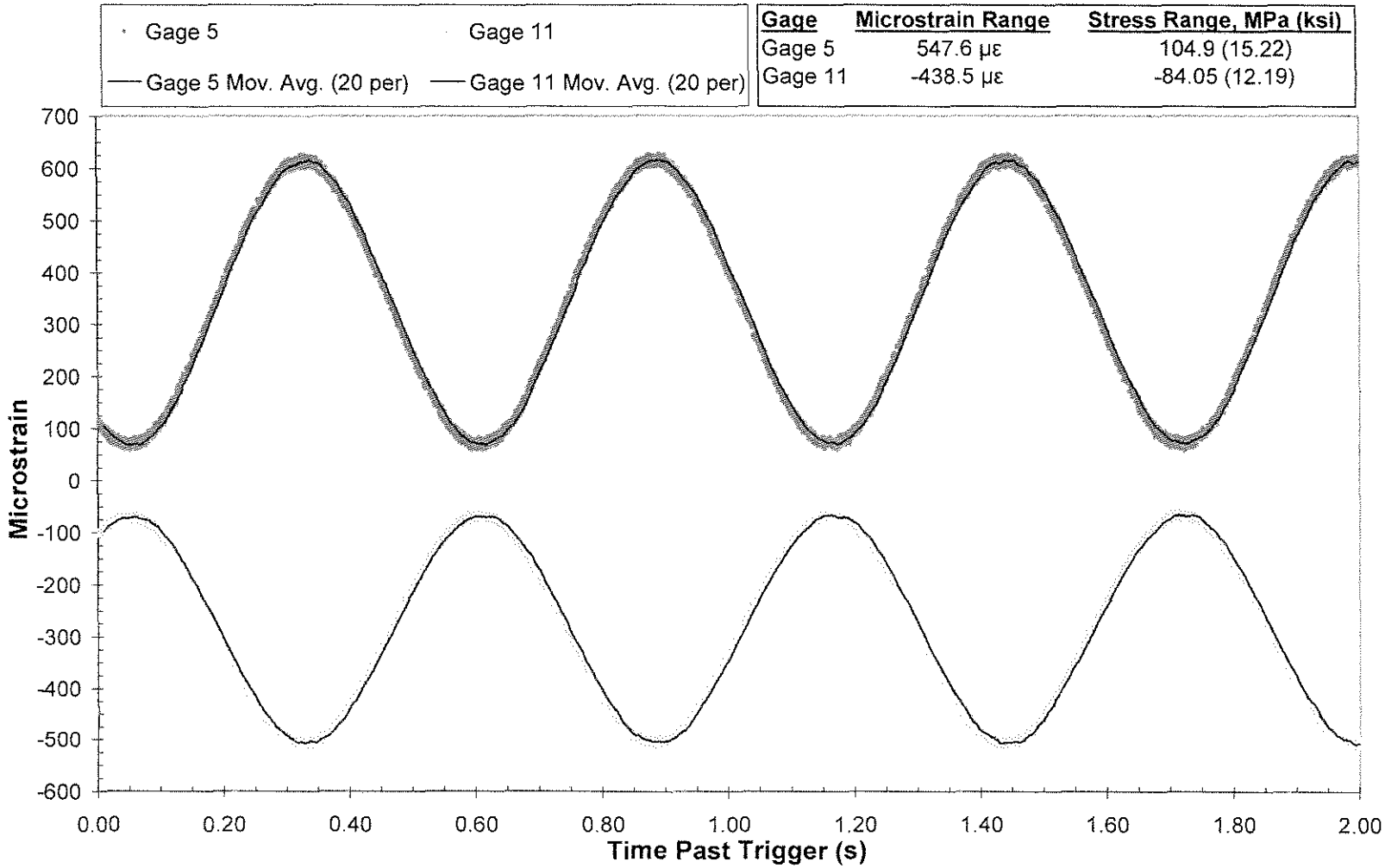

Figure B.5. Microstrain versus time for Gage 5 and Gage 11 on specimen UIT_03 at 263,000 cycles.

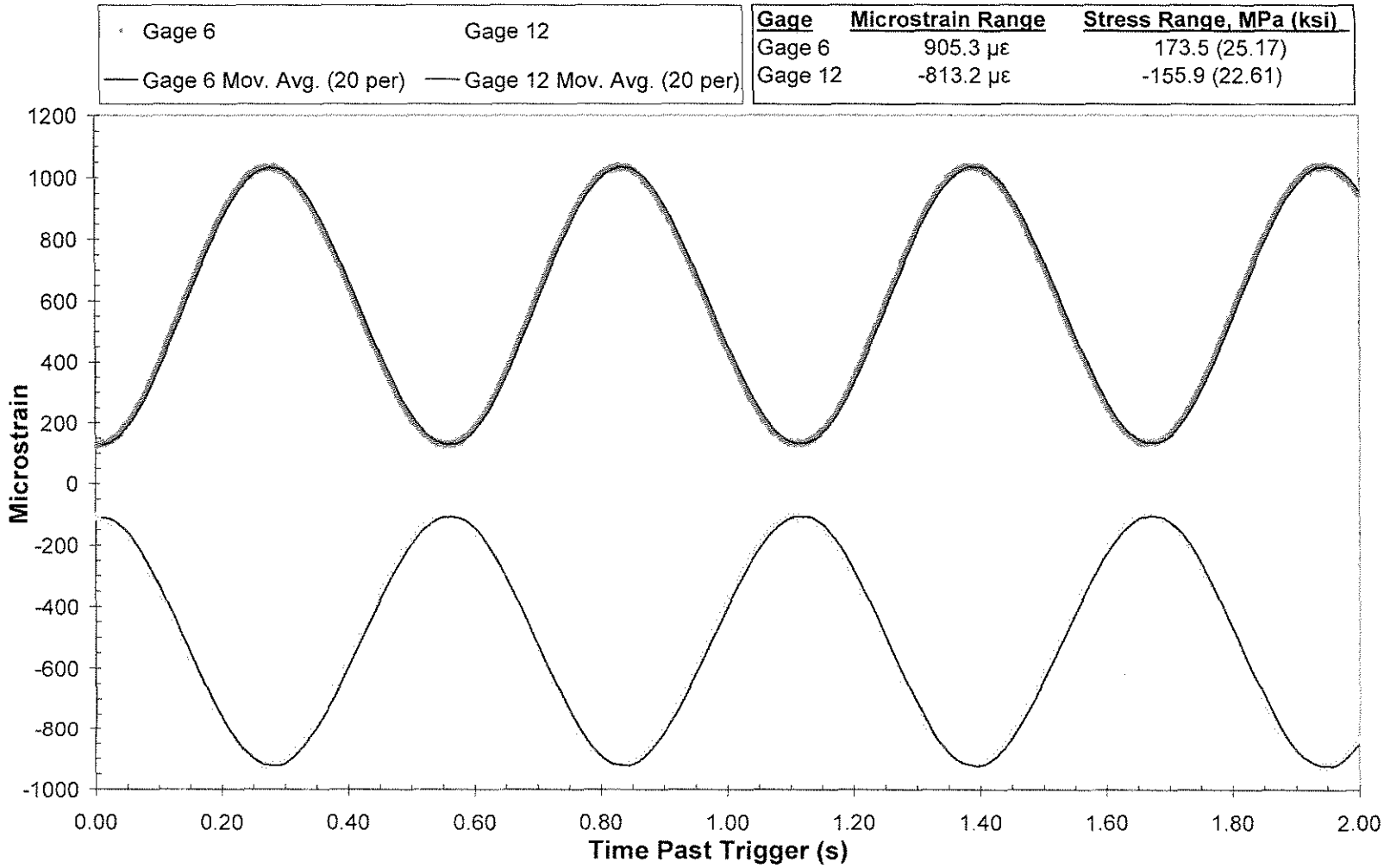

Figure B.6. Microstrain versus time for Gage 6 and Gage 12 on specimen BOLT_02 at 40,000 cycles.

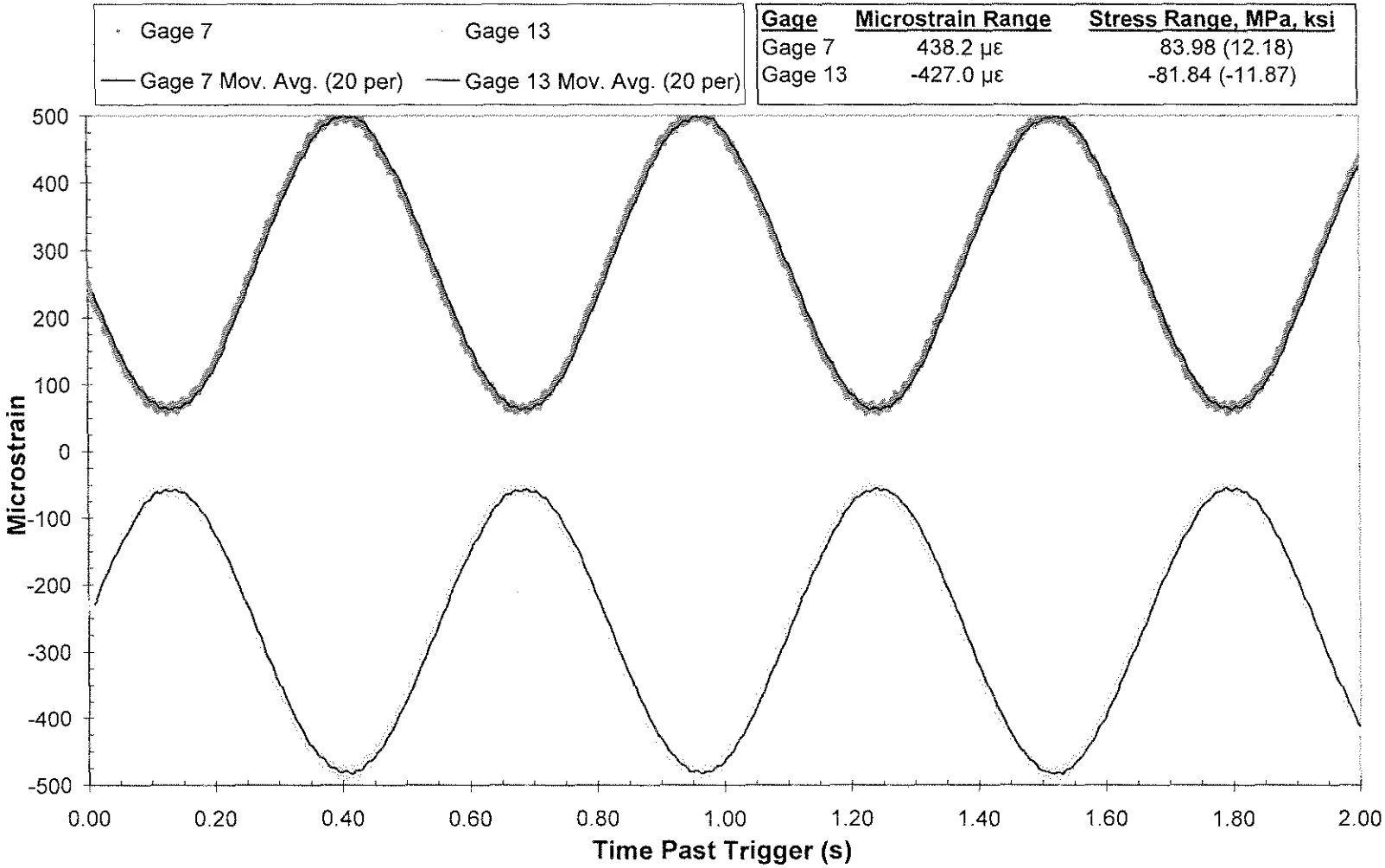

Figure B.7. Microstrain versus time for Gage 7 and Gage 13 on specimen UIT/BOLT_01 at 284,000 cycles.

APPENDIX C STATIC STIFFNESS PLOTS

This appendix displays the results of static stiffness tests performed for specimens tested at a nominal weld toe stress range of 193 MPa (28.0 ksi). Data used to determine static stiffness for each specimen was recorded by the testing machine's internal LVDT and load cell. All plots were generated using Microsoft Excel. Figures C.1 through C.10 show plots of static stiffness versus cycle for all specimens tested at a stress range of 193 MPa (28.0 ksi). Static stiffness was not recorded for preliminary specimens. In Figures C.1 through C.10, the point at which crack initiation was defined is indicated by either a black diamond or a black triangle. A black diamond represents the point at which a fatigue crack was found using dye penetrant. A black triangle represents the point at which a crack was defined using dynamic stiffness data. All plots have identical vertical scales to enable comparison between plots.

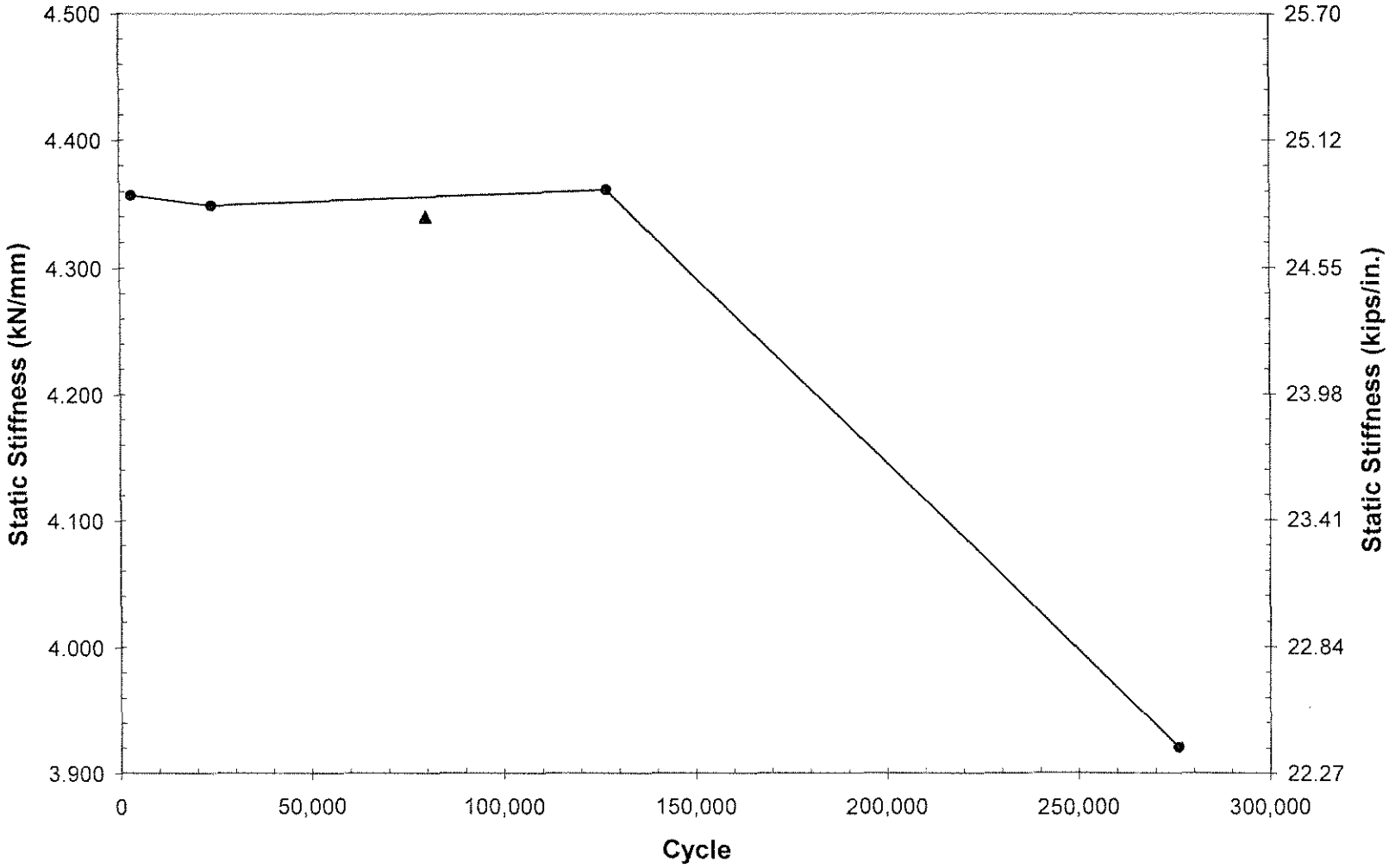

Figure C.1. Static stiffness versus cycle for specimen CONTROL_05.

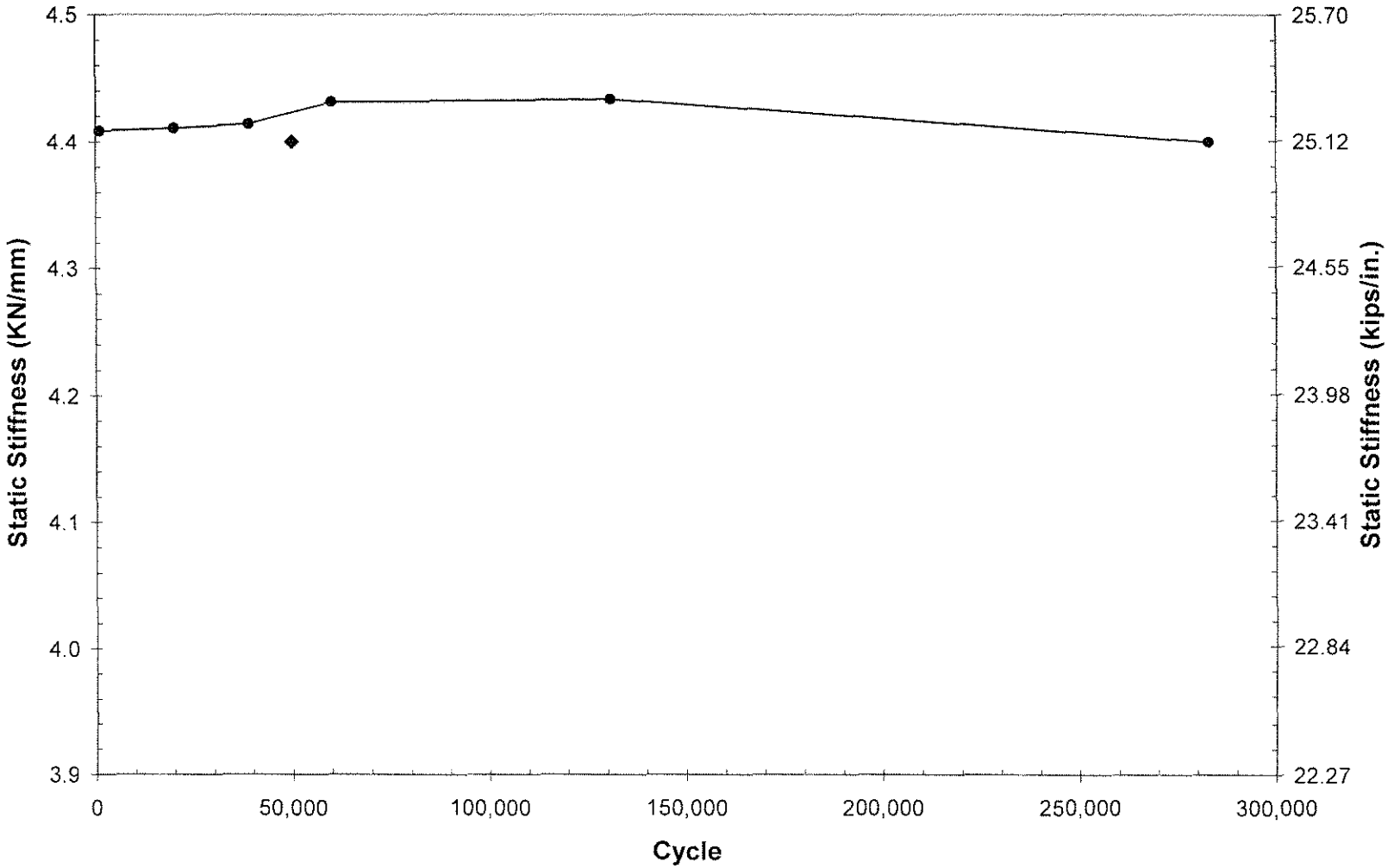

Figure C.2. Static stiffness versus cycle for specimen CONTROL_06.

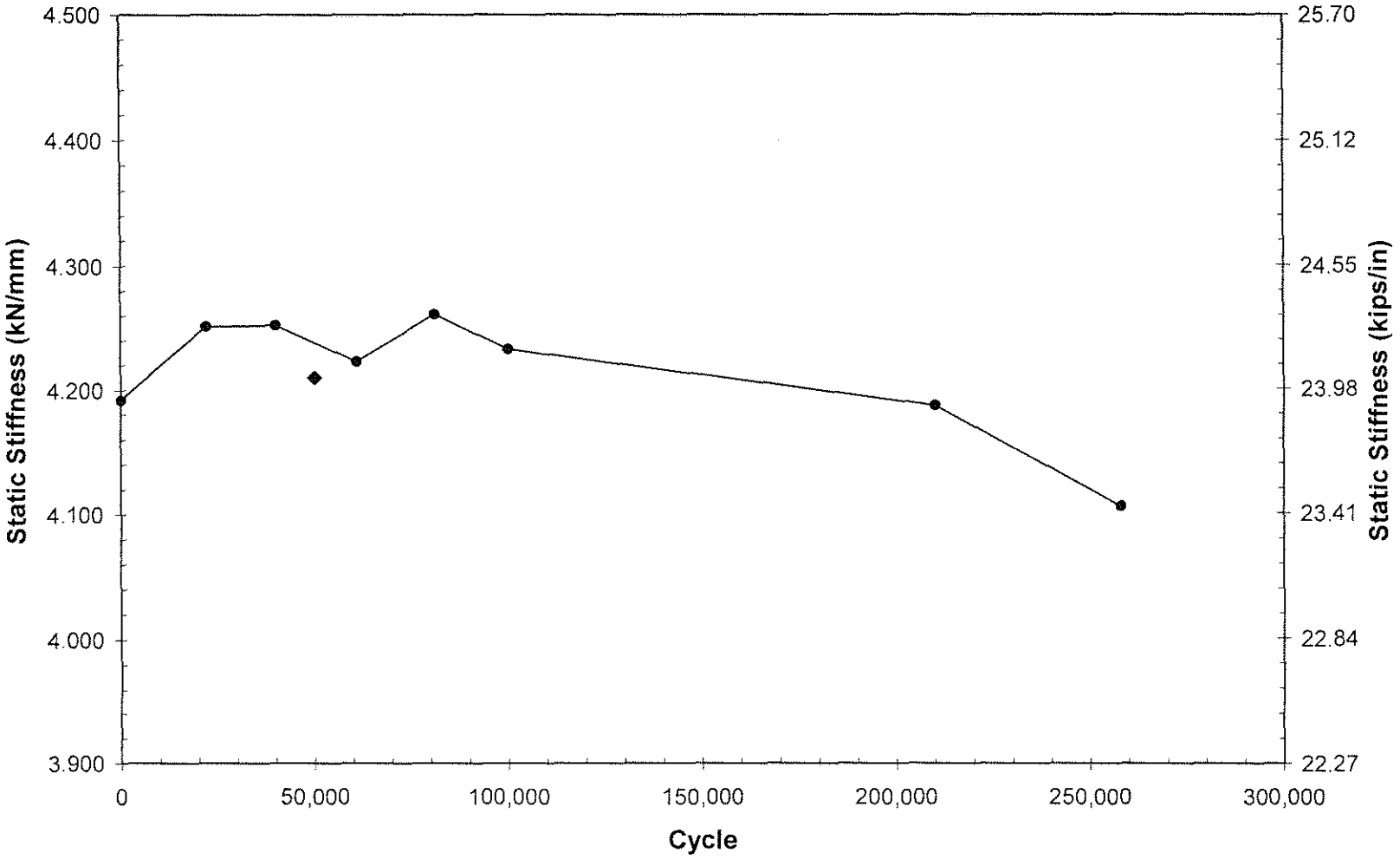

Figure C.4. Static stiffness versus cycle for specimen BOLT_02.

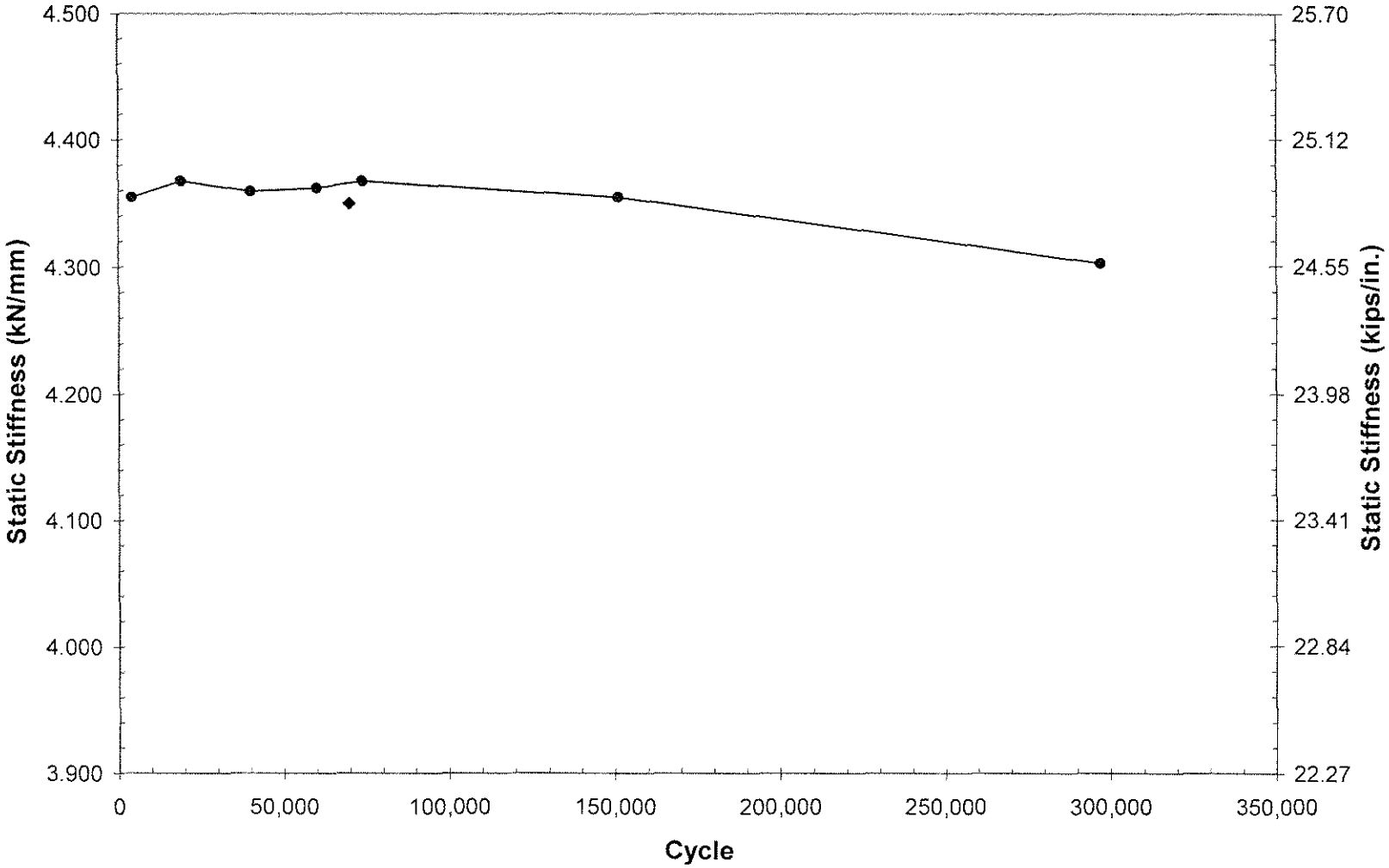

Figure C.5. Static stiffness versus cycle for specimen BOLT_03.

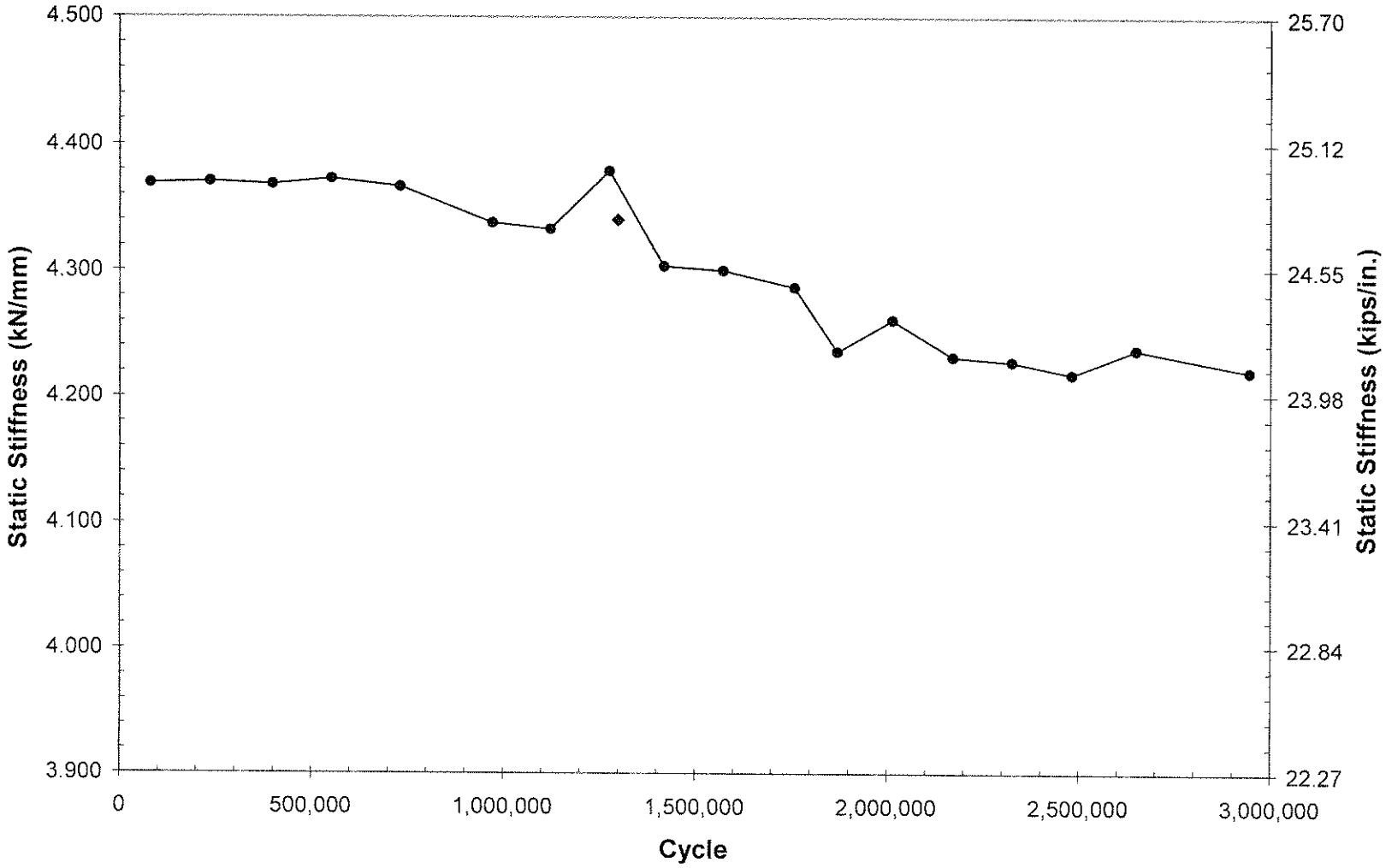

Figure C.6. Static stiffness versus cycle for specimen UIT_02.

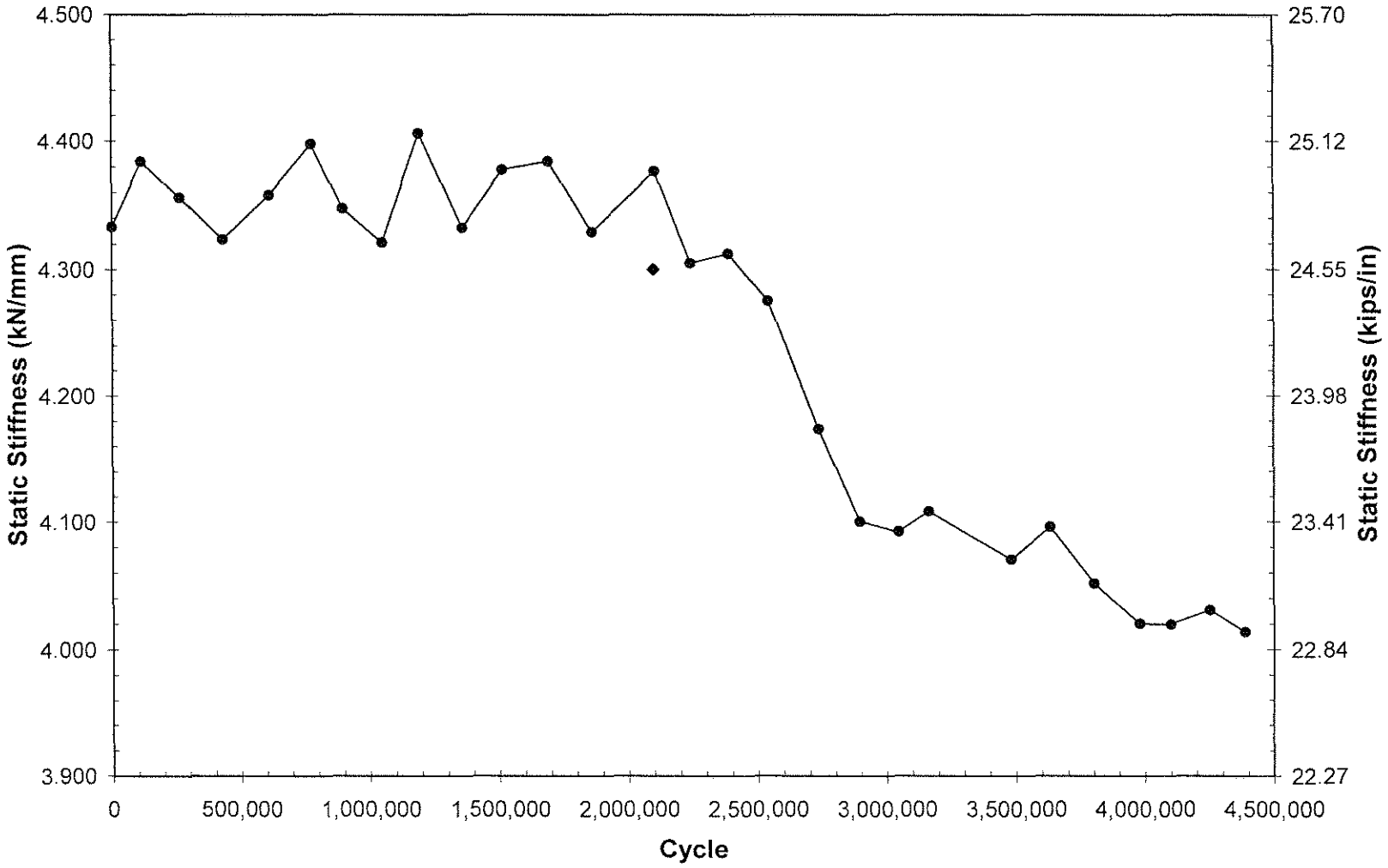

Figure C.7. Static stiffness versus cycle for specimen UIT_03.

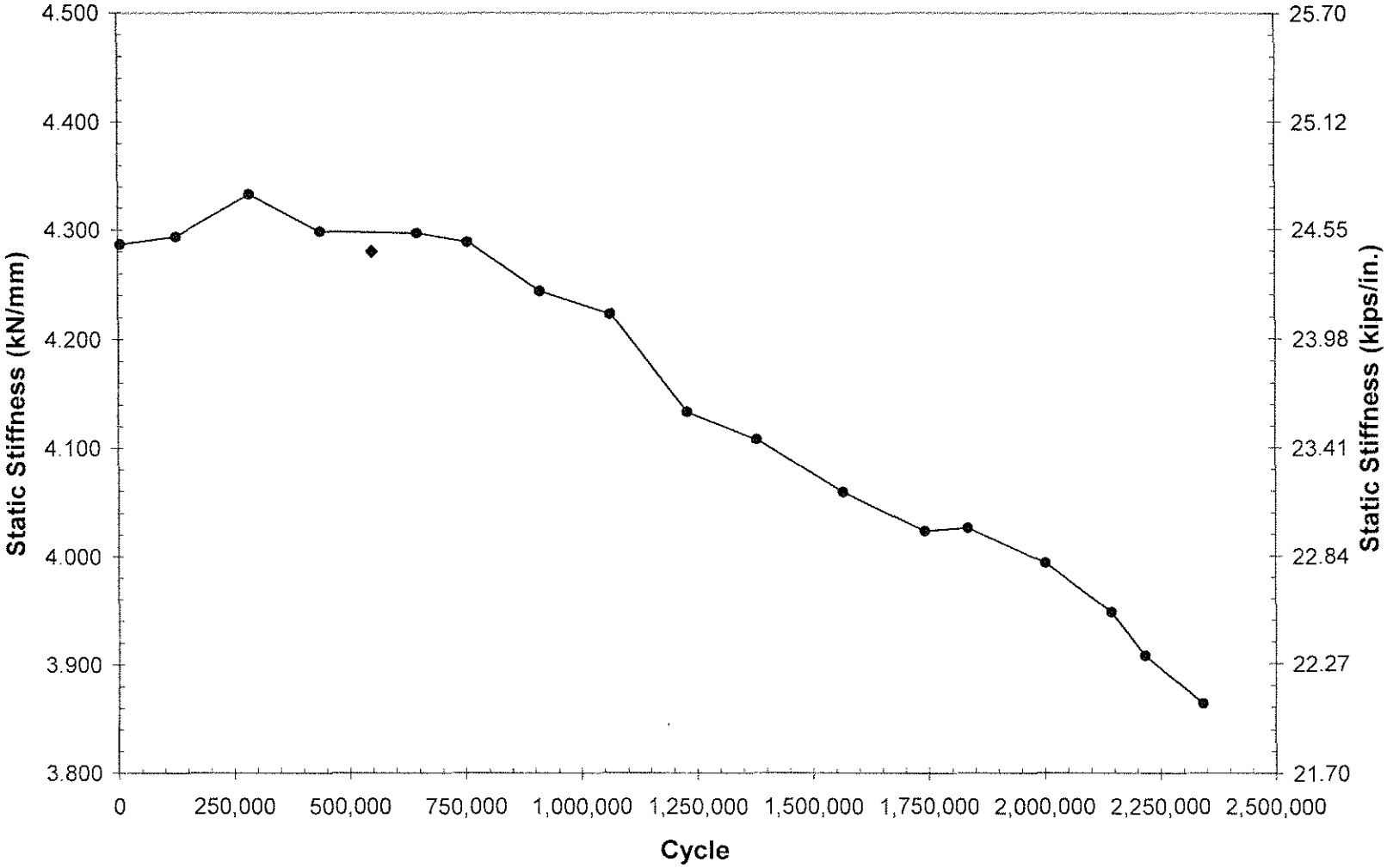

Figure C.8. Static stiffness versus cycle for specimen UIT/BOLT_01.

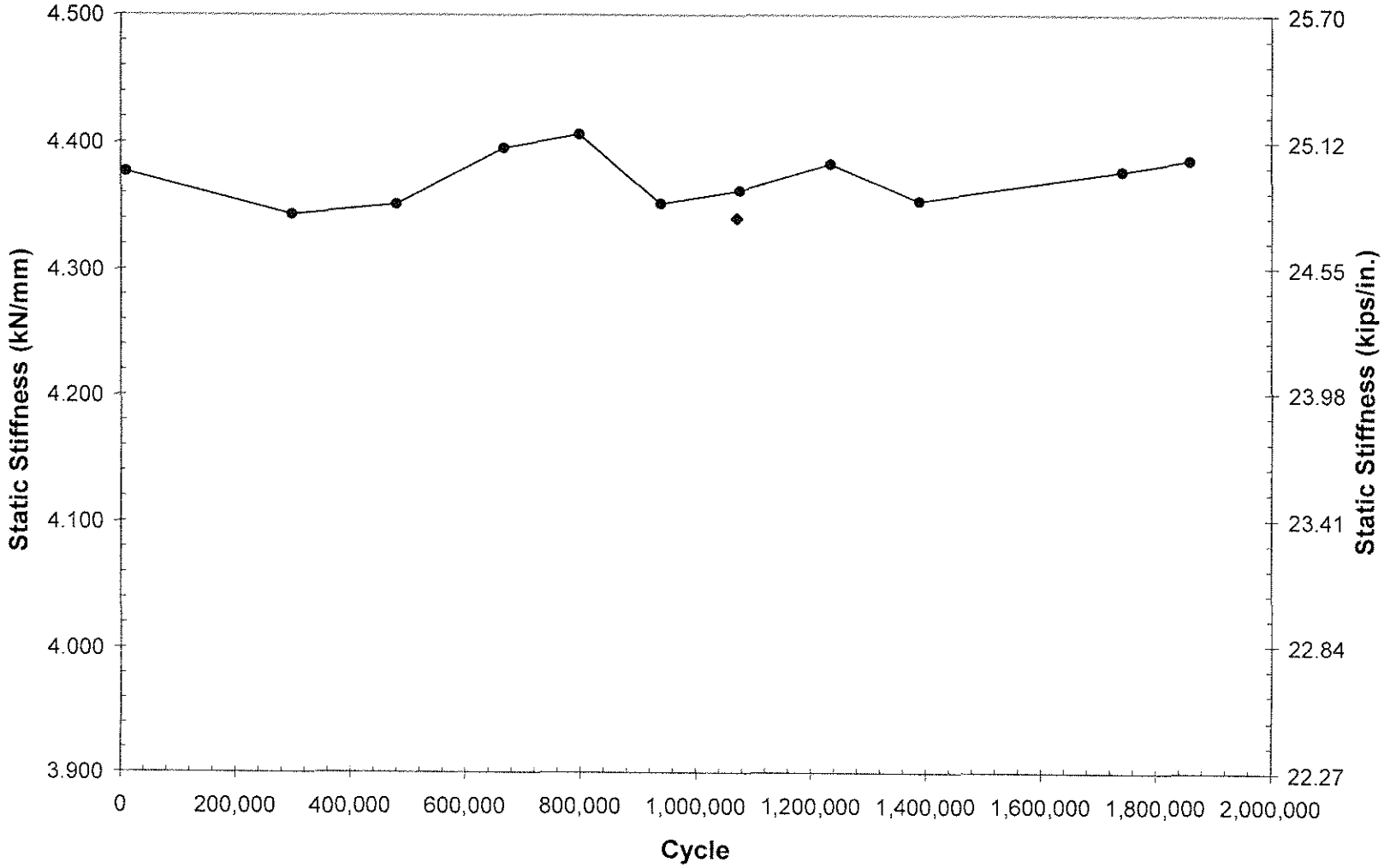

Figure C.9. Static stiffness versus cycle for specimen UIT/BOLT_02.

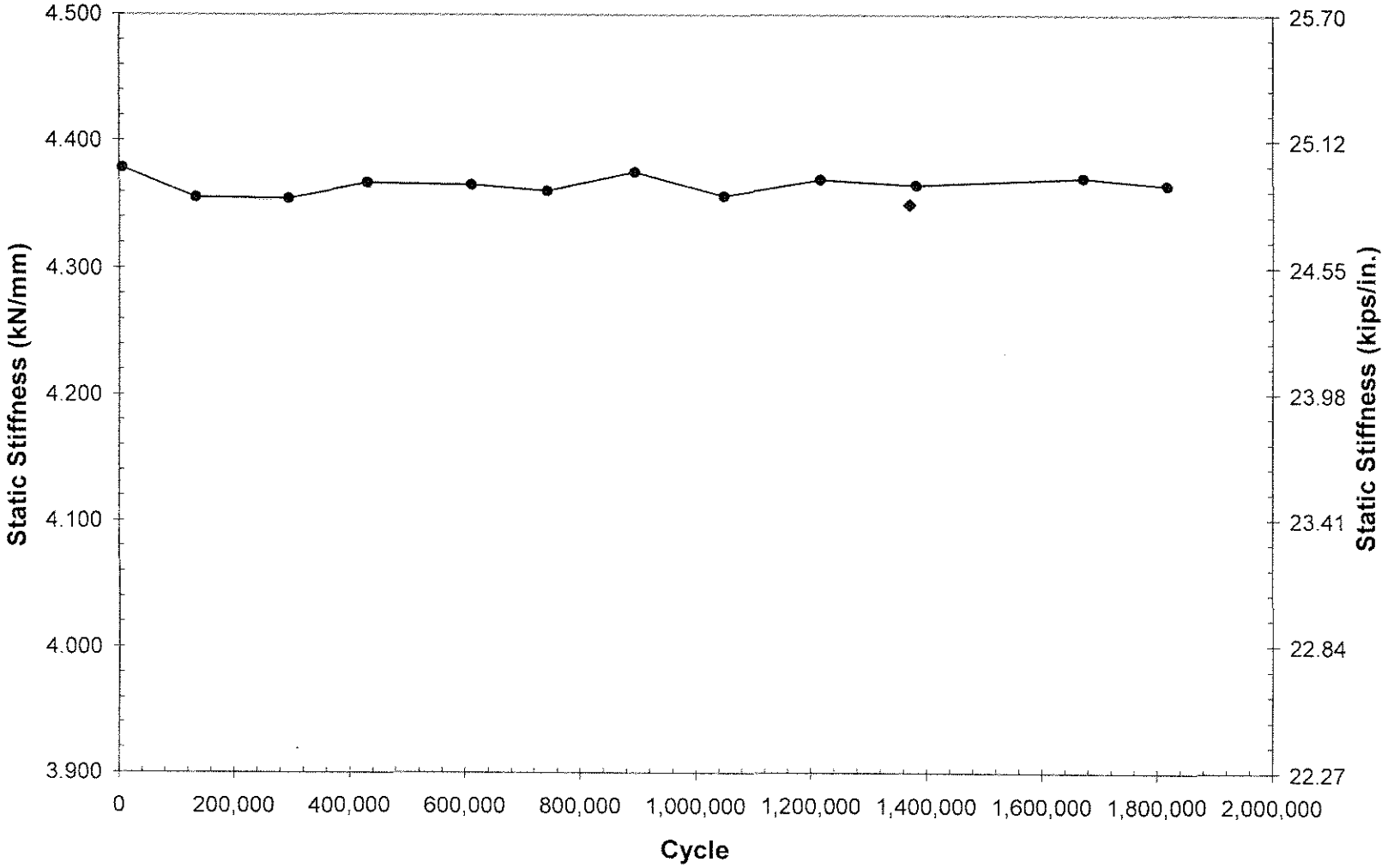

Figure C.10. Static stiffness versus cycle for specimen UIT/BOLT_03.

APPENDIX D STRAIN GAGE CRACK DETECTION PLOTS

In an attempt to predict fatigue crack initiation, changes in stress range at the weld toes were monitored. To monitor stress ranges at the weld toes, the strain ranges measured during fatigue testing by strain gages two and six were recorded and plotted against number of cycles for each fatigue test. Strains were measured using the WaveBook data acquisition system and plots of stress range versus cycle were constructed using Microsoft Excel. This method of crack detection was employed only after the USP was added to the electrical system. Thus, this method was employed for all specimens tested at a weld toe stress range of 193 MPa (28.0 ksi), except specimens BOLT_01 and UIT_02. Plots of stress range versus cycle are shown in Figures D.1 through D.8.

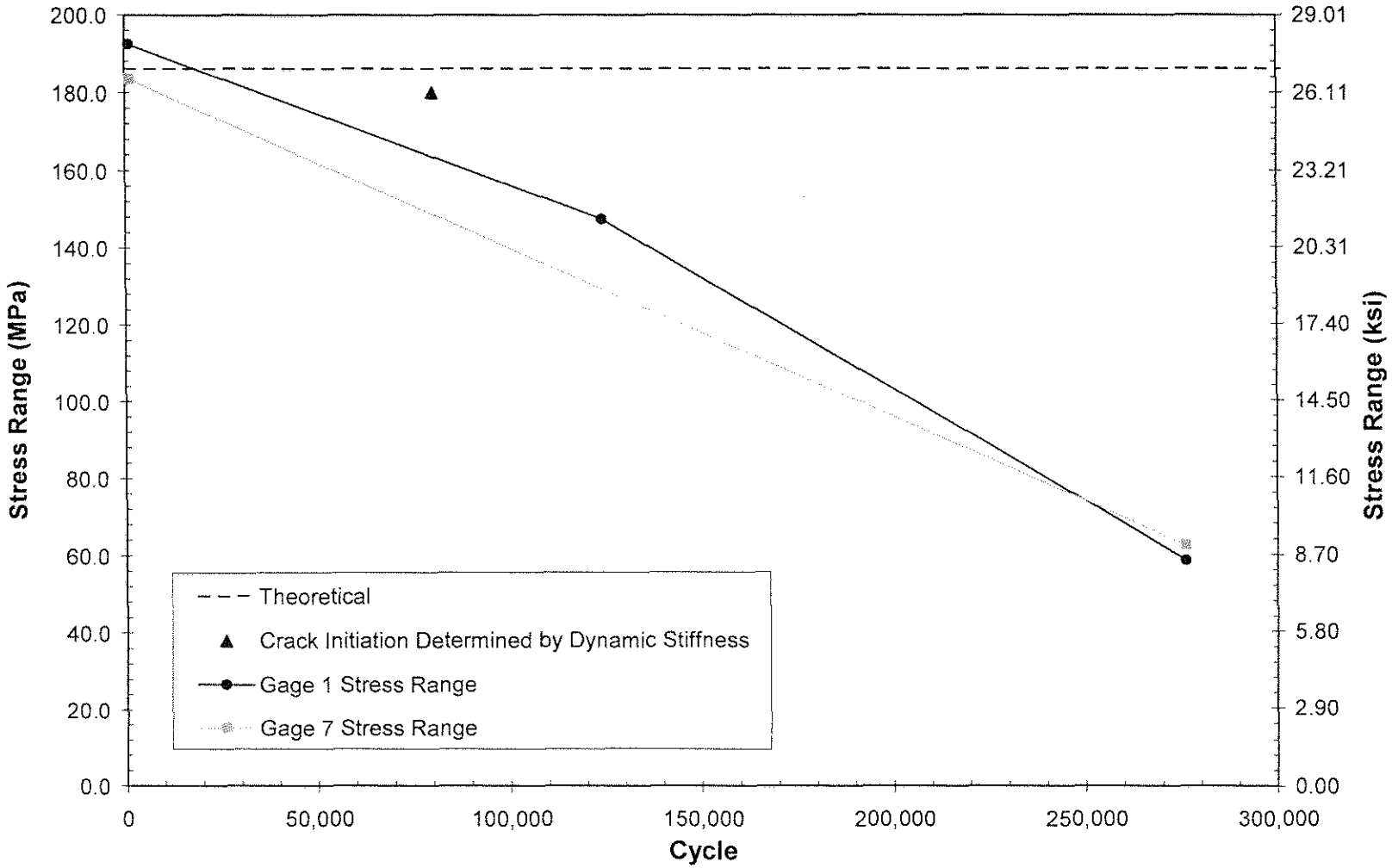

Figure D.1. Stress ranges recorded for Gage 2 and Gage 6 during fatigue testing of CONTROL_05.

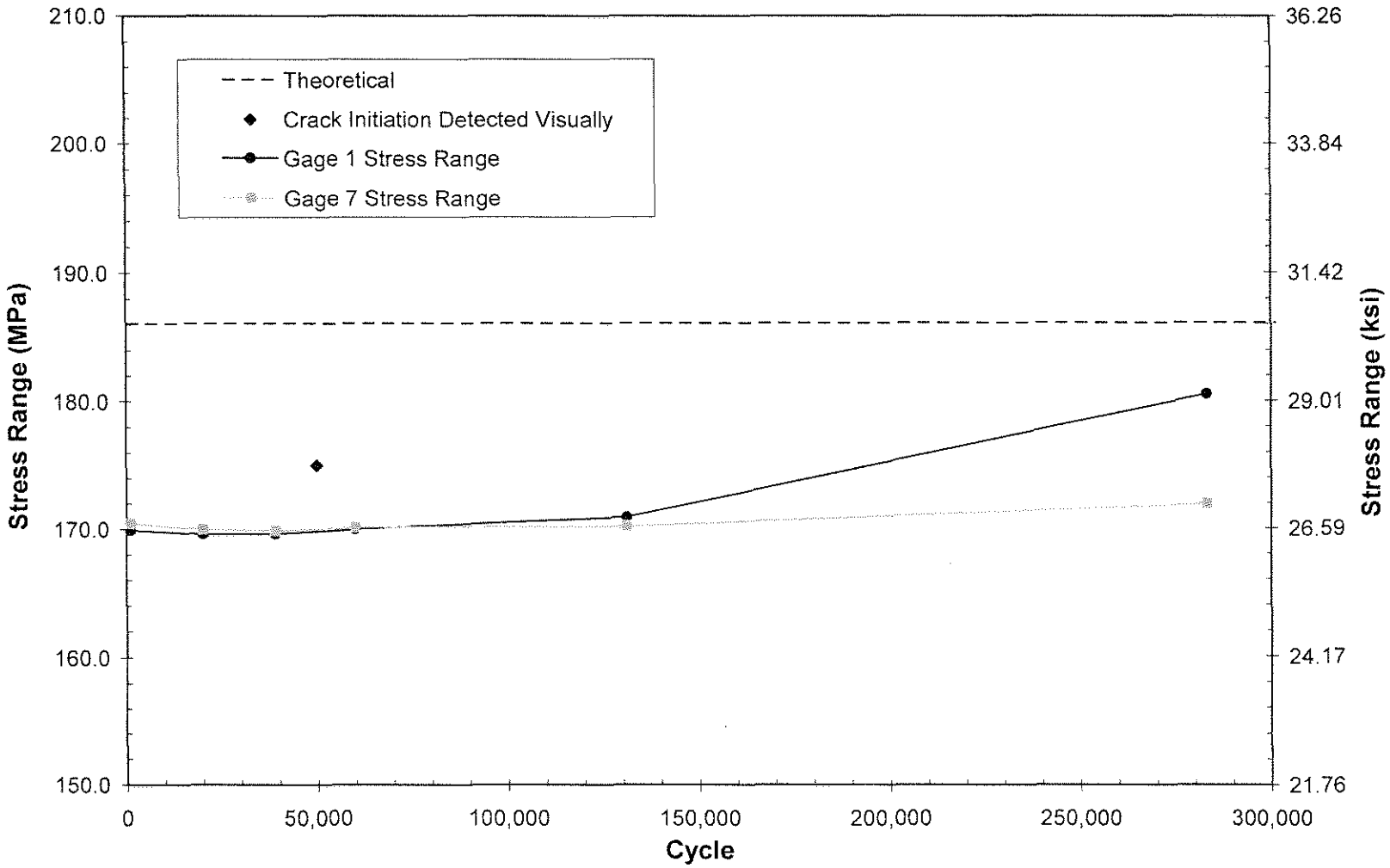

Figure D.2. Stress ranges recorded for Gage 2 and Gage 6 during fatigue testing of CONTROL_06.

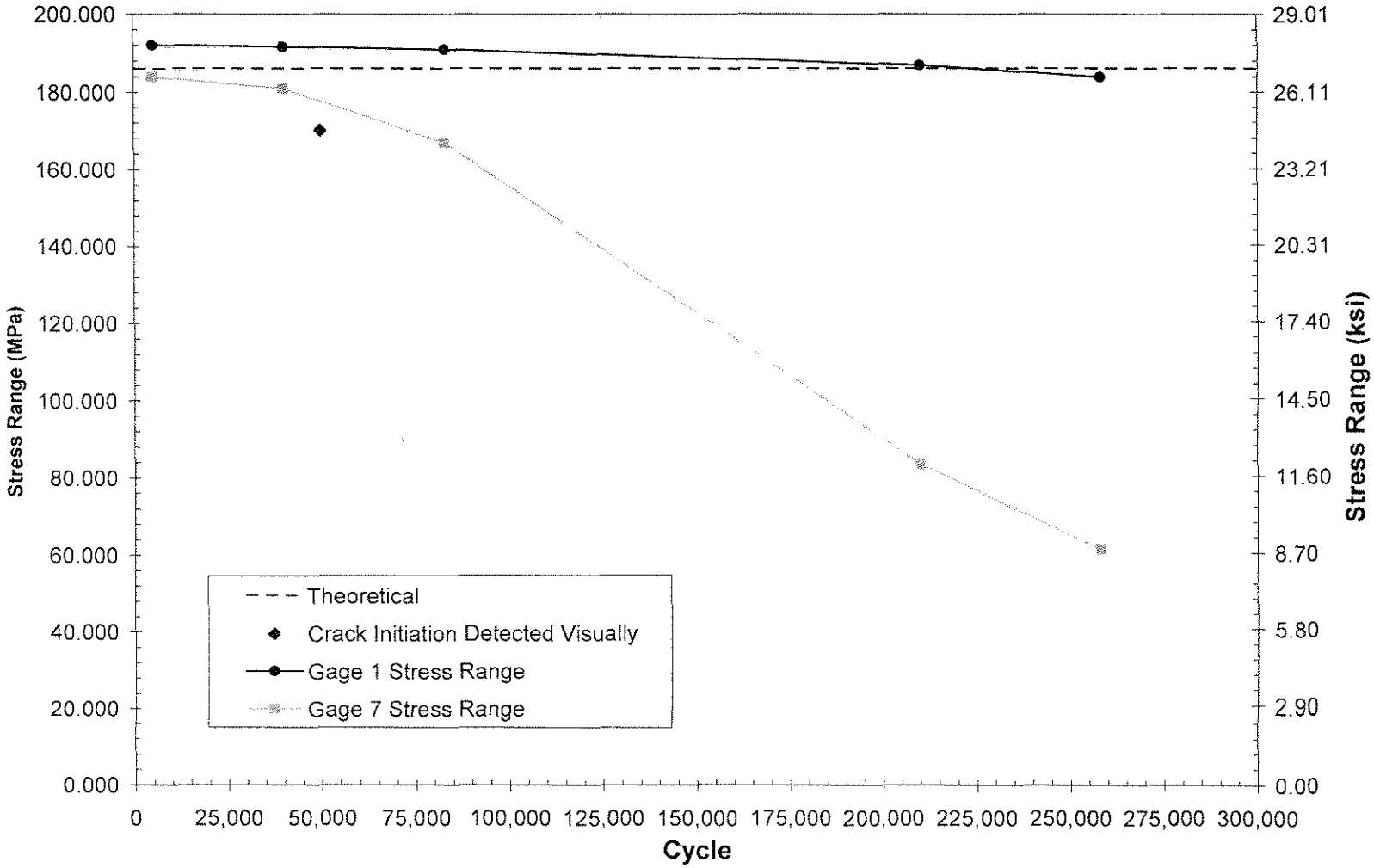

Figure D.3. Stress ranges recorded for Gage 2 and Gage 6 during fatigue testing of BOLT_02.

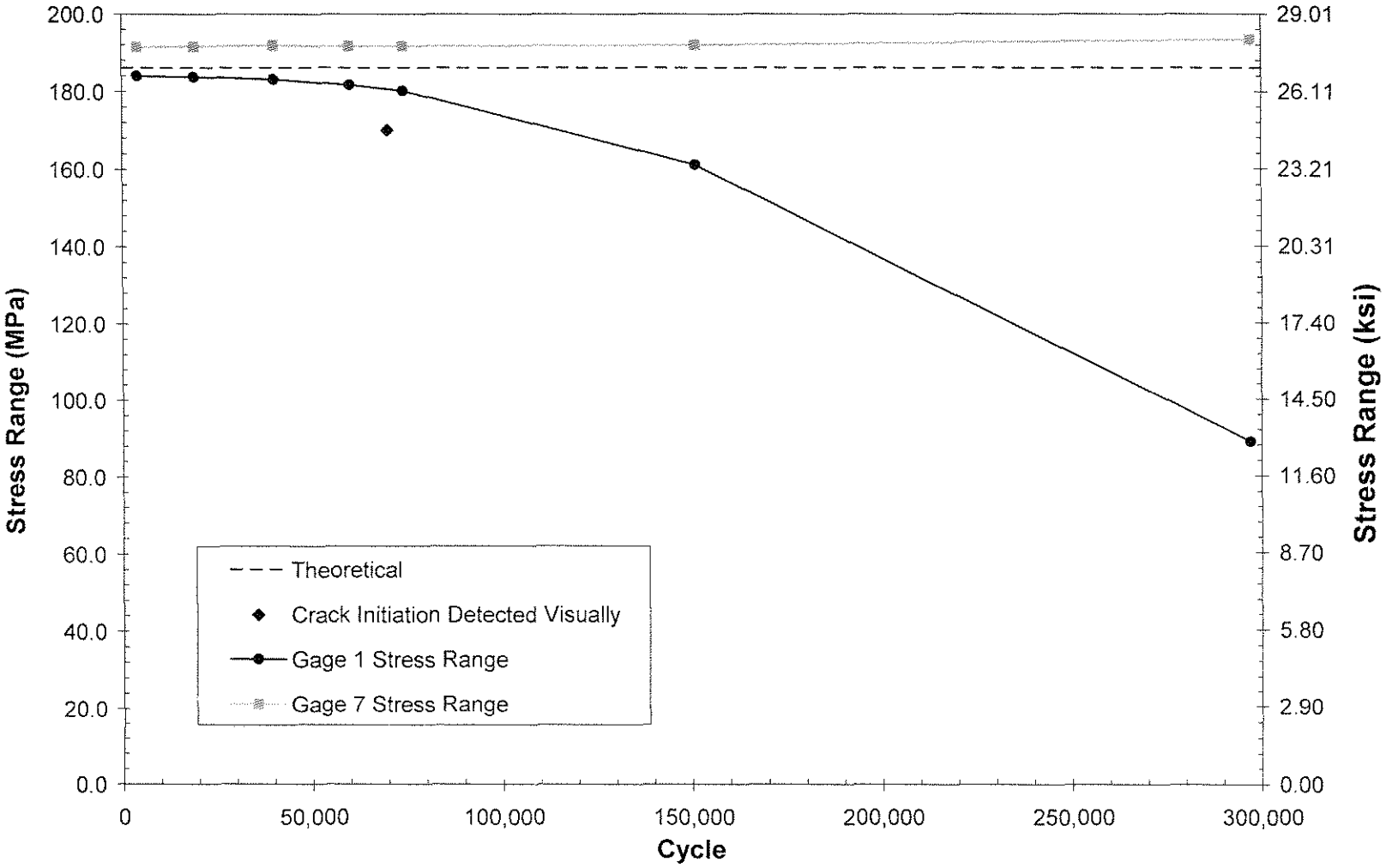

Figure D.4. Stress ranges recorded for Gage 2 and Gage 6 during fatigue testing of BOLT_03.

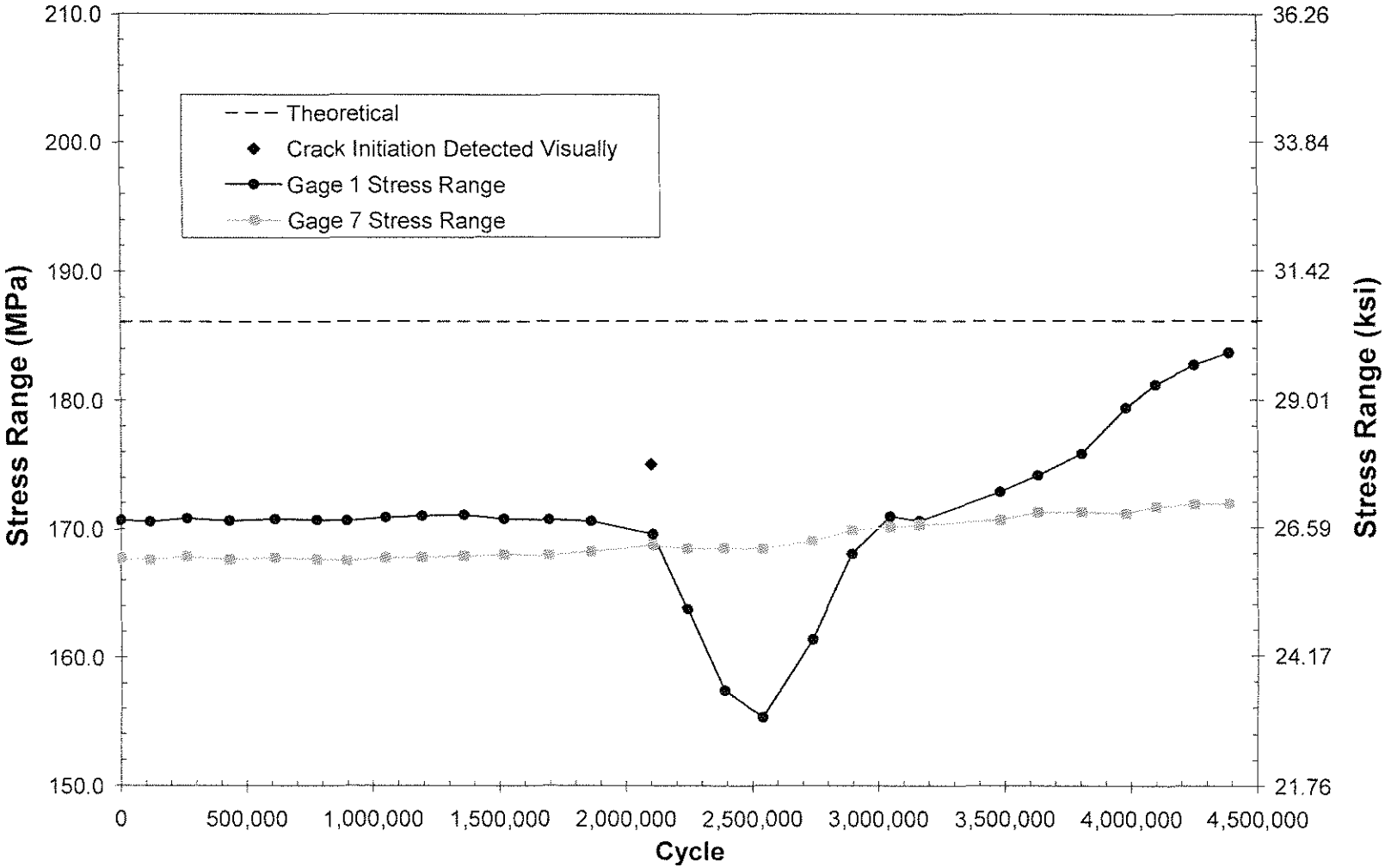

Figure D.5. Stress ranges recorded for Gage 2 and Gage 6 during fatigue testing of UIT_03.

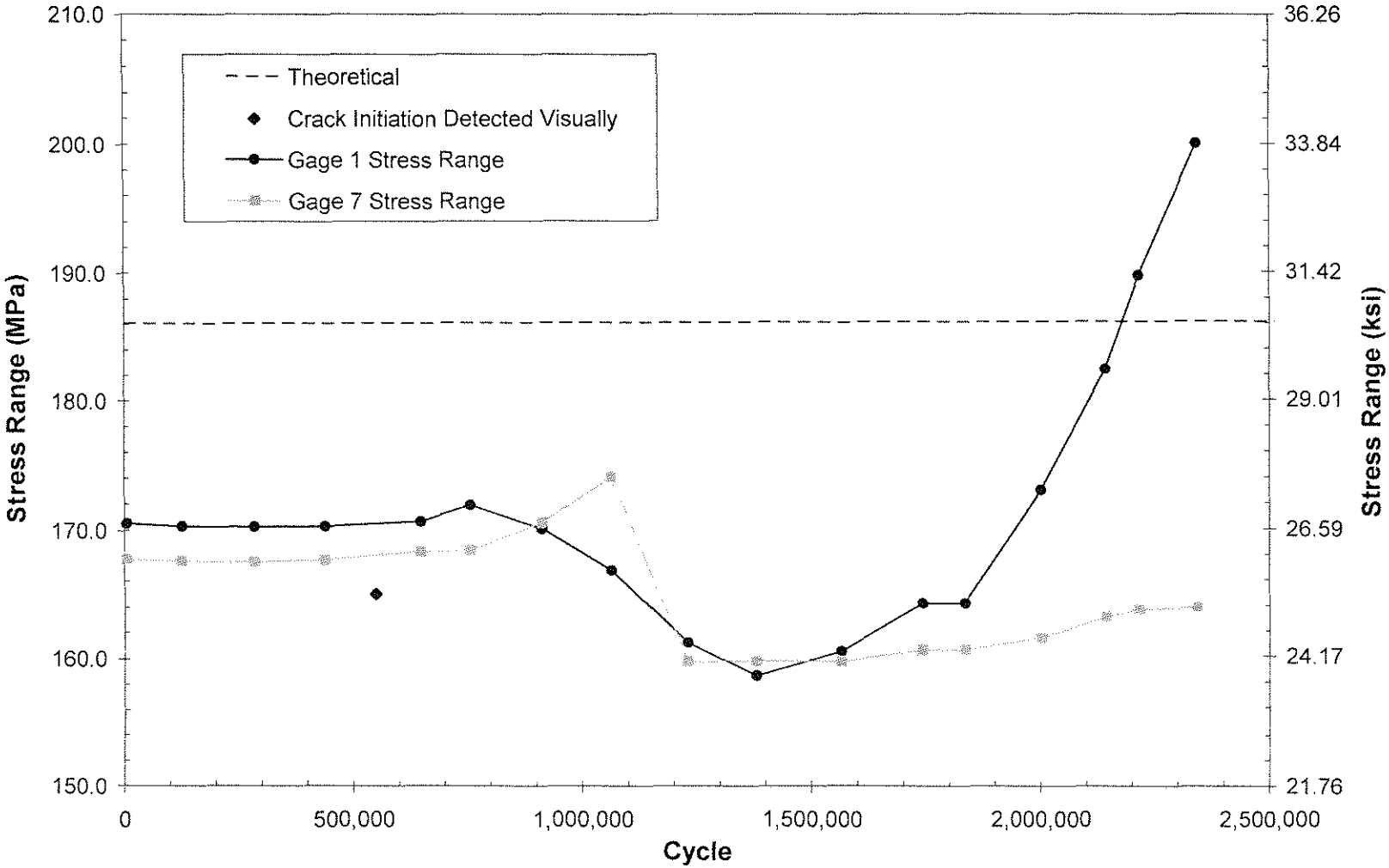

Figure D.6. Stress ranges recorded for Gage 2 and Gage 6 during fatigue testing of UIT/BOLT_01.

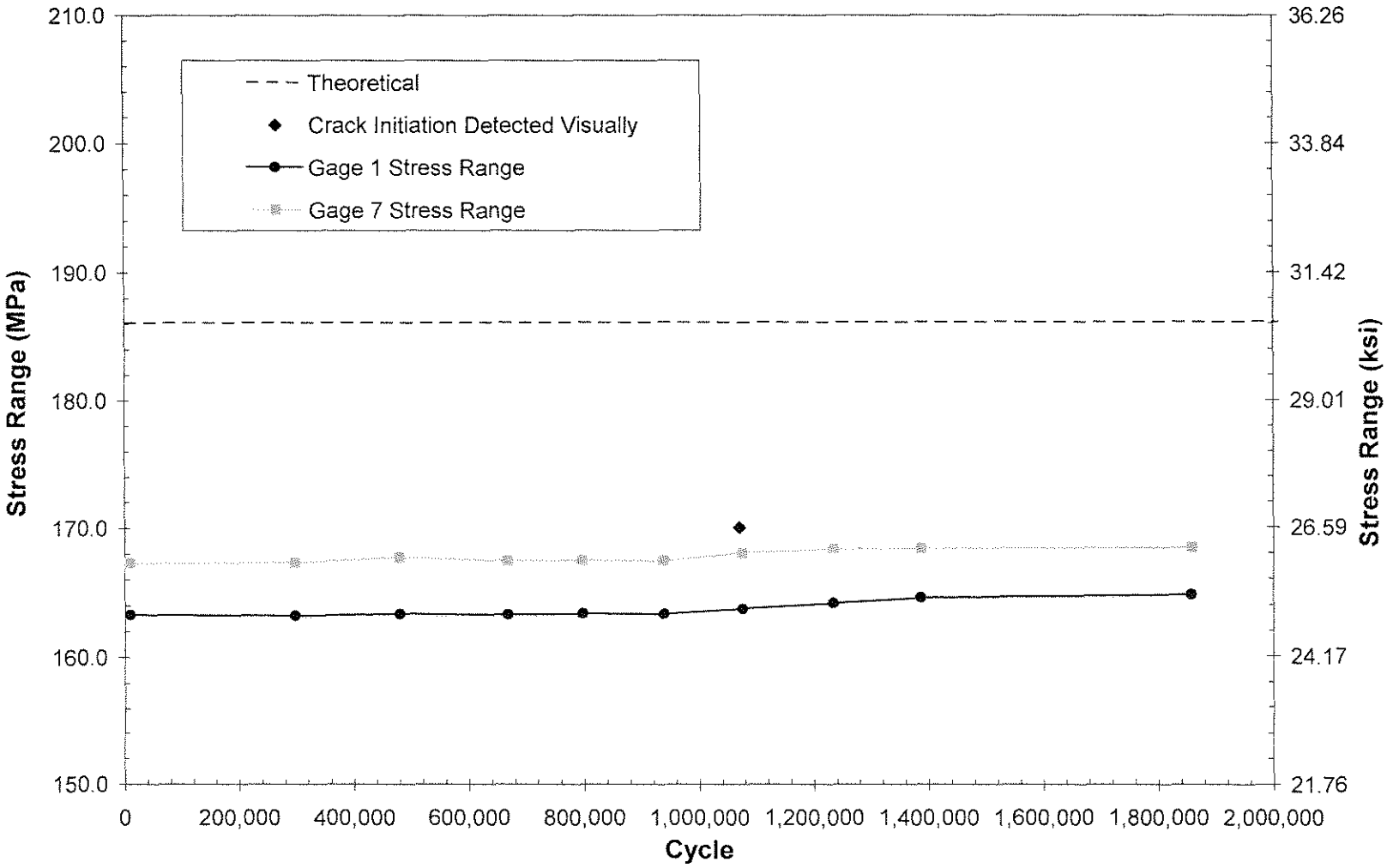

Figure D.7. Stress ranges recorded for Gage 2 and Gage 6 during fatigue testing of UIT/BOLT_02.

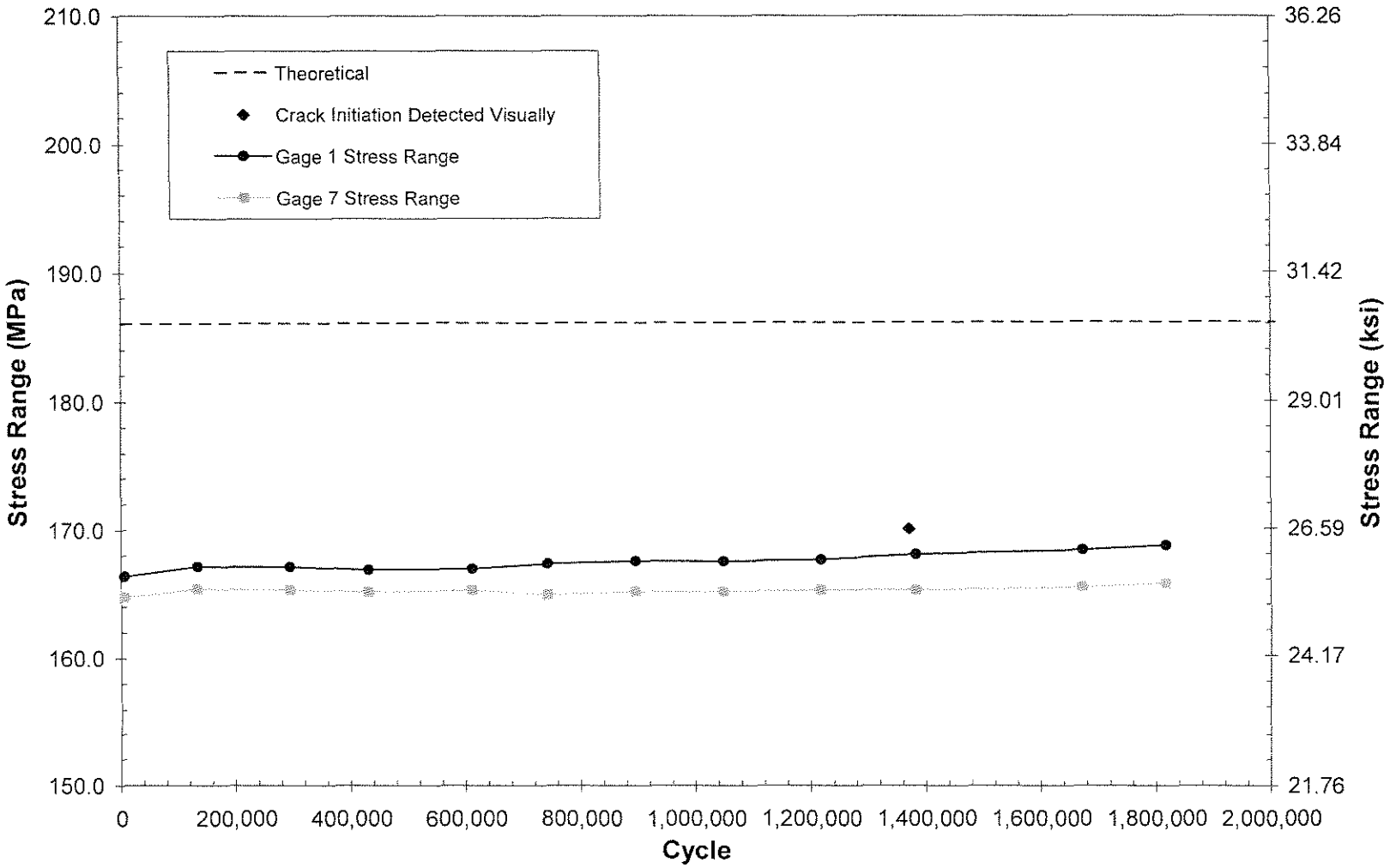

Figure D.8. Stress ranges recorded for Gage 2 and Gage 6 during fatigue testing of UIT/BOLT_03.

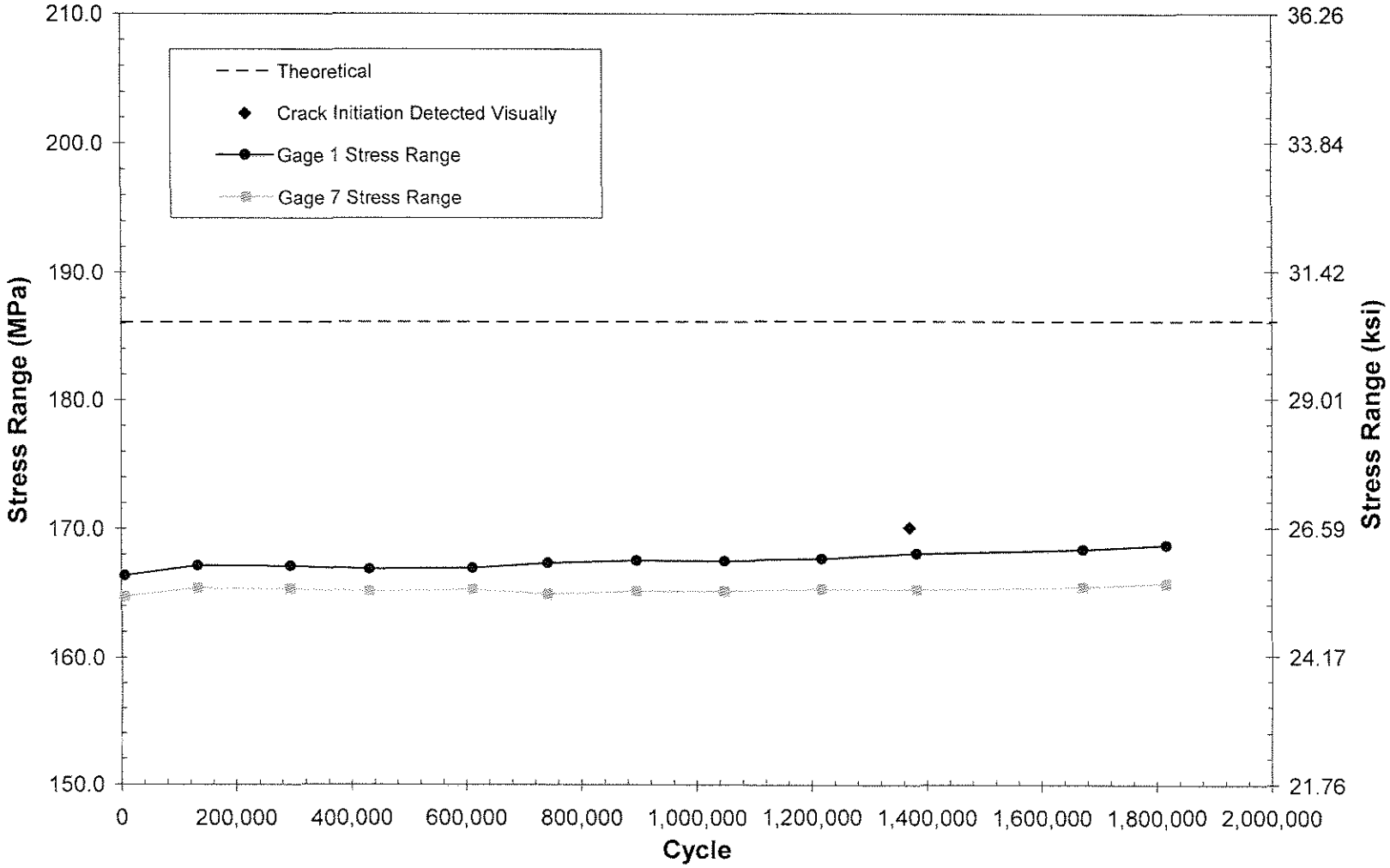

Figure D.8. Stress ranges recorded for Gage 2 and Gage 6 during fatigue testing of UIT/BOLT_03.

APPENDIX E TENSION TEST DATA

E.1 EXTENSOMETER CERTIFICATION

Epsilon

Extensometer Calibration Certificate

Model: 3542-0200-050-ST Date: 24-Jul-07

Extensometer S/N: E84702

Gage Length: 2.000 in. Travel (Tens): +1.000 in. Compression: -.200 in.

Travel (in.)	Output (mV)	
	UP	DOWN
0.000	0.000	0.004
0.200	4.999	4.999
0.400	10.021	10.007
0.600	15.053	15.038
0.800	20.095	20.081
1.000	25.146	25.146

Linearity (best fit)=	0.090 % F.S.
Full Scale Span (best fit)=	25.053 millivolts
Full Scale Span (best fit)=	2.505 mV/V
Max Hysteresis =	-0.050 % F.S.
Slope fit as 40% of FS =	25.150 mV/in.
Intercept =	-0.023 mV
Zero Output (with pin in):	-0.02 mV
Tension Span (end pt):	2.515 mV/V
Compression span (ep):	-0.498 mV/V
Excitation Voltage:	10.000 VDC

Connections for + output on tension:

FUNCTION	PIN	COLOR
Excitation (+)	1	Red
Excitation (-)	2	Black
Output (+)	15	Green
Output (-)	14	
Shield	3	

Instron Style 25 pin D-sub with Factory Code: 1070 (5350 ohms) Shunt Cal. Module

Shunt Calibration Data:	
Shunt Resistor:	SCM ohms
Shunted Reading:	2.505 mV/V
Shunted Reading:	100.002 % strain
(With Shunt Cal. Module plugged-in)	

Meter: Keithley 2000 S/N: 0625965

Calibrator: Epsilon 3590 S/N: A37785

Traceable to NIST standards

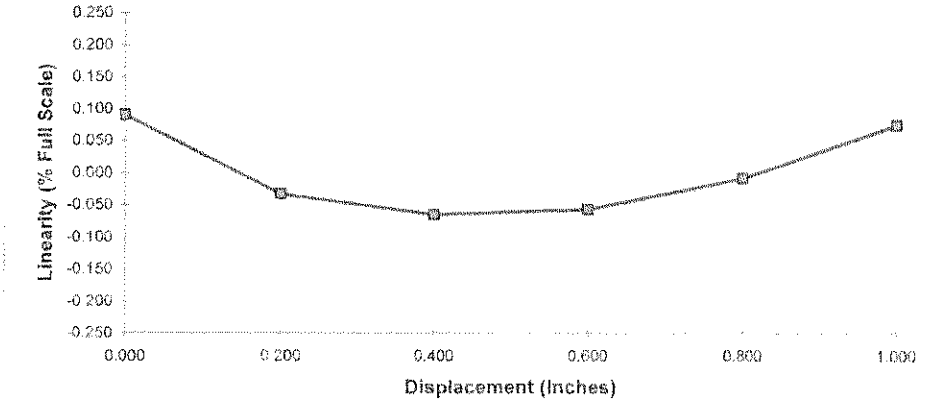

Calibrated by [illegible] Date: 07-24-07

Epsilon Technology Corp.

[illegible]

Figure E.1. Epsilon extensometer calibration certificate.

E.2. LINEAR STRESS-STRAIN BEHAVIOR

This section shows plots of stress versus strain prior to first yielding for 14 tensile specimens. During each tension test, load and strain data were measured by the testing machine's load cell and the Epsilon extensometer, respectively, an recorded by the controller. All data was plotted and analyzed using Microsoft Excel. These plots, shown in Figures E.2 through E.15, were used to determine the modulus of elasticity and yield strength of each tensile specimen. As discussed in section 4.6, the yield strengths calculated from these plots corresponded to the upper yield strength of the material as defined in ASTM test designation E 8 (ASTM 2001). The modulus of elasticity and yield strength are both shown on each plot.

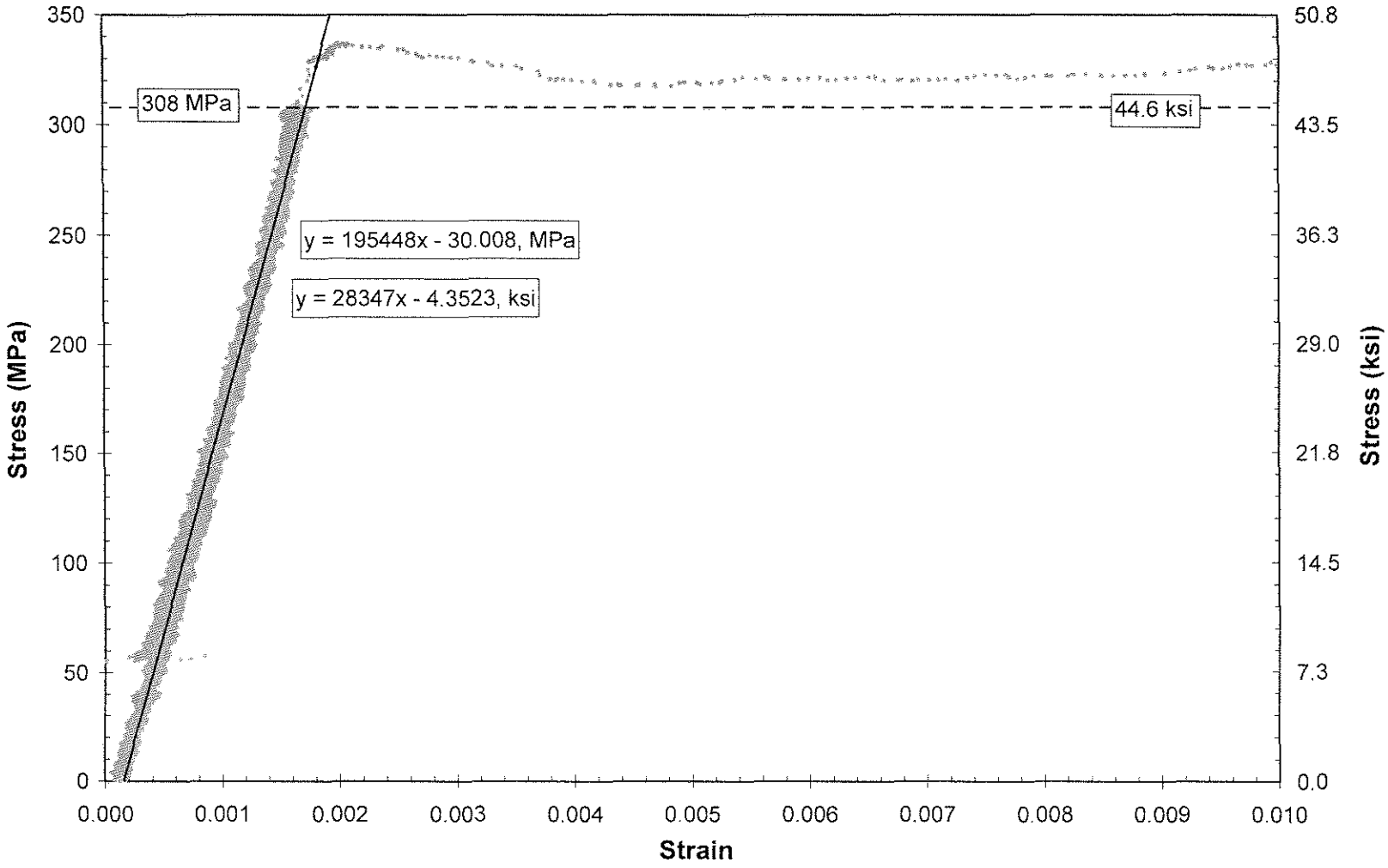

Figure E.2. Stress versus strain plot used to determine yield strength and modulus of elasticity for specimen T1.

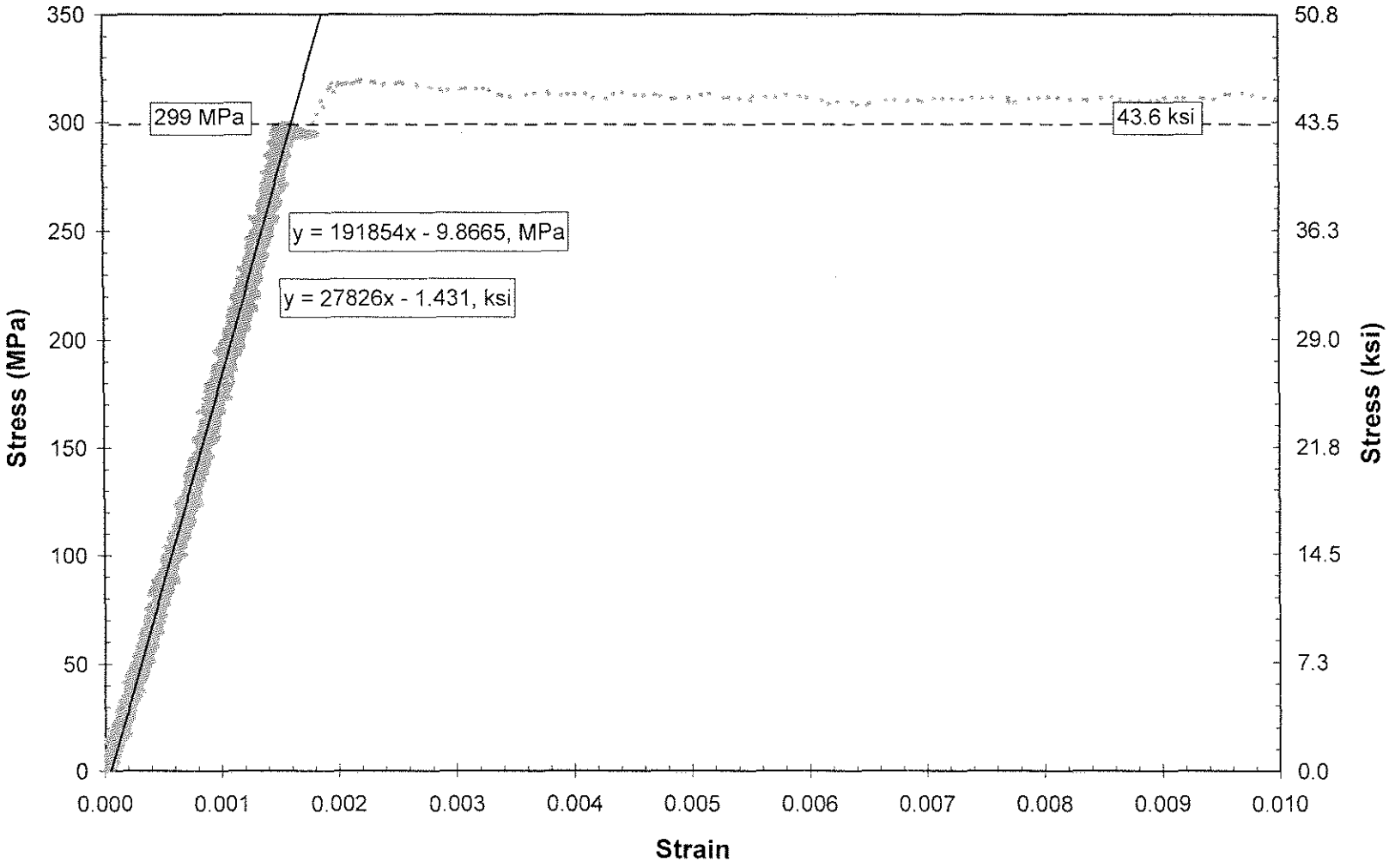

Figure E.3. Stress versus strain plot used to determine yield strength and modulus of elasticity for specimen T2.

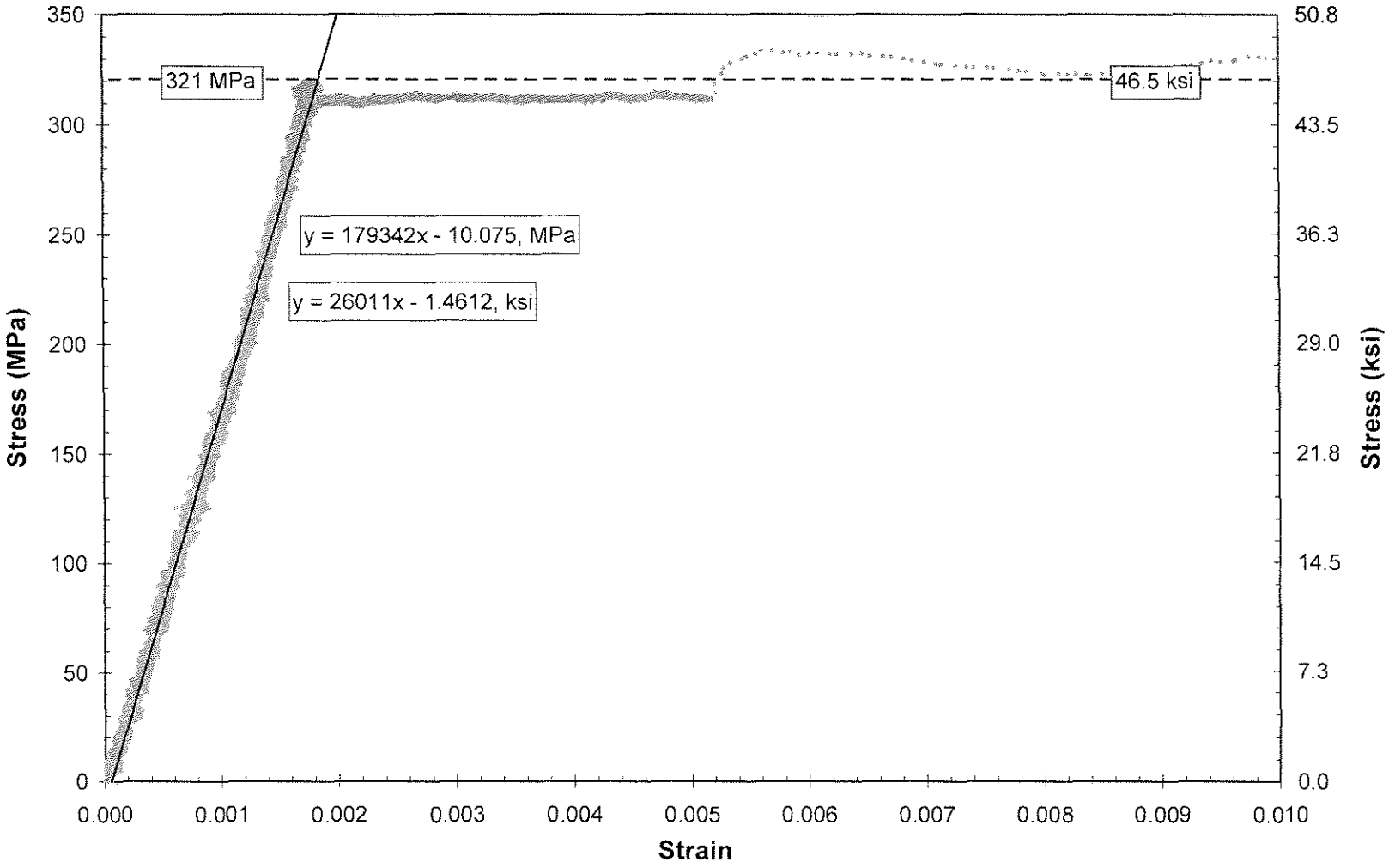

Figure E.4. Stress versus strain plot used to determine yield strength and modulus of elasticity for specimen T3.

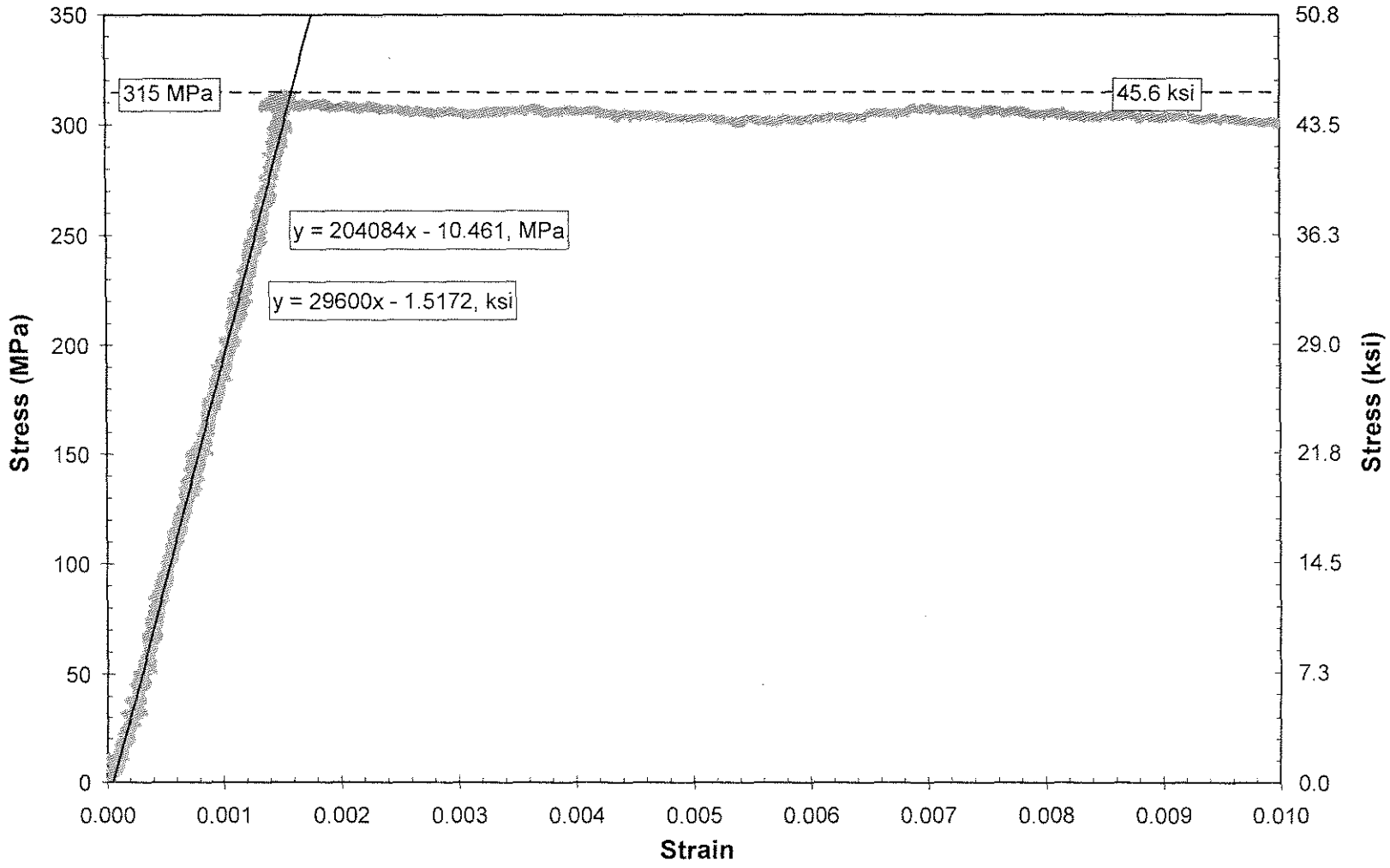

Figure E.5. Stress versus strain plot used to determine yield strength and modulus of elasticity for specimen T4.

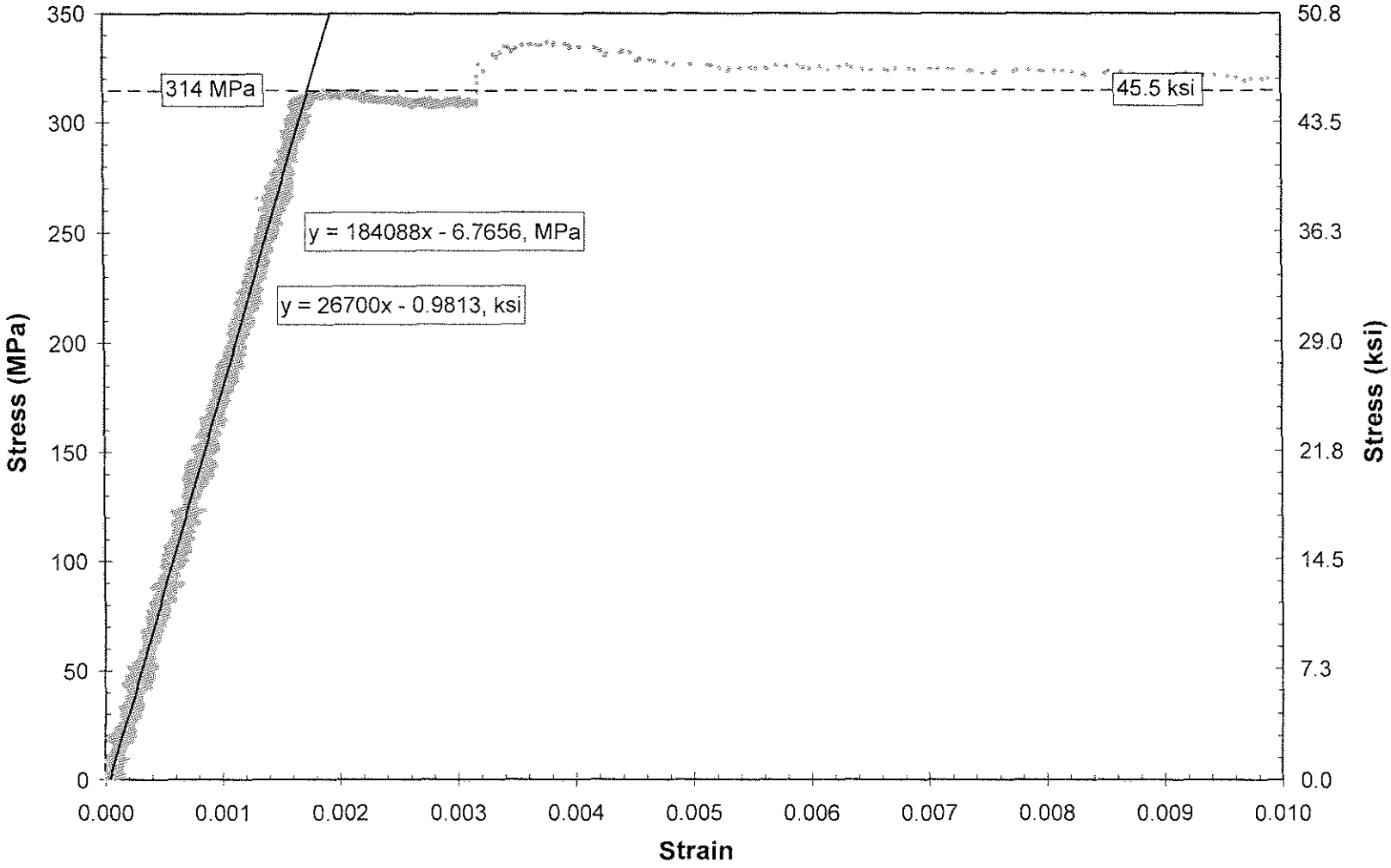

Figure E.6. Stress versus strain plot used to determine yield strength and modulus of elasticity for specimen T5.

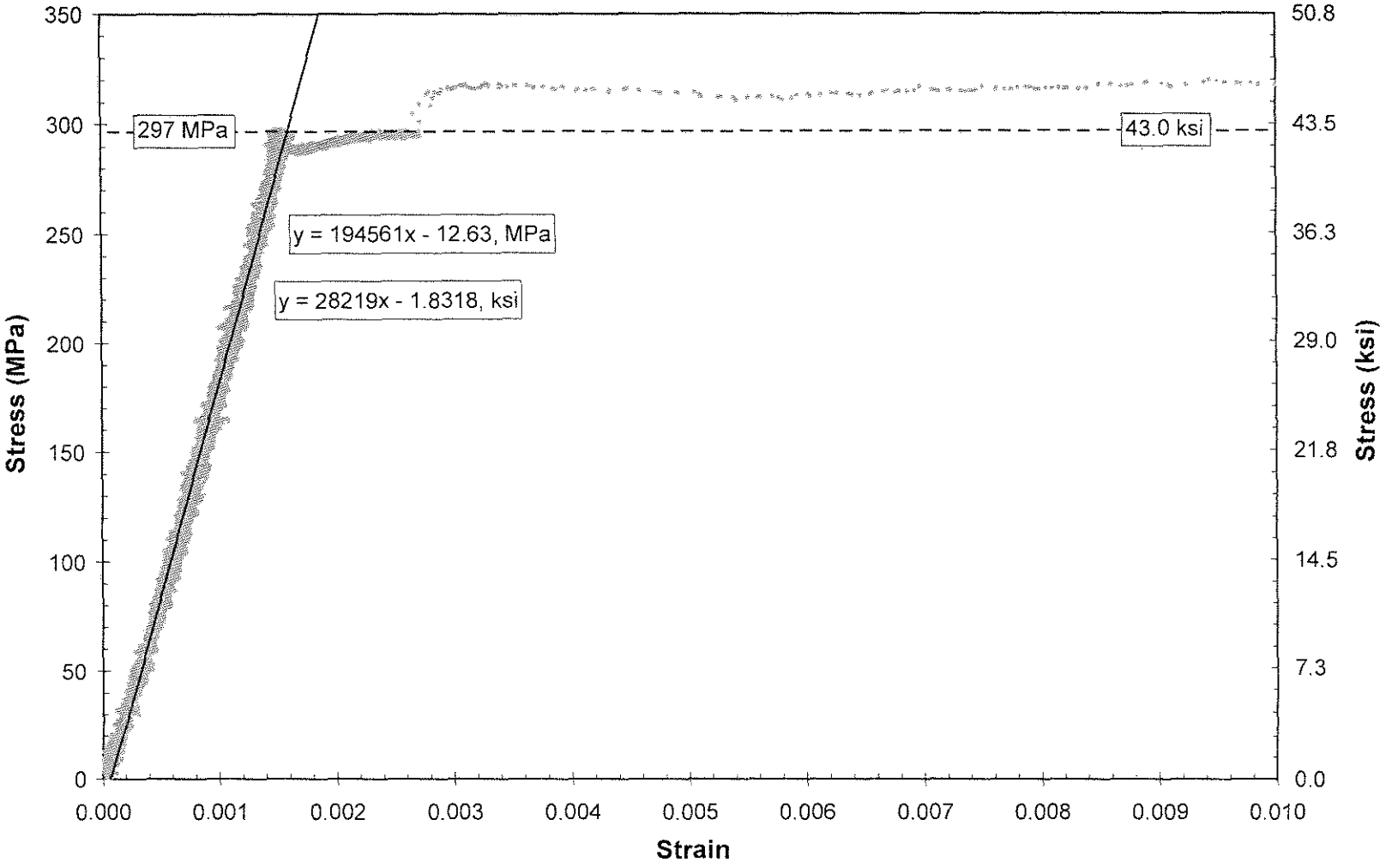

Figure E.7. Stress versus strain plot used to determine yield strength and modulus of elasticity for specimen T6.

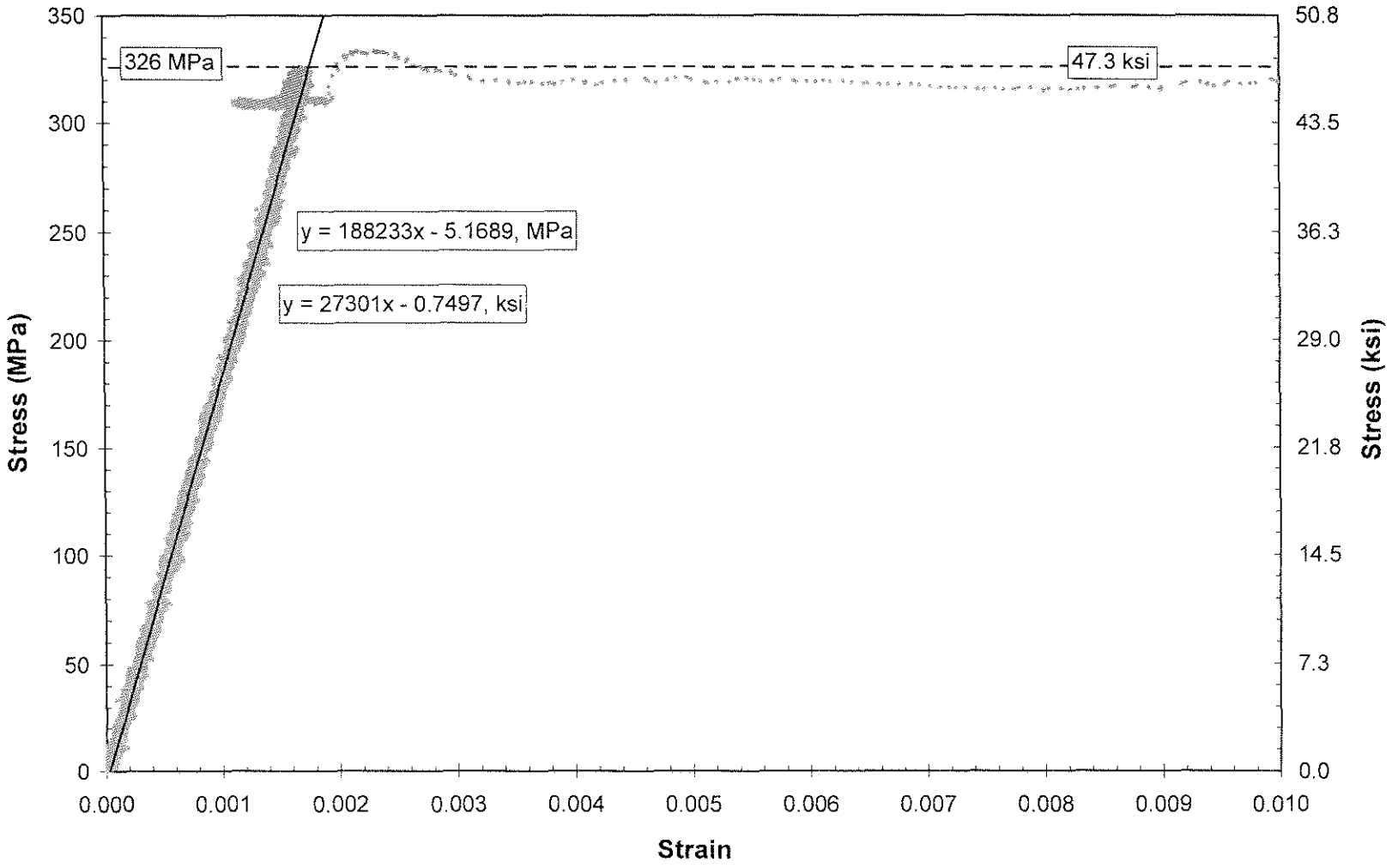

Figure E.8. Stress versus strain plot used to determine yield strength and modulus of elasticity for specimen T7.

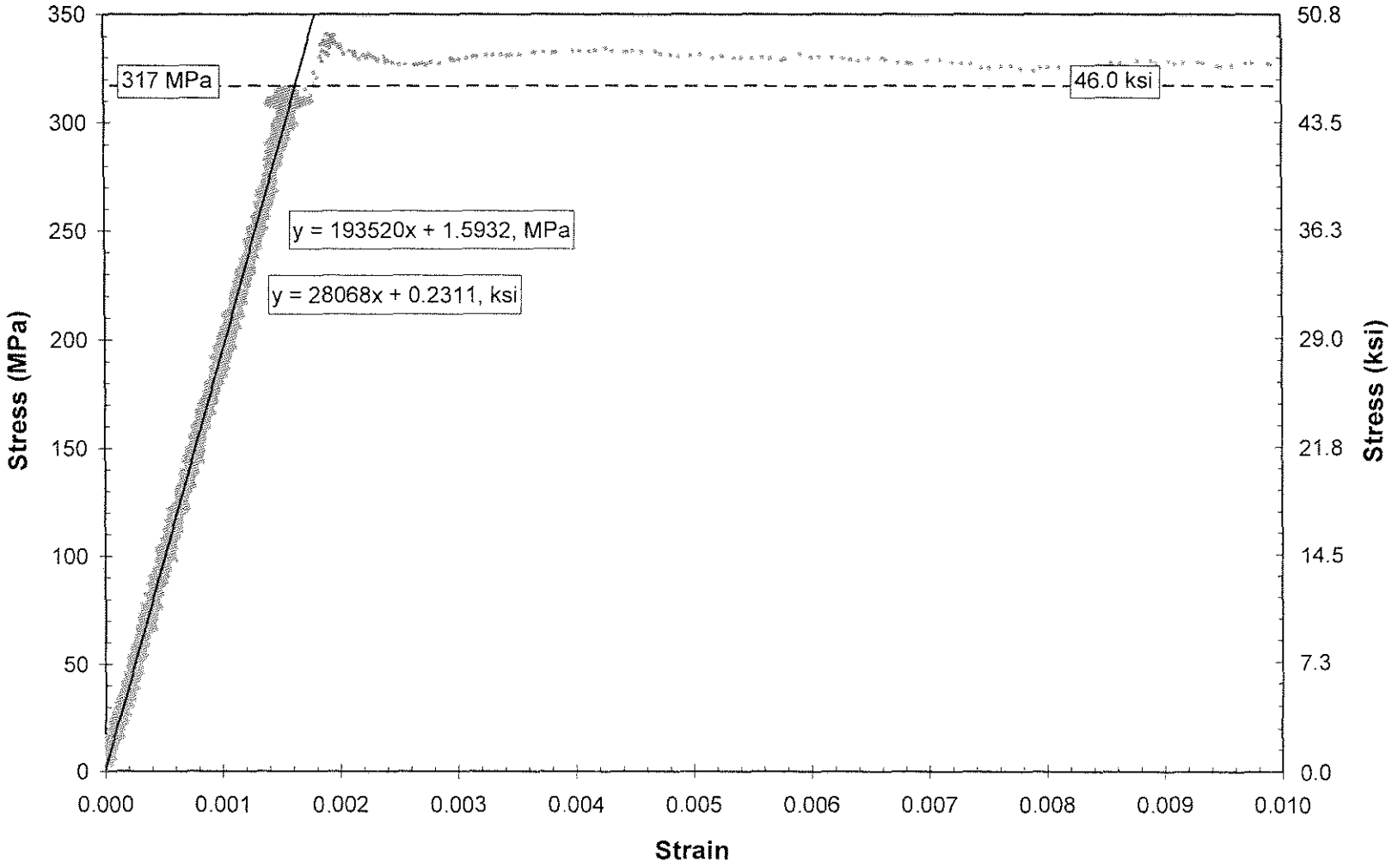

Figure E.9. Stress versus strain plot used to determine yield strength and modulus of elasticity for specimen T8.

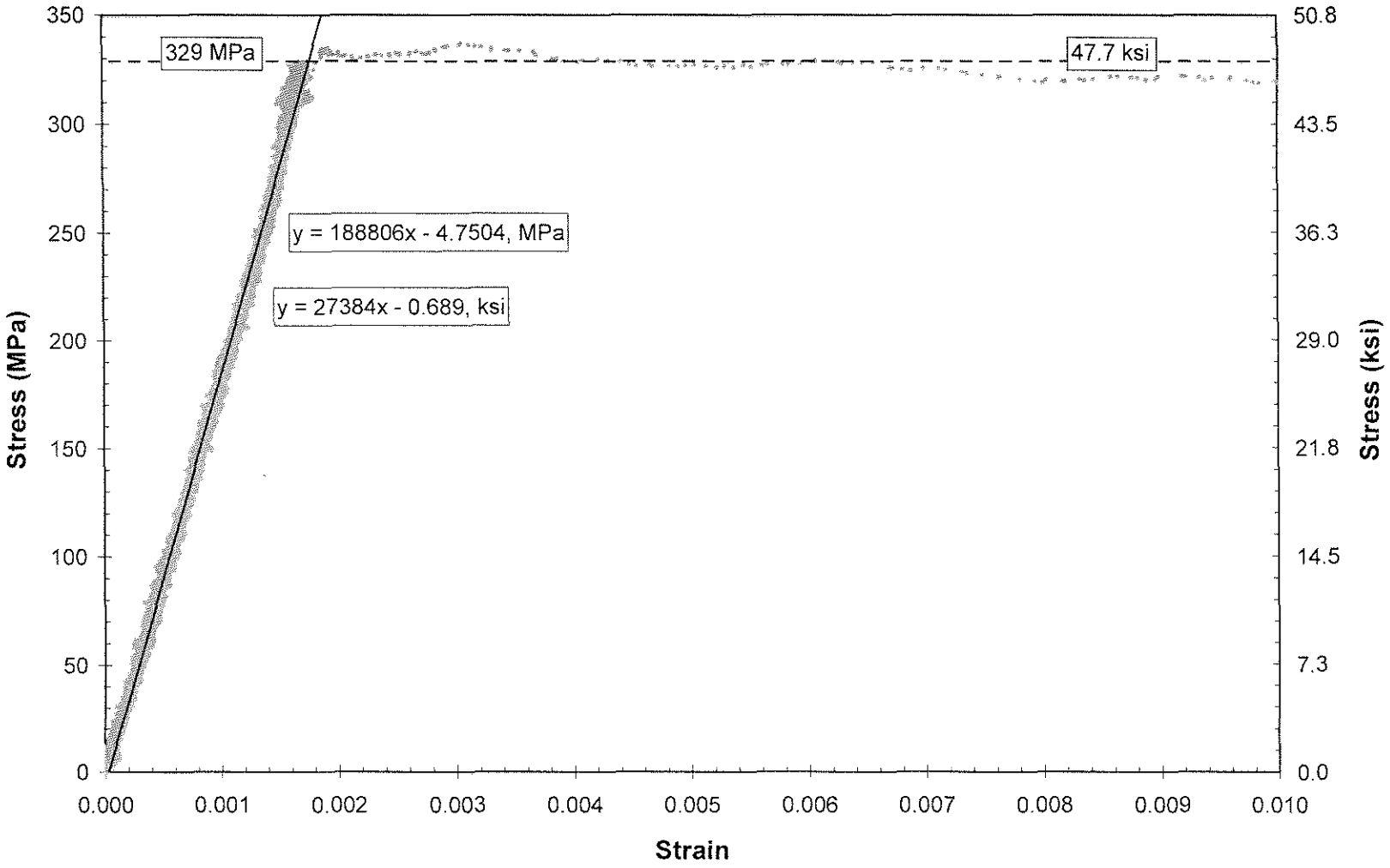

Figure E.10. Stress versus strain plot used to determine yield strength and modulus of elasticity for specimen T9.

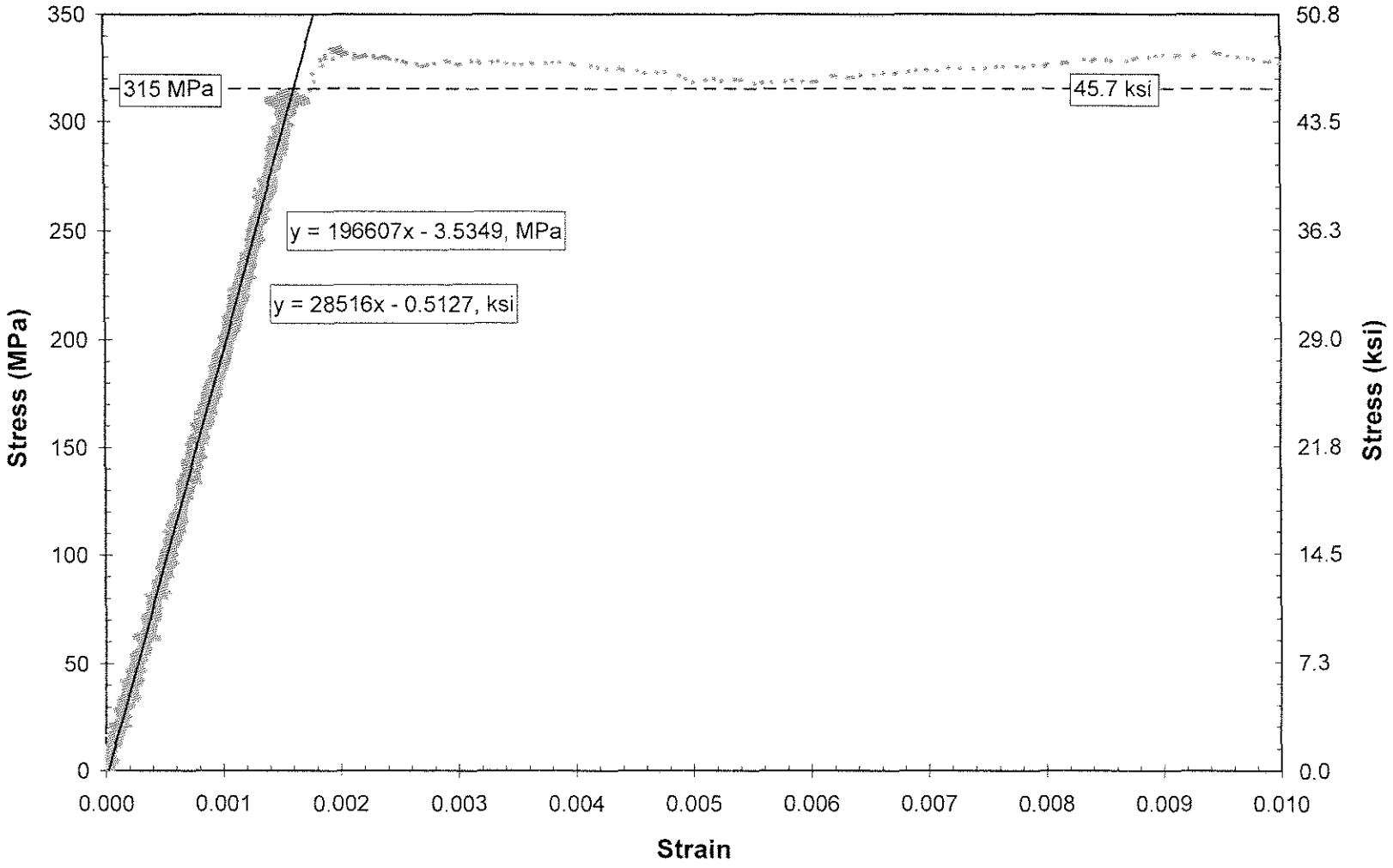

Figure E.11. Stress versus strain plot used to determine yield strength and modulus of elasticity for specimen T10.

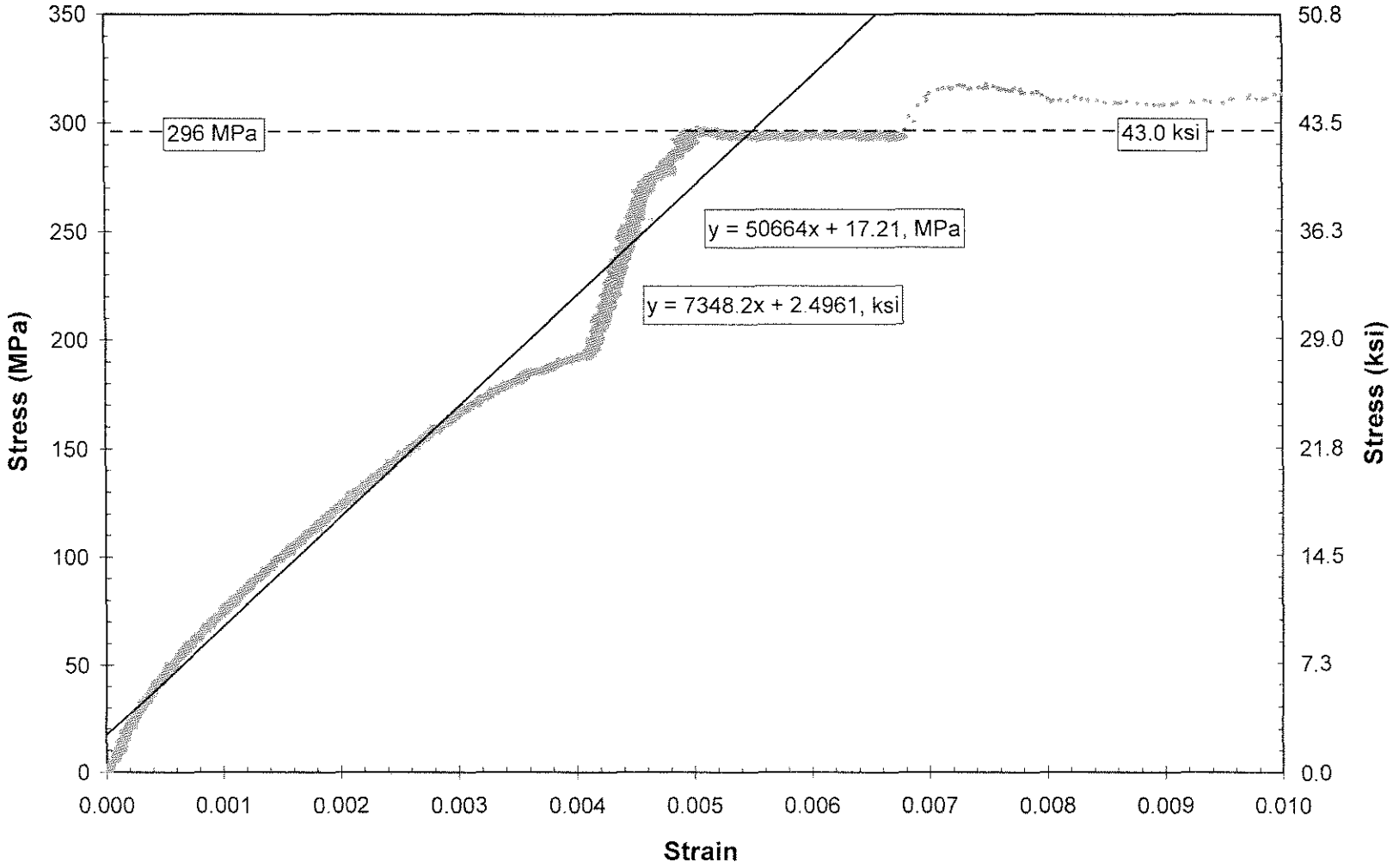

Figure E.12. Stress versus strain plot used to determine yield strength and modulus of elasticity for specimen T11.

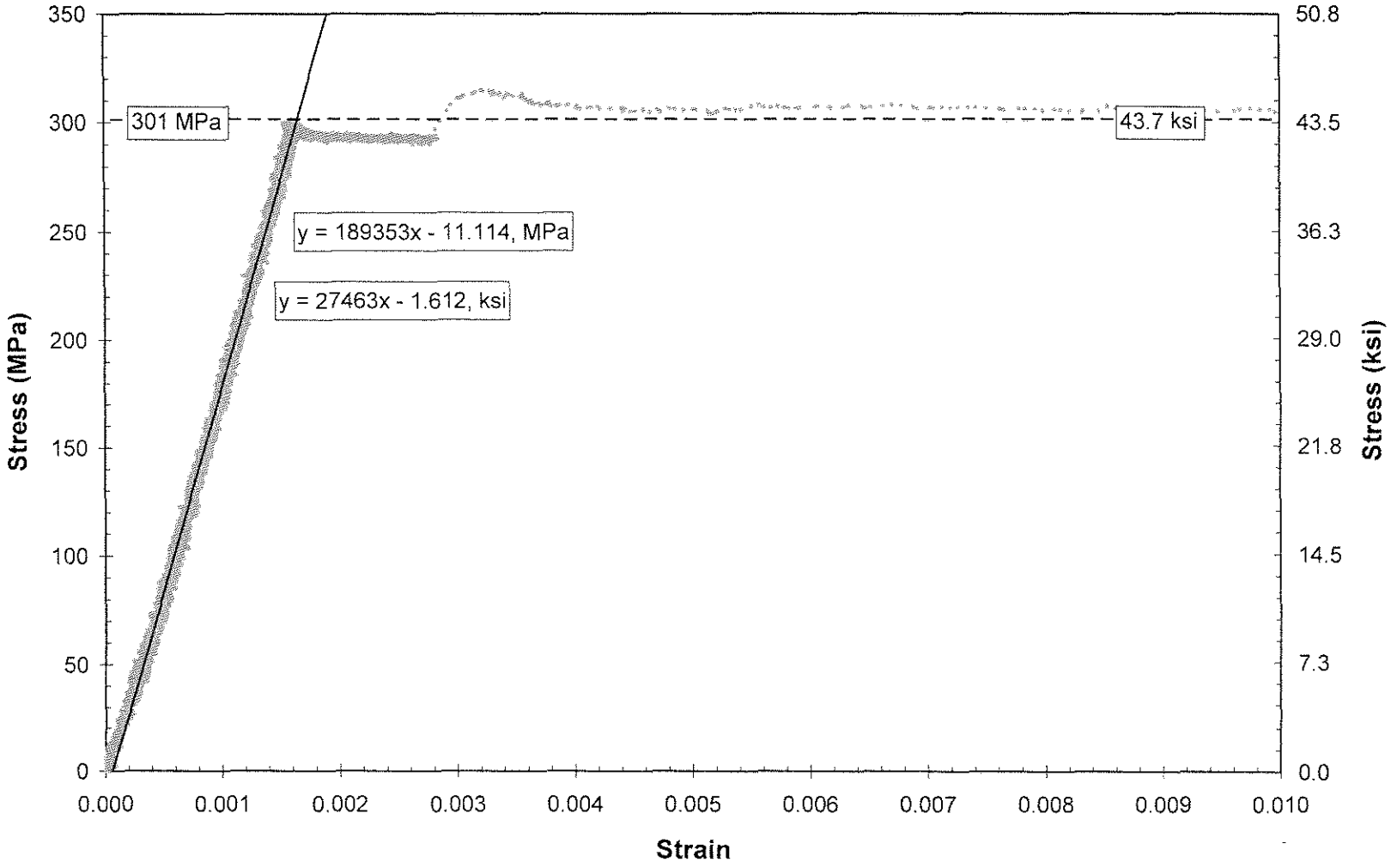

Figure E.13. Stress versus strain plot used to determine yield strength and modulus of elasticity for specimen T12.

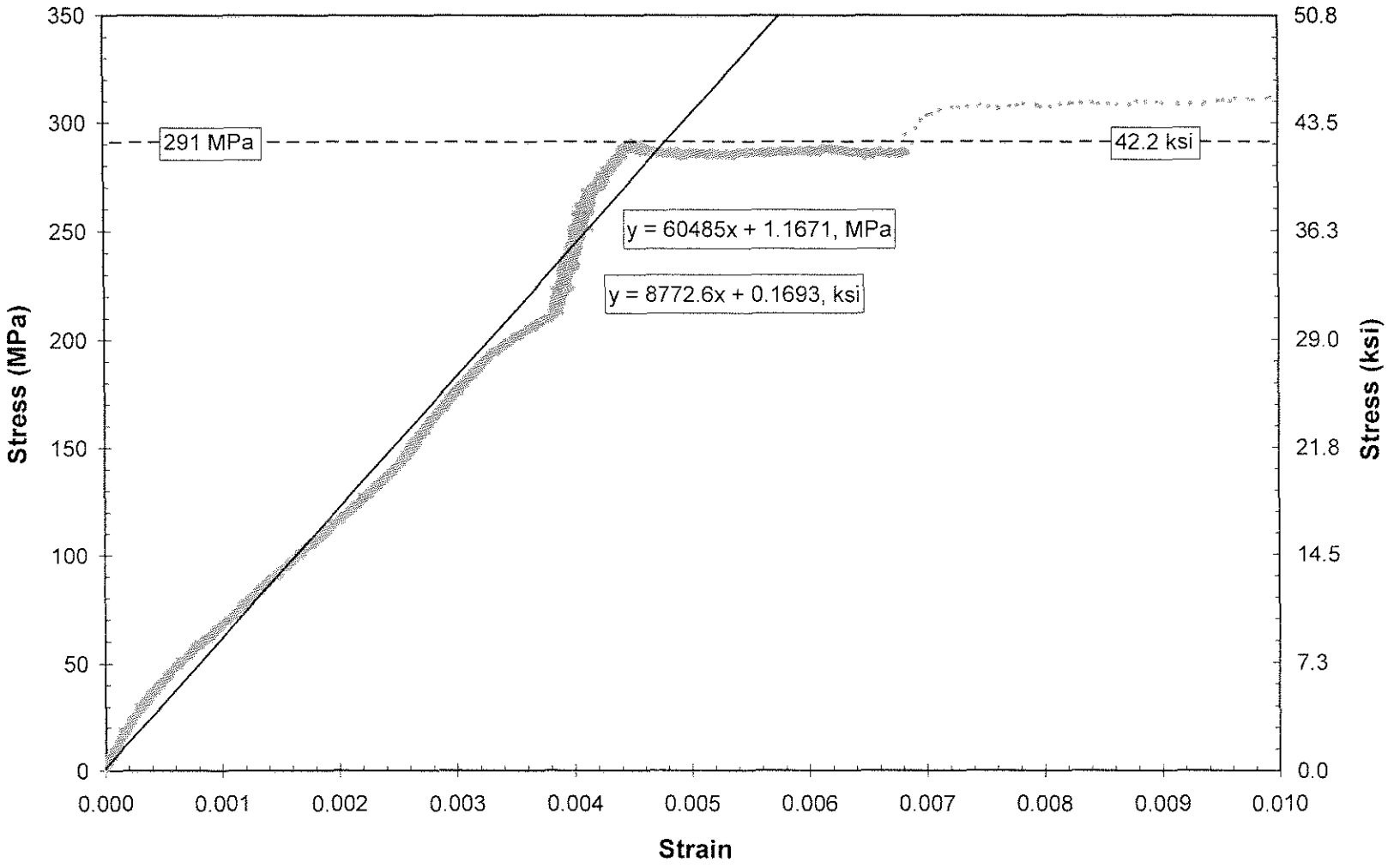

Figure E.14. Stress versus strain plot used to determine yield strength and modulus of elasticity for specimen T13.

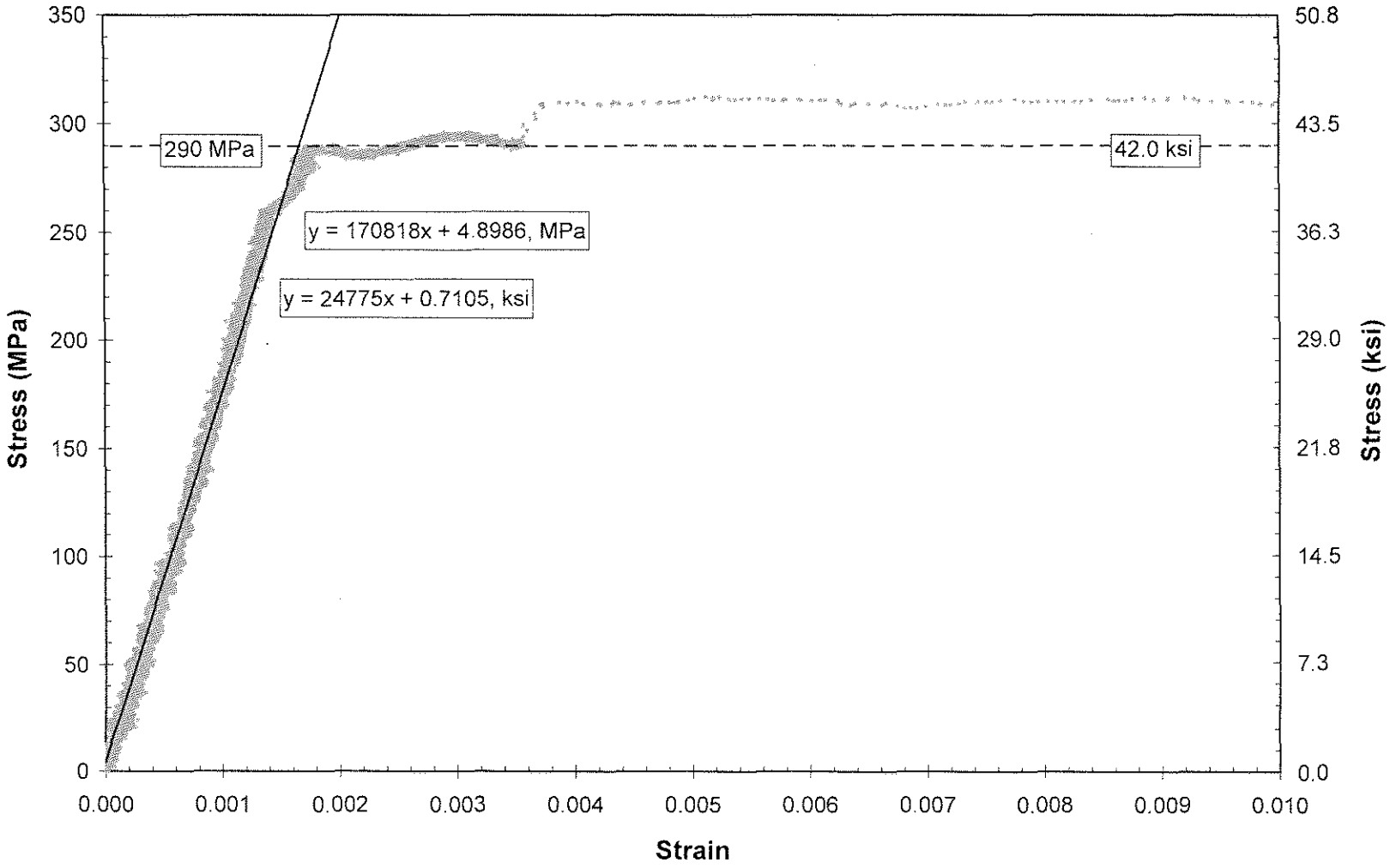

Figure E.15. Stress versus strain plot used to determine yield strength and modulus of elasticity for specimen T14.

E.3 COMPLETE STRESS-STRAIN CURVES

Plots of stress versus strain for the entire duration of each tension test are shown in this section. Data used to plot these curves were measured by the testing machine's load cell and internal LVDT as well as the Epsilon Extensometer. All plots were generated using Microsoft Excel. Per ASTM test designation E 8 (ASTM 2001), the stress-strain curve through the point of first yielding was determined using data measured by the load cell and the extensometer. Close to specimen failure (after tensile strength had been reached), the extensometer was removed so that it would not be damaged when the specimen fractured. To plot the remainder of the stress-strain curve, data measured by the internal LVDT was used in place of the extensometer data. The point at which the extensometer was removed is indicated by the end of black data points and the start of grey data points in Figures E.16 through E.29. These figures also show the tensile strength of each specimen, corresponding to the point of maximum applied load in a specimen.

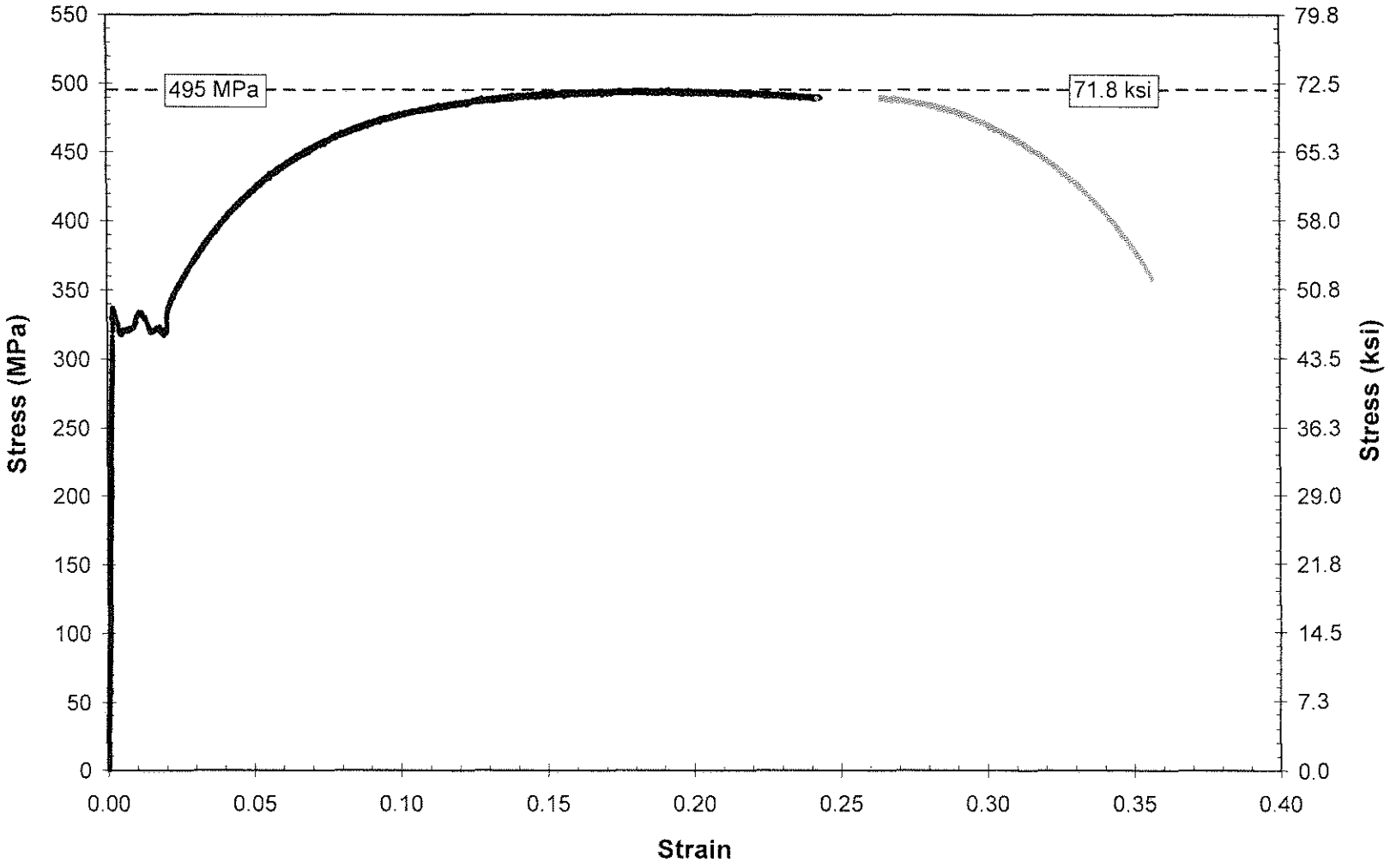

Figure E.16. Stress versus strain plot used to determine tensile strength for specimen T1.

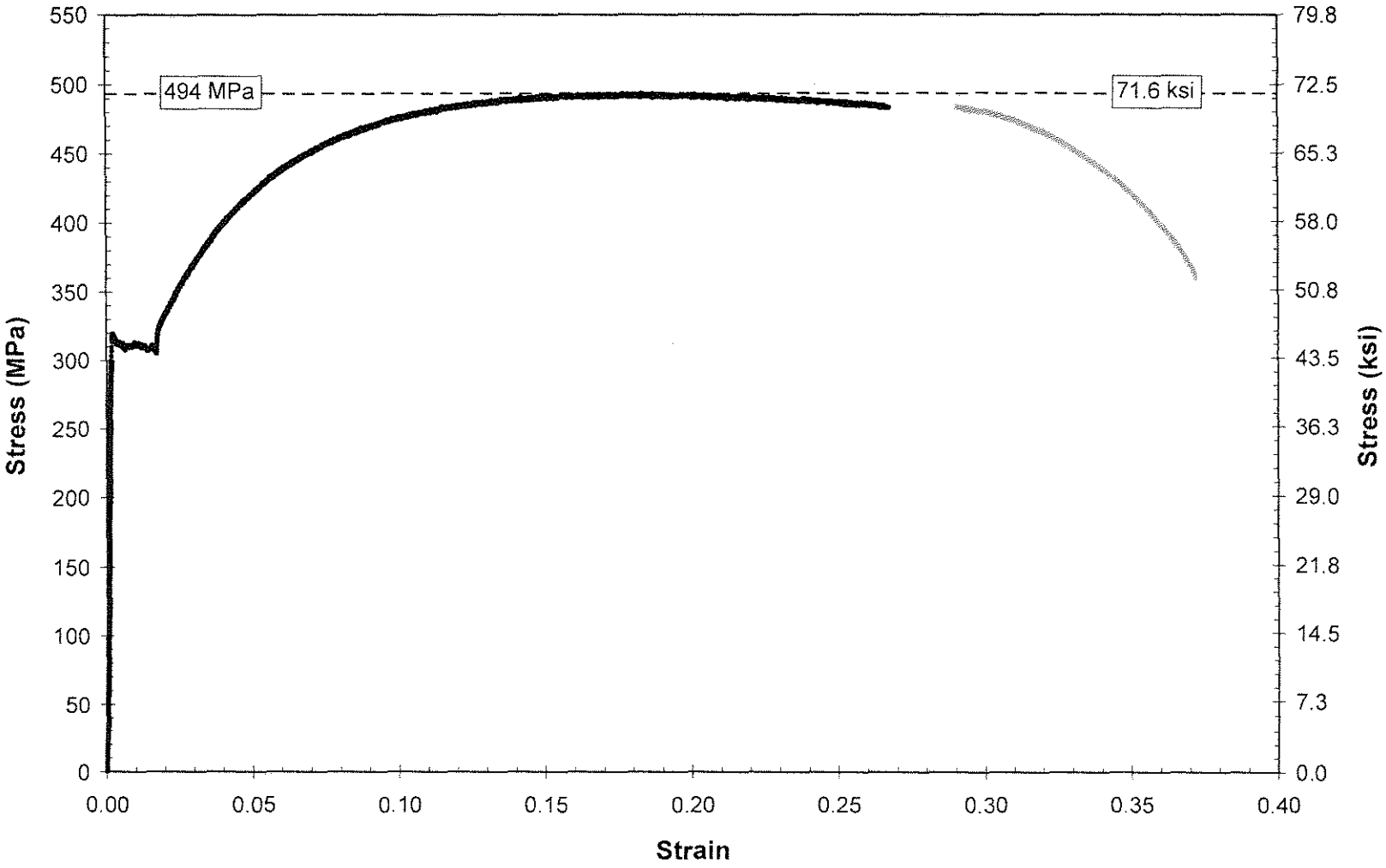

Figure E.17. Stress versus strain plot used to determine tensile strength for specimen T2.

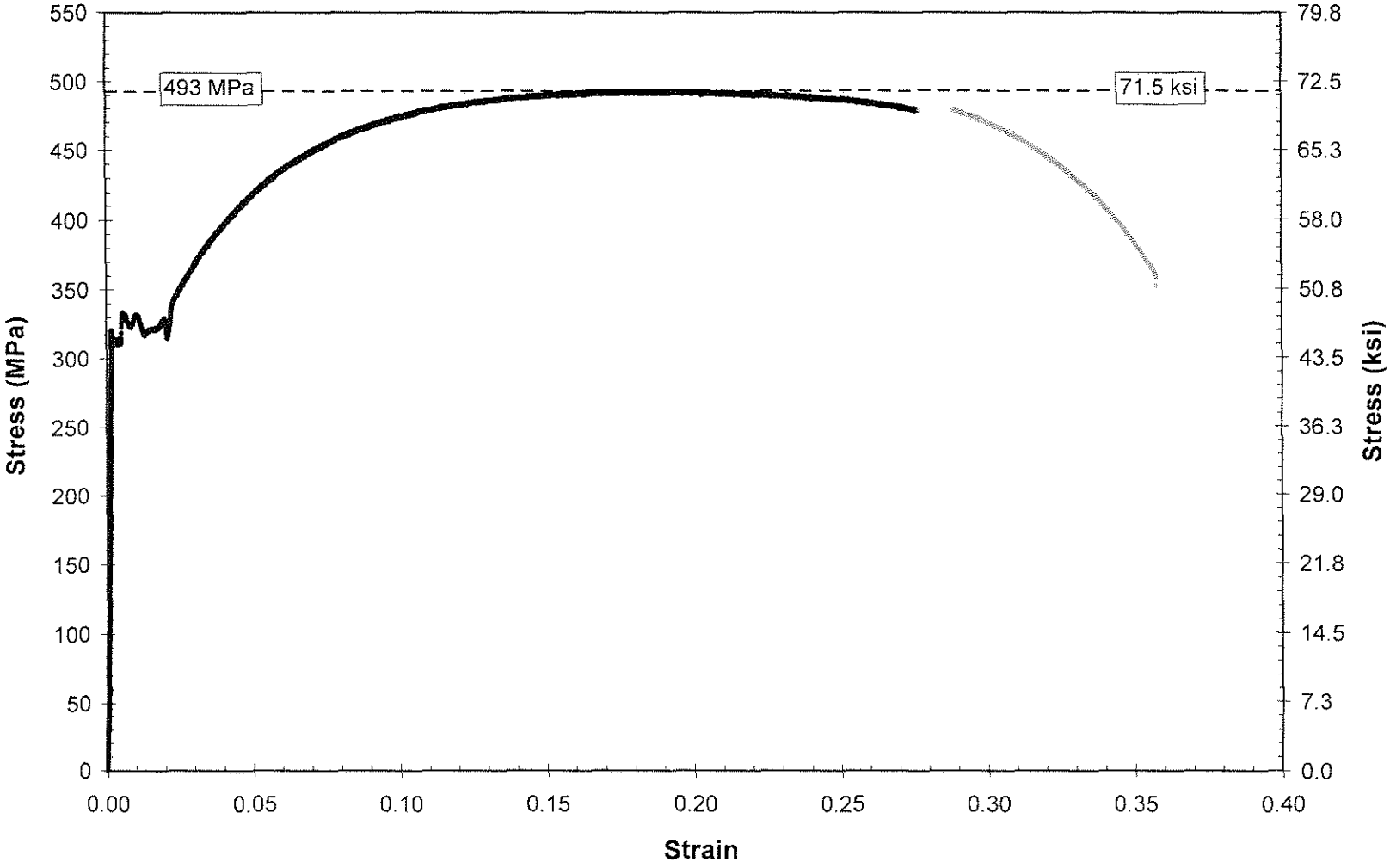

Figure E.18. Stress versus strain plot used to determine tensile strength for specimen T3.

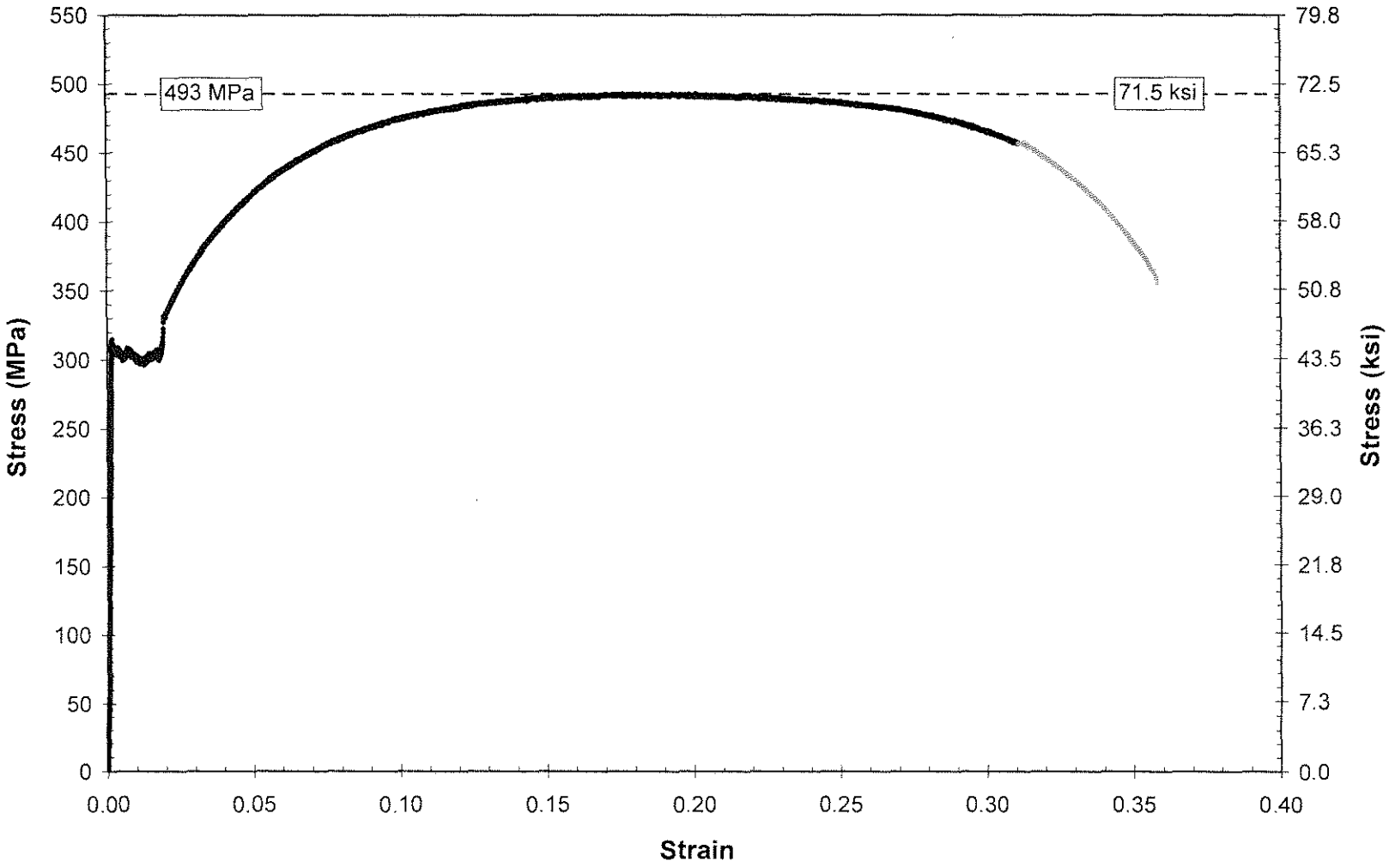

Figure E.19. Stress versus strain plot used to determine tensile strength for specimen T4.

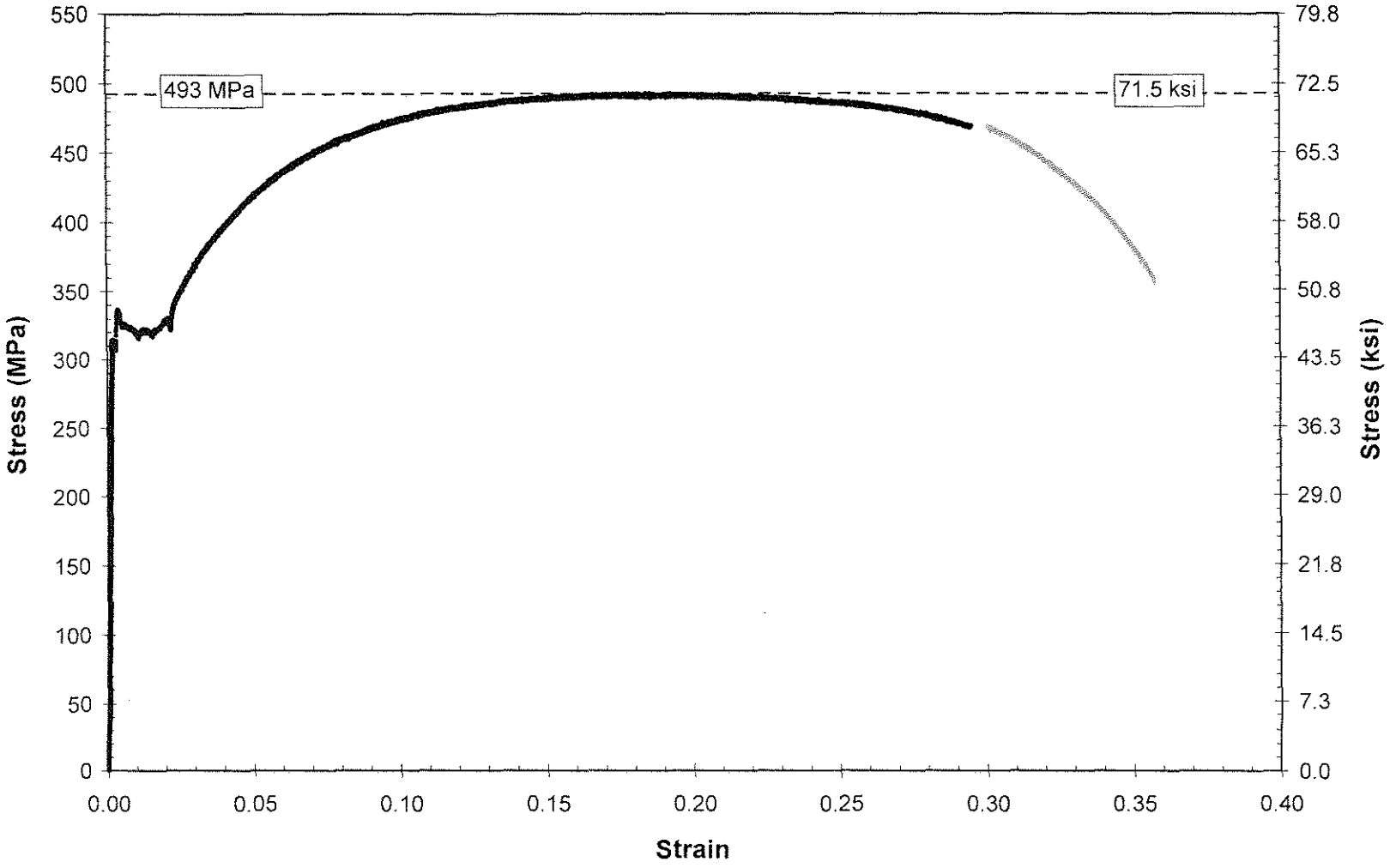

Figure E.20. Stress versus strain plot used to determine tensile strength for specimen T5.

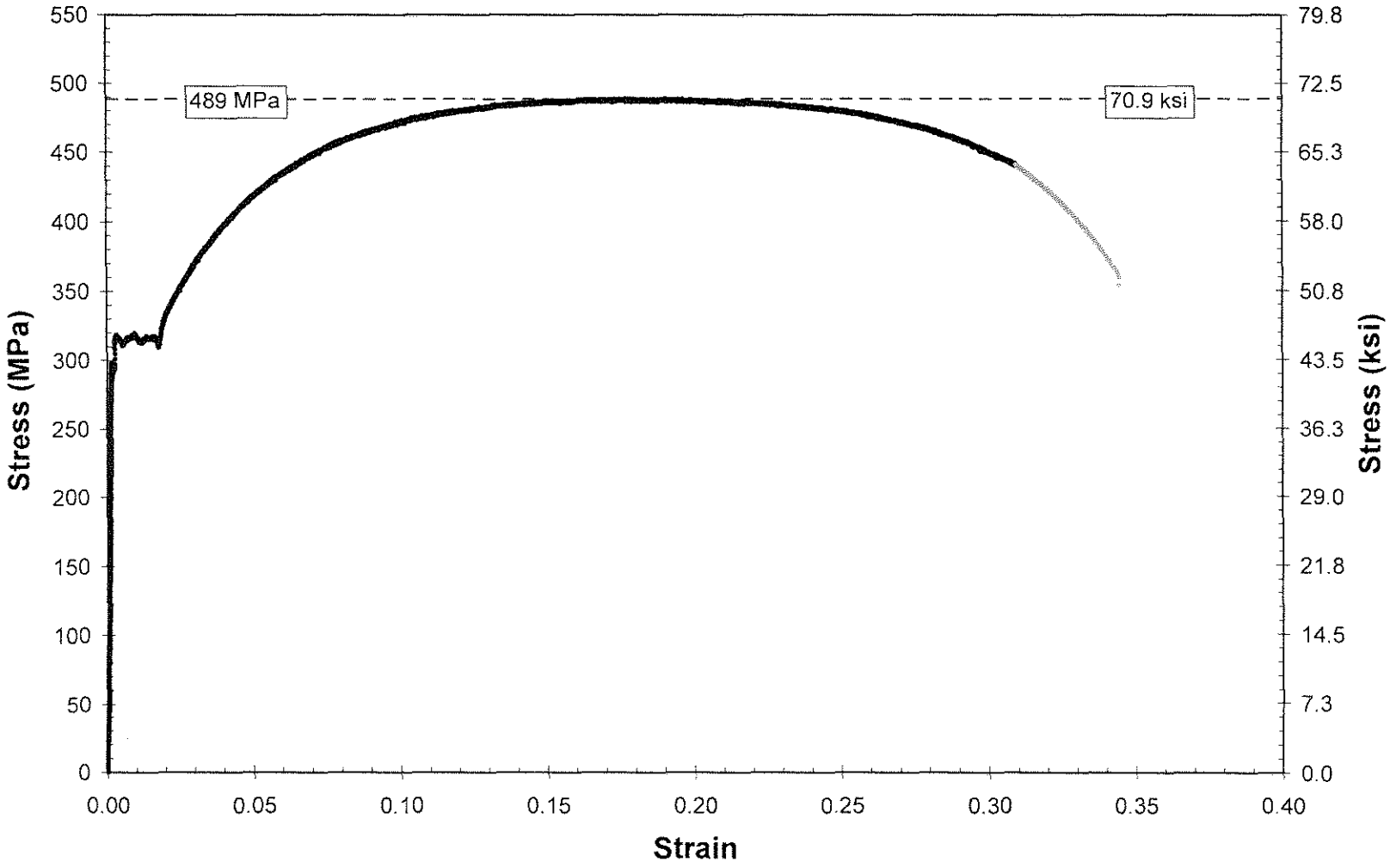

Figure E.21. Stress versus strain plot used to determine tensile strength for specimen T6.

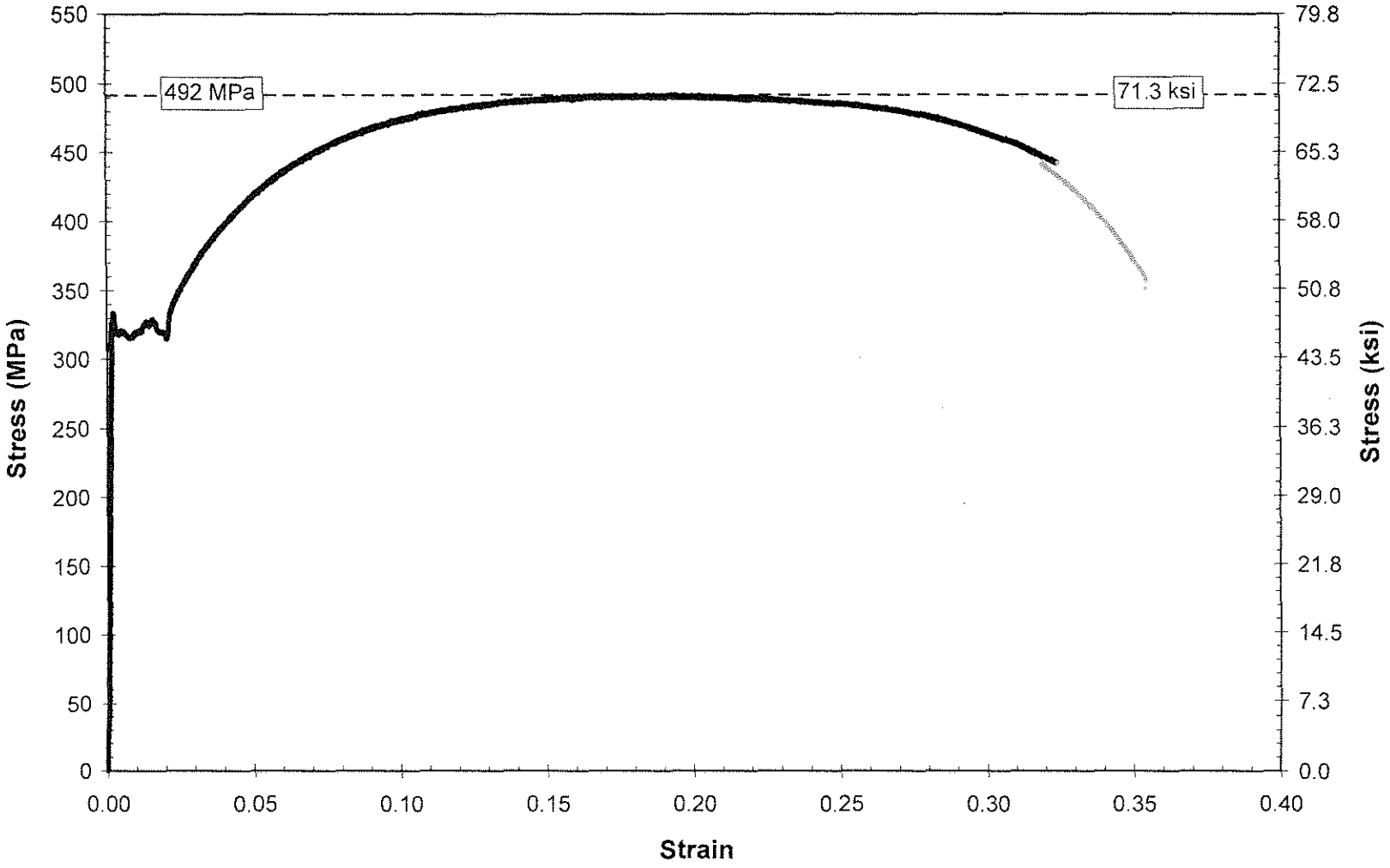

Figure E.22. Stress versus strain plot used to determine tensile strength for specimen T7.

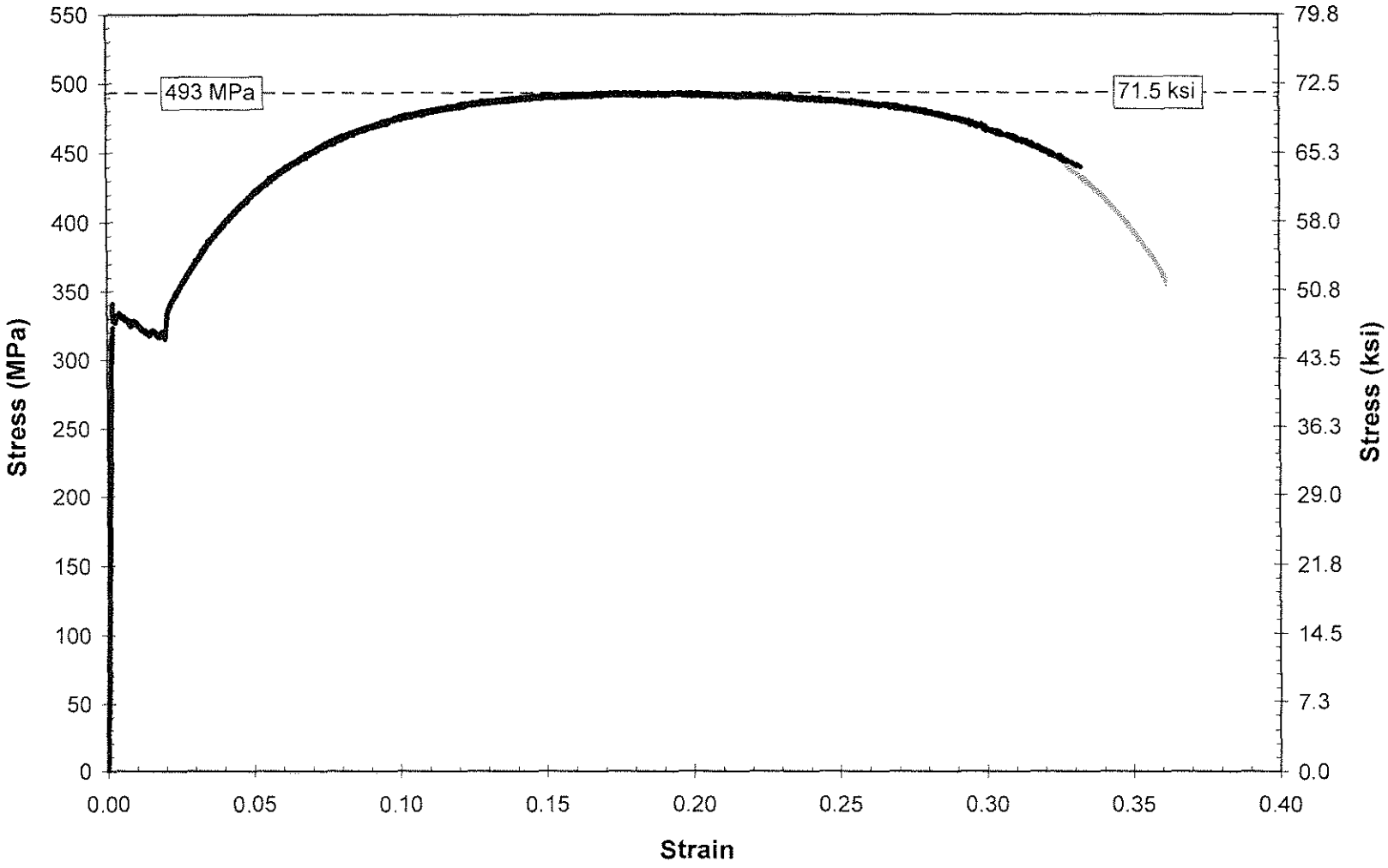

Figure E.23. Stress versus strain plot used to determine tensile strength for specimen T8.

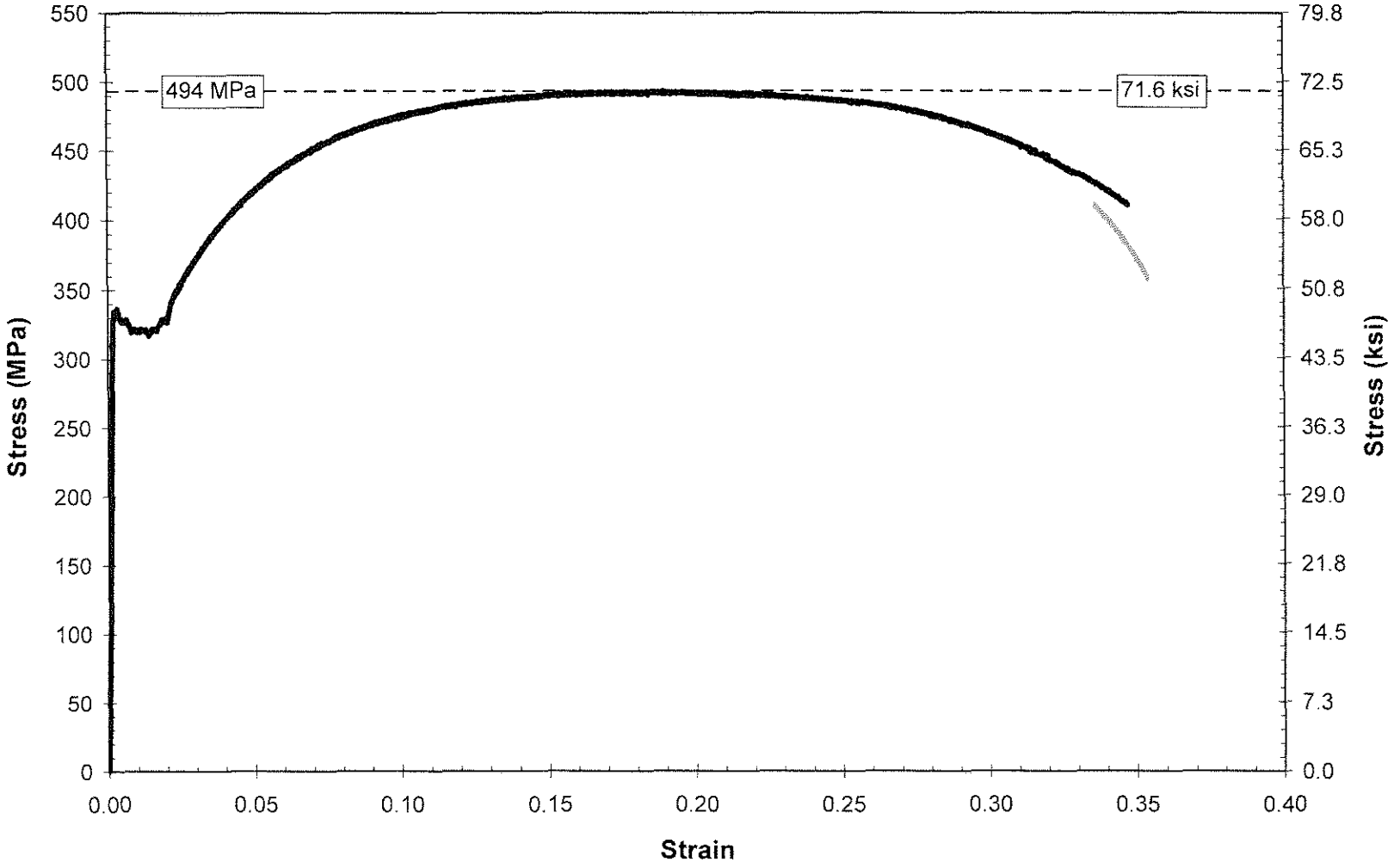

Figure E.24. Stress versus strain plot used to determine tensile strength for specimen T9.

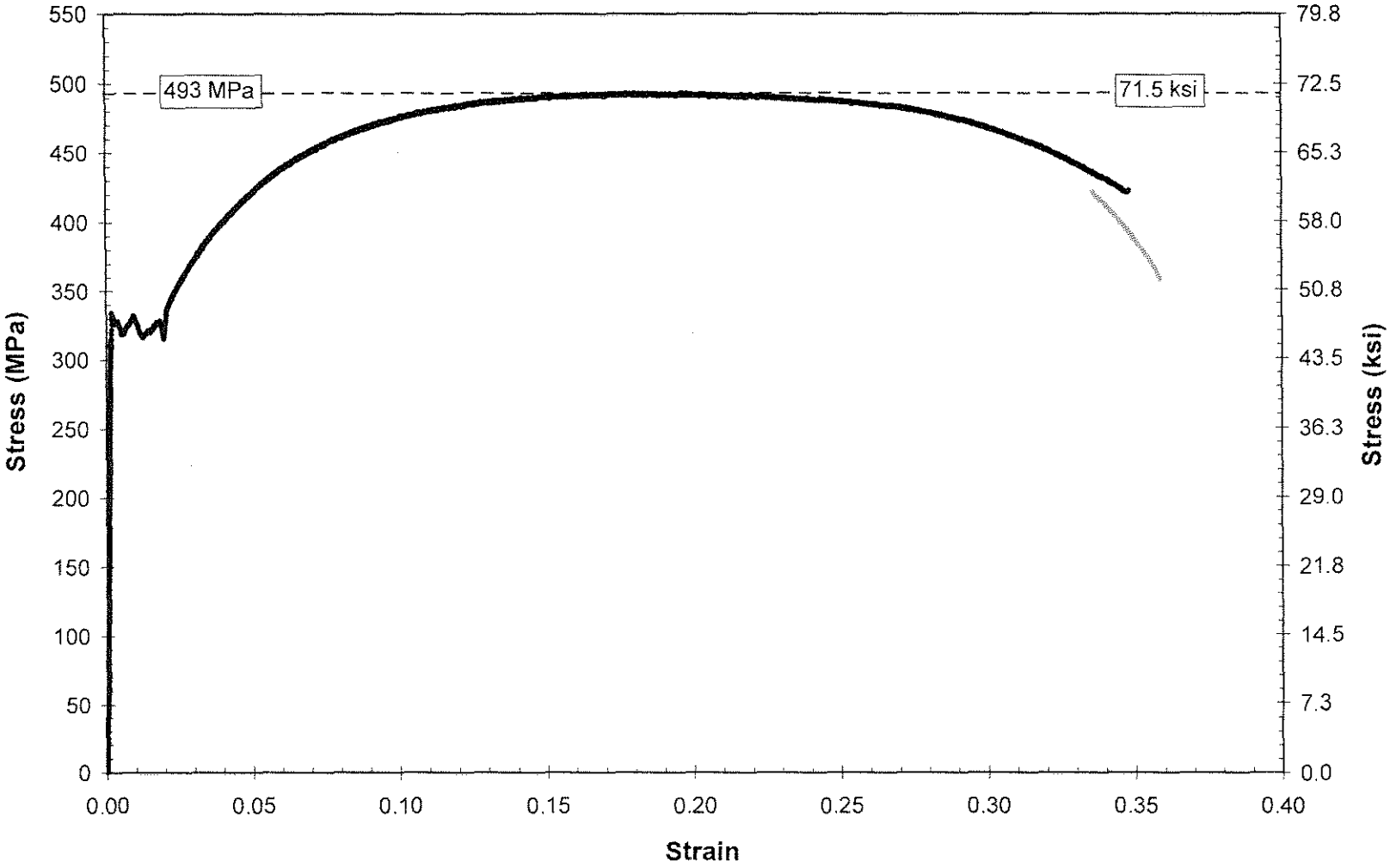

Figure E.25. Stress versus strain plot used to determine tensile strength for specimen T10.

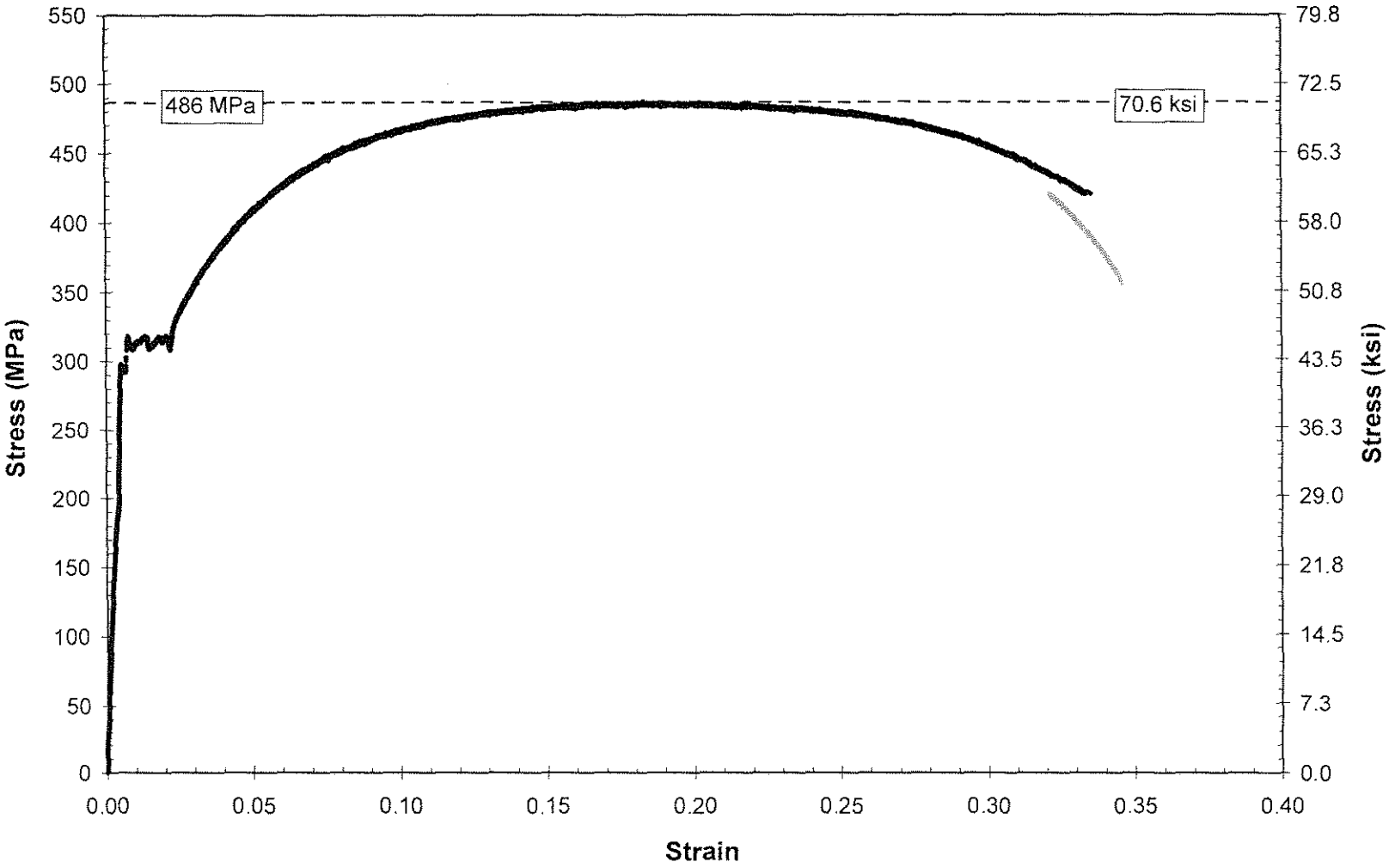

Figure E.26. Stress versus strain plot used to determine tensile strength for specimen T11.

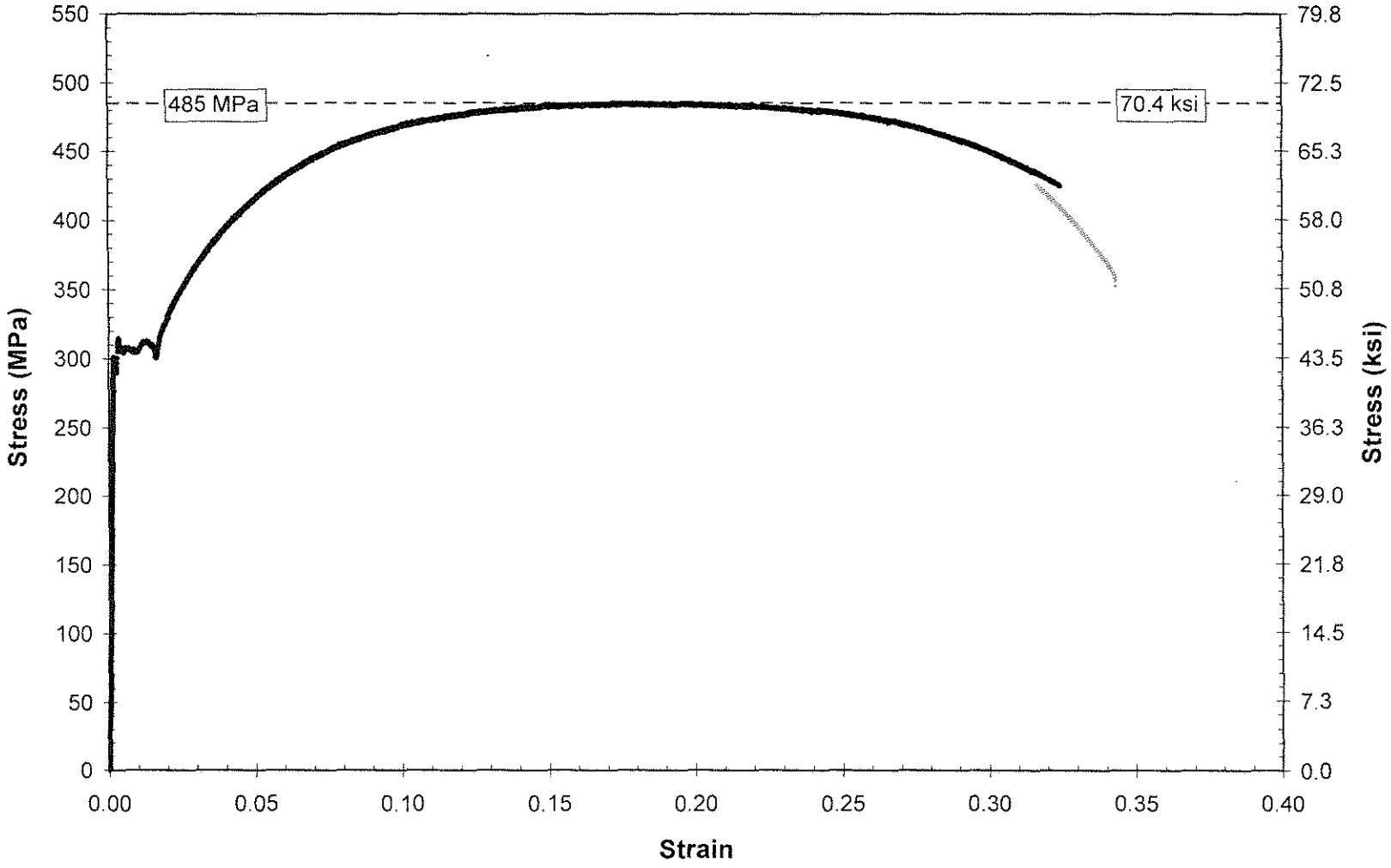

Figure E.27. Stress versus strain plot used to determine tensile strength for specimen T12.

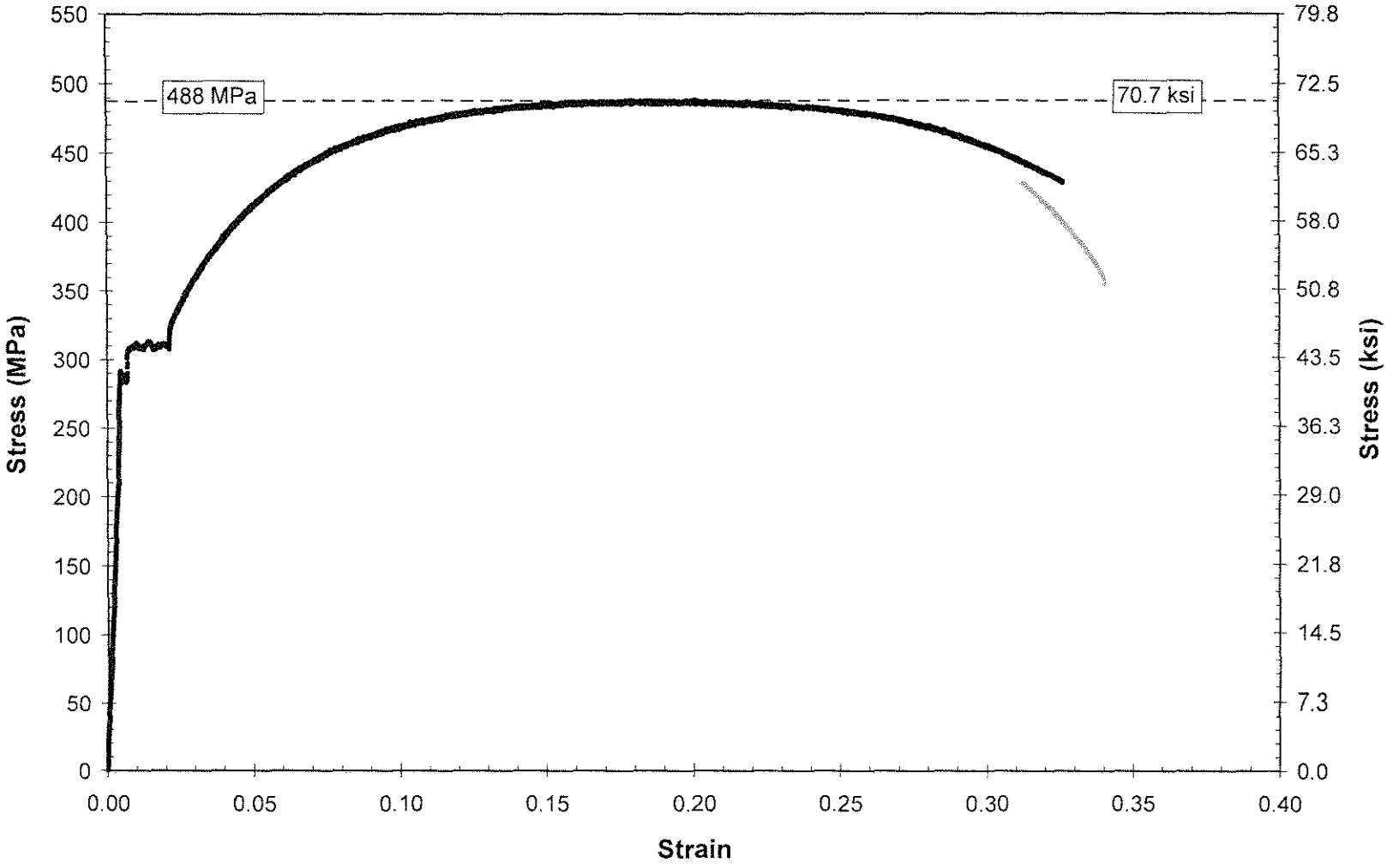

Figure E.28. Stress versus strain plot used to determine tensile strength for specimen T13.

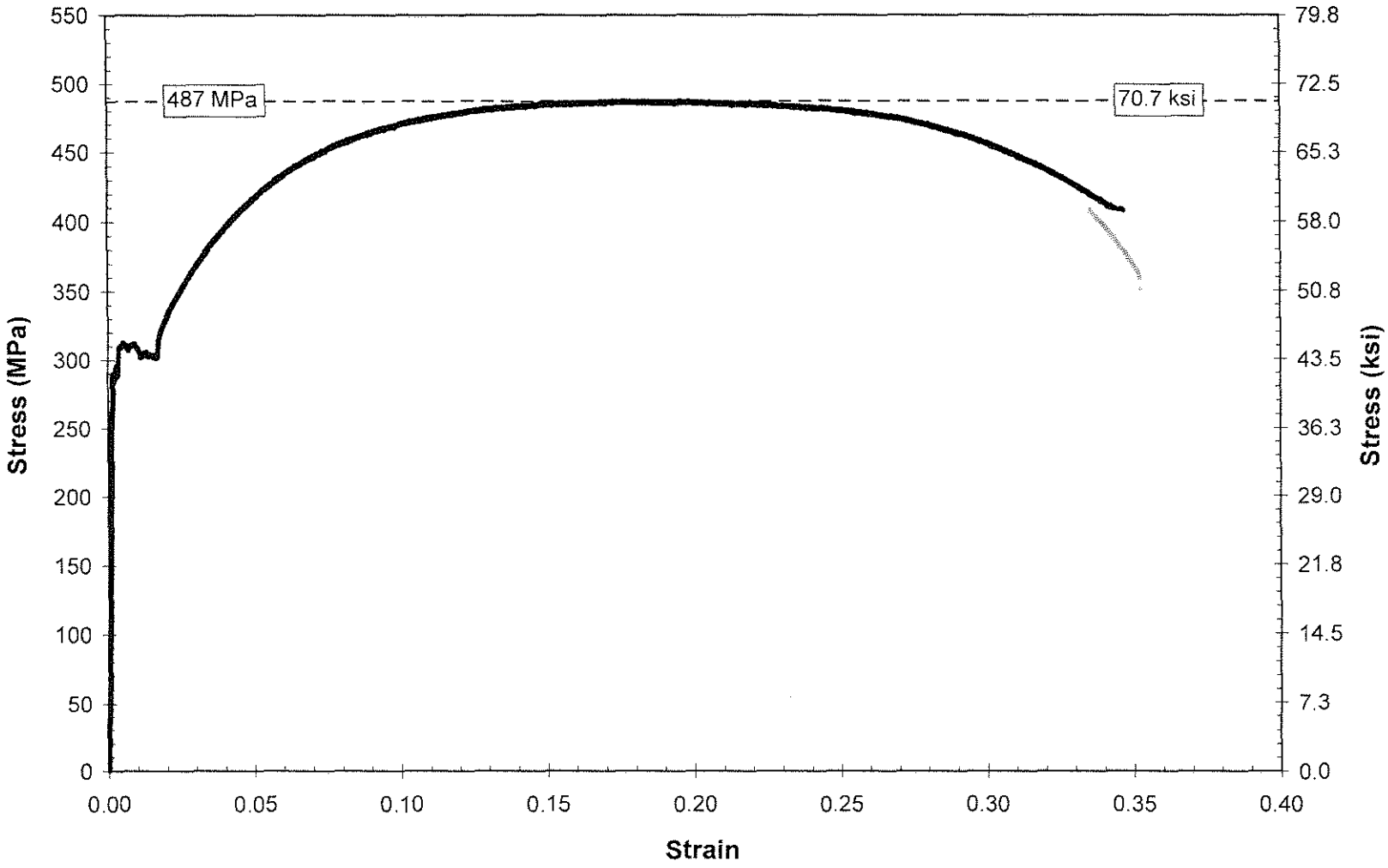

Figure E.29. Stress versus strain plot used to determine tensile strength for specimen T14.

APPENDIX F STRAIN GAGE DATA SHEET

250BG

Vishay Micro-Measurements

VISHAY.

General Purpose Strain Gages - Linear Pattern

GAGE PATTERN DATA

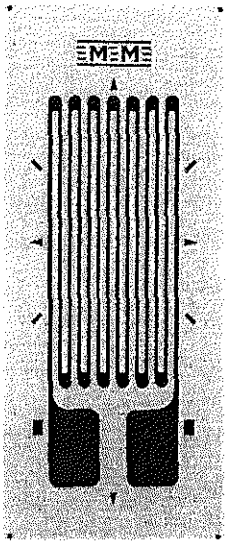

GAGE DESIGNATION See Note 1	RESISTANCE (OHMS) See Note 2	OPTIONS AVAILABLE
EA-XX-250BG-120	120 ± 0.15%	W, E, L, LE, P
ED-DY-250BG-350	350 ± 0.3%	E, L*, LE*
WA-XX-250BG-120	120 ± 0.3%	W*
WK-XX-250BG-350	350 ± 0.3%	W*
EA-XX-250BG-100	100 ± 0.15%	
EP-XX-250BG-120	120 ± 0.15%	
SA-XX-250BG-120	120 ± 0.3%	
SK-XX-250BG-350	350 ± 0.3%	
SD-DY-250BG-350	350 ± 0.6%	
WD-DY-250BG-350	350 ± 0.6%	

DESCRIPTION

Widely used general-purpose gage. Compact geometry. See also 250UN pattern.

GAGE DIMENSIONS Legend: ES = Each Section, S = Section (S1 = Sec 1), CP = Complete Pattern, M = Matrix — inch / millimeter

Gage Length	Overall Length	Grid Width	Overall Width	Matrix Length	Matrix Width
0.250	0.375	0.125	0.125	0.52	0.22
6.35	9.53	3.18	3.18	13.2	5.6

GAGE SERIES DATA See Gage Series data sheet for complete specifications.

Series	Description	Strain Range	Temperature Range
EA	Constantan foil in combination with a tough, flexible, polyimide backing.	±3%	−100° to +350°F [−75° to +175°C]
ED	Isoelastic foil in combination with tough, flexible polyimide film.	±2%	−320° to +400°F [−195° to +205°C]
WA	Fully encapsulated constantan gages with high endurance leadwires.	±2%	−100° to +400°F [−75° to +205°C]
WK	Fully encapsulated K-alloy gages with high-endurance leadwires.	±1.5%	−452° to +550°F [−269° to +230°C]
EP	Annealed constantan foil with tough, high-elongation polyimide backing.	±20%	−100° to +400°F [−75° to +205°C]
SA	Fully encapsulated constantan gages with solder dots.	±2%	−100° to +400°F [−75° to +205°C]
SK	Fully encapsulated K-alloy gages with solder dots.	±1.5%	−452° to +450°F [−269° to +230°C]
SD	Equivalent to WD Series, but with solder dots instead of leadwires.	±1.5%	−320° to +400°F [−195° to +205°C]
WD	Fully encapsulated isoelastic gages with high-endurance leadwires.	±1.5%	−320° to +500°F [−195° to +260°C]

Note 1: Insert desired S-T-C number in spaces marked XX.

Note 2: Tolerance is increased when Option W, E, SE, LE, or P is specified.

*Options available but not normally recommended. See Optional Features data sheet for details.

Figure F.1. Strain Gage Data Sheet (Vishay 2007b)

APPENDIX G RISA-3D RESULTS

Company : University of Kansas CEAE Department
Designer : Brian Vilhauer
Job Number : Three Point Bending Frame

Aug 7, 2007
9:24 AM
Checked By:_____

Joint Deflections

	LC	Joint Label	X [in]	Y [in]	Z [in]	X Rotation [rad]	Y Rotation [rad]	Z Rotation [rad]
1	1	N1	0	-.029	0	0	0	1.289e-3
2	1	N2	0	-.029	0	0	0	-1.289e-3
3	1	N3	0	0	0	0	0	0
4	1	N4	0	-.018	0	0	0	1.289e-3
5	1	N5	0	0	0	0	0	4.685e-4
6	1	N6	0	0	0	0	0	-4.685e-4
7	1	N7	0	-.018	0	0	0	-1.289e-3

Joint Reactions (By Combination)

	LC	Joint Label	X [k]	Y [k]	Z [k]	MX [k-ft]	MY [k-ft]	MZ [k-ft]
1	1	N3	0	6.831	0	0	0	0
2	1	N6	0	6.833	0	0	0	0
3	1	N5	0	9.833	0	0	0	0
4	1	Totals:	0	4.835	0			
5	1	COG (in):	X: 30	Y: 0	Z: 0			

Joint Loads and Enforced Displacements (BLC 1 : Instron Load)

	Joint Label	L,D,M	Direction	Magnitude[k,k-ft,in,rad,k*s^2/in]
1	N4	L	X	-2.417
2	N7	L	X	-2.417

Member Section Deflections (By Combination)

	LC	Member Label	Sec	x [in]	y [in]	z [in]	x Rotation[r	(n) L/y Ratio	(n) L/z Ratio
1	1	M1	1	0	-.029	0	0	NC	NC
2			2	0	-.009	0	0	3005.614	NC
3			3	0	0	0	0	2099.876	NC
4			4	0	-.009	0	0	3005.614	NC
5			5	0	-.029	0	0	NC	NC

Member Section Forces (By Combination)

	LC	Member Label	Sec	Axial[k]	y Shear[k]	z Shear[k]	Torque[k-ft]	y-y Moment[k-...	z-z Moment[k-...
1	1	M1	1	0	0	0	0	0	0
2			2	0	-2.417	0	0	0	1.41
3			3	0	3.416	0	0	0	1.394
4			4	0	2.417	0	0	0	1.41
5			5	0	0	0	0	0	0

Member Section Stresses

	LC	Member Label	Sec	Axial[ksi]	y Shear[ksi]	z Shear[ksi]	y top Bendin	y bot Bendin	z top Bendin	z bot Bendin
1	1	M1	1	0	0	0	0	0	0	0
2			2	0	-1.386	0	-3.356	3.356	0	0
3			3	0	1.959	0	-3.317	3.317	0	0
4			4	0	1.386	0	-3.356	3.356	0	0
5			5	0	0	0	0	0	0	0

RISA-3D Demonstration Version 6.0 [C:\RISA\untitled.r3d] Page 4

Figure G.1. Results of RISA-3D Analysis

Joint Boundary Conditions

	Joint Label	X [k/in]	Y [k/in]	Z [k/in]	X Rot [k-ft/rad]	Y Rot [k-ft/rad]	Z Rot [k-ft/rad]	Footing
1	N3	Reaction	Reaction	Reaction	Reaction	Reaction	Reaction	
2	N6		Reaction					
3	N5		Reaction					

Joint Coordinates and Temperatures

	Label	X [in]	Y [in]	Z [in]	Temp [F]	Detach From Diap
1	N1	0	0	0	0	
2	N2	60	0	0	0	
3	N3	59	0	0	0	
4	N4	8	0	0	0	
5	N5	23.75	0	0	0	
6	N6	36.25	0	0	0	
7	N7	52	0	0	0	

Figure G.2. Results of RISA-3D analysis (cont.)

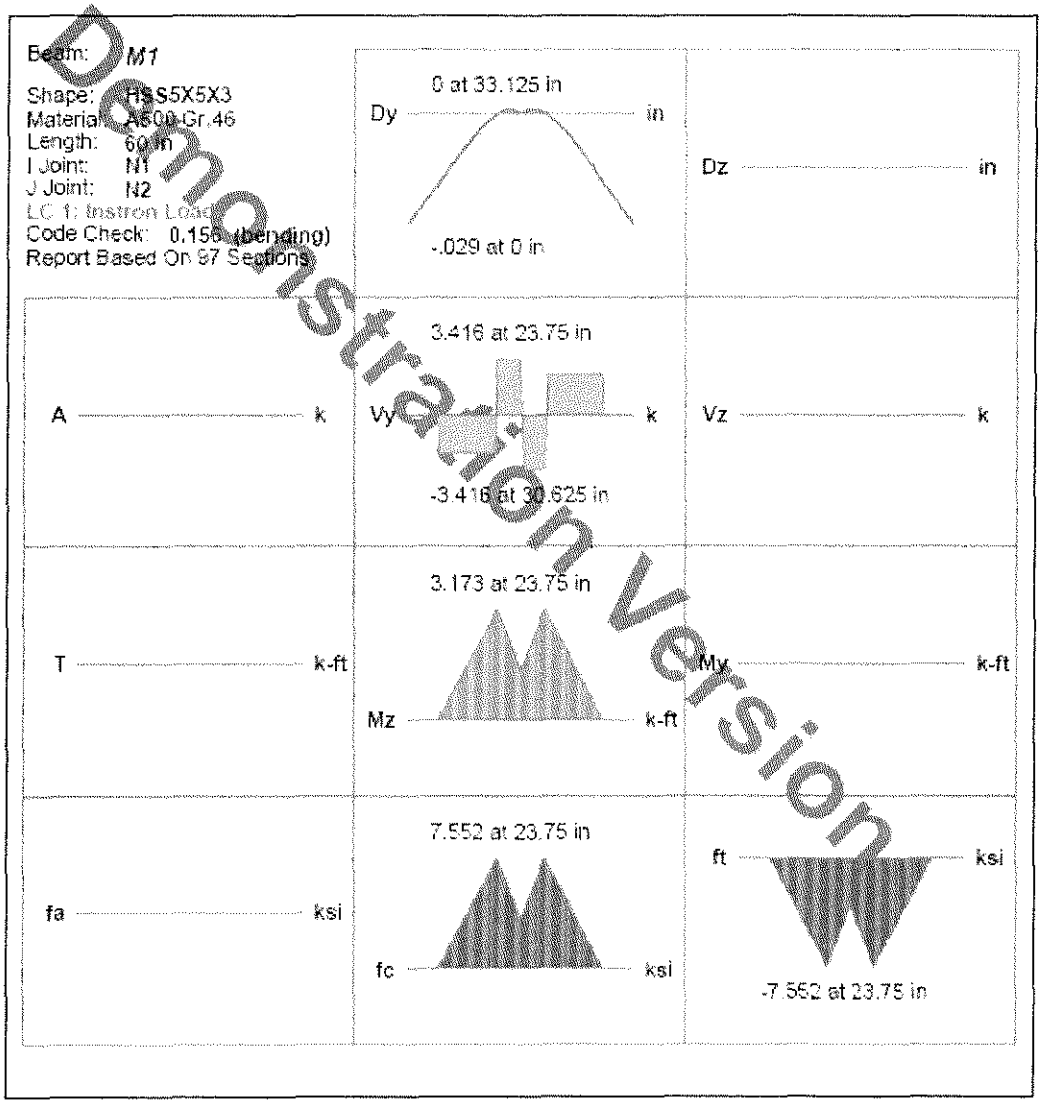

Figure G.3. Bending forces and moment in the tube.

APPENDIX H SAMPLE CALCULATIONS

All sample calculations shown are for a nominal stress range of 193 MPa (28.0 ksi) at the transverse weld toe. All sample calculations shown were performed using U.S. Customary units and subsequently converted to SI units.

H.1 REQUIRED LOAD RANGE

$\sigma_{req} = 28.0\ \text{ksi}$

$$M_{req} = \frac{\sigma_{req} I}{y}$$

$$I = \left(\frac{1}{12}\right) bh^3 = \left(\frac{1}{12}\right)(4.5\ \text{in})(1.0\ \text{in})^3 = 0.375\ \text{in}^4$$

$y = 0.5$ in (At the weld toe)

$$M_{req} = \frac{28\ \text{ksi}\left(0.375\ \text{in}^4\right)}{0.5\ \text{in}} = 21\ \text{kip - in}$$

$M_{req} = \frac{P_{req}}{2} \cdot x$ where x = distance from weld toe to closer outside loading point of the three-point-bending frame = 8.6875 in.

$$P_{req} = \frac{2M_{req}}{x} = \frac{2\left(21\ \text{kip - in}\right)}{8.6875\ \text{in}} = \mathbf{4.835\ kips} = \text{required load range} = P_{range}$$

Conversion:

$$4.835\ \text{kips} \cdot \frac{4.44822\ \text{kN}}{\text{kip}} = \mathbf{21.51\ kN} = \text{required load range (SI)}$$

H.2 MINIMUM AND MAXIMUM LOADS

$$r = 0.1 = \frac{P_{min}}{P_{max}}$$

$$P_{max} = P_{min} + P_{range}$$

$$0.1 = \frac{P_{min}}{P_{min} + P_{range}}$$

$$0.1P_{min} + 0.1P_{range} = P_{min}$$

$$0.1P_{range} = 0.9P_{min}$$

$$P_{min} = \frac{0.1}{0.9} P_{range} = \frac{P_{range}}{9}$$

$$P_{min} = \frac{4.835 \text{ kips}}{9} = \mathbf{0.5372 \text{ kips}} = \mathbf{P_{min}}$$

$$P_{max} = P_{min} + P_{range} = 0.5372 \text{ kips} + 4.835 \text{ kips} = \mathbf{5.3722 \text{ kips}} = \mathbf{P_{max}}$$

H.3 STRESS RANGE CALCULATED FROM STRAIN RANGE

E = 27,800 ksi (determined from tensile testing; see section 4.6)

$$\sigma_{range} = E \cdot \varepsilon_{range}$$

For an assumed ε_{range} (strain range) of 900 $\mu\varepsilon$:

$$\sigma_{range} = 900 \, \mu\varepsilon \bullet \frac{10^{-6} \, \varepsilon}{\mu\varepsilon} \bullet 27{,}800 \text{ ksi} = \mathbf{25.0 \text{ ksi}}$$